POLITECNICO DI MILANO
MOX - DIPARTIMENTO DI MATEMATICA
MODELLI E METODI MATEMATICI PER L'INGEGNERIA

REDUCED-ORDER MODELS FOR INVERSE PROBLEMS AND UNCERTAINTY QUANTIFICATION IN CARDIAC ELECTROPHYSIOLOGY

Doctoral Dissertation of:
Stefano Pagani

Supervisors:
Prof. Alfio Quarteroni
Dr. Andrea Manzoni

The Chair of the Doctoral Program:
Prof. Irene Sabadini

XXIX cycle

Simplicity does not precede complexity,
but follows it
— Alan J. Perlis

Acknowledgements

I would like to sincerely thank my advisor, Prof. Alfio Quarteroni, and my co-advisor, Dr. Andrea Manzoni, for giving me the opportunity, the resources, and the freedom to develop my research activity. In particular, I am thankful to Andrea for his patience and willing to assist me with his advice (all the best to your *growing* family). I would like also to thank the reviewers of the PhD Thesis for their very insightful and constructive feedbacks, which will be of great value also for the continuation of my research activity.
I also want to thank Prof. Anna Maria Paganoni for solving any difficulty with a smile, and Dr. Kevin Carlberg for the stimulating insights and the inspiring discussions on reduced-order model error surrogate.
This work was partially supported by the Italian "National Group of Computing Science" (GNCS-INDAM).

Let's now turn to informal Acknowledgements.
A special thanks to my students (I hope that you have learned from me as I have from you) and to all the PhD students met at summer schools and conferences (among all Marco, Nicola, Giulia, Licia and Valentina).
My period abroad at Ecole Polytechnique Fédérale de Lausanne (EPFL) provides important friendships with Matteo, Nello, Barte, Paolo and Claudia. Skiing, games and fondue were the perfect glue. Above all, a special thanks to Niccolò for the hospitality and for pushing me into new adventures, and to Luca Dedé for his kindness (all the best for the recent changes).
The greatest part of my time has been spent in the legendary 222 office with my fellows Franz, Nich and Mattia. At first, *I don't know half of you half as well as I should like;* but, *dear friends, it comes the end of our fellowship. I will not say: do not weep; for not all tears are an evil.* Alice was surely the fifth fellow (I'm sorry that we missed the chance to work side by side).
Many thanks to all the people who made me feel home in these three years. I've often travelled and having some fixed points (Paris, Lausanne and Milano) was of great support. Special mention for B&U&M, hotel Broetz and its guests: the inspiring chats with Vinicio and Luca have boosted my work and my understanding of the broader picture. I would like to thank my dear friend Marco, my partner in culinary crime Sonia, Clara and all Camilla's friends. Thank you, Lorenzo, for you solid friendship: its value is increasing even with the distance.

I would like to dedicated this work to my grandparents, who have seen the beginning but not the end of this long journey. I am thankful to my parents for constantly giving me the greatest gift: the freedom of managing my time.
In the end, I would like to deeply thank Camilla. You were there for me every step of the way with your love and unconditional support. I keep falling head over heels in love with you.

Abstract

The objective of this Thesis is to develop reduced-order models (ROMs) for the efficient and accurate solution of uncertainty quantification (UQ) and inverse problems arising in cardiac electrophysiology. Cardiac models could be affected by a significant amount of uncertainties related to both physical and geometrical parameters, such as inter-subject and intra-subject variability. Developing UQ and inverse techniques is crucial for a personalization of these models: a notable example is the estimation of myocardial ischemia shape and location in a realistic left ventricle, which represents an important application proposed in this work.
Inverse and UQ problems involve many queries to input-output maps requiring the solution of a nonlinear parametrized coupled system of ordinary and partial differential equations (PDEs), such as the monodomain equation equipped with ionic models. Prohibitive computational costs occur when full-order models (FOMs), relying e.g. on the finite element method, are adopted for the numerical approximation of the PDEs. In order to reduce the computational complexity, we exploit the reduced basis (RB) method to approximate the parametrized PDE solution, using the proper orthogonal decomposition technique for the basis functions construction and hyper-reduction techniques for the efficient evaluation of nonlinear terms. However, applying state of the art RB method is not straightforward for this application, since the electric potential evolution is characterized by a sharp traveling front highly sensible to changes in the model parameters. In order to recover a rapid and reliable approximation, we develop localized-ROMs based on suitable clustering techniques for the sake of local RB spaces selection. Moreover, since classical error estimators are out of reach in this context, we introduce ad hoc statistical error surrogates for error quantification. This latter ingredient is essential for the solution of inverse problems in order to minimize the propagation of the approximation error, which could lead to biased estimates when a FOM is replaced with a ROM.
After providing a detailed analysis and a comparison of these techniques on some suitable numerical tests, we apply the proposed method for sensitivity analysis and uncertainty quantification. In particular, we study how the model parameters affect the electrocardiogram or action-potential shape, providing interesting insights about the role and the importance of cardiac model parameters.
Furthermore, we consider filtering techniques for the solution of parameter estimation problems. We develop a reduced-basis state-parameter ensemble Kalman filter and we analyze its consistency and effectivity. This methodology is finally applied to the estimation of myocardial ischemia shape and location on a patient-specific left ventricle.

Key words: Reduced-order models, reduced basis method, error surrogates, uncertainty quantification, parameter estimation, cardiac electrophysiology.

Sommario

L'obiettivo di questa Tesi è quello di sviluppare modelli ridotti (ROM) per risolvere in modo efficiente e accurato problemi di quantificazione dell'incertezza e problemi inversi nel campo dell'elettrofisiologia cardiaca. I modelli cardiaci possono presentare un significativo grado di incertezza dovuto sia ai parametri fisici che a quelli geometrici, come ad esempio la variabilità tra soggetti e nel soggetto stesso. Lo sviluppo di tecniche per la soluzione di problemi inversi e di quantificazione dell'incertezza è fondamentale per la personalizzazione di questi modelli: un esempio rilevante, che rappresenta un'importante applicazione proposta in questo lavoro, è quello della stima della forma e della posizione di un'ischemia miocardica in un ventricolo sinistro realistico. I problemi inversi e di quantificazione dell'incertezza comportano molte valutazioni della mappa tra gli input e gli output, che richiedono la soluzione di un sistema parametrico non lineare accoppiato di equazioni differenziali parziali (EDP) e ordinarie, come ad esempio l'equazione monodominio accoppiata con modelli ionici. Risolvere numericamente le EDP con modelli full-order (FOM), come ad esempio un metodo a elementi finiti, comporta costi computazionali proibitivi. Per ridurre la complessità computazionale, sfruttiamo il metodo a basi ridotte (RB) per approssimare la soluzione parametrica dell'EDP, utilizzando tecniche di iper-riduzione per valutare in modo efficiente i termini non lineari. Tuttavia, usare il metodo a basi ridotte non è immediato per questa applicazione, poiché l'evoluzione del potenziale elettrico è caratterizzata da un fronte viaggiante piuttosto ripido che è fortemente sensibile a variazioni nei parametri del modello. Per ottenere un'approssimazione rapida e affidabile, sviluppiamo ROM localizzati basati su tecniche di clustering per la scelta degli spazi RB locali. Inoltre, poiché gli stimatori dell'errore classici non sono applicabili in questo contesto, introduciamo dei modelli surrogati per la quantificazione dell'errore. Quest'ultima aggiunta è fondamentale per la soluzione di problemi inversi, in quanto permette di minimizzare la propagazione dell'errore di approssimazione, che può condurre a stime con bias quando un FOM è sostituito da un ROM. Dopo aver analizzato in dettaglio e aver confrontato queste tecniche su alcuni casi test numerici, applichiamo il metodo proposto all'analisi di sensitività e alla propagazione di incertezza. In particolare, studiamo come i parametri del modello influiscano sull'elettrocardiogramma o sulla forma del potenziale di azione, in modo da agevolare la comprensione del ruolo e dell'importanza dei parametri nei modelli cardiaci. Inoltre, consideriamo tecniche di data-assimilation per la soluzione di problemi di stima dei parametri. Sviluppiamo un filtro di Kalman ridotto e ne analizziamo la consistenza e l'efficacia. Infine, questa metodologia viene applicata alla stima della forma e della posizione di un'ischemia miocardica nel ventricolo sinistro in un caso patient-specific.

Parole chiave: modelli ridotti, surrogati dell'errore, metodo a basi ridotte, quantificazione dell'incertezza, stima dei parametri, elettrofisiologia.

Contents

List of Figures

List of Tables

Introduction

Cardiovascular diseases are actually among the most widespread and costly health problems worldwide, representing the major cause of death with more than 17.3 million deaths per year, a number that is expected to grow to more than 23.6 million by 2030 [MBG+16]. A major challenge for medical research is to develop efficient and accurate tools in support of diagnosis and optimal therapy design. Large-scale clinical data are nowadays used to improve clinical decisions and also to define new therapies [CBB+01, KGB+07]. Moreover, technological aids to diagnosis are becoming widely available: imaging techniques, such as magnetic resonance imaging and computed tomography [BS16, HPK+06], provide detailed information about the function and dysfunction of the heart.

Mathematical models and numerical methods can aid medical research: on the one hand, they improve data acquisition, by reducing the noise that affects the measurements; on the other hand, they are able to reproduce accurately in silico cardiovascular (patho)physiology in order to improve the diagnosis of cardiovascular diseases. With this aim, several models have been developed to describe single (and coupled) functionalities, such as cardiac electrophysiology, tissue mechanics and hemodynamics [Qua15, Tra11, NNN+11, SNC+04, NMK+11, NHS08, TDQ15]. Physical indices and outputs of clinical interest can be directly approximated through the numerical solution of the cardiac mathematical models for a given set of parametrized inputs (geometry, physical coefficients, initial and boundary conditions).

For cardiac electrophysiology, input-output evaluations require the solution of a nonlinear parametrized coupled system of ordinary and partial differential equations (PDEs), such as the bidomain or monodomain equations, equipped with suitable ionic models. The so-called *full-order models* (FOMs), obtained by e.g. a finite element, finite volume or spectral methods approximation of the cardiac parametrized PDEs, are computationally expensive.

In order to reduce their computational complexity, reduced-order models (ROMs) represent emerging techniques for the efficient approximation of the parametrized PDE solution. However, applying state of the art ROMs is not straightforward for cardiac problems. For instance in the case of cardiac electrophysiology, the electrical activity is characterized by a sharp traveling front highly sensible to changes in the model parameters, while in the case of cardiac mechanics, the torsion and shortening of the muscle are influenced by model inputs, such as fiber directions and bulk modulus. Depending on the problem at hand, new reduction strategies must be developed in order to recover an efficient approximation of the PDE model.

Integrating large-scale clinical data within mathematical models is a challenging opportunity towards tailoring new subject-specific therapies and assisting cardiac interventions. This is a severe task due to the complexity of the electrophysiology models and the prohibitive computational costs induced by the high number of input/output evaluations.
Moreover, cardiac models contain many uncertainties, due to the several model assumptions and the difficulties in measuring the quantities of interest for the problem. There are many potential sources of error/uncertainty to deal with [KO01], among which we mention:

- measurement errors in experimental data due e.g. to limited accuracy of the measuring apparatus or limitations and simplifications of the experimental procedure;

- inter and intra-subject variability, which affects the parametrized inputs of the mathematical models (namely geometrical and physical coefficients, initial and boundary conditions uncertainties). The exact values of the inputs could be (partially) unknown due to e.g. difficulties in their measurements;

- model uncertainties arising when a physical process is described by a mathematical model, which inevitably simplifies reality. This also includes the discretization error introduced by the selected numerical approximation strategy when e.g. a PDE problem is involved.

These different sources of uncertainty are usually classified in two classes: *epistemic* and *aleatory*. The former stems from a lack of knowledge, caused e.g. by a lack of accuracy in the measurement or in the adopted model. In principle, *epistemic* uncertainties can be reduced by adding information, such as more detailed models or further data. On the other hand, *aleatory* uncertainties are generated by the intrinsic randomness of the phenomenon, so that there is no possibility to reduce them [DKD09].

Therefore, translating mathematical models into clinical procedures is not limited to the estimation of the inputs whose corresponding outputs best fit available clinical data. Data-model integration involves instead many open and challenging problems [SdVM$^+$11, SMC$^+$06, CWH$^+$16, LNN$^+$11]. Some of those include:

1. *model calibration*, which consists in correcting the bias of the simulation output with respect to physical data [KO01];

2. *uncertainty characterization and propagation*, which gives a quantitative characterization and reduction of uncertainties in computational applications [Sul15, Smi13, IH88];

3. *inverse problem* of estimating the inputs of a system from a set of noisy observations [Tar05, Han10, ABT13]; a relevant example is the calibration of the model parameters given noisy data coming from a specific subject (personalization of the model);

4. *data assimilation*, which incorporates sequential observations of the state of the system into the numerical model for the estimation of the current state and/or one or several parameters e.g. using Kalman filtering techniques [Eve09, LSZ15].

The complexity of the cardiac models and of the available data introduces several difficulties when performing these procedures. In this perspective, this Thesis contributes to address the challenges previously described by developing suitable reduction strategies for cardiac electrophysiology problem and by integrating them in uncertainty quantification (UQ) and inversion procedure. The numerical examples provided in this work however deal with simplified mathematical models and representations of electrical potential measurements.

Objectives and contributions of this work

The goal of this Thesis is to develop efficient and accurate reduced-order models to perform *model calibration and uncertainty quantification* and to solve *inverse and data assimilation problems* in the context of cardiac electrophysiology. To this aim, we identify the following main objectives:

1. **To design an efficient reduced-order model for cardiac electrophysiology**.

   A projection-based *reduced-order model* provide a low-dimensional approximation of a parametrized FOM, obtained by reducing the number of equations and of the corresponding unknowns involved in it. To this goal, ROMs are characterized by low-dimensional operators, obtained by projecting the FOM onto a low-dimensional subspace, previously computed during a computationally intensive offline phase.

   When the unsteady nonlinear reaction-diffusion PDEs characterizing the cardiac electrophysiology are considered, the dimensional reduction is not a trivial task to accomplish: the manifold spanned by all the possible solutions is not of small dimension, except for simplified problems. Since we aim at constructing low-dimensional (and consequently efficient) ROMs, we propose in this work to rely on suitable techniques to develop localized-ROMs for the class of problems at hand. In particular, we look at different strategies to construct solution snapshots classifications, based on different indicators of the state of the system (time, parameters and state solution). Unsupervised classification techniques, such as *k-means* clustering, will be crucial for the development of localized-ROMs.

   With respect to the few existing contributions in this field (see e.g. [BSG12, CLM$^+$16, YV16]), we present a complete analysis and comparison of some reduction strategies based on the *offline/online* stratagem. As benchmark numerical test we consider a two-dimensional monodomain model describing the behavior of the cardiac potential in presence of an ischemic region over a simplified slab of the myocardial tissue. The reduction strategy identified as optimal for the case at hand is then adopted in all the other numerical test cases to speed up their numerical solution.

2. **To perform ROM calibration through reduced-order model error surrogates**.

   When a FOM is replaced by a ROM, the operation of evaluating an output is affected by model bias depending on the error between the full-order and the reduced-order output (in short, the reduction error). In principle, this error is a deterministic quantity that can be evaluated through the direct solution of the FOM. However to maintain the computational efficiency, this evaluation is out of reach. The problem of ROM calibration, that is the problem of finding an effective and cheaply computable model of the reduction error, is here solved by means of a statistical ROM error surrogate (ROMES). The ROMES approach [DC15, MPL16] has been exploited only for elliptic problems, where computable error bounds are available at moderate costs. Since this is not the case for cardiac electrophysiology, we adapt the ROMES idea in this context using surrogate models.

3. **To perform efficiently uncertainty quantification**.

   A complete characterization of the role and importance of the input parameters (*sensitivity analysis*) is crucial in order to adopt a parameterized model as an approximation of the physical phenomenon of interest: the goal is to determine those model parameters that are the most significant for an experimenter. Since these parameters are also affected by uncertainties, a complete study consists in providing a full characterization of parameters uncertainties (*uncertatinty characterization*) and how they propagate when the outputs of interest are computed (*forward propagation*).

   A popular approach to perform these studies is the Monte Carlo random sampling. The efficiency of this technique is usually guaranteed by statistical surrogates adopted for the efficient evaluation of the input-output query [QHS$^+$05]. However, these models are not physics-based; they might be inaccurate and they suffer from the curse of dimensionality. Our goal is thus to show how UQ analysis benefits from the adoption of ROMs and ROMESs. The insight gained by performing sensitivity analysis and UQ are also crucial in view of the construction of data-driven ROMs.

   Fast UQ could have a great impact on the data-model integration, providing an efficient tool to perform parameter selection. When the complexity and the number of parameters grow, this analysis is mandatory to ensure an effective model personalization. With respect to the empirical sensitivity analysis reported in [MDS$^+$13a] we adopt in this work variance-based *sensitivity analysis* by directly calculating the Sobol indices to rank the model parameters.

4. **Personalization of electrophysiology models**.

   Once a parametrized model is designed and reduced, it could become a fundamental tool for efficiently solving Bayesian *inverse problems* through (sequential) sampling algorithms. These latter procedures enable to estimate the distribution of the model parameters (and also of the state solution) from noisy (non)-invasive clinical measurements. In particular we focus on Markov chain Monte Carlo (MCMC) sampling for parameter estimation and the ensemble Kalman filter (EnKF) for sequential state/parameter estimation. In both cases we investigate the effect of the ROM on the estimate accuracy, showing how to integrate the developed ROMES in these inversion procedures. Two notable examples are considered to demonstrate the reliability of the proposed

procedures for complex three-dimensional models. First, we show how the parameter estimation benefits from the uncertainty quantification analysis when both geometrical and physical uncertainty are taken into account. Second, we consider the estimation of the shape and location of an myocardial ischemia in a realistic left ventricle.

These objectives have offered the opportunity to merge different techniques coming from numerical analysis, scientific computing and (Bayesian) statistics, providing new interesting approaches for the solution of inverse and data-assimilation problems. We underline that the approach developed in this work is not restricted to the electrophysiology models; indeed, it can be adopted for a larger class of unsteady nonlinear PDEs.

Organization of this work

This Thesis comprises three parts:

Part I - Reduced-order models in cardiac electrophysiology

In Chapter 1 we provide a brief introduction on heart physiology and on the cardiac pathologies such as myocardial infarction. We review the clinical available measures and the most relevant mathematical models for cardiac electrophysiology depending on the scale and the level of accuracy.
In Chapter 2 we firstly introduce the numerical approximation of the electrophysiology models, obtained by considering the finite element method as full-order model. FOMs of this kind are usually very expensive from the computational point of view, due to time and space constraints required by the numerical method to accurately reproduce the electrical activity of the heart. In order to reduce the computational complexity, we exploit the reduced basis (RB) method to approximate the parametrized PDE solution, using the proper orthogonal decomposition technique for the basis functions construction and suitable hyper-reduction techniques for the efficient evaluation of nonlinear terms.
This standard reduction techniques does not provide efficient approximation of the phenomenon, due to the high-dimensionality of the manifold spanned by all the possible solutions of the problem. For these reasons, we propose and compare different localization strategies in order **to design an efficient reduced-order model for cardiac electrophysiology**. The discriminating factors for evaluating the performance of the localized-ROM will be efficiency, accuracy and low memory consumption. Some numerical tests will be presented for a two-dimensional benchmark given by the monodomain equation featuring an ischemic region parametrized with respect to its size and position.
In Chapter 3 we introduce surrogate models and we employ them to **perform ROM calibration through reduced-order model error surrogates** (ROMES). We first propose ROMESs based on Gaussian process regression and kriging interpolation for the estimation of scalar-valued output reduction errors. Then, we extend the ROMES methodology to the case of functional-valued outputs, adopting the curve kriging approach.

Part II - Uncertainty quantification and parameter estimation

In Chapter 4 we address the issue of **efficiently solving uncertainty quantification** problems. We introduce a variance-based approach, based on sampling techniques, to deal with global

sensitivity analysis (GSA) and the uncertainty propagation. These problems fit into a many-query context, since repetitive evaluations of the input-output mapping are required for each new parameters value. In this context, we show how a ROM equipped with a ROMES provides better results in term of accuracy of the computed quantities and indices with respect to surrogate models (SMs) of the input-output mapping. We develop a reduced-order variance-based GSA to study how model parameters influence the shape of a simplified ECG signal and of the action-potential. Finally, we propose to address the results of these analyses for better exploring the parameter space during the construction of (data-driven) SMs and ROMs.
In Chapter 5 we introduce the Bayesian framework for the solution of statistical inverse problems in case of scalar-valued outputs. The goal is to show how substituting the FOM with a ROM impacts on the efficiency of the MCMC procedure, adopted for the resolution of the Bayesian inverse problems. A mathematical analysis of both consistency and accuracy will be presented, in particular by showing how incorporating a ROMES for scalar-valued output errors into the Bayesian estimator could improve the parameters identification. Finally, we assess the performance of the proposed framework on a numerical example of inverse problems governed by a simplified heart-torso electrophysiology model.
In Chapter 6 we introduce the basic concepts related to data-assimilation procedures and we focus on the ensemble Kalman Filter (EnKF) for the parameter estimation (together with a state estimation to update the initial conditions of the model). The EnKF sequentially combines available noisy data with a finite number (ensemble) of model evaluation, in order to update the knowledge on the system parameters. A reduced-order formulation is presented, also equipped with the ROMES for functional-valued data presented in Chapter 3. The consistency and the accuracy of this corrected reduced-order EnKF is verified theoretically.

Part III - Integrating data within models

This last part focuses on the **personalization of electrophysiology models**. Our goal is to demonstrate how the combination of the techniques developed in the previous two Parts lead to accurate and efficient model personalization. In Chapter 7 we investigate the impact of sensitivity analysis and uncertainty propagation on the dependence between the action-potential shape and both physical and geometrical parameters of a three-dimensional left-ventricle. This allows to simplify the parametric dependence in order to apply the reduced MCMC technique developed in Chapter 5.
Finally, in Chapter 8 we present some numerical tests related to the data-assimilation procedure for the inference of the cardiac conductivity field of a realistic left-ventricle. The aim is to identify the presence of ischemic regions, modeled as portions of the tissue presenting a lack of conductivity.

The numerical simulations carried out in this Thesis have been performed using `Matlab`, where we have implemented from scratch the considered electrophysiology model and all the *(i)* (localized) reduced-order models, *(ii)* ROM error surrogates, *(iii)* sensitivity analysis and uncertainty propagation techniques and *(iv)* statistical inversion procedures.
For the implementation of the standard reduced-order strategy we have started from the RB package `redbKIT` [Neg16] developed at CMCS-EPFL. Moreover, we have taken advantage of `Matlab` built-in functions to perform *k-means* clustering and gaussian process regression.

Part I

Reduced-order models in cardiac electrophysiology

1 | Mathematical models for cardiac electrophysiology

In this chapter we provide a brief introduction on the mathematical models describing cardiac electrophysiology and the forward problems that will be considered in this Thesis. In Section 1.1 we review the basic principles of the heart function and its electrical activity, as well as the main pathology related to the propagation of the electrical signal. In particular, we focus on myocardial infarction, one of the most widespread diseases worldwide, and on the available measurements, which can be used for diagnostic purposes. In Section 1.2 we review the most relevant mathematical models for cardiac electrophysiology depending on the scale at hand: at the microscopic level, systems of ordinary differential equations (ODEs) describe the cellular action potential generated by ionic currents through the cellular membrane, while at the macroscopic level partial differential equations (PDEs) characterize the propagation of the action potential on the cardiac tissue. Finally, in Section 1.3 the process of integrating data within model is discussed showing the main challenges arising in this field and our contributions to address some of them.

1.1 Overview

Cardiac electrophysiology studies the electrical activity of the heart with the aim of understanding, diagnosing and treating possible malfunctioning. The rhythmic contraction of the heart is governed by an electrical impulse. A periodic electrical signal travels through the heart according to a regular pattern, inducing heart contraction. Therefore, any irregularity in the electrical signal causes a non physiological heart contraction. For a comprehensive review see e.g. [Kat10, Lil12].

The heart is a muscle that pumps blood through the circulatory system and it is formed by four chambers: right and left ventricles, right and left atria. The right atrium collects blood low in oxygen from the whole body through the veins, the right ventricle then delivers it to the lungs from where the left atrium receives it back oxygenated, ready to be pumped from the left ventricle through the arteries. A healthy cardiac electric cycle starts from the sinoatrial node, located in the right atrium, made of a group of pacemaking cells. From the sinoatrial node, the electrical signal travels along the atria to the atrioventricular node, causing the contraction of the two atria. Then the signal is propagated through the ventricles by means of the Purkinje fibers, in order to sequentially pace the ventricles. At this point a process of repolarization starts: the muscle fibers are relaxed in order to restore the initial condition, after which the muscle is ready to contract again.

There are several heart diseases that affect the electrical activity, such as coronary artery block, which can lead to stroke or heart attack, structural disease (cardiomyopathy), congenital abnormalities of the heart muscle or the valves, and arrhythmia. In particular, the latter is an irregular heartbeat caused by anomalies such as pauses in the normal activity of the sinoatrial node or block of the electrical impulse due to the presence of scars. When the heart has an abnormal sinus rhythm, it cannot pump blood effectively to the whole body, causing possible damages to other organs.

1.1.1 Myocardial infarction

Myocardial infarction (MI), commonly referred to as heart attack, is one of the most widespread heart diseases worldwide. The infarction is a portion of the heart muscle damaged by a lack of blood flow due to an obstruction of a coronary artery [TAW07].

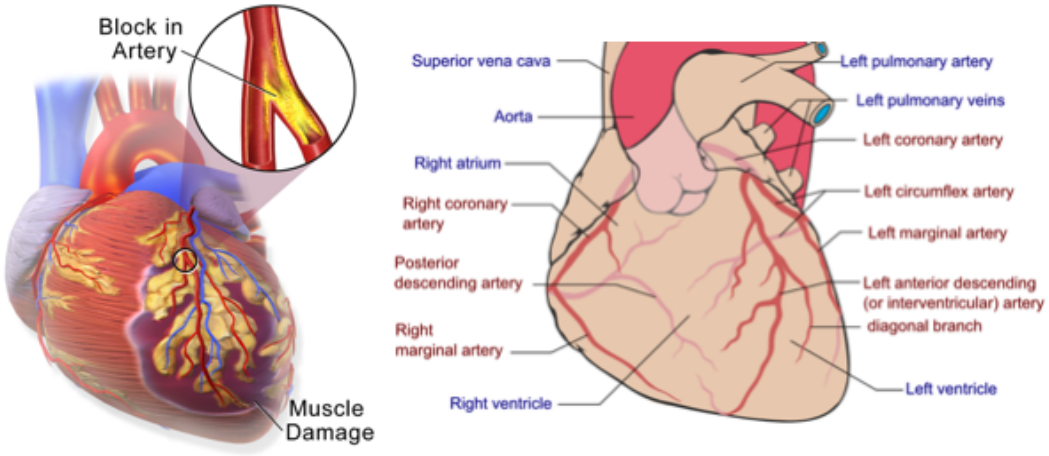

Figure 1.1 – Artery block (left) and arteries scheme (right). Copyright: Blausen Medical Communications, Inc. (left) Patrick J. Lynch, medical illustratorderivative work (right)

Most of the MIs are located in the left ventricle (LV), because the three arteries (cf. Figure 1.1) most often occluded are:

1. the *left anterior descending artery* which supplies blood to the anterior, lateral, and apical wall of the LV and is the most commonly occluded;

2. the *right coronary artery* which supplies blood to the bottom portion of the LV and the back of the septum;

3. the *left circumflex artery* which supplies blood to the side and the back of the LV.

In addition to their location, MIs are also classified by their size: small (if the MI affects less than the 10% of the LV myocardium), moderate (from 10 to 30%) and large (more than the 30%).

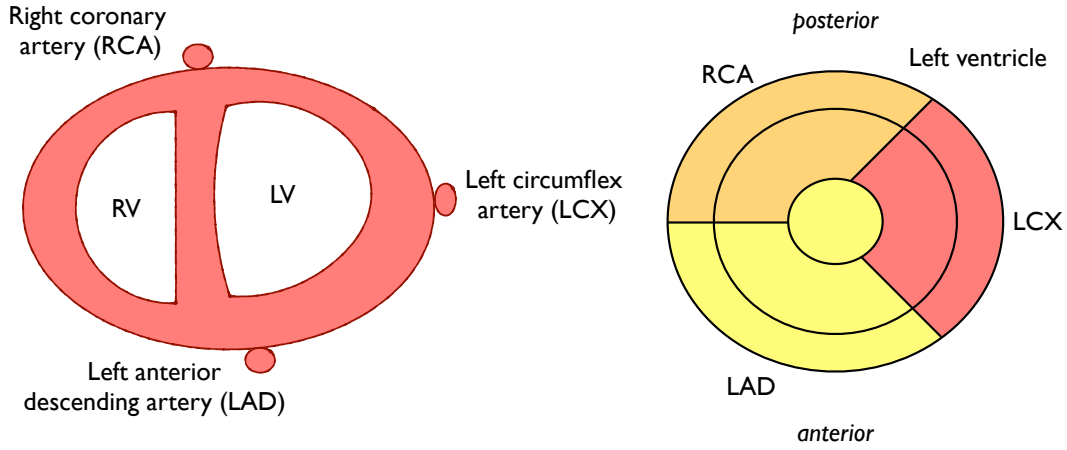

Figure 1.2 – Location of the arteries mainly affected by occlusion (left) and corresponding left ventricle regions perfused

When an artery is occluded, the myocardial cells in the region perfused by the artery do not receive enough oxygen and thus become ischemic: the mechanism of muscle contraction is then locally compromised. After a few minutes this damage is irreversible, as the region turns into a necrotic stage. Severe complications can follow an infarct, such as arrhythmias caused by an anomalous conduction of the electrical signal. As a consequence, the healthy part of the muscle can change shape (i.e. induce some *remodeling* effects) in order to compensate the loss of the capability to contract in the ischemic region, and this situation could end in heart failure. Due to all these complications, it is very important to act as soon as possible. However, the fact that at least 25% of MIs are silent [VLC11], i.e. the classical symptoms are not always sensed by the patient, makes it difficult to diagnose MIs in due time. Hence, it is particularly important to develop accurate tools for early diagnosis of myocardial infarctions. Accurate mathematical models can provide useful insights, by reproducing subject-specific cardiac electrophysiology: given some (noisy) observations of the phenomenon, model personalization is achievable through the solution of data-assimilation and inverse problems. In this way, we are able to reproduce in silico the pathophysiology of a specific patient, to test different scenarios and also to compute quantitative outputs meant to support clinicians in their decisions.

1.1.2 Available measures

Heart continuously produces a sequence of small electric waves during each heart beat, but it is not trivial to measure them in a noninvasive way. The routine noninvasive test is the electrocardiogram (ECG), which is realized by placing electrodes on the patient skin. The conventional 12-leads ECG is obtained by using the following ten electrodes:

- RA and LA, placed one on each arm;
- RL and LL, placed one on each leg (lateral calf muscle);
- $V_1, \dots, V_6$, placed on the torso, as sketched in Figure 1.3 on the left.

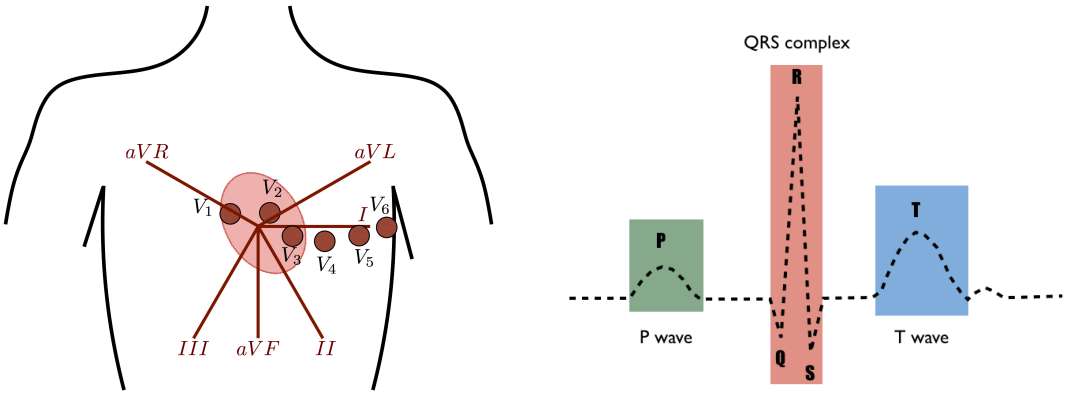

Figure 1.3 – Placement of the electrodes $V_1, \dots, V_6$ on the torso and limb leads directions (left); classical scheme of an ECG signal (right)

Each electrode registers the electric potential difference, which is then properly combined in order to derive the 12 leads. The leads are divided in bipolar if they compare the registered activity of two electrodes (this is the case of limb leads combination of RA, LA and RR), and unipolar if they compare the potential recorded at one electrode with a reference potential, obtained by averaging the bipolar leads (this is the case of the precordial leads relative to $V_1, \dots, V_6$). These signals detect variations in the electric potential during the cardiac electric cycle. A typical ECG, sketched in Figure 1.3, is characterized by the superposition of three waves:

- the P-wave, generated by atrial depolarization;
- the QRS-complex, generated by ventricular depolarization;
- the T-wave, generated by ventricular polarization.

Normal electrical conduction gives this three waves pattern, while deviation from it can be motivated by inter-patient variability or the presence of a pathology. A correct analysis of ECG signals, joined with a complete anamnesis, can lead to the diagnosis of arrhythmia, previous MI (heart attack), defects or abnormalities in the heart shape and size, as well as pathologies related to the electrical conduction from one portion to another (for further details see e.g. [Yan16]). However, there might be false negatives, i.e. normal ECGs in presence of a heart

disease, and false positives, i.e. abnormal ECGs which reflect instead physiological condition on a given patient. Moreover, the ECG measures are polluted by many sources of noise: instrumentation noise, electromagnetic fields interference, defective electrode contact, motion artifacts and muscle activities.

More detailed data can be obtained through invasive techniques, such as intracardiac catheter recording along the endocardium, the inner wall of the heart. The catheter is equipped with small electrodes that are used to locally monitor the cardiac electric potential behavior [EHD+14]. During this procedure the clinician paces locally the endocardium in order to check for anomalous responds. In particular, from the electrodes measurements it is possible to generate endocardial maps of the activation times, defined as the time at which the electric potential in a point reaches its peak value.

1.2 Mathematical models

Mathematical models of cardiac electrophysiology describe the action-potential mechanism of depolarization and polarization, which consists in a rapid variations of the cell membrane electric potential with respect to a resting potential (see Figure 1.4). These models are naturally divided into two families: cellular models, which characterize the electric potential of a single cell, and physiological models, which give a quantitative description of action potential propagation at the tissue level. In this section we briefly review the principal electrophysiology model; for a complete review of the different electrophysiological models see e.g. [CFPS14, CBC+11, PCB05], while for a review of mathematical models for the whole heart physiology see e.g. [QLR+16, Tra11].

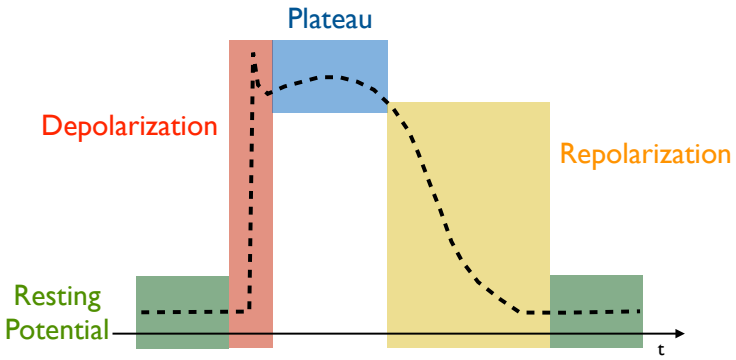

Figure 1.4 – Action potential scheme: after the application of the stimulus, the action-potential depolarizes very quickly; a plateau phase follows, in which the cell remains depolarized and finally the repolarization of the cell begins, returning to the initial state

The cellular models are based on systems of ordinary differential equations (ODEs) which describe the variation of ionic species and ionic currents. These latter variables are responsible of the cellular action-potential dynamics represented in Figure 1.4. The cellular model is

defined through the following problem: find the cell membrane potential $u = u(t)$ such that

$$\begin{cases} C_m \dfrac{du}{dt} + I_{ion}(u, \mathbf{w}, \mathbf{c}) = I_{app}(t), & t \in (0, T] \\ \dfrac{\partial \mathbf{w}}{\partial t} = g_w(u, \mathbf{w}, \mathbf{c}), & t \in (0, T] \\ \dfrac{\partial \mathbf{c}}{\partial t} = g_c(u, \mathbf{w}, \mathbf{c}), & t \in (0, T], \end{cases}$$

where $\mathbf{w} = (w_1, \ldots, w_{m_w})^T$, with $w_i \in (0,1)$, $i = 1, \ldots, m_w$, is the gating variables vector, regulating the ionic currents, while $\mathbf{c} = (c_1, \ldots, c_{m_c})^T$ the vector of ionic species concentrations in the cell. Moreover, C_m $[\mu F/cm^2]$ is the cell membrane capacitance, I_{ion} $[\mu A/cm^2]$ the ionic exchanges current and I_{app} $[\mu A/cm^2]$ the applied exterior stimulus. The system of ODEs is completed by a vector of initial conditions, one for each variable.
Many detailed membrane models involving an increasing number of currents and variables can be found in literature, starting from the adaptation proposed by Noble [Nob62] of the Hodgkin-Huxley model [HH52]. Since these cellular models could be formed by a high number of equations, one for each specific Ionic species, simpler models (defined as phenomenological) are used to efficiently reproduce the action-potential of Figure 1.4 without the direct description of all the ionic currents.

The first phenomenological model was proposed by FitzHugh [Fit61] and Nagumo [NAY62], and is obtained by considering:

$$\begin{cases} C_m \dfrac{du}{dt} + I_{ion} = I_{app}(t), & t \in (0, T] \\ \dfrac{\partial w}{\partial t} = g(u, w), & t \in (0, T], \end{cases} \tag{1.1}$$

where $I_{ion} = ku(u-a)(u-1) + w$ is a cubic nonlinearity, which models the depolarization mechanism, while $g(u,w) = \gamma u - \beta w$ the polarization mechanism. Here the electric potential u is adimensionalized and w is an additional variable used to reproduce the phenomenon of interest (it is no more a gating variable). Finally, k, γ and β are positive parameters, which affect the action potential form. More precise models have been proposed to improve the FitzHugh-Nagumo model, such as the Aliev-Panfilov (AP) model [AP96] and the Mitchell and Schaeffer model [MS03], which both enable the tuning of the depolarization and repolarization shape through the definition of I_{ion} and g. In this work we rely on the AP model, which has six parameters to be tuned in order to carefully reproduce the most representative features of the electric potential, such as action potential duration and conduction velocity restitution curves. In particular, we consider the following expressions:

$$\begin{cases} I_{ion}(u, w) = Ku(u-a)(u-1) + wu \\ g(u, w) = \left(\varepsilon_0 + \dfrac{c_1 w}{c_2 + u}\right)(-w - Ku(u-a-1)). \end{cases} \tag{1.2}$$

The solution of (1.1) equipped with (1.2) is reported in Figure 1.5.
Given that u is an adimensional potential, the correct dimensionality of the electric potential can be recovered by setting

$$V = -80 + 100u \qquad [mV].$$

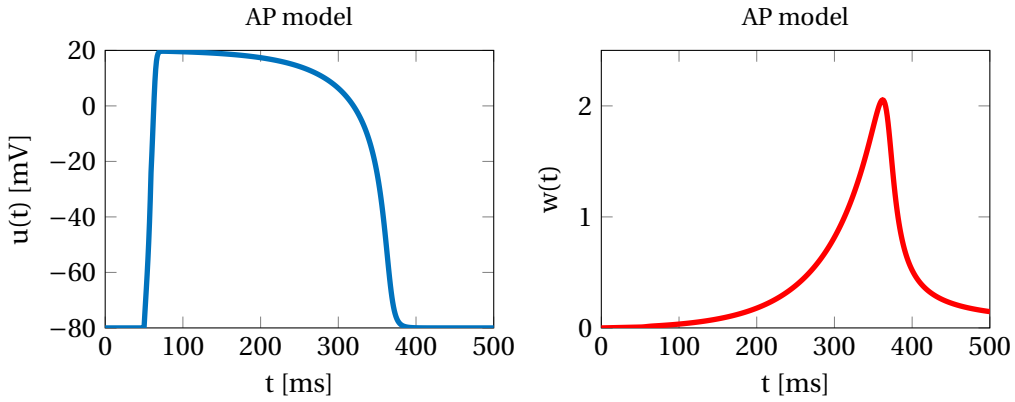

Figure 1.5 – Action potential $u(t)$ and recovery variable $w(t)$ using the AP model with the parameters specified in [AP96]

All these cellular models have been largely validated in experiments [OVV+11, BBOVA+13], more recently also using probabilistic approaches developed in the uncertainty quantification framework [JCB+16].

At the tissue level, the physiological models are derived using homogenization procedures, leading e.g. to the bidomain equations [Hen92], which characterize the behavior of the intra- and extra-cellular potentials $u_i = u_i(\mathbf{x},t)$ and $u_e = u_e(\mathbf{x},t)$, respectively. The problem of finding the resulting transmembrane potential $u(\mathbf{x},t) = u_i(\mathbf{x},t) - u_e(\mathbf{x},t)$ becomes:

$$\begin{cases} A_m\left(C_m\dfrac{\partial u}{\partial t} + I_{ion}(u,w)\right) - \operatorname{div}(\mathbf{D}_i\nabla u) - \operatorname{div}(\mathbf{D}_e\nabla u_e) = A_m I_{app}(\mathbf{x},t) & \mathbf{x}\in\Omega_H, t\in(0,T] \\ -\operatorname{div}((\mathbf{D}_i+\mathbf{D}_e)\nabla u_e) - \operatorname{div}(\mathbf{D}_i\nabla u) = 0 & \mathbf{x}\in\Omega_H, t\in(0,T] \\ \dfrac{\partial w}{\partial t} = g(u,w) & \mathbf{x}\in\Omega_H, t\in(0,T], \end{cases} \tag{1.3}$$

where A_m is the ratio of membrane area per unit volume, $\mathbf{D}_i$ and $\mathbf{D}_e$ $[S/cm]$ are the intra- and the extra-cellular conductivity tensors and Ω_H the myocardial tissue domain. To obtain a well-posed problem, equations (1.3) are completed by initial conditions:

$$\begin{cases} u(\mathbf{x},0) = u_0 & \mathbf{x}\in\Omega_H \\ u_e(\mathbf{x},0) = u_{e,0} & \mathbf{x}\in\Omega_H, \end{cases}$$

for given functions u_0 and $u_{e,0}$, and suitable boundary conditions such homogeneous Neumann boundary conditions modeling an electrically isolated tissue (hence, neglecting the ability of the rest of the body to conduct the electrical signal):

$$\begin{cases} \nabla u(\mathbf{x},t)\cdot\mathbf{n} = 0 & \mathbf{x}\in\partial\Omega_H, t\in(0,T] \\ \nabla u_e(\mathbf{x},t)\cdot\mathbf{n} = 0 & \mathbf{x}\in\partial\Omega_H, t\in(0,T]. \end{cases}$$

A simplified model is given by the monodomain system [NRL+07], written only in terms of the potential u. By assuming that the intra- and the extra-cellular conductivity tensors are such that $\mathbf{D}_i = \lambda\mathbf{D}_e$, it is possible to simplify the bidomain equations (1.3). The resulting

monodomain system reads:

$$\begin{cases} A_m\left(C_m\dfrac{\partial u}{\partial t}+I_{ion}(u,w)\right)-\operatorname{div}(\mathbf{D}_0\nabla u)=A_m I_{app}(t) & \mathbf{x}\in\Omega_H,\, t\in(0,T] \\ \dfrac{\partial w}{\partial t}=g(u,w) & \mathbf{x}\in\Omega_H,\, t\in(0,T] \\ \nabla u(\mathbf{x},t)\cdot\mathbf{n}=0 & \mathbf{x}\in\partial\Omega_H,\, t\in(0,T] \\ u(\mathbf{x},0)=u_0 & \mathbf{x}\in\Omega_H \\ w(\mathbf{x},0)=w_0 & \mathbf{x}\in\Omega_H, \end{cases} \tag{1.4}$$

where $\mathbf{D}_0$ is the effective conductivity tensor, defined as

$$\mathbf{D}_0=\frac{\lambda}{1+\lambda}\mathbf{D}_i.$$

By assuming the isotropic relation $\mathbf{D}_i=\lambda\mathbf{D}_e$, the action potential $u(\mathbf{x},t)$ obtained by solving the monodomain system (1.4) is close to the one given by the bidomain model (1.3), as shown in [PDR+06]. Since the monodomain model consists of a single PDE, its numerical approximation is less computationally demanding compared to the one of the bidomain equations. For these reasons, in the following we propose some test cases based on the monodomain equation. However, we underline that the proposed reduction techniques can in principle be extended also to the bidomain case.

Mathematical models in electrophysiology are also very challenging problems from the Mathematical analysis point of view: a well-posedness analysis of the Mitchell-Schaeffer ODE model can be found in [KM13], while for the bidomain model on varying different ionic models can be found in [CFS02, BCP09, BFG+08]. Finally, a convergence analysis of the homogenization procedure can be found in [PSCF05].

1.2.1 Modeling the torso

In order to reproduce an ECG signal through a mathematical model, we need to take into account the presence of the rest of the body, which acts as a passive and isolated conductor. If we focus on the $V_1,\dots,V_6$ leads (Figure 1.3), we can restrict to the torso, defined here as Ω_T. From the electrical standpoint, the electric potential in the torso $u_T=u_T(\mathbf{x},t)$ can be modeled by the following Laplace equation:

$$\begin{cases} -\operatorname{div}(\mathbf{D}_T\nabla u_T)=0 & \mathbf{x}\in\Omega_T,\, t\in(0,T] \\ \mathbf{D}_T\nabla u_T(\mathbf{x},t)\cdot\mathbf{n}_T=0 & \mathbf{x}\in\partial\Omega_T,\, t\in(0,T], \end{cases} \tag{1.5}$$

being $\mathbf{n}_T$ the external (with respect to the body) normal vector, $\mathbf{D}_T$ the conductivity tensor of the torso and $\partial\Omega_T$ the outer boundary of Ω_T. As a consequence, the boundary conditions of the extracellular potential u_e in equations (1.3) are modified to consider the electric transmission between the heart domain Ω_H and the torso domain Ω_T at the internal boundary:

$$\begin{cases} u_e(\mathbf{x},t)=u_T(\mathbf{x},t) & \mathbf{x}\in\partial\Omega_H,\, t\in(0,T] \\ \mathbf{D}_e\nabla u_e(\mathbf{x},t)\cdot\mathbf{n}_H=\mathbf{D}_t\nabla u_T(\mathbf{x},t)\cdot(-\mathbf{n}_H) & \mathbf{x}\in\partial\Omega_H,\, t\in(0,T], \end{cases} \tag{1.6}$$

where $\mathbf{n}_H$ is the external (with respect to the heart) normal vector. Therefore, a complete model for the coupled heart-torso system can be obtained as follows:

$$\begin{cases} A_m\left(C_m\dfrac{\partial u}{\partial t}+I_{ion}(u,w)\right)-\operatorname{div}(\mathbf{D}_i\nabla u)-\operatorname{div}(\mathbf{D}_e\nabla u_e)=A_m I_{app}(\mathbf{x},t) & \mathbf{x}\in\Omega_H,\, t\in(0,T] \\ -\operatorname{div}((\mathbf{D}_i+\mathbf{D}_e)\nabla u_e)-\operatorname{div}(\mathbf{D}_i\nabla u)=0 & \mathbf{x}\in\Omega_H,\, t\in(0,T] \\ \dfrac{\partial w}{\partial t}=g(u,w) & \mathbf{x}\in\Omega_H,\, t\in(0,T] \\ \operatorname{div}(\nabla\mathbf{D}_T u_T)=0 & \mathbf{x}\in\Omega_T,\, t\in(0,T] \\ \nabla u_T(\mathbf{x},t)\cdot\mathbf{n}_T=0 & \mathbf{x}\in\partial\Omega_T,\, t\in(0,T], \\ u_e(\mathbf{x},t)=u_T(\mathbf{x},t) & \mathbf{x}\in\partial\Omega_H,\, t\in(0,T] \\ \mathbf{D}_e\nabla u_e(\mathbf{x},t)\cdot\mathbf{n}_H=-\mathbf{D}_t\nabla u_T(\mathbf{x},t)\cdot\mathbf{n}_H & \mathbf{x}\in\partial\Omega_H,\, t\in(0,T] \end{cases} \tag{1.7}$$

with e.g. current specification (1.2) and suitable initial conditions:

$$\begin{cases} u(\mathbf{x},0)=u_0 & \mathbf{x}\in\Omega_H \\ u_e(\mathbf{x},0)=u_{e,0} & \mathbf{x}\in\Omega_H \\ u_T(\mathbf{x},0)=u_{T,0} & \mathbf{x}\in\Omega_T. \end{cases}$$

A numerical approximation of the ECG signals can be finally computed by measuring on $\partial\Omega_T$ the potential difference between the locations illustrated in Figure 1.3.
The complete derivation of (1.7) has been proposed in [LGT03], where the bidomain model is adopted in a two dimensional case and some numerical tests can be found in [SLT05]. A state of the art numerical approximation of ECG can be found in [SCG16, FZ10, BCF$^+$10], where three dimensional simulations of the electrical activity of the heart coupled with the full body are presented.

1.2.2 Modeling the presence of an ischemia

The effect of heart disease on the electrical activity of the heart can be accounted for suitable modifications of the mathematical models introduced previously. In this work we are interested not only in a model personalization of the mathematical model in physiological conditions, but also in addressing the pathological case of myocardial ischemia.
According to biological observations, the cells in an infarcted region are no longer excitable. By looking at the cardiac tissue as a circuit of cardiac cells interconnected [MVCDB98], the ischemic tissue can be firstly modeled as a group of cells whose surrounding resistances are greater than the other ones. Moreover, in such a region cells behave as a passive conductor, which means that a stimulation does not cause a complete action potential cycle; rather, the potentials decay with time and distance from the source. In order to take into account this behavior, the cellular models previously introduced should be properly modified by considering a vanishing ionic current in the ODEs system. A more detailed analysis at the cellular level have been proposed in [SR97, CSB01].

In a consistent way, the local difference of the resistances can be modeled at the macroscopic scale by considering a non-homogeneous conductivity tensor and a non-homogeneous ionic current (for further details see e.g. [NLT07]), In particular, we consider the non-homogeneous

conductivity tensor

$$\mathbf{D}(\mathbf{x}) = \mathbf{D}_{hea} g(\mathbf{x}) + \mathbf{D}_{ill}(1 - g(\mathbf{x})), \qquad \mathbf{x} \in \Omega_H,$$

being $\mathbf{D}_{hea}$ the healthy conductivity tensor greater that $\mathbf{D}_{ill}$, the conductivity tensor of the ischemic region, identified by the function $g(\mathbf{x})$. On the other hand, the ionic term is given by

$$I_{ion} = g(\mathbf{x})(Ku(u-a)(u-1) + wu).$$

A different approach is considered in [ÁAARÁ+12], where instead of considering a non-homogeneous ionic current, two parameters of the Mitchell-Schaeffer model are considered to be non-homogeneous in space in order to reproduce the passive conductor behavior.

1.3 Towards translating models into clinical practice

Integrating available measurements of the heart electrical activity within mathematical models is crucial in order to develop useful tools to support clinical practice. What is referred to as *computational medicine* is nowadays an extremely active research field, covering a broad spectrum of applications ranging from molecular medicine to heart diseases (see e.g. [WTG+12, NK09, FQV10] and reference therein).
Focusing on heart function (and disfunction), data-model integration might improve the diagnosis of cardiovascular disease. Some relevant examples of data-cardiovascular model integration can be found in [SdVM+11, MF15, TSR+16]. In cardiac electrophysiology, medical device for rhythm control or catheter ablation have been recently investigated in e.g. [TSD+, TMD+13, RCS+11, AAV+15].

1.3.1 Data-model integration pipeline

The final goal of the integrating data within cardiac model is the development of a pipeline, whose schematic representation is presented in Figure 1.6, for the construction of in silico subject-specific models aiming at simulating different intervention/therapy scenarios. We identify four main steps:

1. the acquisition of available clinical data, necessary for the segmentation of the domain geometry, the construction of the corresponding computational mesh and the imposition of suitable initial and boundary conditions [EPS+08, KvBW+04, VAP+10];

2. the choice of a suitable mathematical model, depending on the target of the simulation (required level of complexity);

3. personalization of the model inputs best fitting the available clinical data. This task can be expressed through either a *PDE-constrained optimization problem*, leading to a deterministic estimate of the unknown inputs, or a *statistical inverse problem*, whose solution is a probabilistic distribution describing the range of most likely inputs. The former is usually the most adopted so far due to the complexity of electrophysiology models, but the additional information (e.g. variance, confidence or credible intervals and quantiles) provided by the latter are fundamental in view of data-model integration;

4. prediction of the electrical potential behavior when different intervention/therapy scenarios are considered.

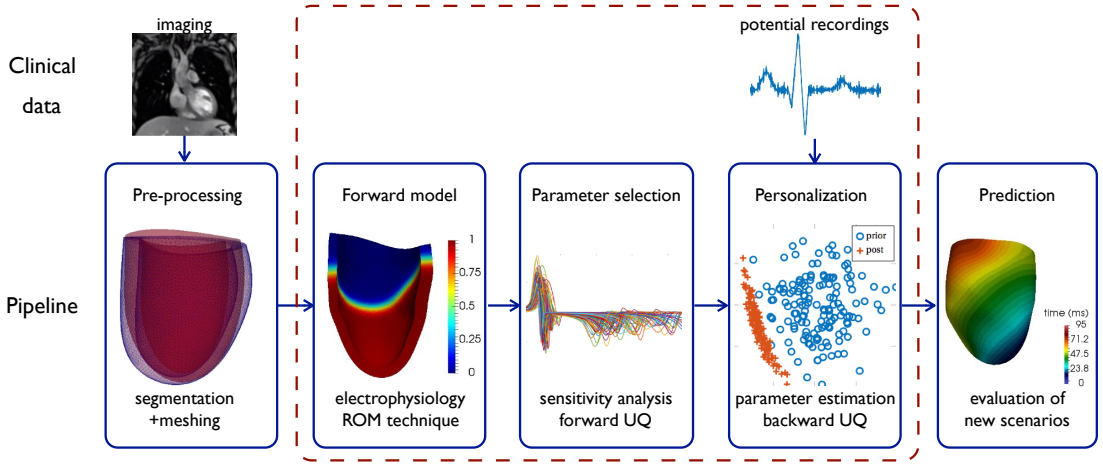

Figure 1.6 – Cardiac data-model integration pipeline. First, the geometry and the initial/boundary conditions are obtained from clinical data. Then, the model and its parametrization is chosen by using sensitivity analysis and forward UQ tools. Model personalization is performed using optimization or statistical inversion algorithms. Finally, the subject-specific model enables to test different scenarios. Copyright MRI image: Biomedizinische NMR Forschungs GmbH, via Wikimedia Commons.

The construction of this pipeline involves several challenges to deal with:

- the limit imposed by the clinical data accuracy, such as the spatial resolution of the clinical heart imaging or the restricted amount of information given by noninvasive measurements, such as ECGs. Thanks to technological innovation, imaging techniques [HAZD$^+$12, IK05] are currently used to directly diagnose MIs (detecting e.g. wall motion abnormalities or using paramagnetic contrast agents to verify the perfusion in the myocardium). However, these procedure are performed only on patients with known or suspected MIs. For this reason, it is also pivotal to improve the diagnosis capability using routine exams, such as ECGs, through subject-specific simulations;

- the high number of uncertainties related to the geometry, physical coefficients, boundary and initial conditions, which make the model definition a critical step of the pipeline. For example, understanding the effect of geometry variability on the outcome of the simulation could be crucial when focusing on mechanical properties of the myocardium, but could be unnecessary during the study of some electrical properties. In the same way, not all the physical coefficients characterizing the ionic model affect specific behaviors of the cardiac potential, such as (de)polarization front velocity. Considering all these sources of uncertainty could entail unbearable computational costs of the forward numerical simulation and consequently jeopardize model personalization. It is thus essential to bound those input variables which directly influence the output of interest and discard the others. In this setting, sensitivity analysis and uncertainty quantification/propagation are essential to address this issue.

- the time required by the pipeline has to be comparable with the one of the current clinical exams (few hours or days). The consequent need of fast simulations required

the development of ad hoc reduced-order models and the integration of these latter in uncertainty quantification and parameter estimation procedures;

- the discrepancy between real data and the output of the mathematical model could affect the estimation procedure and propagate during the prediction phase. This issue of *model calibration* is usually addressed through the personalization step, without considering the simplifications introduced by the mathematical representation;

In the recent years, several groups have focused their attention on these challenges. Applications of electromechanical model personalization from clinical images and ECGs can be found in [MDS+13b, SCC+11, CWH+16, PSA+14, NBG+13, CML+12]. In this context, sensitivity analysis has been performed in [MDS+13a] to automatically select the identifiable input parameters, and reduced-order unscented Kalman filters [MC11] have been considered for reducing the complexity of parameter estimation. However, all these methods require a critical number of full-order simulations, leading to extremely time consuming pipelines.
In cardiac electrophysiology, an example of integrated pipeline for the prediction of depolarization isochrones resulting from different pacing conditions has been presented in [CSL+11]. In this work, models with different levels of accuracy are adopted for an efficient parameter estimation starting from optical mapping and MR images. The role of uncertainty in the electrophysiology model personalization has been taken into account for the first time in [KRC+11], relying however on the Eikonal model, a simple model related exclusively to the electric potential depolarization phase. The challenge of non-invasive personalization (body surface potential mapping and ECG) for cardiac electrophysiology models have been considered in [GRJF+16], with the goal of predicting the activation time in different pacing conditions for patient suffering from premature ventricular contraction, and in [GRFW+16] in the case of bundle branch blocks. Finally, another example of integrated pipeline for the estimation of electrophysiology parameters by combining electrical and mechanical measurements has been considered in [CGM15]. Here, the inverse problems of electrocardiography has been addressed using a sequential data-assimilation procedure based on a POD projection of the state solution for the sake of efficiency.

In this perspective, this Thesis contributes to the process of translating electrophysiology models in clinical care by developing some reduction strategies to deal with the challenges arising in the second and the third step of the pipeline. In this direction, we deal with problems based on a simplified mathematical representation of both type of the measurements previously described.
With this aim, we cast all mathematical models under the general framework of parametrized PDEs, whose solutions depend on a parameter vector $\boldsymbol{\mu} \in \mathscr{P} \subset \mathbb{R}^d$, characterizing both the physical and/or geometrical configurations of the underlying system. Consequently, we are interested in the following input-output mapping

$$\boldsymbol{\mu} \rightarrow u(t;\boldsymbol{\mu}) \rightarrow \mathbf{y}(t;\boldsymbol{\mu})$$

being $u(t;\boldsymbol{\mu})$ the electric potential, e.g. solution of the parametrized PDE (1.4), and $\mathbf{y}(\boldsymbol{\mu})$ a vector of outputs of interest, approximating the available clinical measurements.

2 | Reduced-order model for electrophysiology

The design of efficient reduced-order models for problems arising in electrophysiology is still an open problem, due to the intrinsic complexity of the underlying process: the electrical potential evolution on the myocardial tissue is characterized by a sharp traveling front, highly sensible to changes in the model parameters.
In this chapter, we firstly recall in Section 2.1 the basic numerical techniques for the approximation of electrophysiology equations. Then, in Section 2.2.1 we review the reduced basis (RB) method coupled with suitable hyper-reduction techniques for the efficient solution of nonlinear time-dependent parametrized PDEs. Since a straightforward application of the RB method to the problems arising in electrophysiology does not provide accurate results at moderate computational costs, we investigate different strategies for the construction of localized-ROM in Section 2.3. Finally, in Section 2.4 we propose a detailed comparison of the numerical results by looking at the basic features that should be respected in the design and development of a ROM: efficiency, accuracy and low memory consumption.

2.1 Full-order model

The solution of the nonlinear reaction–diffusion equations (1.3) or (1.4) for electrophysiology is characterized by a traveling wave (depolarization) covering the portion of the cardiac tissue representing the domain where the problem is set. This mechanism, controlled by the ionic current, is then followed by a repolarization phase where the potential returns to its initial value (see Figure 1.4 in Section 1.2). The numerical discretization of this activation-deactivation cycle is already challenging when we rely on classical full-order models, such

as Finite Element method [CFPT05, PLdS+07, GK09, MH89]. A review of computational techniques for the approximation of the electrical activity of the heart is presented e.g. in [SLC+07, VAT02, VDSP+08, CFP04]. One of the main difficulties is indeed correctly capturing the front propagation velocity: the need of a sufficiently small spatial discretization mesh size h and time-step length Δt, usually compromise the computational efficiency of the solver. Several issues of time and space convergence of full-order models for electrophysiology have been addressed in [NKB+11, PHS16] and in [VGG+15] for high-order finite element approximation.

The aim of this section is to introduce some of the typical full-order time-space discretization schemes applied to the solution of problem (1.4), which is the prototype adopted in the test cases of this Thesis.
We consider the generic vector of parameter $\boldsymbol{\mu} \in \mathscr{P} \subset \mathbb{R}^d$ characterizing either the geometrical or physical properties. For $t > 0$, the weak formulation of problem (1.4) reads: given $I_{app}(t;\boldsymbol{\mu}) \in L^2(\Omega)$, find $u(t;\boldsymbol{\mu}) \in X = H^1(\Omega)$ and $w(t;\boldsymbol{\mu}) \in L^2(\Omega)$ such that

$$\begin{cases} \displaystyle\int_\Omega A_m \left(C_m \frac{\partial u}{\partial t} + I_{ion}(u,w;\boldsymbol{\mu}) \right) \psi d\omega + \int_\Omega \mathbf{D}_0(\boldsymbol{\mu}) \cdot \nabla u \nabla \psi d\omega = \int_\Omega A_m I_{app}(t;\boldsymbol{\mu}) \psi d\omega & \forall \psi \in H^1(\Omega) \\ \displaystyle\int_\Omega \frac{\partial w}{\partial t} v d\omega = \int_\Omega g(u,w;\boldsymbol{\mu}) v d\omega & \forall v \in L^2(\Omega) \\ u(0;\boldsymbol{\mu}) = u_0 \\ w(0;\boldsymbol{\mu}) = w_0, \end{cases}$$

where $\Omega = \Omega(\boldsymbol{\mu})$ is a parametrized computational domain of $\mathbb{R}^p$, $p = 2,3$.

We apply the Galerkin-finite element (FE) method relying on a finite-dimensional space $X_h \subset X(\Omega)$ of (usually very large) dimension $\dim(X_h) = N_h$, being h a parameter related to the mesh size of the computational grid. By denoting with $\{\varphi_i\}_{j=1}^{N_h}$ the basis functions of the finite element space X_h, we introduce the following parametrized FE matrices

$$(\mathbf{M}(\boldsymbol{\mu}))_{ij} = \int_{\Omega(\boldsymbol{\mu})} \varphi_i \varphi_j d\omega, \qquad (\mathbf{A}(\boldsymbol{\mu}))_{ij} = \int_{\Omega(\boldsymbol{\mu})} \mathbf{D}_0(\boldsymbol{\mu}) \cdot \nabla \varphi_i \nabla \varphi_j d\omega,$$

and the following parametrized linear FE vector

$$(\mathbf{I}_{app})_j = \int_{\Omega(\boldsymbol{\mu})} A_m I_{app}(t;\boldsymbol{\mu}) \varphi_j d\omega.$$

The solutions $u_h(\mathbf{x},t;\boldsymbol{\mu})$ and $w_h(\mathbf{x},t;\boldsymbol{\mu})$ are thus given by the linear combination of the basis functions:

$$u_h(\mathbf{x},t;\boldsymbol{\mu}) = \sum_{i=1}^{N_h} u_h^i(t;\boldsymbol{\mu}) \varphi_i(\mathbf{x}), \qquad w_h(\mathbf{x},t;\boldsymbol{\mu}) = \sum_{i=1}^{N_h} w_h^i(t;\boldsymbol{\mu}) \varphi_i(\mathbf{x}),$$

where the vectors $\mathbf{u}_h = [u_h^1, \dots, u_h^{N_h}]^T$ and $\mathbf{w}_h = [w_h^1, \dots, w_h^{N_h}]^T$ are obtained by solving the system: given $\boldsymbol{\mu} \in \mathscr{P}$, find $\mathbf{u}_h(t;\boldsymbol{\mu})$ and $\mathbf{w}_h(t;\boldsymbol{\mu})$ such that

$$\begin{cases} \mathbf{M}(\boldsymbol{\mu}) \dfrac{\partial \mathbf{u}_h}{\partial t} + \mathbf{A}(\boldsymbol{\mu}) \mathbf{u}_h + \mathbf{I}_{ion}(\mathbf{u}_h, \mathbf{w}_h; \boldsymbol{\mu}) = \mathbf{I}_{app}(t;\boldsymbol{\mu}) & t \in (0,T] \\ \mathbf{M}(\boldsymbol{\mu}) \dfrac{\partial \mathbf{w}_h}{\partial t} = g(\mathbf{u}_h, \mathbf{w}_h) & t \in (0,T] \\ \mathbf{u}_h(0;\boldsymbol{\mu}) = \mathbf{u}_0(\boldsymbol{\mu}) \\ \mathbf{w}_h(0;\boldsymbol{\mu}) = \mathbf{w}_0(\boldsymbol{\mu}). \end{cases} \tag{2.1}$$

Here, the parametrized nonlinear FE vectors $\mathbf{I}_{ion}(\mathbf{u_h}, \mathbf{w_h}; \boldsymbol{\mu})$ and $\mathbf{g}(\mathbf{u_h}, \mathbf{w_h}; \boldsymbol{\mu})$, depending both on the finite element solutions $\mathbf{u}_h$ and $\mathbf{w}_h$, are defined as

$$(\mathbf{I}_{ion}(\mathbf{u_h}, \mathbf{w_h}; \boldsymbol{\mu}))_j = \int_{\Omega(\boldsymbol{\mu})} A_m I_{ion}(\mathbf{u_h}, \mathbf{w_h}; \boldsymbol{\mu}) \varphi_j \, d\omega, \qquad (\mathbf{g}(\mathbf{u_h}, \mathbf{w_h}; \boldsymbol{\mu}))_j = \int_{\Omega(\boldsymbol{\mu})} g(\mathbf{u_h}, \mathbf{w_h}; \boldsymbol{\mu}) \varphi_j \, d\omega.$$

Given a partition $(t^{(\ell)}, t^{(\ell+1)})$, $\ell = 0, \dots, N_t - 1$ of the time interval $(0, T)$ into N_t subintervals of length Δt, different time-advancing schemes can be adopted. In the case of an explicit, a semi-implicit or an operator splitting time-advancing scheme, at each time-step the non-linear vector $\mathbf{I}_{ion}$ is evaluated using the solution coming from the previous steps. This means that at each iteration we need to solve only a linear system, e.g. in the case of the semi-implicit Euler (one-step) method we have: given $\boldsymbol{\mu} \in \mathscr{P}$, find $\mathbf{u}_h^{(\ell+1)}$, $\ell = 0, \dots, N_t - 1$, and $\mathbf{w}_h = \mathbf{w}_h(t; \boldsymbol{\mu})$, such that

$$\begin{cases} \left(\dfrac{\mathbf{M}(\boldsymbol{\mu})}{\Delta t} + \mathbf{A}(\boldsymbol{\mu}) \right) \mathbf{u}_h^{(\ell+1)} = \dfrac{\mathbf{M}(\boldsymbol{\mu})}{\Delta t} \mathbf{u}_h^{(\ell)} + \mathbf{I}_{app}^{(\ell+1)}(\boldsymbol{\mu}) - \mathbf{I}_{ion}(\mathbf{u}_h^{(\ell)}, \mathbf{w}_h^{(\ell)}; \boldsymbol{\mu}) & \ell = 0, \dots, N_t - 1 \\ \mathbf{u}_h^{(0)} = \mathbf{u}_0(\boldsymbol{\mu}) & \\ \dfrac{\partial \mathbf{w}_h}{\partial t} = g(\mathbf{u}_h, \mathbf{w}_h; \boldsymbol{\mu}) & t \in (0, T] \\ \mathbf{w}_h^{(0)}(0; \boldsymbol{\mu}) = \mathbf{w}_0(\boldsymbol{\mu}). & \end{cases} \tag{2.2}$$

At each time-step $t^{(\ell+1)}$, $\ell = 0, \dots, N_t - 1$, a parametrized linear system coupled with an ODE for the gating variable $\mathbf{w}$ is then solved. The ODE can be solved using the same time advancing scheme applied point-wise (by considering the values of the potential on the mesh nodes) or by a Galerkin-projection of the ODE onto the finite dimensional space X_h, as done in (2.1). Here, the two problems are automatically uncoupled, since the nonlinear term depends only on the solutions $\mathbf{u}_h^{(\ell)}$ and $\mathbf{w}_h^{(\ell)}$ at the previous time-step $t^{(\ell)}$. In conclusion, we solve: given $\boldsymbol{\mu} \in \mathscr{P}$, find $\mathbf{u}_h^{(\ell+1)}$ and $\mathbf{w}_h^{(\ell+1)}$ such that

$$\begin{cases} \left(\dfrac{\mathbf{M}(\boldsymbol{\mu})}{\Delta t} + \mathbf{A}(\boldsymbol{\mu}) \right) \mathbf{u}_h^{(\ell+1)} = \dfrac{\mathbf{M}(\boldsymbol{\mu})}{\Delta t} \mathbf{u}_h^{(\ell)} + \mathbf{I}_{app}^{(\ell+1)}(\boldsymbol{\mu}) - \mathbf{I}_{ion}(\mathbf{u}_h^{(\ell+1)}; \boldsymbol{\mu}) & \ell = 0, \dots, N_t - 1 \\ \mathbf{u}_h^{(0)} = \mathbf{u}_0(\boldsymbol{\mu}) & \\ \mathbf{w}_h^{(\ell+1)} = \mathbf{w}_h^{(\ell)} + \Delta t \, \mathbf{g}(\mathbf{u}_h^{(\ell)}, \mathbf{w}_h^{(\ell)}; \boldsymbol{\mu}) & \ell = 0, \dots, N_t - 1 \\ \mathbf{w}_h^{(0)} = \mathbf{w}_0(\boldsymbol{\mu}). & \end{cases} \tag{2.3}$$

The major computational costs are generated by the nonlinear term $\mathbf{I}_{ion}$ assembly and by the solution of the linear system. Since Δt is required to be sufficiently small to ensure the convergence of the method [EB08], the computational cost can considerably grow.

When the implicit Euler method is adopted for time advancing, the numerical problem becomes: given $\boldsymbol{\mu} \in \mathscr{P}$, find $\mathbf{u}_h^{(\ell+1)}$ and $\mathbf{w}_h^{(\ell+1)}$ such that

$$\begin{cases} \left(\dfrac{\mathbf{M}(\boldsymbol{\mu})}{\Delta t} + \mathbf{A}(\boldsymbol{\mu}) \right) \mathbf{u}_h^{(\ell+1)} + \mathbf{I}_{ion}(\mathbf{u}_h^{(\ell+1)}, \mathbf{w}_h^{(\ell+1)}; \boldsymbol{\mu}) = \dfrac{\mathbf{M}(\boldsymbol{\mu})}{\Delta t} \mathbf{u}_h^{(\ell)} + \mathbf{I}_{app}^{(\ell+1)}(\boldsymbol{\mu}) & \ell = 0, \dots, N_t - 1 \\ \dfrac{\mathbf{M}(\boldsymbol{\mu})}{\Delta t} \mathbf{w}_h^{(\ell+1)} = \dfrac{\mathbf{M}(\boldsymbol{\mu})}{\Delta t} \mathbf{w}_h^{(\ell)} + \mathbf{g}(\mathbf{u}_h^{(\ell)}, \mathbf{w}_h^{(\ell)}; \boldsymbol{\mu}) & \ell = 0, \dots, N_t - 1 \\ \mathbf{u}_h^{(0)} = \mathbf{u}_0(\boldsymbol{\mu}) & \\ \mathbf{w}_h^{(0)} = \mathbf{w}_0(\boldsymbol{\mu}), & \end{cases} \tag{2.4}$$

which is a parametrized nonlinear system coupled with an ODE for the gating variable $\mathbf{w}_h$. To solve the coupled nonlinear problem (2.4), we can rely on the Newton method as follows: at each time step $\ell = 0, \dots, N_t - 1$, while $\|\boldsymbol{\delta}_u^\iota\| < tol$, we solve

$$\mathbf{J}\left(\begin{bmatrix}\mathbf{u}_{h,\iota}^{(\ell+1)}\\ \mathbf{w}_{h,\iota}^{(\ell+1)}\end{bmatrix}\right)\begin{bmatrix}\boldsymbol{\delta}_u^\iota\\ \boldsymbol{\delta}_w^\iota\end{bmatrix} = \mathbf{r}\left(\begin{bmatrix}\mathbf{u}_{h,\iota}^{(\ell+1)}\\ \mathbf{w}_{h,\iota}^{(\ell+1)}\end{bmatrix}\right), \qquad \begin{bmatrix}\mathbf{u}_{h,\iota+1}^{(\ell+1)}\\ \mathbf{w}_{h,\iota+1}^{(\ell+1)}\end{bmatrix} = \begin{bmatrix}\mathbf{u}_{h,\iota}^{(\ell+1)}\\ \mathbf{w}_{h,\iota}^{(\ell+1)}\end{bmatrix} + \begin{bmatrix}\boldsymbol{\delta}_u^\iota\\ \boldsymbol{\delta}_w^\iota\end{bmatrix} \qquad \iota = 1, \dots, \tag{2.5}$$

being $\mathbf{u}_{h,0}^{(\ell+1)} = \mathbf{u}_h^{(\ell)}$, $\mathbf{w}_{h,0}^{(\ell+1)} = \mathbf{w}_h^{(\ell)}$ and $tol > 0$ a fixed small tolerance. The Jacobian matrix $\mathbf{J}$ and the residual vector $\mathbf{r}$ of the problem (2.1) are respectively given by

$$\mathbf{J}\left(\begin{bmatrix}\mathbf{u}\\ \mathbf{w}\end{bmatrix}\right) = \begin{bmatrix}\dfrac{\mathbf{M}(\boldsymbol{\mu})}{\Delta t} + \mathbf{A}(\boldsymbol{\mu}) + \mathbf{J}_{\mathbf{I}_{ion}}^u(\mathbf{u},\mathbf{w};\boldsymbol{\mu}) & \mathbf{J}_{\mathbf{I}_{ion}}^w(\mathbf{u},\mathbf{w};\boldsymbol{\mu})\\ \mathbf{J}_g^u(\mathbf{u},\mathbf{w};\boldsymbol{\mu}) & \dfrac{\mathbf{M}(\boldsymbol{\mu})}{\Delta t} + \mathbf{J}_g^w(\mathbf{u},\mathbf{w};\boldsymbol{\mu})\end{bmatrix} \in \mathbb{R}^{2N_h \times 2N_h}, \tag{2.6}$$

$$\mathbf{r}\left(\begin{bmatrix}\mathbf{u}\\ \mathbf{w}\end{bmatrix}\right) = \begin{bmatrix}\mathbf{I}_{app}^{(\ell+1)}(\boldsymbol{\mu}) - \frac{\mathbf{M}(\boldsymbol{\mu})}{\Delta t}(\mathbf{u} - \mathbf{u}_h^{(\ell)}) - \mathbf{A}(\boldsymbol{\mu})\mathbf{u} - \mathbf{I}_{ion}(\mathbf{u},\mathbf{w};\boldsymbol{\mu})\\ -\dfrac{\mathbf{M}(\boldsymbol{\mu})}{\Delta t}(\mathbf{w} - \mathbf{w}_h^{(\ell)}) + \mathbf{g}(\mathbf{u},\mathbf{w};\boldsymbol{\mu})\end{bmatrix} \in \mathbb{R}^{2N_h}, \tag{2.7}$$

being $\mathbf{J}_I^v \in \mathbb{R}^{N_h \times N_h}$ the Jacobian matrix of the nonlinear term $\mathbf{I}$ with respect to the variable v. The implicit scheme gives flexibility on the choice of Δt; however the nonlinearity imposes additional subiterations, during which the nonlinear terms $\mathbf{I}_{ion}$ and $\mathbf{g}$ with their Jacobians need to be assembled. Since the matrix assembly is in general the most costly operation, it is usually preferred to adopt semi-implicit or operator-splitting schemes. However, the ROM technique is easily extendible also to manage the full-implicit case.

2.2 Reduced-order model

The solution of many-query problems, such as parameter estimation, data assimilation and uncertainty quantification, involves the repetitive evaluation of parametrized PDEs on varying the input parameters. In the context of cardiac electrophysiology, full-order models lead to unbearable computational costs, preventing the integration of these procedures in the clinical routines.

A reduced-order model (ROM) provide an approximation of a parametrized full-order model (FOM) characterized by low-dimensional operators, obtained by reducing the number of equations and of the corresponding unknowns. The construction of such a ROM is based on the assumption that the manifold spanned by all possible solutions of the parametrized problem has a considerably smaller dimension with respect to the space spanned by the basis functions of a classical full-order model (see Figure 2.1). Therefore, the ROM solution

$$u_n(\mathbf{x}, t; \boldsymbol{\mu}) = \sum_{i=1}^{n} u_i^n(t; \boldsymbol{\mu})\phi_i(\mathbf{x})$$

is obtained as a linear combination of problem-specific reduced-space basis functions $\{\phi_i(\mathbf{x})\}$, computed during a first computationally demanding *offline* phase. During this phase the basis functions are calculated from snapshots of the full-order solution computed for some parameter values. Then, the ROM low-dimensional operators are obtained by projecting the FOM operators onto the reduced-space. Finally, in an *online* phase, the ROM can be exploited to efficiently approximate the problem solution for each new value of the parameters.

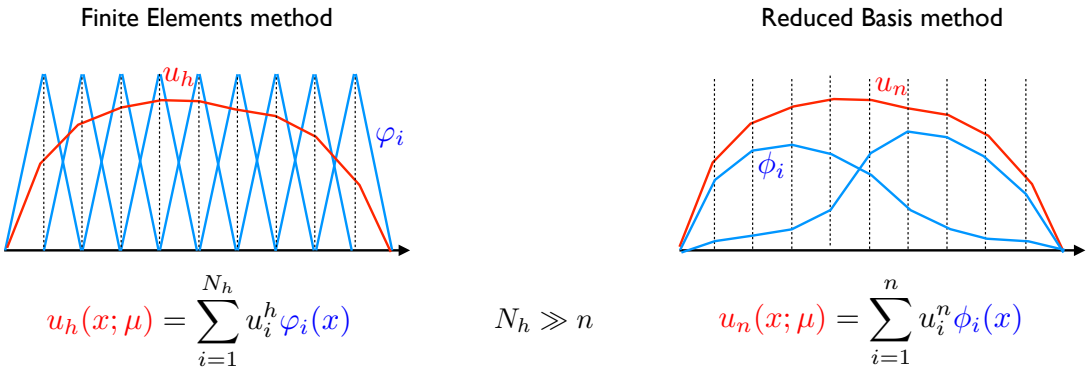

Figure 2.1 – Full-order and reduced-order approximation of the 1D solution $u(x;\boldsymbol{\mu})$.

Projection-based ROM have been successfully applied to linear steady system [HRS16, RHP08] and linear time-dependent systems [GP05], whose parameter-dependent operators are affine functions of the parameters (a complete survey of the methods exploited so far can be respectively found in [ASG01] and [BGW15a] and references therein). Some issues of computational efficiency arise when non-affine or nonlinear operators are considered: in this case the ROM can be equipped with additional techniques, known as hyper-reduction methods [AZF12, GMN+07, NMA15], to overcome these shortcomings. So far the combination of these techniques has led to a collection of methods successfully applied in a broad range of applications, such as structural dynamics and elasticity [WP02, ACC+09, Ver03, BMQ16], aerodynamics [CFC+13, BTWG08, BTDW04], cardiovascular fluid-dynamics [MQR12, CDQ14, BFI+16] and many other fields.

The application of projection-based ROMs to cardiac electrophysiology poses several challenges, due to the specific traveling-wave behavior of the solution: the manifold of all possible solutions cannot be expressed by combining a small number of basis functions.
The benchmark accuracy measure for reduced-order models is given by the Kolmogorov n-width of the solution manifold S (i.e. the space spanned by all possible solutions of the parametrized PDE), which is defined as follows:

Definition 1. *Given $S \subset X$ and a generic finite dimension subspace $X_n \subset X$ such that $dim(X_n) = n$, the Kolmogorov n-width of S in X is given by*

$$d_n(S,X) = \inf_{X_n \subset X} \left\{ \sup_{u \in S} \inf_{u_n \in X_n} \|u - u_n\|_X : X_n \text{ a n-dimensional subspace of } X \right\}.$$

In the case of affine parameter-dependent operator, one can prove that the n-widths are sub-exponentially convergent [OR15] (for further details on the n-width see e.g. [LMQ+13a, MMT16]). Unfortunately, advection dominated problems suffer from a very slow decay of the n-widths, especially when the diffusion term is parametrized.

For this reason the standard ROM approach described before can only be applied efficiently when the conductivity tensor is constant in space (in [BSG12, CLM+16] there are some numerical results that confirm this behavior). A first attempt to introduce a different point of view on the problem is the Lax-Pairs approach, recently introduced in [GL14, GLS15]. The main

feature of this approach is the fact that the basis functions are moved in time accordingly to the movement of the front: in this way no *offline* phase is required, entailing, consequently, additional *online* costs. In view of solving inverse and uncertainty quantification problems, this could penalize the overall computational performances. For this reason we will adopt a localized ROM approach based on the offline/online stratagem; since it is the first time that this approach is used in this context, we will analyze and compare all possible strategies to construct localized subspaces. In particular, we evaluate the ROMs by looking at the basic features that should be respected in the design and development of a ROM:

- **efficiency**: the solution evaluation should be performed rapidly with respect to the full-order one. As a measure of this quantity, we look at the speedup in the computational time;
- **accuracy**: the approximation error between the ROM and FOM should be uniformly small on the parameter space. In this case, we empirically compare the error on an additional set of parameter values randomly chosen in the parameter space;
- **low memory consumption**: the memory usage required to store ROM arrays should not exceed predefined thresholds in order to be portable on every device. With this aim, we compare the dimensionality and the pattern of sparsity of the ROM operators.

2.2.1 Reduced basis method

In the following section we briefly recall the basic features of the reduced basis method, by applying it to the cardiac electrophysiology problem.
In order to introduce all the basic ingredients of the RB method, we start from a simplified version of problem (2.1), obtained by neglecting the recovery variable w (and the corresponding ODE). For $t > 0$ and $\boldsymbol{\mu} \in \mathscr{P}$, we consider the following semi-discretized full-order system:

$$\begin{cases} \mathbf{M}(\boldsymbol{\mu})\dfrac{\partial \mathbf{u}_h}{\partial t} + \mathbf{A}(\boldsymbol{\mu})\mathbf{u}_h + \mathbf{N}(\mathbf{u}_h;\boldsymbol{\mu}) = \mathbf{I}_{app}(t;\boldsymbol{\mu}) \quad t \in (0,T] \\ \mathbf{u}_h(0;\boldsymbol{\mu}) = \mathbf{u}_0(\boldsymbol{\mu}). \end{cases} \tag{2.8}$$

The RB method is a projection-based ROM which computes an approximation $\mathbf{u}_n(t;\boldsymbol{\mu})$ of $\mathbf{u}_h(t;\boldsymbol{\mu})$ by means of a Galerkin projection on a reduced subspace $X_n \subset X_h$ of very small dimension $n \ll N_h$ (see e.g. [QMN16] for a detailed overview). In the following, we review the main ingredients of the RB approximation.

First ingredient: basis construction

Here we show how to construct the reduced-space by means of the *proper orthogonal decomposition* (POD) technique [Cha00, KV01]. We consider a training set $P_{train} \subset \mathscr{P}$ of N_{train} parameter vectors sampled in the space $\mathscr{P}$ of admissible parameters. For each parameter vector $\boldsymbol{\mu} \in P_{train}$ we solve the full-order system (2.8) by adopting a suitable time-advancing scheme. At the end of this procedure we end up with the so-called snapshots matrix

$$\mathbf{S}_u = [\mathbf{u}_h(t^{(0)};\boldsymbol{\mu}_1), \mathbf{u}_h(t^{(1)};\boldsymbol{\mu}_1), \ldots, \mathbf{u}_h(t^{(0)};\boldsymbol{\mu}_2), \mathbf{u}_h(t^{(1)};\boldsymbol{\mu}_2), \ldots,] \in \mathbb{R}^{N_h \times N_s}, \tag{2.9}$$

being $N_s = N_{train} N_t$, with N_t the number of time-steps of the chosen time-advancing scheme. We then consider the SVD decomposition of the snapshots matrix

$$\mathbf{S}_u = \mathbf{Z}\mathbf{\Sigma}\mathbf{H}^T,$$

where $\mathbf{\Sigma}$ is the diagonal matrix containing the singular values $\{\sigma_i\}_{i=1}^{N_s}$ of $\mathbf{S}_u$, while $\mathbf{Z}$ and $\mathbf{H}^T$ are two orthogonal matrices containing the singular vectors.
The POD technique selects as basis functions of the reduced-space the first n singular vectors (corresponding to the largest n singular values) of the snapshots matrix. The restriction of $\mathbf{Z}$ to the first n columns corresponds to the matrix $\mathbf{V} \in \mathbb{R}^{N_h \times n}$, whose columns are the reduced basis functions. It is possible to guarantee that the projection is controlled by a suitable tolerance ϵ_{tol}, by satisfying the following relationship:

$$\frac{\sum_i^n \sigma_i}{\sum_i^{N_s} \sigma_i} \geq 1 - \epsilon_{tol}^2.$$

An alternative method for the construction of the basis functions is the so-called greedy algorithm [PRV+02, BMP+12], which is an iterative procedure based on the evaluation of efficient error estimates of the error between the FOM and the ROM. Since in time-dependent and nonlinear case we do not have easy computable and effective error bounds, we adopt the POD approach in our test cases.

Second ingredient: Galerkin projection

The reduced-basis solution $\mathbf{u}_n = [u_n^1, \dots, u_n^n]^T$ of dimension $n \times 1$ is determined by requiring that an orthogonality criterion is satisfied.
We first consider the residual of the full-order problem (2.8)

$$\mathbf{r}_h(\mathbf{v}_h) = \mathbf{I}_{app}(t;\boldsymbol{\mu}) - \mathbf{M}(\boldsymbol{\mu})\frac{\partial \mathbf{v}_h}{\partial t} - \mathbf{A}(\boldsymbol{\mu})\mathbf{v}_h - \mathbf{N}(\mathbf{v}_h;\boldsymbol{\mu}) \qquad \forall \mathbf{v}_h \in X_h.$$

By projecting $\mathbf{r}_h(\mathbf{V}\mathbf{u}_n)$ onto the space generated by the columns of $\mathbf{V} \in \mathbb{R}^{N_h \times n}$ we obtain the identity:

$$\mathbf{V}^T \mathbf{r}_h(\mathbf{V}\mathbf{u}_n) = 0.$$

This latter gives the RB nonlinear parametrized dynamical system: for $t > 0$ and $\boldsymbol{\mu} \in \mathscr{P}$ find $\mathbf{u}_n(t;\boldsymbol{\mu}) \in \mathbb{R}^n$ as the solution of the following ODE system:

$$\begin{cases} \mathbf{M}_n(\boldsymbol{\mu})\dfrac{\partial \mathbf{u}_n}{\partial t} + \mathbf{A}_n(\boldsymbol{\mu})\mathbf{u}_n + \mathbf{V}^T\mathbf{N}(\mathbf{V}\mathbf{u}_n;\boldsymbol{\mu}) = \mathbf{I}_{app,n}(t;\boldsymbol{\mu}), \quad t \in (0,T] \\ \mathbf{u}_n(0;\boldsymbol{\mu}) = \mathbf{V}^T\mathbf{u}_0, \end{cases} \tag{2.10}$$

where the reduced arrays are given by

$$\mathbf{M}_n(\boldsymbol{\mu}) = \mathbf{V}^T\mathbf{M}(\boldsymbol{\mu})\mathbf{V}, \qquad \mathbf{A}_n(\boldsymbol{\mu}) = \mathbf{V}^T\mathbf{A}(\boldsymbol{\mu})\mathbf{V}, \qquad \mathbf{I}_{app,n} = \mathbf{V}^T\mathbf{I}_{app}.$$

Third ingredient: hyper-reduction techniques

The efficient evaluation of the reduced arrays appearing in (2.10) as time and parameters vary is still a challenging task in order to achieve an efficient online evaluation of a ROM when dealing with nonlinear and/or complex nonaffine terms. Indeed, under the assumption of affine parametric dependence, those arrays can be expressed as the finite sum of products between $\boldsymbol{\mu}$-dependent functions and $\boldsymbol{\mu}$-independent arrays [QMN16]. In the case of nonaffine parameter dependence, an affine approximation can be recovered through the *empirical interpolation method* (EIM), see e.g. [MNP$^+$09, BMN$^+$04]. For instance, given a nonaffine matrix $\mathbf{A}(\boldsymbol{\mu})$, the EIM approximation reads

$$\mathbf{A}(\boldsymbol{\mu}) \approx \sum_{j=1}^{m_{\mathrm{E}}} \beta_j^A(\boldsymbol{\mu})\mathbf{A}^j$$

where for any $\boldsymbol{\mu} \in \mathscr{P}$, the coefficients $\{\beta_j^A(\boldsymbol{\mu})\}_{j=1}^{m_{\mathrm{E}}}$ are evaluated by solving a linear system of dimension $m_{\mathrm{E}} \times m_{\mathrm{E}}$, arising by the imposition of m_{E} interpolation constraints over a set of m_{E} magic points selected according to a suitable greedy procedure (see [MNP$^+$09] for further details). Given this approximation, the reduced matrix can then be obtained by projecting each $\boldsymbol{\mu}$-independent matrix $\mathbf{A}^j$, that is,

$$\mathbf{A}_n(\boldsymbol{\mu}) = \sum_{j=1}^{m_{\mathrm{E}}} \beta_j^A(\boldsymbol{\mu})\mathbf{A}_n^j, \qquad \mathbf{A}_n^j = \mathbf{V}^T\mathbf{A}^j\mathbf{V}.$$

In this way, computations can be split into an expensive $\boldsymbol{\mu}$-independent *offline* stage and a very inexpensive $\boldsymbol{\mu}$-dependent *online* stage, to be performed several times during many-query procedures, such as parameter estimation, data-assimilation and uncertainty quantification.

Unfortunately, when dealing with the nonlinear operator $\mathbf{N}(\cdot;\boldsymbol{\mu}) \in \mathbb{R}^{N_h}$, evaluating $\mathbf{V}^T\mathbf{N}(\mathbf{V}\cdot;\boldsymbol{\mu})$ would also depend on the FOM size N_h, and would be still a very expensive task. To overcome this problem, the *(discrete) empirical interpolation method* (DEIM) can be exploited at each time-step to handle the $\boldsymbol{\mu}$-dependent nonlinear terms efficiently, as proposed in [CS10].
In particular, the DEIM approximation of a nonlinear operator is computed through the following steps:

- compute the snapshots matrix of the nonlinear term $\mathbf{N}$:

$$S_N = [\mathbf{N}(\mathbf{u}_h(t^{(0)};\boldsymbol{\mu}_1);\boldsymbol{\mu}_1), \mathbf{N}(\mathbf{u}_h(t^{(1)};\boldsymbol{\mu}_1);\boldsymbol{\mu}_1), \ldots, \mathbf{N}(\mathbf{u}_h(t^{(0)};\boldsymbol{\mu}_2);\boldsymbol{\mu}_2), \ldots] \in \mathbb{R}^{N_h \times N_s};$$

- compute the matrix of basis functions $\mathbf{U} = [\phi_1, \ldots, \phi_{m_{\mathrm{D}}}]$ by applying the POD technique on S_N;

- select m_{D} degrees of freedom $\{i_1, \ldots, i_{m_{\mathrm{D}}}\}$ according to the same procedure adopted for the calculation of the EIM magic points (described in [MNP$^+$09]); in particular, we construct the index matrix

$$\mathbf{P} = [\mathbf{e}_{i_1}, \ldots, \mathbf{e}_{i_{m_{\mathrm{D}}}}] \qquad (\mathbf{e}_i)_j = \delta_{ij}.$$

Given a new $\boldsymbol{\mu}$ and the relative reduced solution $\mathbf{u}_n$ at a given time-step, the DEIM approximation reads as

$$\mathbf{V}^T\mathbf{N}(\mathbf{V}\mathbf{u}_n;\boldsymbol{\mu}) \approx \underbrace{\mathbf{V}^T\mathbf{U}(\mathbf{P}^T\mathbf{U})^{-1}}_{n \times m_{\mathrm{D}}} \underbrace{\mathbf{N}(\mathbf{P}^T\mathbf{V}\mathbf{u}_n;\boldsymbol{\mu})}_{m_{\mathrm{D}} \times 1}.$$

We emphasize that $\mathbf{P}$ selects only a subset of indexes from the full-order solution vector: this means that we do not need to assemble the nonlinear operator on the entire mesh, but only on the elements related to the degrees of freedom selected by the DEIM algorithm. In the following we will refer to this group of elements as *reduced mesh*.
In the case of an implicit time-advancing scheme, also the Jacobian $\mathbf{J}_N$ of the nonlinear term has to be assembled efficiently at each Newton step. For the case at hand, we can directly differentiate the previous formula, yielding

$$\mathbf{J}_N(\mathbf{u}_n;\boldsymbol{\mu}) \approx \underbrace{\mathbf{V}^T\mathbf{U}(\mathbf{P}^T\mathbf{U})^{-1}}_{n\times m_\mathrm{D}} \underbrace{\mathbf{J}_N(\mathbf{P}^T\mathbf{V}\mathbf{u}_n;\boldsymbol{\mu})}_{m_\mathrm{D}\times m_\mathrm{D}} \underbrace{\mathbf{P}^T\mathbf{V}}_{m_\mathrm{D}\times n}.$$

Also in this case the Jacobian is assembled only on the elements of the *reduced mesh*. Alternative solutions can be obtained by considering an extension of DEIM for sparse Jacobians, known as *matrix* DEIM; see also the related discussion in [NMA15, ŞS16].

Extension to coupled electrophysiology models

The RB methodology introduced in this Section yields the following reduced dynamical system (obtained by projecting the problem (2.2)): given $\boldsymbol{\mu}\in\mathscr{P}$ find $\mathbf{u}_n^{(\ell+1)}$ and $\mathbf{w}_h^{(\ell+1)}$ such that

$$\begin{cases} \left(\dfrac{\mathbf{M}_n(\boldsymbol{\mu})}{\Delta t}+\mathbf{A}_n(\boldsymbol{\mu})\right)\mathbf{u}_n^{(\ell+1)} = -\mathbf{V}^T\mathbf{I}_{ion}(\mathbf{V}\mathbf{u}_n^{(\ell)},\mathbf{w}_h^{(\ell)};\boldsymbol{\mu}) + \dfrac{\mathbf{M}_n(\boldsymbol{\mu})}{\Delta t}\mathbf{u}_n^{(\ell)} + \mathbf{I}_{app,n}^{(\ell+1)}(\boldsymbol{\mu}), & \ell=0,\dots,N_t-1 \\ \mathbf{P}^T\mathbf{w}_h^{(\ell+1)} = \mathbf{P}^T\mathbf{w}_h^{(\ell)} + \Delta t\,\mathbf{g}(\mathbf{P}^T\mathbf{u}_h^{(\ell)},\mathbf{P}^T\mathbf{w}_h^{(\ell)};\boldsymbol{\mu}) & \ell=0,\dots,N_t-1 \\ \mathbf{u}_n^{(0)} = \mathbf{V}^T\mathbf{u}_0(\boldsymbol{\mu}) \\ \mathbf{w}_h^{0} = \mathbf{w}_0(\boldsymbol{\mu}), \end{cases} \tag{2.11}$$

where the nonlinear ionic term is approximated using the DEIM approach:

$$\mathbf{V}^T\mathbf{I}_{ion}(\mathbf{V}\mathbf{u}_n,\mathbf{w}_h;\boldsymbol{\mu}) \approx \underbrace{\mathbf{V}^T\mathbf{U}(\mathbf{P}^T\mathbf{U})^{-1}}_{n\times m_\mathrm{D}} \underbrace{\mathbf{I}_{ion}(\mathbf{P}^T\mathbf{V}\mathbf{u}_n,\mathbf{P}^T\mathbf{w}_h;\boldsymbol{\mu})}_{m_\mathrm{D}\times 1}.$$

This means that the point-wise approximation of the ODE could be advanced in time only in those dofs forming the *reduced mesh*, gaining an additional speedup in the resolution of the problem.
Alternatively, the ODE could be reduced by applying the RB method, as done for the potential u. Starting from the snapshots matrix formed by full-order solutions $\mathbf{w}(t^{(\ell)};\boldsymbol{\mu})$, for $\ell=0,\dots,N_t$ and $\boldsymbol{\mu}\in P_{train}$, the basis functions of the reduced-space $X_n^w\subset X_h$ are computed by means of the POD. In the same way, the DEIM method gives an efficient approximation of $\mathbf{g}(\mathbf{u}_h,\mathbf{w}_h;\boldsymbol{\mu})$.

The implicit Euler method leads instead to the following nonlinear dynamical system: given $\boldsymbol{\mu}\in\mathscr{P}$ find $\mathbf{u}_n^{(\ell+1)}$ and $\mathbf{w}_h^{(\ell+1)}$ such that

$$\begin{cases} \left(\dfrac{\mathbf{M}_n(\boldsymbol{\mu})}{\Delta t}+\mathbf{A}_n(\boldsymbol{\mu})\right)\mathbf{u}_n^{(\ell+1)} + \mathbf{V}^T\mathbf{I}_{ion}(\mathbf{V}\mathbf{u}_n^{(\ell+1)},\mathbf{w}_h^{(\ell+1)};\boldsymbol{\mu}) = \dfrac{\mathbf{M}_n(\boldsymbol{\mu})}{\Delta t}\mathbf{u}_n^{(\ell)} + \mathbf{I}_{app}^{(\ell+1)}(\boldsymbol{\mu}) & \ell=0,\dots,N_t-1 \\ \dfrac{\mathbf{M}(\boldsymbol{\mu})}{\Delta t}\mathbf{w}_h^{(\ell+1)} = \dfrac{\mathbf{M}(\boldsymbol{\mu})}{\Delta t}\mathbf{w}_h^{(\ell)} + \mathbf{g}(\mathbf{u}_h^{(\ell)},\mathbf{w}_h^{(\ell)};\boldsymbol{\mu}) & \ell=0,\dots,N_t-1 \\ \mathbf{u}_n^{(0)} = \mathbf{V}^T\mathbf{u}_0(\boldsymbol{\mu}) \\ \mathbf{w}_h^{(0)} = \mathbf{w}_0(\boldsymbol{\mu}). \end{cases} \tag{2.12}$$

Due to the presence of the nonlinear term $\mathbf{I}_{ion}(\cdot,\cdot;\boldsymbol{\mu})$, we use the Newton method as follows: while $\|\boldsymbol{\delta}^{\iota}_{u_n}\| < \epsilon_{tol}$, we solve

$$\mathbf{J}_n\left(\begin{bmatrix}\mathbf{u}^{(\ell+1)}_{n,\iota}\\ \mathbf{w}^{(\ell+1)}_{h,\iota}\end{bmatrix}\right)\begin{bmatrix}\boldsymbol{\delta}^{\iota}_{u,n}\\ \boldsymbol{\delta}^{\iota}_{w}\end{bmatrix} = \mathbf{r}_n\left(\begin{bmatrix}\mathbf{u}^{(\ell+1)}_{n,\iota}\\ \mathbf{w}^{(\ell+1)}_{h,\iota}\end{bmatrix}\right), \qquad \begin{bmatrix}\mathbf{u}^{(\ell+1)}_{n,\iota+1}\\ \mathbf{w}^{(\ell+1)}_{h,\iota+1}\end{bmatrix} = \begin{bmatrix}\mathbf{u}^{(\ell+1)}_{n,\iota}\\ \mathbf{w}^{(\ell+1)}_{h,\iota}\end{bmatrix} + \begin{bmatrix}\boldsymbol{\delta}^{\iota}_{u,n}\\ \boldsymbol{\delta}^{\iota}_{w}\end{bmatrix} \qquad \iota = 1,\dots, \quad (2.13)$$

with $\mathbf{u}^{(\ell+1)}_{n,0} = \mathbf{u}^{(\ell)}_n$ and $\mathbf{w}^{(\ell+1)}_{h,0} = \mathbf{w}^{(\ell)}_h$. The linear part of the reduced Jacobian matrix $\mathbf{J}_n$ and of the reduced residual vector $\mathbf{r}_n$ appearing in (2.11) are obtained by the Galerkin projection of respectively the matrix (2.6) and (2.7) on the matrix $\mathbf{V}$, as shown previously.

By combining all these tools we are able to obtain a robust *offline*/*online* decomposition yielding the computational speedup needed in a many-query context. During the *offline* phase an affine decomposition of the nonaffine and nonlinear terms is developed, the construction of the basis functions is performed and the reduced matrices are assembled. These computational expensive tasks are performed only once, then an inexpensive *online* phase, consisting in the ROM evaluation, can be performed for each new $\boldsymbol{\mu} \in \mathscr{P}$. At each time-step the ROM query required only to assemble the nonlinear terms on the *reduced mesh* and to solve the linear system (2.11) (or the nonlinear system (2.12)). We sum up this POD-DEIM approach in Algorithm 1.

2.3 Localized Reduced basis method

In complex applications such as the ones arising from cardiac electrophysiology, the dimensions n and m_D of the ROM, and thus the computational cost of each online query, do not yield a considerable speedup. This is due the fact that n and m_D are not considerably small, because of the great variability of the electrical potential evolution when different model parameters are considered. For this reason, also memory issues affect the offline procedure, preventing a positive trade-off between offline and online phases. A possible way to overcome these issues is to rely on multiple local reduced-subspaces when performing the RB approximation of the PDE solution and the DEIM approximation of the nonlinear term. These subspaces are built during a computationally intense *offline* procedure formed by the following steps:

1. the snapshots matrix $\mathbf{S}_u$ (defined in (2.9)) is partitioned into N_c submatrices (clusters) $\mathbf{S}^k_u$, $k = 1,\dots,k$: each column of $\mathbf{S}_u$ is assigned to a cluster accordingly to a given criterium. In the same way, the snapshots matrix $\mathbf{S}_I$ of the nonlinear term is partitioned into N_c submatrices $\mathbf{S}^k_I$, $k = 1,\dots,k$;

2. the construction of the localized basis functions to express the problem solution (and respectively the nonlinear term) is performed through the POD technique applied to each one of the N_c submatrices $\mathbf{S}^k_u$ ($\mathbf{S}^k_I$), $k = 1,\dots,N_c$; the resulting basis functions are stored in the corresponding matrices $\mathbf{V}_k$ ($\mathbf{U}_k$), $k = 1,\dots,N_c$;

3. the reduced matrices and vectors forming the reduced system are computed by means of the Galerkin projection onto $\mathbf{V}_k$ for each cluster $k = 1,\dots,N_c$.

The online query is then performed using the local RB matrices and vectors and local DEIM approximation associated to the reduced-subspace selected by the given criterium used in step 1. This reduction approach was firstly proposed in [AZF12] and in [PBW+14], only for the

Algorithm 1 Standard POD-DEIM procedure

procedure [ROM ARRAYS] = OFFLINE(FOM ARRAYS, P_{train}, ϵ_{tol})
  Full-order matrices:
  $\{\beta_j^M(\boldsymbol{\mu}), \mathbf{M}_j\} \leftarrow$ affine decomposition of $\mathbf{M}(\boldsymbol{\mu})$
  $\{\beta_j^A(\boldsymbol{\mu}), \mathbf{A}_j\} \leftarrow$ affine decomposition of $\mathbf{A}(\boldsymbol{\mu})$
  $\{\beta_j^{app}(\boldsymbol{\mu})\mathbf{I}_{app,j}\} \leftarrow$ affine decomposition of $\mathbf{I}_{app}$
  for $\boldsymbol{\mu} \in P_{train}$ **do**
    for $\ell = 1, \dots, N_t$ **do**
      $\mathbf{S}_u = [\mathbf{S}_u, \mathbf{u}_h^{(\ell)}(\boldsymbol{\mu})]$;
      $\mathbf{S}_I = [\mathbf{S}_I, \mathbf{I}_{ion}(\mathbf{u}_h^{(\ell)}, \mathbf{w}_h^{(\ell)}; \boldsymbol{\mu})]$;
    end for
  end for
  $\mathbf{V} \leftarrow POD(\mathbf{S}_u, \epsilon_{tol})$;
  $\mathbf{U} \leftarrow POD(\mathbf{S}_I, \epsilon_{tol})$;
  $\mathbf{P} \leftarrow DEIMindices(\mathbf{U})$;
  Reduced-order matrices:
  $\{\mathbf{M}_{n,j}, \mathbf{A}_{n,j}, (\mathbf{I}_{app,n})_j\} \leftarrow$ projection of the full order matrices onto $\mathbf{V}$
end procedure

procedure [$\mathbf{u}_n$] = ONLINE QUERY(ROM ARRAYS, $\boldsymbol{\mu}$, $\mathbf{u}_{n,0}$, $\mathbf{P}^T\mathbf{w}_0$)
  reduced-order matrices:
  $\mathbf{M}_n(\boldsymbol{\mu}) = \sum_j \beta_j^M(\boldsymbol{\mu})\mathbf{M}_{n,j}$;
  $\mathbf{A}_n(\boldsymbol{\mu}) = \sum_j \beta_j^A(\boldsymbol{\mu})\mathbf{A}_{n,j}$;
  $\mathbf{I}_{app,n} = \sum_j \beta_j^{app}(\boldsymbol{\mu})(\mathbf{I}_{app,n})_j$;
  for $\ell = 1, \dots, N_t$ **do**
    assemble over the reduced mesh $\mathbf{I}_{ion}(\mathbf{P}^T\mathbf{V}\mathbf{u}_n^{(\ell)}, \mathbf{P}^T\mathbf{w}_h^{(\ell)}; \boldsymbol{\mu})$;
    DEIM approximation $\leftarrow \mathbf{V}^T\mathbf{U}(\mathbf{P}^T\mathbf{U})^{-1}\mathbf{I}_{ion}(\mathbf{P}^T\mathbf{V}\mathbf{u}_n^{(\ell)}, \mathbf{P}^T\mathbf{w}_h^{(\ell)}; \boldsymbol{\mu})$;
    $\mathbf{u}_n^{(\ell+1)} \leftarrow$ solve linear system (2.11);
  end for
end procedure

DEIM approximation of the nonlinear terms. In the following we will apply this methodology in the context of electrophysiology, covering all the possible different strategies for the selection of subspaces subdivision.

Time-based subdivision

Since the system dynamics consists of a traveling front characterizing the depolarization mechanism of the electrical potential, a natural subdivision in clusters of $\mathbf{S}_u$ could be obtained by considering different temporal windows. With this aim, we introduce a coarse partition of the time interval $(0, T)$ into N_c windows $(\tau^{(k)}, \tau^{(k+1)})$ of length $\Delta\tau = K\Delta t$, with $k = 0, \dots, N_c - 1$ and $K > 1$ (a sketch is reported in Fig. 2.2).

In this case the time-step $t^{(\ell)}$ becomes the cluster indicator, that is, each solution $\mathbf{u}_h^{(\ell)}(\boldsymbol{\mu})$ is assigned to a specific cluster k if $t^{(\ell)} \in (\tau^{(k-1)}, \tau^{(k)}]$ (see Figure 2.3).

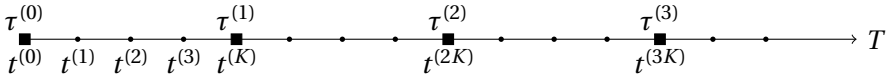

Figure 2.2 – A partition of the time interval in windows of length $\Delta\tau = K\Delta t$, $K = 4$.

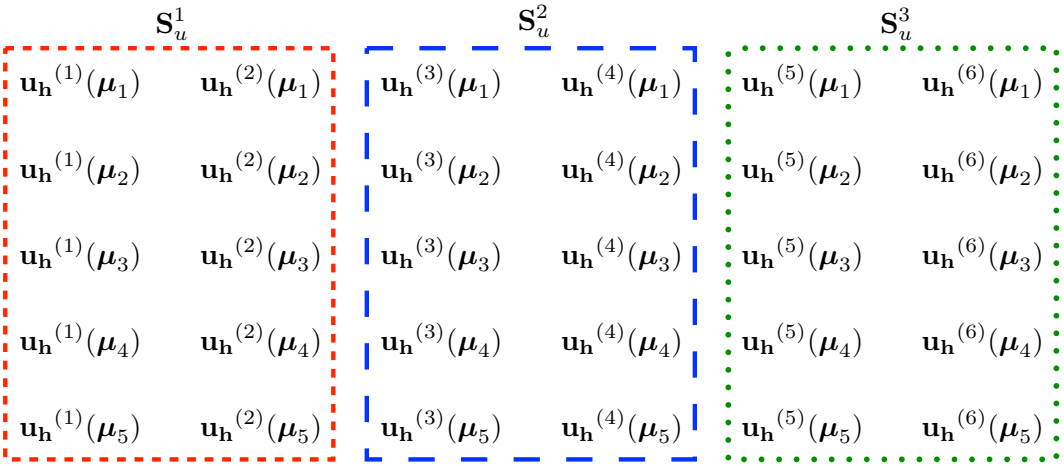

Figure 2.3 – Example of snapshots time-based classification.

Then, the matrices $\mathbf{V}_k \in \mathbb{R}^{N_h \times n_k}$, $k = 1,\dots,N_c$, which collect the localized basis functions computed by the POD technique, enable to approximate the full-order solution as

$$\mathbf{u}_h^{(\ell)}(\boldsymbol{\mu}) \approx \mathbf{V}_k \mathbf{u}_{n_k}^{(\ell)}(\boldsymbol{\mu}) \qquad \text{with } k \; s.t. \; t^{(\ell)} \in (\tau^{(k-1)}, \tau^{(k)}].$$

Similarly, the matrices $\mathbf{U}_k \in \mathbb{R}^{N_h \times m_{D,k}}$, $k = 1,\dots,N_c$ containing the localized basis functions of the DEIM approximation, allow to express the non-linear term as

$$\mathbf{I}_{ion}(\mathbf{u}_n^{(\ell)}, \mathbf{w}_h^{(\ell)}; \boldsymbol{\mu}) \approx \underbrace{\mathbf{V}_k^T \mathbf{U}_k (\mathbf{P}_k^T \mathbf{U}_k)^{-1}}_{n_k \times m_k} \underbrace{\mathbf{I}_{ion}(\mathbf{P}_k^T \mathbf{V}_k \mathbf{u}_n^{(\ell)}, \mathbf{P}_k^T \mathbf{w}_h^{(\ell)}; \boldsymbol{\mu})}_{m_k \times 1} \qquad \text{with } k \; s.t. \; t^{(\ell)} \in (\tau^{(k-1)}, \tau^{(k)}].$$

This approach, summarized in Algorithm 2, is effective if the velocity of the propagation of the signal is constant with respect to the parameters. If not (e.g. when the conductivity field is parametrized), similar solutions could be assigned to different clusters, affecting the overall efficiency of the proposed localized-ROM.

Parameter-based subdivision

An alternative approach is obtained by considering the vector of parameters as clusters indicator, that is, by assigning each solution $\mathbf{u}_h^{(\ell)}(\boldsymbol{\mu})$ of $\mathbf{S}_u$ to a specific cluster k if $\boldsymbol{\mu} \in \mathscr{P}_k$, where $\mathscr{P} = \cup_k \mathscr{P}_k$ is a suitable subdivision of the parameter space (see Figure 2.4). Except for this new criterium used for subdividing the snapshots matrix $\mathbf{S}_u$, the offline procedure is very similar to the one proposed in Algorithm 2: for each cluster the basis functions of the solution and of the nonlinear term are computed through the POD technique and consequently stored (see Algorithm 3).

Algorithm 2 Offline procedure: time-based approach

procedure [ROM ARRAYS] = OFFLINE(FOM ARRAYS, P_{train}, ϵ_{tol}, N_c)
  Loop over each cluster:
  for $k = 1, \dots, N_c$ **do**
    for $\boldsymbol{\mu} \in P_{train}$ **do**
      for $t^{(\ell)} \in (\tau^{(k-1)}, \tau^{(k)}]$ **do**
        $\mathbf{S}_u^k = [\mathbf{S}_u^k, \mathbf{u}_h^{(\ell)}(\boldsymbol{\mu})]$;
        $\mathbf{S}_I^k = [\mathbf{S}_I^k, \mathbf{I}_{ion}(\mathbf{u}_h^{(\ell)}, \mathbf{w}_h^{(\ell)}; \boldsymbol{\mu})]$;
      end for
    end for
    $\mathbf{V}_k \leftarrow POD(\mathbf{S}_u^k, \epsilon_{tol})$;
    $\mathbf{U}_k \leftarrow POD(\mathbf{S}_I^k, \epsilon_{tol})$;
    $\mathbf{P}_k \leftarrow DEIMindices(\mathbf{U}_k)$;
    Reduced-order matrices:
    $\{\mathbf{M}_{n_k}^j, \mathbf{A}_{n_k}^j, \mathbf{I}_{app,n_k}^j\} \leftarrow$ projection of the full order matrices onto $\mathbf{V}_k$
  end for
end procedure

The problem is then shifted to finding the optimal subdivision $\{\mathscr{P}_k\}_{k=1}^{N_c}$ to obtain low dimensional localized-ROMs. A sequential partitioning has been firstly proposed in [HDO11], where the parameter domain is subdivided using grid-adaptive refinement until each partition satisfies a given accuracy and size of the local reduced space. This procedure could easily lead to a high number of clusters, thus yielding high *offline* computational costs. Moreover, this partitioning also neglects the possibility that different parameter could generate similar solutions for different time-steps. In cardiac electrophysiology an approach for the subdivision of the

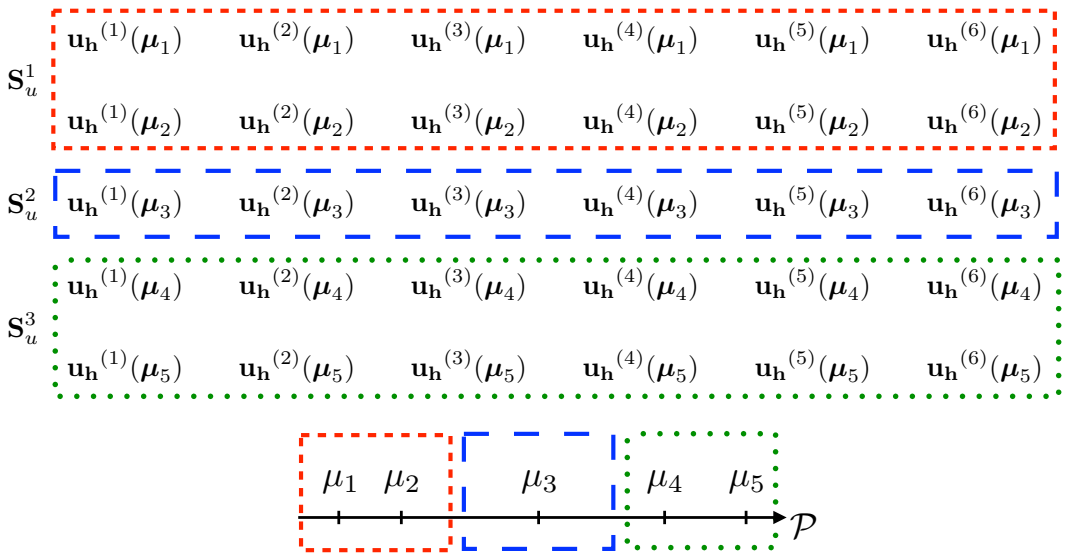

Figure 2.4 – Example of snapshots parameter-based classification.

parameter domain has been first proposed in [YV16]: it is based on the empirical observation of the approximation error between the full-order model and a POD-DEIM ROM.
Given a set of training points P_{train}, for each $\boldsymbol{\mu}_k \in P_{train}$ a localized POD-DEIM ROM is built from the snapshots matrix:

$$\mathbf{S}_u^k = [\mathbf{u}_h(t^{(0)}, \boldsymbol{\mu}_k), \mathbf{u}_h(t^{(1)}, \boldsymbol{\mu}_k), \dots, \mathbf{u}_h(t^{(N_t)}, \boldsymbol{\mu}_k)].$$

This construction of the localized ROMs might generate a high number of small subregions and similar drawbacks of the sequential partitioning proposed in [HDO11]. To avoid the high-memory consumption drawback, an informed exploration of the parameter space should be performed. The parameters that mainly affect the solution of the problem should be accurately sampled, by means e.g. of a sparse grid [BG04]. Numerical tools for the data-driven exploration of the parameters space will be presented in Chapter 4. Moreover, suitable modification of the greedy algorithm should be investigated: efficient ROM error surrogates, developed in Chapter 3, can be used in replacement of the non available error bounds during the iterative basis construction.

Algorithm 3 Offline procedure: parameter-based approach

procedure [ROM ARRAYS] = OFFLINE(FOM ARRAYS,P_{train},ϵ_{tol},N_c)
  Loop over each cluster:
  for $k = 1, \dots, N_c$ **do**
    for $\boldsymbol{\mu} \in \mathscr{P}_k$ **do**
      for $\ell = 1, \dots, N_t$ **do**
        $\mathbf{S}_u^k = [\mathbf{S}_u^k, \mathbf{u}_h^{(\ell)}(\boldsymbol{\mu})]$;
        $\mathbf{S}_I^k = [\mathbf{S}_I^k, \mathbf{I}_{ion}(\mathbf{u}_h^{(\ell)}, \mathbf{w}_h^{(\ell)}; \boldsymbol{\mu})]$;
      end for
    end for
    $\mathbf{V}_k \leftarrow POD(\mathbf{S}_u^k, \epsilon_{tol})$;
    $\mathbf{U}_k \leftarrow POD(\mathbf{S}_I^k, \epsilon_{tol})$;
    $\mathbf{P}_k \leftarrow DEIMindices(\mathbf{U}_k)$;
    Reduced-order matrices:
    $\{\mathbf{M}_{n_k}^j, \mathbf{A}_{n_k}^j, \mathbf{I}_{app,n_k}^j\} \leftarrow$ projection of the full order matrices onto $\mathbf{V}_k$
  end for
end procedure

State-based subdivision

Finally, a general approach based on the current state solution as cluster indicator is proposed. Clustering techniques are unsupervised machine learning techniques [XW05, FHT01], exploited to subdivide similar snapshots $\{\mathbf{u}_h^{(\ell)}(\boldsymbol{\mu}_k)\}_{k=1}^{N_c}$, $\ell = 1, \dots, N_t$ and $\boldsymbol{\mu}_j \in P_{train}$ into N_c clusters (see Figure 2.5).

The clusters are constructed in such a way that the snapshots within each group are similar to each other, while snapshots in different groups are different from each other with respect to a chosen metric. The two most popular approaches are the k-means clustering [Llo82, HW79],

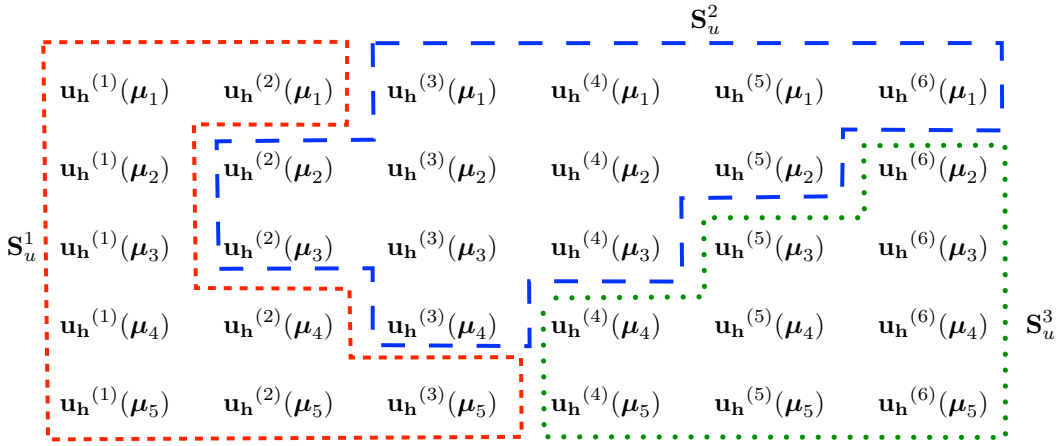

Figure 2.5 – Example of snapshots state-based classification.

which subdivides the snapshots into a selected number N_c of non-overlapping groups, and the hierarchical clustering [Joh67, WJ63], which explores all the possible subdivisions in a given dataset (through the so-called dendogram). For the sake of computational efficiency, in this work we will rely on the former option. In the numerical results we have tested the k-means algorithm by selecting several different choices of the number N_c of clusters, looking for the best balance between accuracy and efficiency.

K-means clustering aims to partition the snapshots matrix $\mathbf{S}_u$ into N_c submatrices $\{\mathbf{S}_u^1,\dots,\mathbf{S}_u^{N_c}\}$ in order to minimize the distance between each vector in the cluster and the cluster sample mean. In other words, its objective is to find:

$$\{\mathbf{S}_u^1,\dots,\mathbf{S}_u^k\} = \arg\min_{\mathbf{S}_u} \sum_{k=1}^{N_c} \sum_{\mathbf{u}_h \in \mathbf{S}_u^k} \|\mathbf{u}_h - \mathbf{c}_h^k\|, \qquad \mathbf{c}_h^k = \frac{1}{|\mathbf{S}_u^k|} \sum_{\mathbf{u}_h \in \mathbf{S}_u^k} \mathbf{u}_h.$$

Here, $\{\mathbf{c}_h^k\}_{k=1}^{N_c}$ are the so-called centroids selected by the k-means algorithm with respect to the selected norm $\|\cdot\|$. Once the *offline* procedure (Algorithm 4) is completed, a local ROM is then selected with respect to the current solution of the system $\mathbf{u}_h$ by minimizing the distance between $\mathbf{u}_h$ and the centroids:

$$\bar{k} = \arg\min_k \|\mathbf{u}_h - \mathbf{c}_h^k\|. \tag{2.14}$$

The main advantage of this approach is the automatic detection of the similarities between the snapshots performed by the k-means algorithm, which thus fixes the risk of misclassification present in the time- and parameter-based localization strategies.
The additional cost of solving the minimization problem (2.14) decreases when the reduced arrays are considered: indeed the objective in (2.14) can be rewritten as:

$$\|\mathbf{V}\mathbf{u}_n - \mathbf{c}_h^k\| = ((\mathbf{V}\mathbf{u}_n - \mathbf{c}_h^k)^T \mathbf{X}^{-1} (\mathbf{V}\mathbf{u}_n - \mathbf{c}_h^k))^{\frac{1}{2}}, \tag{2.15}$$

where $\mathbf{X} \in \mathbb{R}^{N_h \times N_h}$ is a symmetric positive definite matrix defining the chosen metric. We then rewrite the right-hand side of (2.15) as

$$((\mathbf{V}\mathbf{u}_n - \mathbf{c}_h^k)^T \mathbf{X}^{-1} (\mathbf{V}\mathbf{u}_n - \mathbf{c}_h^k))^{\frac{1}{2}} = (\mathbf{u}_n^T (\mathbf{V}^T \mathbf{X}^{-1} \mathbf{V}^T) \mathbf{u}_n - 2\mathbf{u}_n^T (\mathbf{V}^T \mathbf{X}^{-1} \mathbf{c}_h^k) + \|\mathbf{c}_h^k\|^2)^{\frac{1}{2}},$$

Algorithm 4 Offline procedure: state-based approach

procedure [ROM ARRAYS] = OFFLINE(FOM ARRAYS, P_{train}, ϵ_{tol}, N_c)
  Clustering construction:
  for $\boldsymbol{\mu} \in P_{train}$ **do**
    for $\ell = 1, \dots, N_t$ **do**
      $\mathbf{S}_u = [\mathbf{S}_u, \mathbf{u}_h^{(\ell)}(\boldsymbol{\mu})]$;
    end for
  end for
  $\{\mathbf{c}_h^k\} \leftarrow kmeans(\mathbf{S}_u)$
  Loop over each cluster:
  for $\boldsymbol{\mu} \in P_{train}$ **do**
    for $\ell = 1, \dots, N_t$ **do**
      $\bar{k} = \arg\min_k \|\mathbf{u}_h - \mathbf{c}_h^k\|$
      $\mathbf{S}_u^{\bar{k}} = [\mathbf{S}_u^{\bar{k}}, \mathbf{u}_h^{(\ell)}(\boldsymbol{\mu})]$;
      $\mathbf{S}_I^{\bar{k}} = [\mathbf{S}_I^{\bar{k}}, \mathbf{I}_{ion}(\mathbf{u}_h^{(\ell)}, \mathbf{w}_h^{(\ell)}; \boldsymbol{\mu})]$;
    end for
  end for
  for $k = 1, \dots, N_c$ **do**
    $\mathbf{V}_k \leftarrow POD(\mathbf{S}_u^k, \epsilon_{tol})$;
    $\mathbf{U}_k \leftarrow POD(\mathbf{S}_I^k, \epsilon_{tol})$;
    $\mathbf{P}_k \leftarrow DEIMindices(\mathbf{U}_k)$;
    Reduced-order matrices:
    $\{\mathbf{M}_{n_k}^j, \mathbf{A}_{n_k}^j, \mathbf{I}_{app,n_k}^j\} \leftarrow$ projection of the full order matrices onto $\mathbf{V}_k$
  end for
end procedure

in order to separate the constant term from the other ones depending only on the RB solution. As a consequence, during the offline phase the norms $\|\mathbf{c}_h^k\|^2$ can be precomputed for each $k = 1, \dots, N_c$ and the reduced matrices $\mathbf{V}^T\mathbf{X}^{-1}\mathbf{V}^T$ and $\mathbf{V}^T\mathbf{X}^{-1}\mathbf{c}_h^k$ can be preassembled. Then, the online evaluation of the k norms (2.15) can be performed efficiently only relying on low-dimensional arrays.

2.4 Test case: Monodomain equation

In order to highlight the main features of the proposed methods we analyze the different localized RB strategies on a two-dimensional monodomain model (1.4) describing the behavior of the cardiac potential in presence of an ischemic region over a simplified slab of the myocardial tissue $\Omega = (0,1)^2$. We assume an isotropic conductivity tensor $\mathbf{D}_0 = \sigma_v(\mathbf{x};\boldsymbol{\mu})\mathbf{I}$, being $\sigma_v(\mathbf{x};\boldsymbol{\mu})$ a non-homogeneous parametrized conductivity field:

$$\sigma_v(\mathbf{x};\boldsymbol{\mu}) = \sigma_h g(\mathbf{x};\boldsymbol{\mu}) + \sigma_i(1 - g(\mathbf{x};\boldsymbol{\mu})) \qquad g(\mathbf{x};\boldsymbol{\mu}) = 1 - exp\left(-\frac{(x_1-\mu_1)^2 + (x_2-\mu_2)^2}{2\mu_3^2}\right), \qquad \mathbf{x} \in \Omega,$$

where $\mu_1 \in [0.25, 0.75]$ and $\mu_2 \in [0.25, 0.75]$ indicate the position of the center of the ischemia, and $\mu_3 \in [0.05, 0.4]$ its size. Here, we neglect the role of the recovery variable w: as a conse-

quence, the model is only able to describe depolarization patterns, which are represented in Figure 2.6 for different choices of the parameters vector $\boldsymbol{\mu} = (\mu_1, \mu_2, \mu_3)^T$.

Therefore, the model consists of the following parabolic nonlinear PDE: given $\boldsymbol{\mu} \in \mathscr{P} \subset \mathbb{R}^3$, find $u = u(\mathbf{x}, t; \boldsymbol{\mu})$ s.t.:

$$\begin{cases} \dfrac{\partial u}{\partial t} - \nabla \cdot (\sigma_v(\mathbf{x}; \boldsymbol{\mu}) \nabla u) + I_{ion}(u; \boldsymbol{\mu}) = I_{app}(\mathbf{x}, t) & \mathbf{x} \in \Omega, t \in (0, T] \\ \sigma_v(\mathbf{x}; \boldsymbol{\mu}) \nabla u \cdot \mathbf{n} = 0 & \mathbf{x} \in \partial\Omega, t \in (0, T] \\ u(\mathbf{x}, 0; \boldsymbol{\mu}) = u_0 & \mathbf{x} \in \Omega, \end{cases} \tag{2.16}$$

where $I_{ion}(u; \boldsymbol{\mu}) = g(\mathbf{x}; \boldsymbol{\mu}) u(u-a)(u-1)$ is the ionic current and

$$I_{app}(\mathbf{x}, t) = C exp\left(-\frac{x_1^2 + x_2^2}{0.02}\right) \mathbb{1}_{[0, \Delta t]}(t)$$

the initial applied stimulus. Here $\mathbb{1}$ denotes the indicator function, defined as

$$\mathbb{1}_{(a,b)}(t) = \begin{cases} 0 & \text{if } t \notin (a, b) \\ 1 & \text{if } t \in (a, b). \end{cases}$$

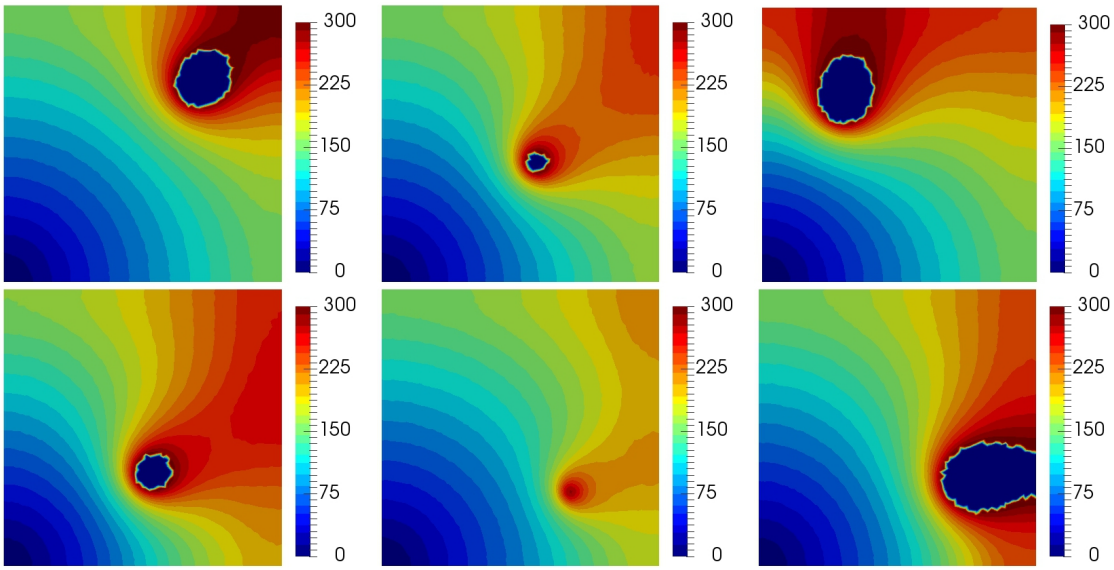

Figure 2.6 – Depolarization time [ms] for six different values of the parameter vector $\boldsymbol{\mu}$. The velocity of the depolarization front considerably slow down, when the signal reaches the ischemic region.

This test case will be adopted for the comparison of different numerical strategies for the construction of reduced-order models in cardiac electrophysiology. Despite of all the simplifying assumptions that we have made, the solution of problem (2.16) shows a great variability due to the different front propagation patterns caused by the ischemic region location and dimensions (see Figure 2.6). As a consequence, this problem represents a very challenging test case for developing efficient reduction techniques.

In this case, the matrix $\mathbf{A}(\boldsymbol{\mu})$ is non-affine, because of the presence of the term $g(\mathbf{x};\boldsymbol{\mu})$. Given that $\mathbf{g}(\boldsymbol{\mu})$ is the vector obtained by evaluating $g(\mathbf{x};\boldsymbol{\mu})$ on the mesh nodes, the affine approximation of $g(\boldsymbol{\mu})$ is given by the discrete empirical interpolation method (DEIM):

$$\mathbf{g}_{DEIM}(\boldsymbol{\mu}) = \sum_{j=1}^{60} \beta_j(\boldsymbol{\mu})\zeta^j.$$

Here, ζ^j, $j = 1,\dots,60$, are the basis functions of the non-affine term g, computed using the POD techniques. The number of basis functions $m_D = 60$ satisfies the following criterium (see Figure 2.7):

$$m_D = \arg\min_k \left(\frac{\sum_i^k \sigma_i}{\sum_i^{N_s} \sigma_i} \geq 0.99. \right),$$

Then, an affine approximation of the matrix $\mathbf{A}(\boldsymbol{\mu})$ follows:

$$\mathbf{A}(\boldsymbol{\mu}) = \sum_{j=1}^{60} \beta_j(\boldsymbol{\mu})\mathbf{A}^j$$

where the $\mathbf{A}^j$, $j = 1,\dots,60$, are full-order matrices assembled considering as diffusive term $(\sigma_h - \sigma_i)\zeta^j + \sigma_i$. In this way, a suitable offline-online decomposition is achievable by adopting the RB method for the approximation of the solution u, equipped with an hyper-reduction technique in order to manage the nonlinear term.

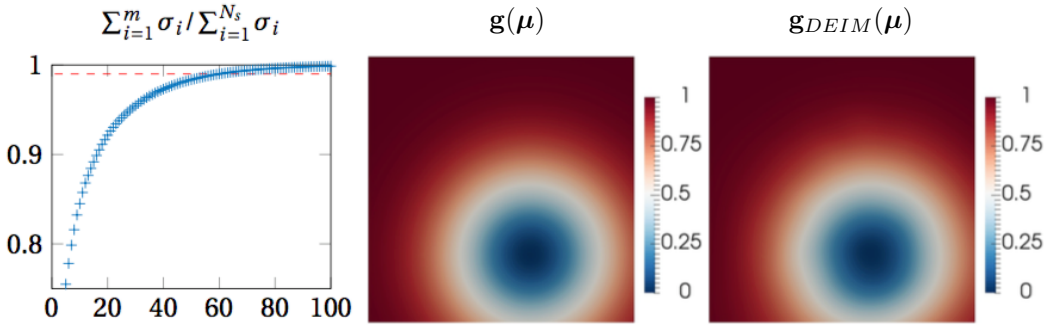

Figure 2.7 – The behavior of the ratio between the truncated and the total cumulative sums of the singular values shows how much variability of $\mathbf{g}$ is captured by the POD approximation. For $\boldsymbol{\mu} = [0.39, 0.26, 0.22]$ we compare the exact vector $\mathbf{g}(\boldsymbol{\mu})$ with its DEIM approximation.

2.4.1 POD-DEIM approach

In this subsection we show how the standard approach is not feasible for the solution of this test case, since the manifold of the solutions is considerably complex. In fact, the lack of conductivity substantially modify the form of the traveling front, which differs from a parameter to another (see the activation times reported in Figure 2.6). This difficulty affects both the dimensionality of the training set P_{train} (database of pre-computed simulations) and the resulting number of POD-DEIM basis functions (POD tolerance set to $\epsilon_{tol} = 10^{-2}$). With this aim, we construct different ROMs by varying the dimension $N_{train} = \{5, 10, 25, 50, 75, 100\}$

of the parameters training set P_{train} (the corresponding snapshots matrix $\mathbf{S}_u$ is formed by $N_s = 300N_{train}$ full-order vectors, being 300 the number of time-steps adopted by the semi-implicit time-advancing scheme). The numerical results, summarized in Figure 2.8, left, show that the training set needs to be sufficiently rich (at least $N_{train} = 75$) in order to correctly approximate the state solution for parameters different from the ones forming the training set.

To test our procedure in the *online* phase by selecting additional $N_{oob} = 25$ parameters to perform the so-called out-of-bag prediction: for each parameter in the set P_{oob} we compute the maximum, the mean and the integral over $(0, T)$ of the error with respect to the full-order solution (see right Figure 2.8). The error continues to decrease when considering higher training sets (and correspondingly higher snapshots matrices): in particular, by taking $N_{train} = 100$, the same accuracy required on the training set is reached also on the out-of-bag set P_{oob}.

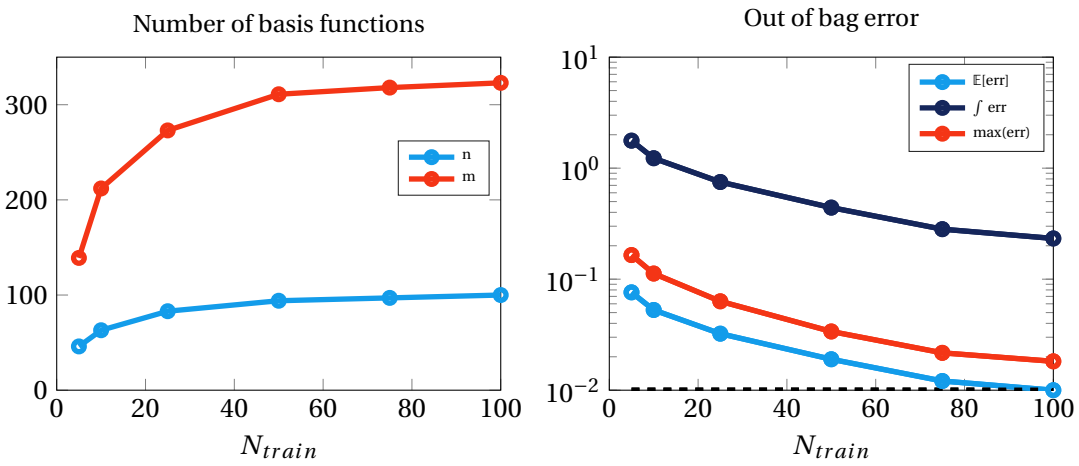

Figure 2.8 – Number of basis functions forming the POD-DEIM ROMs on varying the number of training points (left) and *online* error in approximating the state solution on P_{oob} (right). The number of basis function continues to increase when additional snapshots are considered: this means that there is a great variability in the solution.

The need of this high-dimensional database of pre-computed solution poses non negligible issues: the construction of the database and of POD-DEIM basis functions are extremely demanding both in terms of time and memory (even in this simple case we cannot rely on a common laptop to perform the offline phase). Moreover, the CPU time required for the *online* solution increases, as a larger dimensional POD-DEIM ROM is considered. In the case where the POD-DEIM ROM is built on the snapshots matrix of dimension $N_h \times 300N_{train}$, with $N_{train} = 100$, we obtain $n = 100$ basis functions for the solution u and $m_D = 323$ basis functions for the nonlinear term I_{ion}. The resulting POD-DEIM ROM gains a speedup of $5.4x$ with respect to the full-order approximation: this is mainly due to the high dimensionality of the reduced mesh used to assemble the nonlinear term during the DEIM-procedure (see Figure 2.9). In fact, the parametrized ischemic region could be centered in all the different points of the domain, as shown in Figure 2.6. We need a high number of basis functions to explain the variability of the nonlinear term, which indeed depends nonlinearly on the solution $\mathbf{u}_h$ and also on $\mathbf{g}(\boldsymbol{\mu})$.

N_{train}	5	10	25	50	75	100
time LS	0.0370	0.0430	0.0640	0.0900	0.0940	0.0980
time DEIM	1.6880	2.6750	3.4350	4.0020	4.1020	4.1770
total time	1.7250	2.7180	3.4990	4.0920	4.1960	4.2750
speedup	13.3x	8.5x	6.6x	5.6x	5.5x	5.4x

Table 2.1 – Computational time [s] using the standard POD-DEIM approach versus the dimension of the training sample. The total time is divided between the solution of the low-dimensional linear system (time LS) and the computation of the nonlinear term approximation through the DEIM algorithm (time DEIM).

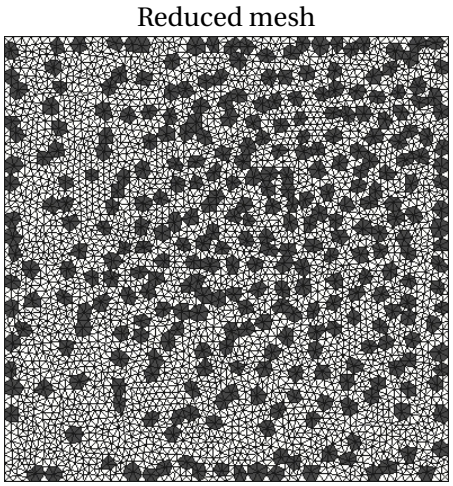

Figure 2.9 – Reduced mesh in the case $N_{train} = 100$. A large number of DEIM points are required to well capture the complexity of the nonlinear term. As a consequence, there is not a considerable speed up in assembling the nonlinear vector.

2.4.2 Localized POD-DEIM approach

Constructing localized ROMs is a possible way to improve the rather modest speedup (5.4x) obtained by the standard POD-DEIM approach. The challenge is then to find an optimal criterion to subdivide the snapshots matrix used for the construction of the local basis functions. A detailed comparison of the different strategies described in Section 2.3 is presented in the following subsections.

Time-based subdivision

In this first case, the subdivision of the snapshots matrix $\mathbf{S}_u$ of dimensions $N_s = 300N_{train}$, with $N_{train} = 100$ is given by considering as cluster indicator the time variable $t^{(\ell)}$. In particular we consider $N_c = \{6, 10, 15\}$ subdivisions of the time interval $(0, T)$, and for each localized-ROM we compare the *online* approximation error between the full and the reduced-order model computed on the out-of-bag set P_{oob} (see Figure 2.10, right) and the number of basis functions required for each cluster (see Figure 2.10,left), as done for the standard POD-DEIM approach.

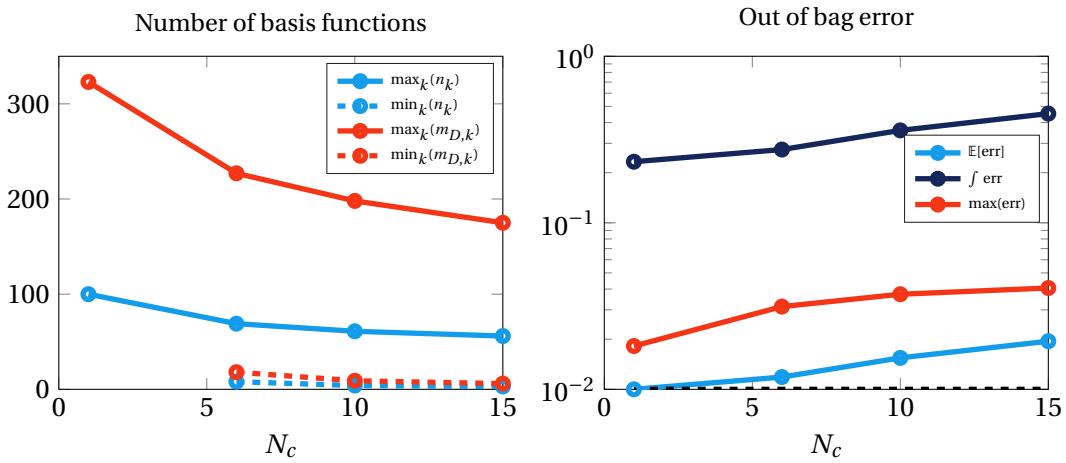

Figure 2.10 – Maximum and minimum number of basis functions forming the time-based localized POD-DEIM ROMs on varying the number of clusters (left). *Online* error in approximating the state solution on P_{oob} (right). The clusters corresponding to the initial windows can be approximated with a low-number of basis function. This is not true for the other time windows, where the variability of the solution considerably increases.

The cluster which generates the local ROM with the smallest dimensions is the one corresponding to the first window: here the solutions do not show a great variability since the initial impulse I_{app} is not parametrized. As a matter of fact, we end up with $n_1 = 8$ basis functions for the state solution and $m_1 = 18$ terms for the DEIM approximation of the nonlinear term, when $N_c = 6$ windows are considered. By increasing N_c, less basis functions are required in the initial windows ($n_1 = 3$ and $m_{D,1} = 6$ for $N_c = 15$). Unfortunately the subsequent time windows contain solutions showing much higher variability, since the fronts are modified by the various locations of the ischemia. As a consequence, the DEIM approximation of the nonlinear term is not assembled on a small reduced mesh: for instance, in the case $N_c = 6$ we have $m_{D,3} = 156$, $m_{D,4} = 227$ and $m_{D,5} = 207$. There is also a small error propagation, resulting from the approximation error arising from the change of local ROMs during the online simulation. To minimize this error propagation, it is possible to use overlapping windows by enriching consequently the dimensionality of the local ROMs. Despite of these drawbacks, we obtain a considerable speedup of $17x$, for $N_c = 15$, which is mainly due to the considerable computational savings obtained in the initial windows (see Table 2.2 for the complete list of the results).

N_{clust}	1	6	10	15
time DEIM	4.1770	1.7600	1.3820	1.2375
total time	4.2750	1.8800	1.4537	1.3548
speedup	$5.4x$	$12.2x$	$15.8x$	$17x$

Table 2.2 – Computational time $[s]$ using the time-based localized POD-DEIM approach. The computational bottleneck is mainly represented by the DEIM approximation: high execution times arise from the assembly of the nonlinear term approximation on the reduced mesh.

Parameter-based subdivision

In this case we consider instead the subdivision of the snapshots matrix given by considering the vector of parameters $\boldsymbol{\mu}$ as cluster indicator. We take two different subdivisions of the snapshots matrix $\mathbf{S}_u$ of dimensions $N_s = 300N_{train}$, with $N_{train} = 100$, based on $N_c = 8$ or $N_c = 14$ clusters (see e.g. Figure 2.11). Moreover, we also test the approach proposed in [YV16], building a ROM for each parameter in P_{cal} (we refer to this case as $N_c = 100$).

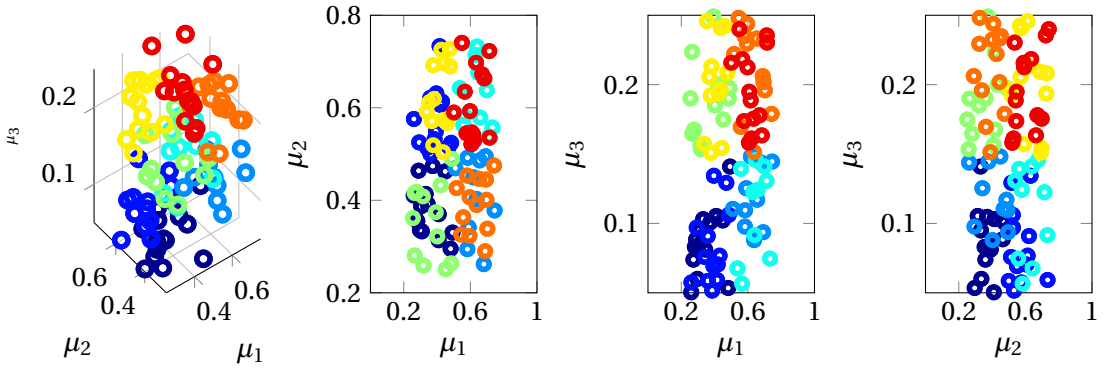

Figure 2.11 – Clusters in the parameters space for $N_c = 8$.

When we consider $N_c = 8$ or $N_c = 14$ we obtain similar results to those given by the previous approach: there is still a cluster with a large number of basis functions and the out-of-bag error increases when a large number of clusters is considered. This latter drawback is motivated by the fact that solutions corresponding to parameters which are on the boundary of a cluster $\mathscr{P}_k$ might be poorly approximated by the localized ROM. Also in this case, clusters overlapping could represent a possible way to fix the problem, sacrificing the computational efficiency. Moreover, in this case we are not able to build a substantially low-dimensional localized ROM: e.g. we end up respectively with 64 (136) basis functions for the DEIM approximation when $N_c = 14$ (8) clusters are considered (see Figure 2.12).

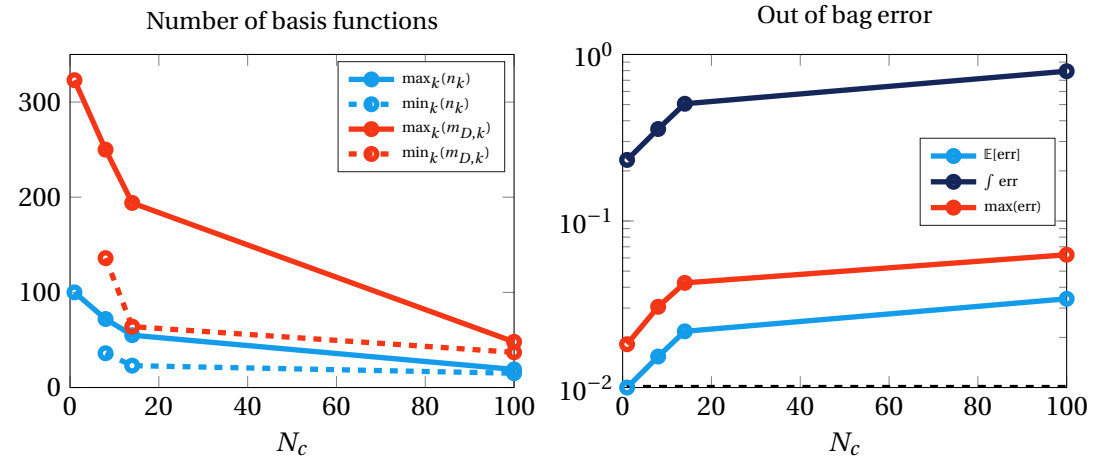

Figure 2.12 – Maximum and minimum number of basis functions forming the parameter-based localized POD-DEIM ROMs on varying the number of clusters (left). *Online* error in approximating the state solution on P_{oob} (right). In this case, there is not a cluster with a very low-number of basis functions.

Because of the presence of traveling front solutions, each local ROM built for $N_c = 100$ has roughly the same dimensions: $n_k = \{15, \dots, 19\}$ and $m_{D,k} = \{37, \dots, 48\}$. Since small variations in the parameter values induce different traveling fronts, the approximation of the online solution on the out-of-bag set P_{oob} is affected by a mean error of 3.5% on average. The sensitivity of the solution with respect to the parameters should be better investigated in order to properly design this approach.

In order to have a resulting speedup of $31.1x$, we need to construct 100 localized-ROMs. As a consequence, the computational resource that is mainly involved is the memory, since all the RB matrices of dimensions $n_k \times n_k$ and $n_k \times m_D$ are not sparse. On the other hand, as highlighted in Table2.3, the cases $N_c = 8$ or $N_c = 14$ seems not to be as promising as the previous approach.

N_{clust}	1	8	14	100
time DEIM	4.1770	2.1647	1.716	0.691
total time	4.2750	2.2647	1.8582	0.738
speedup	$10.15x$	$12.4x$	$15.8x$	$31.1x$

Table 2.3 – Computational time $[s]$ using the parameter-based localized POD-DEIM approach.

State-based subdivision

Finally, we test the *k-means* algorithm for the clustering of the snapshots matrix $\mathbf{S}_u$. We have tested different numbers of clusters $N_c = \{4, 6, 8, 10, 12, 14\}$ in order to obtain a detailed comparison of the resulting localized-ROMs.
We highlight that the dimensions of localized-ROMs change quite remarkably on different clusters (see Figure 2.13,left). Moreover, the online error evaluated on the out-of-bag set of parameters is smaller with respect to the other presented approaches (see Figure 2.13,right). In fact, the *k-mean* subdivision is based directly on the similarities of the state solutions: this means that the online changes from a local ROM to another do not introduce a considerable approximation error.

As expected, the algorithm performs better in terms of execution times with respect to the time-based approach (compare the computational times in Table 2.4 with the ones in Table 2.2), even if at each iteration we have the additional cost of identifying the current cluster, by solving the minimization problem (2.14).

N_{clust}	1	4	6	8	10	12	14
time DEIM	4.1770	1.7441	1.5747	1.4566	1.3365	1.2087	1.1392
total time	4.2750	1.9508	1.7170	1.6083	1.4886	1.3950	1.3375
speedup	$5.4x$	$11.8x$	$13.4x$	$14.3x$	$15.45x$	$16.5x$	$17.2x$

Table 2.4 – Computational time $[s]$ using the state-based localized POD-DEIM approach.

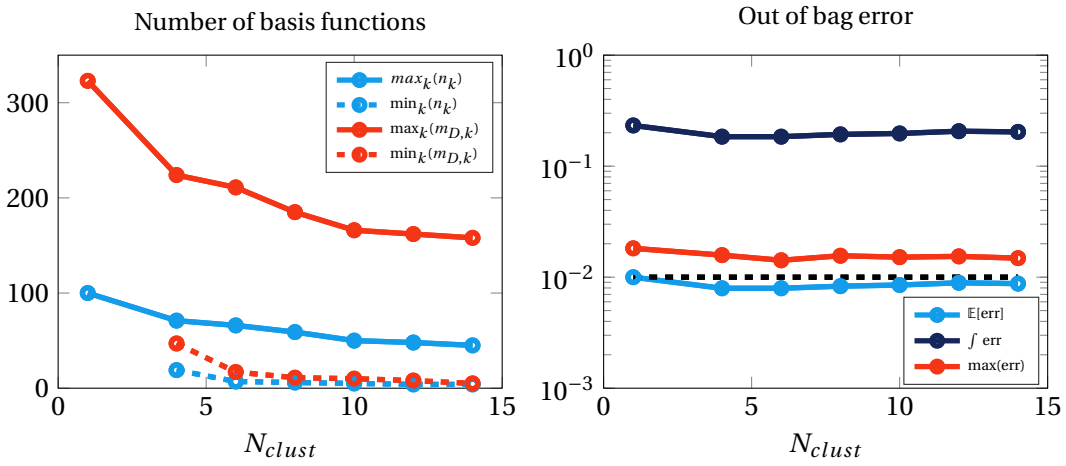

Figure 2.13 – Maximum and minimum number of basis functions forming the state-based localized POD-DEIM ROMs on varying the number of clusters (left). *Online* error in approximating the state solution on P_{oob} (right). In this case the error propagation is minimized, because the subdivision given by the *k-means* is based directly on the snapshots similarities.

By looking at the centroids selected by the algorithm (see Figure 2.14), we notice that a primal subdivision is done with respect to time (case $N_c = 4, 6, 8$). Nevertheless, this approach is more flexible with respect to the time-based one, because the front propagation velocity is taken into account by the *k-means* (the cluster is assigned with respect to the current state). Also the reduced mesh (see Figure 2.15) takes advantage of this subdivision, showing a good pattern of sparsity for some clusters. Moreover, by considering more clusters, we have that also the parameters variation plays an important role: for the case $N_c = 12$ we have two centroids that describe two situations where the ischemic region is not on the main diagonal.

2.5 Conclusions

In this Chapter we have tested different strategies to build localized-ROMs for the monodomain model, featuring the presence of an ischemic region parametrized with respect to its position and dimension. We have highlighted how the standard POD-DEIM approach is not feasible for the model order reduction of this problem: the large number of training snapshots in $\mathbf{S}_u$, and of resulting basis functions, clearly affects the performance of the POD-DEIM ROM. As outlined by Table 2.5, this is the worst option in terms of efficiency with respect to the other proposed localized-ROMs.

Among the proposed localized-ROMs, the parameter-based one with $N_c = 100$ is the best option in terms of efficiency, but it suffers from error propagation and memory consumption (it is indeed the worst option in terms of accuracy and memory consumption).
The state-based localized-ROM is the best option: the *k-means* algorithm provide a way to select automatically clusters of snapshots, whose local ROM has a small number of basis functions; moreover, the propagation of the error is minimized by the fact that there is a smooth transition from one cluster to another, finally, it features the second best speedup among the considered schemes.
We have shown that localized-ROM methodology is a promising approach for the efficient

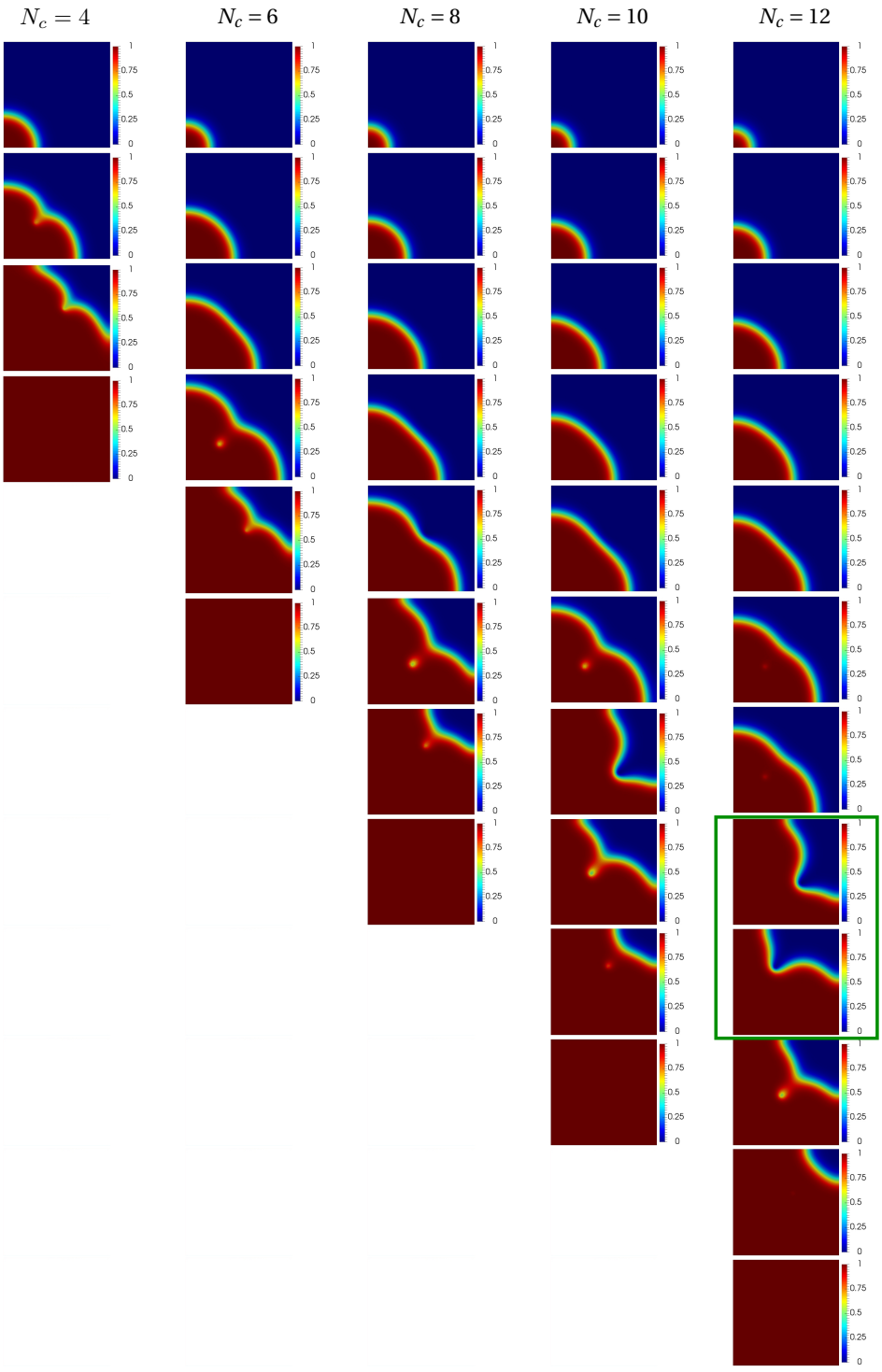

Figure 2.14 – Centroids obtained with the *k-means* algorithm for the monodomain problem versus the number of clusters N_c. The subdivisions take into account the dependence of the solution with respect to time and parameters: the two highlighted centroids describe two situations where the ischemic region is not on the main diagonal.

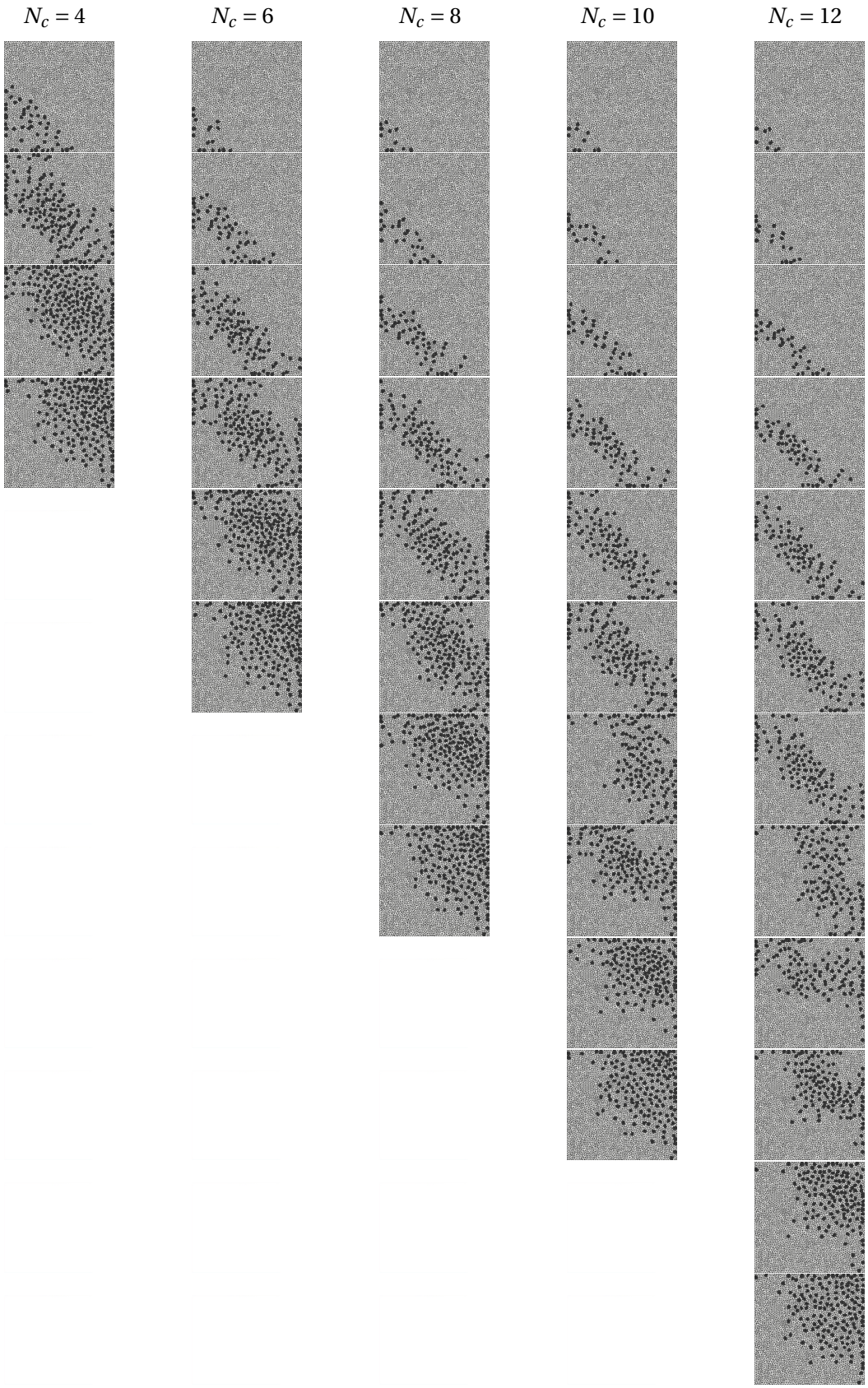

Figure 2.15 – Reduced meshes for the different clusters

N_{clust}	speedup	mean error	memory consumption
standard POD-DEIM	$5.4x$	$1 \cdot 10^{-2}$	9.8 [MB]
time-based LROM ($N_c = 15$)	$17x$	$1.94 \cdot 10^{-2}$	41.9 [MB]
parameter-based LROM ($N_c = 14$)	$15.8x$	$2.17 \cdot 10^{-2}$	49.2 [MB]
parameter-based LROM ($N_c = 100$)	$31.1x$	$3.41 \cdot 10^{-2}$	123.7 [MB]
state-based LROM ($N_c = 14$)	$17.2x$	$0.87 \cdot 10^{-2}$	31.7 [MB]

Table 2.5 – ROMs ranking. We highlight the performances using colors from red (worst) to green (best).

solution of complex electrophysiology problems. Different classification procedures could be used for the subdivision of the snapshots matrix and the consequent construction of the localized-ROMs.

3 | Surrogate models and error estimation

The goal of this Chapter is to develop kriging-based error surrogate models for the approximation of the reduction error between a full- and a reduced-order output.
In particular, in Section 3.1 we introduce the error estimation problem and in Section 3.2 we show how to construct a kriging-based surrogate model for the efficient approximation of a parametrized real-valued quantity. In Section 3.3 we construct the kriging-based ROM error surrogate (ROMES), exploited for the efficient approximation of the reduction error between a full- and a reduced-order output. We perform some numerical tests dealing with the monodomain equation considered in Chapter 2, by giving also a comparison between the proposed ROMES and the so-called Gaussian Process regression presented in [BGW15b]. Then, in Section 3.4 we extend the ROMES methodology to the case of time-dependent outputs, following the approach we have proposed in [PMQ16]. Also in this case we provide some numerical tests based on the two-dimensional monodomain problem with a parametrized ischemic region.

3.1 Error indicators

The problems arising in cardiac electrophysiology contain features, such as nonlinearities and front propagation, which make the construction of efficient ROMs a challenging task, as shown in Chapter 2. These difficulties arise also in the construction of suitable error bounds, which are used to guarantee the reliability of the results obtained with a ROM and to construct efficient greedy strategies for the basis functions computation [QMN16, GP05, RHP08]. The properties typically required to the error bounds for both the solution or the output are:

1. to be *effictive*, meaning that the error bound is capable of approximating from above the real error in a tight way;

2. to be *cheaply computable*, which means that the *online* evaluation of the error bound has negligible computational costs with respect to the reduced solution approximation.

When unsteady nonlinear parametrized PDEs are involved, it is difficult to ensure these two properties of the error bounds, due to the many source of errors arising during the solution of the PDE problem, such as the propagation of the nonlinear term and solution approximation errors.

The goal of this Chapter it to derive data-fit surrogates models (SM) for the efficient estimation of the reduction error between a FOM and a ROM output. A data-fit surrogate model is an interpolation or regression method used for the numerical approximation of an input/output map. In the literature, the most exploited surrogate models are Gaussian process regression [RW06, KO01], kriging interpolation [Cre15], polynomial response surfaces [KC96] and artificial neural networks [Hay04]. The surrogate models can be used instead of a FOM or a ROM to directly evaluate an input/output map in a very cheap way. However, data-fit SMs are not physics-based models, since they treat the forward problem as a black box. For this reason they could suffer from the curse of dimensionality and they could be less accurate in approximating the output with respect to projection-based ROMs. We instead propose to adopt data-fit SMs for the approximation of the mapping from the input parameters to the reduction output error. These ROM error surrogates (ROMESs) can be used either for error estimation instead of the standard error bounds or for model calibration (the ROMES estimation of the reduction error provides a correction of the bias introduced by the reduced-order output).

Since we are interested in solving parameter estimation and uncertainty quantification (UQ) problems using ROMs, it is crucial to quantify the reduction error to avoid biased overall results. These many query problems require multiple evaluations of the underlying forward model in order to compute some outputs of interest. Clearly, the efficiency of these procedures is considerably improved by substituting the FOM with a ROM. However the approximation error arising from the replacement of the FOM with a ROM usually affects the evaluated outputs and as a matter of fact the final solution of the parameter estimation or UQ problem. The ROMES model calibration proposed in this Chapter is thus crucial to recover the accuracy in the overall results without compromising the computational efficiency reached by the ROM.

3.2 Surrogate models for real-valued output

We consider the full-order input/output relationship:

$$\boldsymbol{\mu} \rightarrow u_h(t;\boldsymbol{\mu}) \rightarrow y_h(\boldsymbol{\mu}),$$

which maps the input vector of parameters $\boldsymbol{\mu} \in \mathscr{P} \subset \mathbb{R}^d$ into a real valued output $y_h(\boldsymbol{\mu})$ through the solution $u_h(t;\boldsymbol{\mu})$ of a parametrized PDE.
In this Section we show how to construct surrogate models of the input/output relationship

$$\boldsymbol{\mu} \rightarrow y_s(\boldsymbol{\mu}) + \varepsilon_s(\boldsymbol{\mu}),$$

where $y_s(\boldsymbol{\mu})$ is the surrogate output prediction and $\varepsilon_s(\boldsymbol{\mu})$ its output error. The main features of the SMs are the computationally efficiency and the direct characterization of $\varepsilon_s(\boldsymbol{\mu})$, in particular of the prediction error variance σ_s^2. Unfortunately, SMs suffer from the curse of dimensionality and they might present a lack of accuracy since they completely ignore the underlying physics. These SMs will be adopted in this work for the construction of ROM error surrogates and also for the efficient solution of parameter estimation and uncertainty quantification problems.
We start from a basic introduction of the statistical tools which will be used in this Chapter for the SM formulation.

3.2.1 Problem formulation

Let $(\Theta, \mathscr{F}, \mathbb{P})$ be a probability space, the function $Y : \Theta \to \mathbb{R}$ is a real-valued random field of the generic output $y_h(\boldsymbol{\mu})$. Given Y, we can associate a continuous probability density function (pdf) $f(Y)$, which is a function describing the likelihood for Y to take a given value y. Instead of working directly with $f(Y)$ it is usually convenient to rely on some indicators, such as the expected value of Y:

$$\mathbb{E}[Y] = \int_\Theta y f(y) dy,$$

and the variance of Y

$$\mathrm{Var}(Y) = \mathbb{E}[(Y - \mathbb{E}[Y])^2].$$

Finally, given two random variables Y and Z, we can define their covariance as:

$$\mathrm{Cov}(Y, Z) = \mathbb{E}[(Y - \mathbb{E}[Y])(Z - \mathbb{E}[Z])].$$

In order to construct a surrogate model for the unknown random field $\{Y(\boldsymbol{\mu}), \boldsymbol{\mu} \in \mathscr{P}\}$ we consider a set of full-order realizations

$$\{y_h(\boldsymbol{\mu}_1), y_h(\boldsymbol{\mu}_2), \ldots, y_h(\boldsymbol{\mu}_{N_{train}-1}), y_h(\boldsymbol{\mu}_{N_{train}})\},$$

given at N_{train} parameters in $P_{train} = \{\boldsymbol{\mu}_1, \ldots, \boldsymbol{\mu}_{N_{train}}\}$.
The aim of surrogate modeling is to construct a statistical model $y_s(\boldsymbol{\mu})$ of the output as accurate as possible, by properly combining the available full-order realizations. In this setting, the choice of P_{train} is an important issue for the construction of an accurate SM: a review of the possible strategies can be found in [RW06, SWN13, QHS+05].
In the following we recall the definitions and the algorithms for the construction of kriging-based surrogate models. For a complete introduction on this methodology see e.g. [Cre15].

3.2.2 Kriging interpolation

The kriging method is a technique of statistical inference for spatially-dependent data. The goal is to infer the random field $\{Y(\boldsymbol{\mu}),\ \boldsymbol{\mu} \in \mathscr{P}\}$, starting from a given set of partial observation of the full-order output $\{y_h(\boldsymbol{\mu}), \boldsymbol{\mu} \in P_{train}\}$ with $P_{train} = \{\boldsymbol{\mu}_1, \ldots, \boldsymbol{\mu}_{N_{train}}\}$. With respect to the standard geophysical applications, in our case the spatial data are represented by the parameters.

We assume that $Y(\boldsymbol{\mu})$ is a second-order stationary and isotropic random process, that is:

1. the mean is constant with respect to $\boldsymbol{\mu} \in \mathscr{P}$,

$$\mathbb{E}[Y(\boldsymbol{\mu})] = m_Y,$$

2. the variance and the covariance depend only on $\delta = \|\boldsymbol{\mu}_\alpha - \boldsymbol{\mu}_\beta\|$,

$$\mathrm{Cov}(Y(\boldsymbol{\mu}_\alpha), Y(\boldsymbol{\mu}_\beta)) = c(\boldsymbol{\mu}_\alpha, \boldsymbol{\mu}_\beta) = c(\delta), \qquad \boldsymbol{\mu}_\alpha, \boldsymbol{\mu}_\beta \in \mathscr{P},$$

$$\mathrm{Var}(Y(\boldsymbol{\mu}_\alpha) - Y(\boldsymbol{\mu}_\beta)) = \mathbb{E}[(Y(\boldsymbol{\mu}_\alpha) - Y(\boldsymbol{\mu}_\beta))^2] = 2\gamma(\delta), \qquad \boldsymbol{\mu}_\alpha, \boldsymbol{\mu}_\beta \in \mathscr{P},$$

where c and γ are the covariogram and the variogram, respectively. These two functions are related via the following relationship:

$$\gamma(\delta) = c(0) - c(\delta) \qquad \forall \delta \in \mathbb{R}^d.$$

Given a sample of known outputs of the random process $\{y_h(\boldsymbol{\mu}_q)\}_{q=1}^{N_{cal}}$, the kriging method requires first to identify the covariance structure of $Y(\boldsymbol{\mu})$ or, in other words, to find a model for the variogram γ. Then, the prediction $y_s(\boldsymbol{\mu}_0)$ is given by the best linear unbiased predictor (BLUP) of $\{Y(\boldsymbol{\mu}_0)\}$, for each new $\boldsymbol{\mu}_0 \in \mathscr{P}$, which is a linear combination of known data:

$$y_s(\boldsymbol{\mu}_0) = \sum_{q=1}^{N_{train}} \lambda_q(\boldsymbol{\mu}_0) y_h(\boldsymbol{\mu}_q).$$

The weights $\lambda_q(\boldsymbol{\mu}_0)$ are obtained by imposing that the mean square error of $y_s(\boldsymbol{\mu}_0)$ is minimized, i.e.,

$$[\lambda_1(\boldsymbol{\mu}_0), \dots, \lambda_{N_{train}}(\boldsymbol{\mu}_0)]^T = \arg \min_{\lambda_1, \dots, \lambda_{N_{train}}} \mathbb{E}\left[(Y(\boldsymbol{\mu}_0) - y_s(\boldsymbol{\mu}_0))^2\right], \tag{3.1}$$

under the constraint that $y_s(\boldsymbol{\mu}_0)$ is unbiased, that is

$$\mathbb{E}[(y_s(\boldsymbol{\mu}_0)] = \mathbb{E}[Y(\boldsymbol{\mu}_0)] = 0. \tag{3.2}$$

The weights can then be determined as solution of a linear system of the form:

$$\begin{bmatrix} \gamma(0) & \dots & \gamma(\|\boldsymbol{\mu}_1 - \boldsymbol{\mu}_{N_{train}}\|) & 1 \\ \vdots & \ddots & \vdots & \vdots \\ \gamma(\|\boldsymbol{\mu}_{N_{train}} - \boldsymbol{\mu}_1\|) & \dots & \gamma(\|\boldsymbol{\mu}_{N_{train}} - \boldsymbol{\mu}_{N_{train}}\|) & 1 \\ 1 & \dots & 1 & 0 \end{bmatrix} \begin{bmatrix} \lambda_1 \\ \vdots \\ \lambda_{N_{train}} \\ v \end{bmatrix} = \begin{bmatrix} \gamma(\|\boldsymbol{\mu}_i - \boldsymbol{\mu}_0\|) \\ \vdots \\ \gamma_t(\|\boldsymbol{\mu}_{N_{train}} - \boldsymbol{\mu}_0\|) \\ 1 \end{bmatrix}. \tag{3.3}$$

This system is derived by imposing that the gradient of the Lagrangian function corresponding to (3.1)-(3.2) is null; the detailed derivation of the linear system is shown in Section 3.4.1 for the more general case of functional data. This method also provides in a closed form the prediction variance, which is crucial to construct an estimate of the prediction error $\varepsilon_s(\boldsymbol{\mu}_0)$. Therefore, the kriging variance is defined as

$$\sigma_s^2(\boldsymbol{\mu}_0) = \sum_{q=1}^{N_{train}} \lambda_q(\boldsymbol{\mu}_0)\gamma(\|\boldsymbol{\mu}_0 - \boldsymbol{\mu}_q\|) - v. \tag{3.4}$$

To compute the components appearing in the arrays of the system (3.3), a (theoretical) semi-variogram model $\gamma(\delta)$ must be provided. Usually, the choice is restricted to a family of parametrized models exploited in the literature, such as [CD09]:

- the exponential model

$$\gamma(\delta;[\theta_1,\theta_2]) = \begin{cases} \theta_1\left(1-\exp\left(-\frac{\delta}{\theta_2}\right)\right) & \delta > 0 \\ 0 & \delta = 0; \end{cases} \tag{3.5}$$

- the spherical model

$$\gamma(\delta;[\theta_1,\theta_2]) = \begin{cases} \theta_1\left(1.5\frac{\delta}{\theta_2} - 0.5\left(\frac{\delta}{\theta_2}\right)^3\right) & \delta \le \theta_2 \\ \theta_1 & \delta > \theta_2; \end{cases} \tag{3.6}$$

- the gaussian model

$$\gamma(\delta;[\theta_1,\theta_2]) = \begin{cases} \theta_1\left(1-\exp\left(-\left(\frac{\delta}{\theta_2}\right)^2\right)\right) & \delta > 0 \\ 0 & \delta = 0. \end{cases} \tag{3.7}$$

The choice of the semi-variogram model should reflect the expected smoothness of the random field being estimated. In particular, the previous three parametric models have different behaviors around the origin, modeling different correlation patterns with respect to the distance. Once a (theoretical) semi-variogram model is chosen, the two parameters $[\theta_1,\theta_2]$ are fitted using a least square approach from available data. The fitting is usually performed on the empirical semi-variogram estimate, under the form:

$$\hat{\gamma}(\delta) = \frac{1}{2|N(\delta)|}\sum_{i,j\in N(\delta)} (y(\boldsymbol{\mu}_i) - y(\boldsymbol{\mu}_j))^2 \tag{3.8}$$

being $N(\delta) = \{(\boldsymbol{\mu}_i,\boldsymbol{\mu}_j) : \|\boldsymbol{\mu}_i - \boldsymbol{\mu}_j\| = \delta\}$. In practice, the empirical semi-variogram is estimated at M discrete values of δ: $\{\delta_1,\dots,\delta_M\}$. Through the values $\{\hat{\gamma}(\delta_1),\dots,\hat{\gamma}(\delta_M)\}$, a parametric semi-variogram model (spherical, exponential or gaussian) is fitted using a least squares approach.

An example of kriging-based SM for the approximation of the input/output map $\boldsymbol{\mu} \to y(\boldsymbol{\mu})$ will be presented in Chapter 4. The surrogate model, built starting from a finite number of observations of the full-order output, will be adopted to perform a sensitivity analysis and uncertainty propagation in an efficient way. However, we will show how the additional source of error $\varepsilon_s(\boldsymbol{\mu})$ might pollute the results.

3.3 Reduced-order model error surrogate for real-valued output

Using a ROM to evaluate the output of the forward PDE system greatly reduces the cost entailed by the evaluation of the input/output relationship:

$$\boldsymbol{\mu} \to u_n(t;\boldsymbol{\mu}) \to y_n(\boldsymbol{\mu}),$$

which maps the input parameters vector $\boldsymbol{\mu} \in \mathscr{P} \subset \mathbb{R}^d$ into a real-valued output $y_n(\boldsymbol{\mu})$ through the solution of the parametrized PDE projected onto the reduced space.

ROMs are usually preferred to surrogate models, since they are built by requiring the physical principles fulfilled by the full-order approximation to be still satisfied, into a much lower-dimensional approximation space. This reduction strategy ensures more accuracy in approximating the output, even if in some cases the computational costs can considerably grow, as shown in the previous chapter. On the other hand efficient low-dimensional ROM might introduce an additional source of error:

$$y_h(\boldsymbol{\mu}) = y_n(\boldsymbol{\mu}) + \underbrace{y_h(\boldsymbol{\mu}) - y_n(\boldsymbol{\mu})}_{\text{reduction error}} \qquad \forall \boldsymbol{\mu} \in \mathscr{P}.$$

Hence, if the reduction error $y_h(\boldsymbol{\mu}) - y_n(\boldsymbol{\mu})$ is not negligible, the output provided by the ROM is biased. For this reason, developing an efficient estimate of the reduction error $y_h(\boldsymbol{\mu}) - y_n(\boldsymbol{\mu})$ is crucial for the construction of an accurate and reliable input/output map based on ROMs. In the following, we review the possible strategies for error analysis and we propose a ROM error surrogate. The goal of this section is to construct a statistical output error estimate $m_{\text{ROM}}(\boldsymbol{\mu})$ such that:

$$y_h(\boldsymbol{\mu}) = y_n(\boldsymbol{\mu}) + \varepsilon_{\text{ROM}}(\boldsymbol{\mu}) \qquad \forall \boldsymbol{\mu} \in \mathscr{P},$$

where $\varepsilon_{\text{ROM}}(\boldsymbol{\mu})$ is a random variable with mean $m_{\text{ROM}}(\boldsymbol{\mu})$ and variance σ^2_{ROM}, representing the estimation error.

For projection-based ROM, the classical error analysis consists in the evaluation of rigorous, residual-based a posteriori error bounds $\Delta_y(\boldsymbol{\mu})$ such that

$$|y_h(\boldsymbol{\mu}) - y_n(\boldsymbol{\mu})| \leq \Delta_y(\boldsymbol{\mu}) \qquad \forall \boldsymbol{\mu} \in \mathscr{P}.$$

Starting from the elliptic case [RHP08], error bounds have been derived also for time-dependent problems [GP05], and some steady nonlinear problems [VPR$^+$03, VP05, Man14]. However, in the nonlinear time-dependent case we have that:

- the efficient evaluation of the residual of the problem is complicated by the high number of arrays generated by the discrete empirical interpolation method (DEIM) for the nonaffine and nonlinear terms;
- the error bounds are functions of the residual and other quantities, such as the stability factors [MN15], which should be properly estimated for the problem at hand;
- the extension of the error bounds for parabolic PDEs [GP05] to nonlinear problems requires the assumption of monotonicity of the nonlinear term [GMN$^+$07];
- the output error bound requires the solution of an additional PDE problem (the so-called dual problem) backward in time [GMN$^+$07] (dual-weighted residual);
- the sign of the error is not approximated;
- the error bounds are often non effective, which means that:

$$\eta(\boldsymbol{\mu}) = \frac{\Delta_y(\boldsymbol{\mu})}{|y_h(\boldsymbol{\mu}) - y_n(\boldsymbol{\mu})|} \gg 1.$$

For these many reasons, adopting rigorous error bounds for the output correction is not feasible when nonlinear parametrized PDEs, such as the ones arising in cardiac electrophysiology, are considered.

We instead look for a statistical model of the reduction error which is unbiased and has low variance. With this goal, we propose a kriging-based reduced-order model error surrogate (ROMES), which provides an approximation of the input/reduction-error mapping:

$$\boldsymbol{\mu} \to y_h(\boldsymbol{\mu}) - y_n(\boldsymbol{\mu}).$$

Given a sample of known output reduction errors $\{y_h(\boldsymbol{\mu}_q) - y_n(\boldsymbol{\mu}_q)\}_{q=1}^{N_{cal}}$, the ROMES is constructed in the following steps:

1. a semi-variogram model $\gamma(\delta; [\theta_1, \theta_2])$ is fitted using the empirical empirical semi-variogram (3.8) estimated at M discrete values $\{\delta_1, \dots, \delta_M\}$;

2. given $\boldsymbol{\mu}_0 \in \mathscr{P}$, the prediction $m_{\mathrm{ROM}}(\boldsymbol{\mu}_0)$ is given by the linear combination of known output errors:

   $$m_{\mathrm{ROM}}(\boldsymbol{\mu}_0) = \sum_{q=1}^{N_{cal}} \lambda_q(\boldsymbol{\mu}_0)(y_h(\boldsymbol{\mu}_q) - y_n(\boldsymbol{\mu}_q)),$$

   and the ROMES variance by:

   $$\sigma^2_{\mathrm{ROM}}(\boldsymbol{\mu}_0) = \sum_{q=1}^{N_{cal}} \lambda_q(\boldsymbol{\mu}_0)\gamma(\|\boldsymbol{\mu}_0 - \boldsymbol{\mu}_q\|) - \upsilon,$$

   where λ_q and υ are the solutions of the linear system (3.3) with the semi-variogram model γ fitted at the previous step.

The resulting ROMES can be used to ensure the reliability of the considered ROM or as error indicator during a greedy procedure. Moreover, the ROMES enables ROM output calibration: it improves the accuracy of the output evaluation given by a ROM, without loosing efficiency in the output approximation. In fact, the computational costs of solving the linear system (3.3) are negligible with respect to the time required by the ROM solution.

This approach could suffer from the curse of dimensionality, and could fail in approximating small oscillating ROM errors. However, the ROM error is clearly dependent on the selected parameter vector: it is almost zero if the parameter vector belongs to the training set and grows as the distance between the selected parameter vector and the training ones increases. This local structure suggests that the second-order stationary and isotropic assumptions are verified and that a kriging model is able to capture the most important features of the output error, as we will show in the numerical results.

Remark 1. *The alternative reduction error models proposed in [MPL16, DC15] are out of reach in the electrophysiology context since it is not possible to provide cheaply computable error bounds Δ_y. The extension of these statistical models to different cheaply physics-based error indicators represents a possible future investigation.*

Alternative approach: GP regression

An alternative approach for the ROMES construction, adopted e.g. in [BGW15b], consists in modeling the relationship between the full-order output $y_h(\boldsymbol{\mu})$ (response variable) and the reduced-order output $y_n(\boldsymbol{\mu})$ (regressor), omitting the dependence from the input variable $\boldsymbol{\mu}$. When the outputs of a low fidelity model (in our case a ROM) and of the corresponding FOM present a well-defined dependence, it is possible to map the low fidelity outputs into the full-order ones. If the relation between the outputs is linear a simple linear regression can be fitted, otherwise a regression can be constructed using the kriging method described in Section 3.2.2 with response variable $y_h(\boldsymbol{\mu})$ and input $y_n(\boldsymbol{\mu})$. In the literature this approach is also defined as Gaussian process (GP) regression [RW06].

In particular, given a sample of known full-order outputs $\{y_h(\boldsymbol{\mu}_q)\}_{q=1}^{N_{cal}}$ together with the corresponding reduced-order outputs $\{y_n(\boldsymbol{\mu}_q)\}_{q=1}^{N_{cal}}$ the regression is constructed as follows: given $\boldsymbol{\mu}_0 \in \mathscr{P}$, the prediction $m_{\text{reg}}(y_n(\boldsymbol{\mu}_q))$ is obtained as a linear combination of known reduced output:

$$m_{\text{reg}}(y_n(\boldsymbol{\mu}_q)) = \sum_{q=1}^{N_{cal}} \lambda_q(y_n(\boldsymbol{\mu}_q)) y_h(\boldsymbol{\mu}_q),$$

and the regression variance becomes:

$$\sigma^2_{\text{reg}}(y_n(\boldsymbol{\mu}_q)) = \sum_{q=1}^{N_{cal}} \lambda_q(y_n(\boldsymbol{\mu}_q)) \gamma(\|y_n(\boldsymbol{\mu}_0) - y_n(\boldsymbol{\mu}_q)\|) - \upsilon.$$

As done previously, the weights λ_q and υ are the solutions of a linear system like (3.3).
Unfortunately, the assumption that a low fidelity model and a FOM have a well-defined dependence is not verified in general: it usually holds only when low-fidelity models are constructed by coarsening the mesh, or employing lower-order finite elements discretization. For projection-based ROMs the error between the ROM and the FOM could present complicated patterns (e.g. oscillating reduction errors).

3.3.1 Numerical results

In this section we perform some numerical tests of the developed ROMES methodology for the approximation of the reduction error. With this aim, we consider as output of the monodomain model (see the test case 2 in Section 2.4) the activation time:

$$y(\boldsymbol{\mu}) = \arg\min_t \left(u(\mathbf{x}, t; \boldsymbol{\mu})\big|_{\mathbf{x}=\bar{\mathbf{x}}} > 0.9 \right) \qquad [ms],$$

where $\bar{\mathbf{x}} = (1, 0.5)$ is a point lying on the boundary $\partial\Omega$ (see Figure3.1).
The model consists in the following parabolic nonlinear PDE: given $\boldsymbol{\mu} \in \mathscr{P} \subset \mathbb{R}^3$, find $u = u(\mathbf{x}, t; \boldsymbol{\mu})$ s.t.:

$$\begin{cases} \dfrac{\partial u}{\partial t} - \nabla \cdot (\sigma_v(\mathbf{x}; \boldsymbol{\mu}) \nabla u) + I_{ion}(u; \boldsymbol{\mu}) = I_{app}(\mathbf{x}, t) & \mathbf{x} \in \Omega,\ t \in (0, T] \\ \sigma_v(\mathbf{x}; \boldsymbol{\mu}) \nabla u \cdot \mathbf{n} = 0 & \mathbf{x} \in \partial\Omega,\ t \in (0, T] \\ u(\mathbf{x}, 0; \boldsymbol{\mu}) = u_0 & \mathbf{x} \in \Omega, \end{cases} \tag{3.9}$$

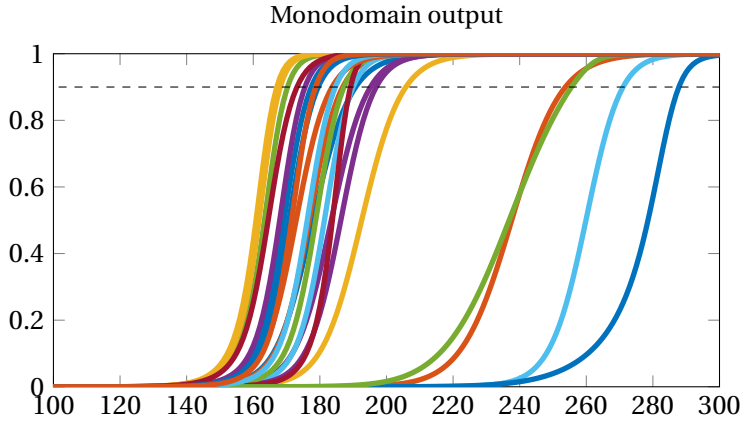

Figure 3.1 – The activation time is calculated as the time when a solid line $(u(t;\boldsymbol{\mu})|_{\mathbf{x}=\bar{\mathbf{x}}})$ crosses the dotted black line. The solid lines are obtained starting from different parameters values $\boldsymbol{\mu} = [\mu_1, \mu_2, \mu_3]$, representing the location and the size of the ischemic region.

where $I_{ion}(u;\boldsymbol{\mu}) = g(\mathbf{x};\boldsymbol{\mu})u(u-a)(u-1)$ is the ionic current and

$$I_{app}(\mathbf{x},t) = Cexp\left(-\frac{x_1^2+x_2^2}{0.02}\right)\mathbb{1}_{[0,\Delta t]}(t)$$

the initial applied stimulus. The conductivity $\sigma_v(\mathbf{x};\boldsymbol{\mu})$ is a non-homogeneous parametrized field:

$$\sigma_v(\mathbf{x};\boldsymbol{\mu}) = \sigma_h g(\mathbf{x};\boldsymbol{\mu}) + \sigma_i(1-g(\mathbf{x};\boldsymbol{\mu})) \qquad g(\mathbf{x};\boldsymbol{\mu}) = 1 - exp\left(-\frac{(x_1-\mu_1)^2+(x_2-\mu_2)^2}{2\mu_3^2}\right), \qquad \mathbf{x}\in\Omega,$$

where $\mu_1 \in [0.25, 0.75]$ and $\mu_2 \in [0.25, 0.75]$ indicate the position of the center of the ischemic region, and $\mu_3 \in [0.05, 0.4]$ its size.

In order to test the ROMES method in this context, we consider three ROMs from Section 2.4.1:

- ROM #1 is obtained starting from $N_{train} = 10$ training points and it consists of $n = 63$ basis functions for the solution and $m_D = 212$ basis functions for the nonlinear term;
- ROM #2 is obtained starting from $N_{train} = 25$ training points and it consists of $n = 83$ basis functions for the solution and $m_D = 273$ basis functions for the nonlinear term;
- ROM #3 is obtained starting from $N_{train} = 50$ training points and it consists of $n = 94$ basis functions for the solution and $m_D = 311$ basis functions for the nonlinear term.

For each ROM, we first construct a kriging-based ROMES on a set of N_{cal} output reduction errors $\{y_h(\boldsymbol{\mu}_q) - y_n(\boldsymbol{\mu}_q)\}$, $q = 1,\dots,N_{cal}$, and then we evaluate its ability in minimizing the error on a new set of N_{oob} parameter vectors.

Kriging-based ROMES

The construction of an effective kriging-based ROMES is based on the assumptions that the error is a second-order stationary and isotropic random field. In order to verify these assumptions we represent in Figure 3.2 $N_{cal} = 100$ parameter vectors with the associated reduction

error $\{y_h(\boldsymbol{\mu}_q) - y_n(\boldsymbol{\mu}_q)\}$, $q = 1,\dots,N_{cal}$, generated by ROM #1. The values $y_h(\boldsymbol{\mu}_q) - y_n(\boldsymbol{\mu}_q)$ are characterized by the different colors of the markers. We observe that high values of the error are associated to parameter vectors describing ischemic regions located in the bottom part of the domain and with large size.

The reduction error arises indeed from the different propagation velocities of the FOM and the ROM, which are particularly affected by the ischemic region. Since we are measuring the activation time in $\bar{\mathbf{x}} = (1, 0.5)$, it is reasonable that the high values of the error are concentrated in the bottom part of the domain. Moreover, when the ischemia is small there are small modification of the front leading to small reduction error. For these reasons, the assumptions of second-order stationary and isotropic random field could be considered verified.

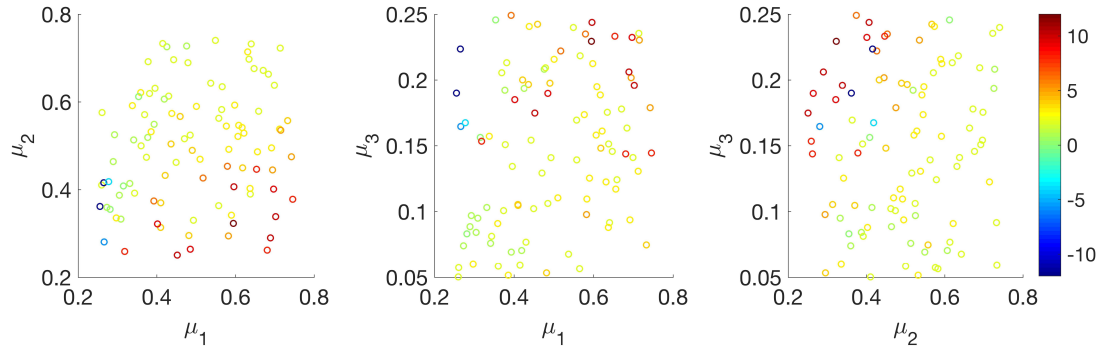

Figure 3.2 – Distribution of $N_{cal} = 100$ parameter vectors in the parameter space. We associate to each dot $\boldsymbol{\mu}_q$ the corresponding value of the reduction error $\{y_h(\boldsymbol{\mu}_q) - y_n(\boldsymbol{\mu}_q)\}$, $q = 1,\dots,N_{cal}$, represented through different colors of the markers. The discrepancies between the full and the reduced-order activation times $\{y_h(\boldsymbol{\mu}_q) - y_n(\boldsymbol{\mu}_q)\}$, $q = 1,\dots,N_{cal}$, arise form the different propagation velocities of the FOM and the ROM.

These assumptions are also confirmed by the trend of the empirical semi-variogram estimate (3.8), represented by the blue dots in Figure 3.3 for different ROMs. In all the cases, the empirical semi-variogram grows as the distance $\delta = \|\boldsymbol{\mu}_i - \boldsymbol{\mu}_j\|$ between the calibration parameters vectors increases. This means that parameters vectors that are close to each other show similar values of the error, while parameters vectors that are far from each other present considerably different values.

An exponential theoretical semi-variogram model (3.5) is fitted on the empirical semi-variogram data (red solid line). Given the fitted exponential semi-variogram model $\gamma(\delta; [\theta_1, \theta_2])$ and a set of N_{cal} output reduction errors, the matrix forming the ordinary kriging system (3.3) is assembled. For each new value of the parameter vector $\boldsymbol{\mu}_0$ the ROMES prediction $m_{\text{ROM}}(\boldsymbol{\mu}_0)$ is computed as a weighted linear combination of known errors.
In order to test the constructed ROMES, we compute the full- and the reduced-order outputs for a set P_{oob} of $N_{oob} = 25$ parameters vectors and we compare the output reduction error $y_h(\boldsymbol{\mu}) - y_n(\boldsymbol{\mu})$ with its corrected version $y_h(\boldsymbol{\mu}) - y_n(\boldsymbol{\mu}) - m_{\text{ROM}}(\boldsymbol{\mu})$. The numerical results, presented in Figure 3.4, show how the correction is effective in all cases: the kriging model gives an additive correction to the ROM output, which well captures the output bias.

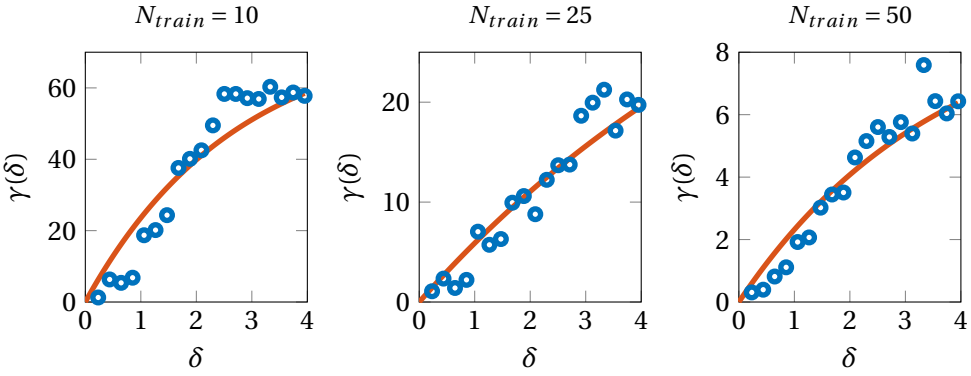

Figure 3.3 – Empirical variogram (blue dots) and fitted exponential semi-variogram $\gamma(\delta;\theta)$ (solid line)

Moreover, the corrected output $y_n(\boldsymbol{\mu}) + m_{\text{ROM}}(\boldsymbol{\mu})$ given by ROM #1 is even more close to the full-order output $y_h(\boldsymbol{\mu})$ than the reduced-output $y_n(\boldsymbol{\mu})$ given by ROM #3 (which is the considered ROM with the largest dimensions). This means that the inexpensive ROMES enables to rely on a low-dimensional ROM, such as ROM #1, without considerably affecting the output evaluation.
In order to quantify the performance of the proposed kriging-based ROMES, we compute for each $\boldsymbol{\mu} \in P_{oob}$ the effectivity index:

$$\eta(\boldsymbol{\mu}) = \frac{|m_{\text{ROM}}(\boldsymbol{\mu})|}{|y_h(\boldsymbol{\mu}) - y_n(\boldsymbol{\mu})|} \qquad \forall \boldsymbol{\mu} \in P_{oob}.$$

If $\eta(\boldsymbol{\mu})$ is much larger or smaller than one, then the ROM surrogate model is not able to reproduce correctly the reduction error. On the other hand, values of $\eta(\boldsymbol{\mu})$ close to one indicate that the error surrogate well approximates the reduction error. For each $\boldsymbol{\mu} \in P_{oob}$ we have computed $\eta(\boldsymbol{\mu})$ on varying the considered ROM and the size of the calibration set used for the ROMES construction. The boxplots representing the distributions of $\eta(\boldsymbol{\mu})$ in the different cases are collected in Figure 3.5.

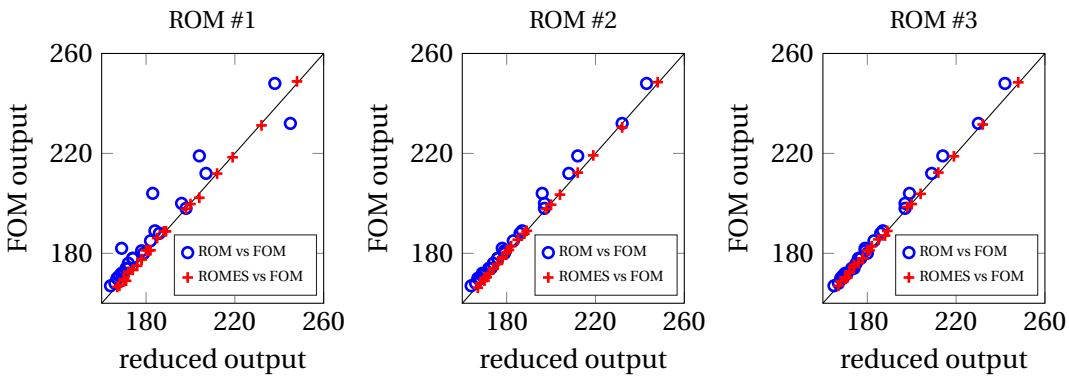

Figure 3.4 – Out-of-bag prediction ($N_{oob} = 25$) $y_n(\boldsymbol{\mu})$ (blue dots) and $y_n(\boldsymbol{\mu}) + m_{\text{ROM}}(\boldsymbol{\mu})$ (red crosses) versus $y_h(\boldsymbol{\mu})$ for each $\boldsymbol{\mu} \in P_{oob}$. The comparison is also done with respect to different ROMs (from left to right). In all cases, the ROMES correction effectively correct the error between the FOM and the ROM.

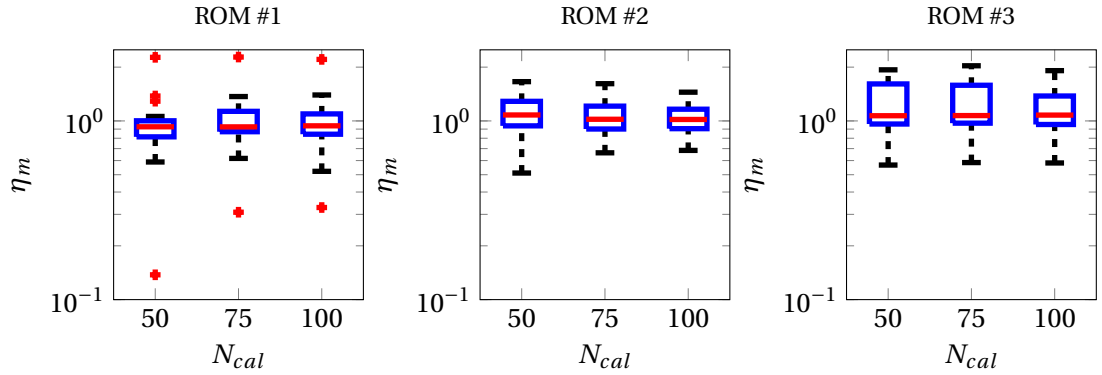

Figure 3.5 – Boxplots of the efficiency index $\eta(\boldsymbol{\mu})$, $\boldsymbol{\mu} \in P_{oob}$, distributions obtained on varying the calibration set for the ROMES construction and the ROMs dimensions

In all cases the median (red line) is almost one, confirming that the ROMES provides a good approximation of the error. As expected, the variability of η described by the height of each boxplot decreases when larger calibration sets are considered.

Finally, if we also consider the kriging error (described by the variance $\sigma^2_{\text{ROM}}(\boldsymbol{\mu})$ defined in (3.4)), the performance of the proposed kriging-based ROMES can be quantified by computing the confidence band

$$[m_{\text{ROM}}(\boldsymbol{\mu}) - 2\sigma_{\text{ROM}}(\boldsymbol{\mu}), m_{\text{ROM}}(\boldsymbol{\mu}) + 2\sigma_{\text{ROM}}(\boldsymbol{\mu})] \qquad \forall \boldsymbol{\mu} \in P_{oob}.$$

The match between the corrected output and the FOM output, represented by the black line in Figure 3.6, is always contained inside the ROMES confidence bands. Moreover the variability of the corrected output is much smaller with respect to uncorrected case presented in Figure 3.4.
For the case at hand we can conclude that the proposed kriging-based ROMES respects all the desired features of a reduction error model: it is unbiased, it has low variance and it is cheaply computable.

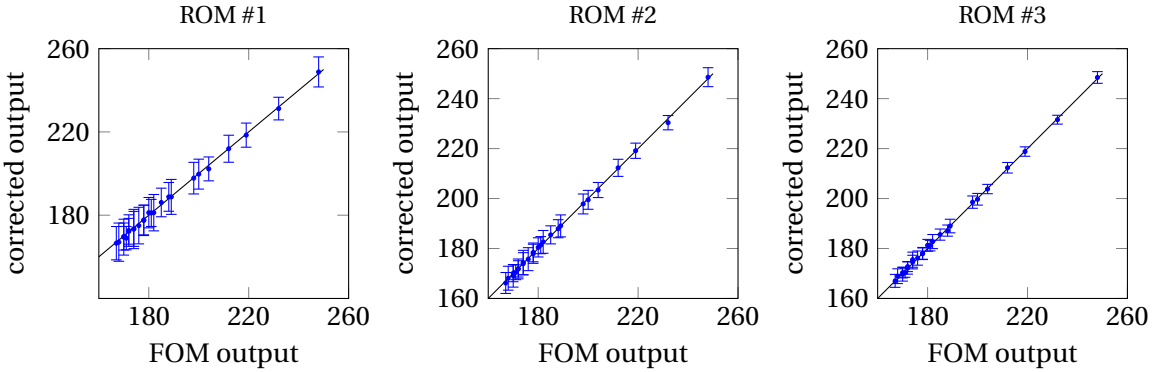

Figure 3.6 – Confidence bands of the ROMES corrected output $y_n(\boldsymbol{\mu}) + m_{\text{ROM}}$, $\boldsymbol{\mu} \in P_{oob}$, obtained on varying the ROMs dimensions

GP regression

We first check the assumption that the full-order output y_h (response variable) presents a well-defined dependence (e.g. linear or quadratic) from the reduced-order output y_n (regressor). With this goal, we represent in Figure 3.7 the couples $(y_n(\boldsymbol{\mu}), y_h(\boldsymbol{\mu}))$ for each $\boldsymbol{\mu}$ in the calibration set P_{cal}.

When ROM #1 is considered, there is not a simple dependence (e.g. linear) between $y_n(\boldsymbol{\mu})$ and $y_h(\boldsymbol{\mu})$. The error $y_h(\boldsymbol{\mu}) - y_n(\boldsymbol{\mu})$ generated by ROM #1, which is the model with the smallest number of basis functions, affects considerably the reduced input-output map. As a consequence, a regression model is not able to describe successfully the relationship between y_h and y_n. Meanwhile, in the case of a ROM #2, we observe that even a linear regression is able to well describe the relationship between the outputs, and that the variability of the reduction error is much smaller with respect to ROM #1.

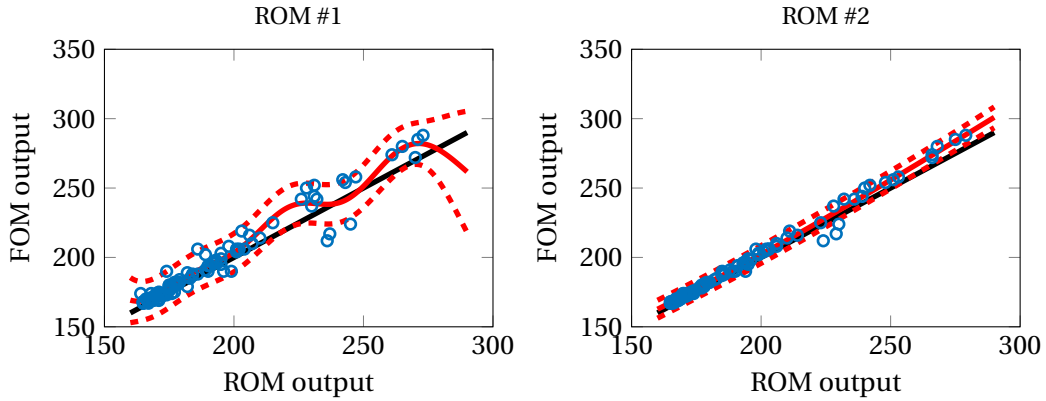

Figure 3.7 – Scatter plot of 100 values of $y_n(\boldsymbol{\mu})$ against $y_h(\boldsymbol{\mu})$ in the case of ROM #1 (left) and ROM #2 (right). The solid red line represents the Gaussian process regression and the dotted lines the relative confidence intervals. The differences between the blue dots and the black line represent the reduction error.

Given a new $\boldsymbol{\mu}_0 \in \mathscr{P}$, the Gaussian process regression $m_{reg}(y_n(\boldsymbol{\mu}))$ (solid red line in Figure 3.7) is then used to map each new reduced output $y_n(\boldsymbol{\mu}_0)$ to its corrected value $m_{reg}(y_n(\boldsymbol{\mu}_0))$ in order to minimize the reduction error (i.e. the difference between a blue dot and the black line). The comparison between the full-order, the reduced-order and the corrected outputs is presented in Figure 3.8: we highlight that the GP regression is not able to correct the output when ROM #1 is used.

When a more detailed and computationally costly ROM is considered, such as ROM #2, the reduced output y_n is statistically close to the full-order ones. In this case, the combined use of the ROM and the GP regression results in an improved accuracy of the output approximation (as confirmed by the boxplots of the error distribution presented in Figure 3.9).

In conclusion kriging-based ROM error surrogates perform better than the GP regression, especially when low dimensional ROM are considered.

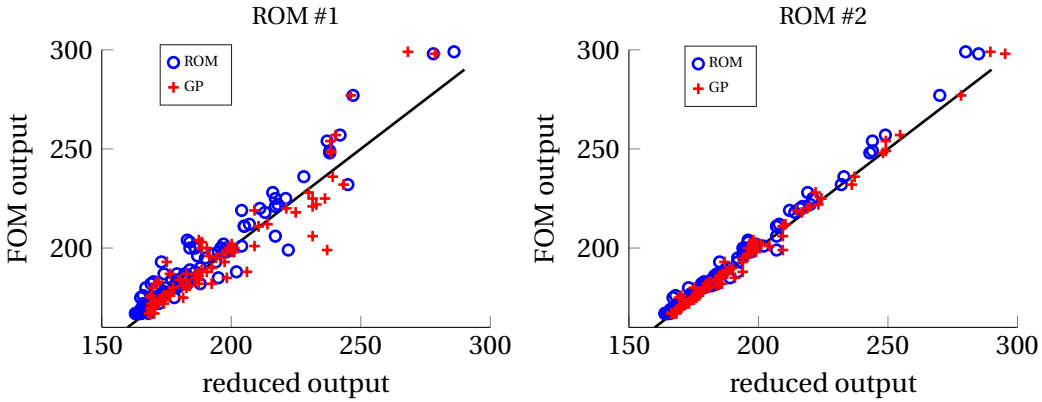

Figure 3.8 – Scatter plots of $y_n(\boldsymbol{\mu})$ and $m_{\text{reg}}(y_n(\boldsymbol{\mu}))$ versus the full-order output $y_h(\boldsymbol{\mu})$. The correction of the output given by the GP regression is effective only for ROM #2.

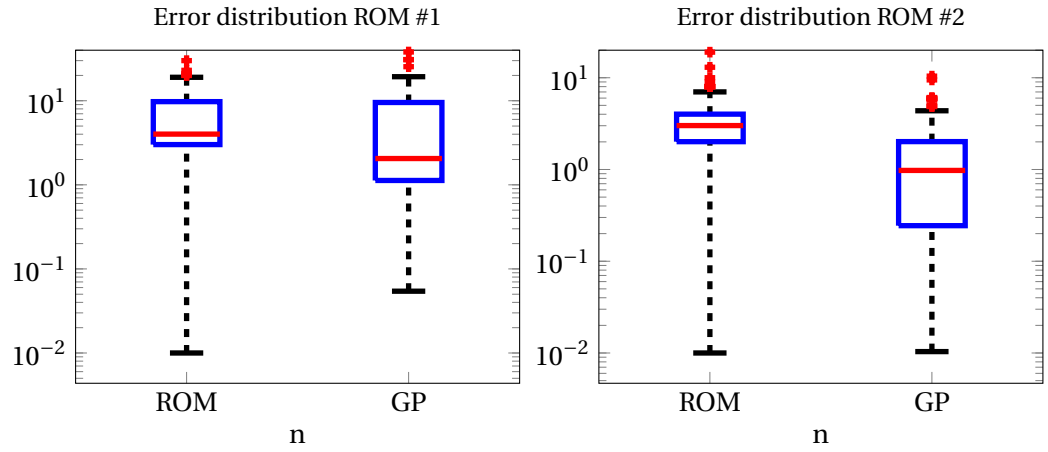

Figure 3.9 – Box-plots of the distributions of the reduction error $|y_h(\boldsymbol{\mu}) - y_n(\boldsymbol{\mu})|$ and the error of the corrected output $|y_h(\boldsymbol{\mu}) - m_{reg}(y_n(\boldsymbol{\mu}))|$ when ROM #1 and ROM #2 are considered.

3.4 Surrogate models for time-dependent outputs

In this section we extend the kriging-based ROMES to the case of time-dependent outputs, e.g. obtained from measurements related to cardiac electrophysiology such as the ECG signal and the intracardiac catheter recording along the endocardium. These outputs will be considered in Chapter 6 and 7 as inputs of the data-assimilation procedures for state and parameter estimation.

A time dependent output can be described as a vector, whose elements are given by

$$y_h^{(\ell)} = \mathbf{H}\mathbf{u}_h^{(\ell)} \qquad \ell = 1, \dots, N_t,$$

where N_t is the number of time-steps of the chosen time-advancing scheme for the resolution of a parametrized PDE of interest and $\mathbf{H}$ an array corresponding to the full-order discretization of an observation operator.

A reduced-order model provides an efficient way to evaluate the output:

$$y_n^{(\ell)} = \mathbf{H}_n \mathbf{u}_n^{(\ell)} \qquad \ell = 1, \dots, N_t,$$

where $\mathbf{u}_n^{(\ell)}$ is the solution of reduced-order system approximating the parametrized PDE of interest and $\mathbf{H}_n$ the reduced observation operator obtained by projecting $\mathbf{H}$ onto the reduced space. As in the real-valued output case, a low-dimensional ROM might introduce a non negligible reduction error, which can be modeled as:

$$y_h^{(\ell)}(\boldsymbol{\mu}) = y_n^{(\ell)}(\boldsymbol{\mu}) + \underbrace{y_h^{(\ell)}(\boldsymbol{\mu}) - y_n^{(\ell)}(\boldsymbol{\mu})}_{\text{reduction error}} \qquad \ell = 1, \dots, N_t, \ \forall \boldsymbol{\mu} \in \mathscr{P}.$$

In this time-dependent case it is not possible to simply rely on the strategies developed for the real-valued output. In fact, at each time step we have not only the error arising from the ROM approximation but also the propagation of the errors coming from the previous time-steps. For example, a regression model could be used to describe the ROM error at each time-step, but it is not possible to take into account in this model the error propagation. For this reason, we develop a kriging-based approach for the approximation of the vector of reduction errors:

$$\boldsymbol{\mu} \to \{y_h^{(\ell)}(\boldsymbol{\mu}) - y_n^{(\ell)}(\boldsymbol{\mu})\}_{\ell=1}^{N_t}.$$

In this way the kriging prediction will directly describe both the components of the output error, taking into account the propagation of the error committed at each time-step. For the derivation of the kriging error surrogate, we model the error vector as a functional random field $\{\chi_t(\boldsymbol{\mu}),\ \boldsymbol{\mu} \in \mathscr{P}\}$, that is, a set of (functional) random variables indexed by $\boldsymbol{\mu} \in \mathscr{P}$, taking values in $L^2(a,b)$, with $(a,b) \subseteq (0,T)$.

In this section, we recall the definitions of functional kriging method and the corresponding algorithm, which will be then adopted to construct a ROMES for time-dependent outputs. For an introduction see e.g. [GDM11, MSDR13].

3.4.1 Kriging for functional output

We assume that $\chi_t(\boldsymbol{\mu})$ is a second-order stationary and isotropic random process, that is:

1. the mean and the variance are constant with respect to $\boldsymbol{\mu} \in \mathscr{P}$,

$$\mathbb{E}[\chi_t(\boldsymbol{\mu})] = m_\chi(t), \qquad Var[\chi_t(\boldsymbol{\mu})] = \sigma_\chi^2(t), \qquad t \in (a,b);$$

2. the covariance depends only on the lag $\delta = \|\boldsymbol{\mu}_\alpha - \boldsymbol{\mu}_\beta\|$,

$$Cov(\chi_{t_1}(\boldsymbol{\mu}_\alpha), \chi_{t_2}(\boldsymbol{\mu}_\beta)) = c_{t_1,t_2}(\boldsymbol{\mu}_\alpha, \boldsymbol{\mu}_\beta) = c_{t_1,t_2}(\delta), \qquad \boldsymbol{\mu}_\alpha, \boldsymbol{\mu}_\beta \in \mathscr{P}, \quad t_1, t_2 \in (a,b);$$

   moreover, if $t_1 = t_2 = t$, we denote by $c_t(\delta) = c_{t_1,t_2}(\delta)$.

Given a sample of known functions of the random process $\{\chi_t(\boldsymbol{\mu}_q)\}_{q=1}^{N_{cal}}$, the best linear unbiased predictor (BLUP) of $\{\chi_t(\boldsymbol{\mu}_0)\}$, for each new $\boldsymbol{\mu}_0 \in \mathscr{P}$, is given by the linear combination

$$\hat{\chi}_t(\boldsymbol{\mu}) = \sum_{q=1}^{N_{cal}} \lambda_q(\boldsymbol{\mu}) \chi_t(\boldsymbol{\mu}_q) \qquad \forall \boldsymbol{\mu} \in \mathscr{P}$$

whose weights are obtained by imposing that the mean square error of $\hat{\chi}_t(\boldsymbol{\mu}_0)$ is minimized, i.e.,

$$[\lambda_1(\boldsymbol{\mu}_0),\dots,\lambda_{N_{cal}}(\boldsymbol{\mu}_0)]^T = \arg\min_{\lambda_1,\dots,\lambda_{N_{cal}}} \int_a^b Var\left[\hat{\chi}_t(\boldsymbol{\mu}_0) - \chi_t(\boldsymbol{\mu}_0)\right] dt \tag{3.10}$$

under the constraint that $\hat{\chi}_t(\boldsymbol{\mu}_0)$ is unbiased, that is

$$\mathbb{E}[\hat{\chi}_t(\boldsymbol{\mu}_0) - \chi_t(\boldsymbol{\mu}_0)] = 0. \tag{3.11}$$

Finding the BLUP thus yields a constrained quadratic programming problem to be solved (for each $\boldsymbol{\mu}_0$):

$$\begin{aligned} Var(\hat{\chi}_t(\boldsymbol{\mu}_0) - \chi_t(\boldsymbol{\mu}_0)) &= \sum_{q,p=1}^{N_{cal}} \lambda_q(\boldsymbol{\mu}_0)\lambda_p(\boldsymbol{\mu}_0)c_t(\boldsymbol{\mu}_q,\boldsymbol{\mu}_p) + c_t(\boldsymbol{\mu}_0,\boldsymbol{\mu}_0) - 2\sum_{q=1}^{N_{cal}} \lambda_q(\boldsymbol{\mu}_0)c_t(\boldsymbol{\mu}_i,\boldsymbol{\mu}_0) \\ \mathbb{E}[\hat{\chi}_t(\boldsymbol{\mu}_0) - \chi_t(\boldsymbol{\mu}_0)] &= \sum_{q=1}^{N_{cal}} \lambda_q(\boldsymbol{\mu}_0)\mathbb{E}[\hat{\chi}_t(\boldsymbol{\mu}_q)] - \mathbb{E}[\hat{\chi}_t(\boldsymbol{\mu}_0)] = \mathbb{E}[\hat{\chi}_t(\boldsymbol{\mu}_0)]\left(\sum_{q=1}^{N_{cal}} \lambda_q(\boldsymbol{\mu}_0) - 1\right) \end{aligned} \tag{3.12}$$

thanks to assumption 1. Denoting by

$$\mathscr{L}(\lambda_1,\dots,\lambda_{N_{cal}},\upsilon) = \int_a^b Var(\hat{\chi}_t(\boldsymbol{\mu}_0) - \chi_t(\boldsymbol{\mu}_0))dt + \upsilon\int_a^b \mathbb{E}[\hat{\chi}_t(\boldsymbol{\mu}_0)dt - \chi_t(\boldsymbol{\mu}_0)]$$

the Lagrangian functional associated to problem (3.10)–(3.11) and by requiring that the gradient of the Lagrangian function $\mathscr{L}$ is null, we get the following linear system to be solved, for each $\boldsymbol{\mu}_0$:

$$\begin{bmatrix} \int_a^b c_t(\boldsymbol{\mu}_1,\boldsymbol{\mu}_1)dt & \dots & \int_a^b c_t(\boldsymbol{\mu}_1,\boldsymbol{\mu}_{N_{cal}})dt & 1 \\ \vdots & \ddots & \vdots & \vdots \\ \int_a^b c_t(\boldsymbol{\mu}_{N_{cal}},\boldsymbol{\mu}_1)dt & \dots & \int_a^b c_t(\boldsymbol{\mu}_{N_{cal}},\boldsymbol{\mu}_{N_{cal}})dt & 1 \\ 1 & \dots & 1 & 0 \end{bmatrix} \begin{bmatrix} \lambda_1 \\ \vdots \\ \lambda_{N_{cal}} \\ \upsilon \end{bmatrix} = \begin{bmatrix} \int_a^b c_t(\boldsymbol{\mu}_i,\boldsymbol{\mu}_0)dt \\ \vdots \\ \int_a^b c_t(\boldsymbol{\mu}_{N_{cal}},\boldsymbol{\mu}_0)dt \\ 1 \end{bmatrix}.$$

Thanks to assumption 2, $c_t(\boldsymbol{\mu}_q,\boldsymbol{\mu}_p) = Cov(\chi_t(\boldsymbol{\mu}_q),\chi_t(\boldsymbol{\mu}_p)) = c_t(\|\boldsymbol{\mu}_q - \boldsymbol{\mu}_p\|)$ so that, by denoting

$$\gamma_t(\delta) = c_t(0) - c_t(\delta),$$

the previous linear system can be equivalently rewritten as:

$$\begin{bmatrix} \int_a^b \gamma_t(0)dt & \dots & \int_a^b \gamma_t(\|\boldsymbol{\mu}_1 - \boldsymbol{\mu}_{N_{cal}}\|)dt & 1 \\ \vdots & \ddots & \vdots & \vdots \\ \int_a^b \gamma_t(\|\boldsymbol{\mu}_{N_{cal}} - \boldsymbol{\mu}_1\|)dt & \dots & \int_a^b \gamma_t(\|\boldsymbol{\mu}_{N_{cal}} - \boldsymbol{\mu}_{N_{cal}}\|)dt & 1 \\ 1 & \dots & 1 & 0 \end{bmatrix} \begin{bmatrix} \lambda_1 \\ \vdots \\ \lambda_{N_{cal}} \\ \upsilon \end{bmatrix} = \begin{bmatrix} \int_a^b \gamma_t(\|\boldsymbol{\mu}_i - \boldsymbol{\mu}_0\|)dt \\ \vdots \\ \int_a^b \gamma_t(\|\boldsymbol{\mu}_{N_{cal}} - \boldsymbol{\mu}_0\|)dt \\ 1 \end{bmatrix}. \tag{3.13}$$

Finally, we define the prediction trace-variance $\hat{\sigma}^2_\chi(\boldsymbol{\mu}_0)$ of the functional ordinary kriging as

$$\hat{\sigma}^2_\chi(\boldsymbol{\mu}_0) = \int_a^b Var(\hat{\chi}_t(\boldsymbol{\mu}_0) - \chi_t(\boldsymbol{\mu}_0))dt.$$

Using (3.12), we get

$$\hat{\sigma}^2_\chi(\boldsymbol{\mu}_0) = \int_a^b \left(\sum_{q,p=1}^{N_{cal}} \lambda_q(\boldsymbol{\mu}_0)\lambda_p(\boldsymbol{\mu}_0)c_t(\boldsymbol{\mu}_q,\boldsymbol{\mu}_p) + c_t(\boldsymbol{\mu}_0,\boldsymbol{\mu}_0) - 2\sum_{q=1}^{N_{cal}} \lambda_q(\boldsymbol{\mu}_0)c_t(\boldsymbol{\mu}_i,\boldsymbol{\mu}_0)\right) dt. \tag{3.14}$$

Since $\{\lambda_p(\boldsymbol{\mu}_0)\}_{p=1}^{N_{cal}}$ and v are the solution of the linear system (3.13), it holds

$$\int_a^b \left(\sum_{p=1}^{N_{cal}} \lambda_p(\boldsymbol{\mu}_0) c_t(\boldsymbol{\mu}_p, \boldsymbol{\mu}_q) \right) dt = \int_a^b c_t(\boldsymbol{\mu}_q, \boldsymbol{\mu}_0) dt - v \qquad \forall q = 1, \dots, N_{cal},$$

so that, by substituting this latter relation in (3.12), we finally get

$$\begin{aligned}\hat{\sigma}^2_\chi(\boldsymbol{\mu}_0) &= \int_a^b \left(\sum_{q=1}^{N_{cal}} \lambda_q(\boldsymbol{\mu}_0)(c_t(\boldsymbol{\mu}_q, \boldsymbol{\mu}_0) + c_t(\boldsymbol{\mu}_0, \boldsymbol{\mu}_0)) - 2 \sum_{q=1}^{N_{cal}} \lambda_q(\boldsymbol{\mu}_0) c_t(\boldsymbol{\mu}_q, \boldsymbol{\mu}_0) \right) dt - \underbrace{\sum_{q=1}^{N_{cal}} \lambda_q(\boldsymbol{\mu}_0)}_{=1} v \\ &= \int_a^b \left(\sum_{q=1}^{N_{cal}} \lambda_q(\boldsymbol{\mu}_0) \underbrace{(c_t(\boldsymbol{\mu}_0, \boldsymbol{\mu}_0) - c_t(\boldsymbol{\mu}_q, \boldsymbol{\mu}_0))}_{=\gamma_t(\|\boldsymbol{\mu}_q - \boldsymbol{\mu}_0\|)} \right) dt - v = \sum_{q=1}^{N_{cal}} \lambda_q(\boldsymbol{\mu}_0) \gamma(\|\boldsymbol{\mu}_q - \boldsymbol{\mu}_0\|) - v.\end{aligned} \tag{3.15}$$

The key feature of this procedure is its computational efficiency: the weights are computed by solving a linear system of dimensions $(N_{cal}+1) \times (N_{cal}+1)$, which are the same dimensions of the kriging-based ROMES for the real-valued output.

3.4.2 ROMES: time-dependent case

The goal of this section is to develop a functional kriging ROMES to approximate the time-dependent error $\{y_h^{(\ell)}(\boldsymbol{\mu}_0) - y_n^{(\ell)}(\boldsymbol{\mu}_0)\}$, with $\ell = 1, \dots, N_t$, for each new value $\boldsymbol{\mu}_0 \in P_{cal}$. The functional kriging error surrogate is constructed from a given set of observations of the output $\{y_h^{(\ell)}(\boldsymbol{\mu}) - y_n^{(\ell)}(\boldsymbol{\mu}), \boldsymbol{\mu} \in P_{cal}\}$ with $\ell = 1, \dots, N_t$, $P_{cal} = \{\boldsymbol{\mu}_1, \dots, \boldsymbol{\mu}_{N_{cal}}\}$, being $P_{train} \subset P_{cal}$. We underline that these evaluations have to be performed only once, after the ROM has been built (during the so-called offline phase). In particular, we can choose P_{cal} such that $P_{train} \subset P_{cal}$ so that we can take advantage of the snapshots already computed for the ROM basis construction. By doing so, we also ensure not to overestimate the reduction error in those training points. Under the assumption that $\chi_t(\boldsymbol{\mu})$ is a second-order stationary and isotropic random process, the ROMES prediction of the error for each new $\boldsymbol{\mu}_0 \in \mathscr{P}$ is given by:

$$m^{(\ell)}_{\mathrm{ROM}}(\boldsymbol{\mu}_0) = \sum_{q=1}^{N_{cal}} \lambda_q(\boldsymbol{\mu}_0)(y_h^{(\ell)}(\boldsymbol{\mu}_q) - y_n^{(\ell)}(\boldsymbol{\mu}_q)) \qquad \ell = 1, \dots, N_t,$$

where the weights $\{\lambda_q(\boldsymbol{\mu}_0)\}_{q=1}^{N_{cal}}$ are obtained by solving the linear system (3.13). As done in the previous case, we can also compute in a closed form the ROMES variance

$$\sigma^2_{\mathrm{ROM}}(\boldsymbol{\mu}_0) = \sum_{q=1}^{N_{cal}} \lambda_q(\boldsymbol{\mu}_0) \int_a^b \gamma_t(\|\boldsymbol{\mu}_0 - \boldsymbol{\mu}_q\|) - v.$$

3.4.3 Numerical results

In this section we perform some numerical tests of the proposed functional kriging ROMES for the approximation of the time-dependent output error. With this aim, we consider as output of the monodomain model (3.9) the vector:

$$y^{(\ell)}(\boldsymbol{\mu}) = u(\mathbf{x},, t^{(\ell)}; \boldsymbol{\mu})\Big|_{\mathbf{x}=\bar{\mathbf{x}}}, \qquad \ell = 1, \dots, N_t,$$

where $\bar{\mathbf{x}} = (1, 0.5)$ is a point on $\partial\Omega$. Since the real-valued output considered in Section 3.3.1 is a landmark of this vector, the assumptions that the error is a second-order stationary and isotropic field could be considered verified also in this case. In fact, the different locations and dimensions of the ischemia affect the error propagation: it is reasonable to assume that parameters which are close to each other present a similar error vector.

We then construct the functional kriging-based ROMES starting from N_{cal} samples of the reduction error $\{y_h(\boldsymbol{\mu})^{(\ell)} - y_n(\boldsymbol{\mu})^{(\ell)}\}_{\ell=1}^{N_t}$ with $\boldsymbol{\mu} \in \{\boldsymbol{\mu}_1, \dots, \boldsymbol{\mu}_{N_{cal}}\}$.
As test case, we consider ROM #1 and $N_{cal} = 100$ parameter values for the ROMES construction. We first compute the empirical semivariogram estimate (blue dots in Figure 3.10):

$$\hat{\gamma}(\delta) = \frac{1}{2|N(\delta)|} \sum_{i,j \in N(\delta)} \int_0^T (y(\boldsymbol{\mu}_i) - y(\boldsymbol{\mu}_j))^2 dt.$$

An exponential theoretical semi-variogram model (3.5) is fitted on the empirical semi-variogram data (red line). Five random outputs are shown in Figure 3.10 to highlight the effect of the reduction error and of the ROMES correction. The five corrected outputs are closer to the full-order one with respect to the reduced-order ones (however, small oscillating errors are not captured by the model).

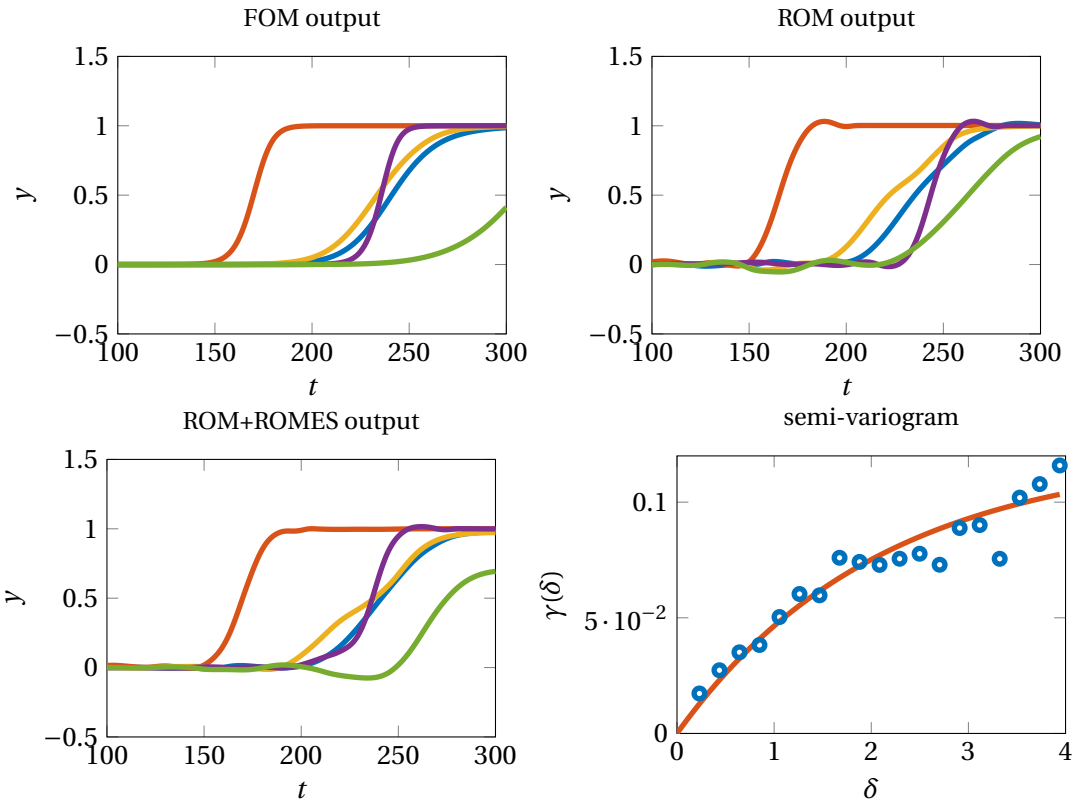

Figure 3.10 – Five random realization of the time-dependent output $\{y^{(\ell)}\}_{\ell=1}^{N_t}$ of the mon-odomain model $u(\mathbf{x}, t^{(\ell)}; \boldsymbol{\mu})|_{\mathbf{x}=\bar{\mathbf{x}}}$ approximated using the FOM and ROM #1 with and without ROMES correction (the fitted exponential semi-variogram is reported on the left).

In order to evaluate the performances of the functional kriging ROMES we compute the maximum error

$$\max_{\ell=1,\dots,N_t} |y_h^{(\ell)}(\boldsymbol{\mu}) - y_n^{(\ell)}(\boldsymbol{\mu}) - m_{\mathrm{ROM}}^{(\ell)}(\boldsymbol{\mu})| \qquad \boldsymbol{\mu} \in P_{oob},$$

and an approximation of the integral error given by

$$\sum_{\ell=1}^{N_t} \Delta t |y_h^{(\ell)}(\boldsymbol{\mu}) - y_n^{(\ell)}(\boldsymbol{\mu}) - m_{\mathrm{ROM}}^{(\ell)}(\boldsymbol{\mu})| \qquad \boldsymbol{\mu} \in P_{oob},$$

where P_{oob} is a random set of parameter values P_{oob} of dimension $N_{oob} = 40$. In particular we consider the case when no correction is provided ($m_{\mathrm{ROM}}^{(\ell)}(\boldsymbol{\mu}) = 0$) and the case when a functional kriging error surrogate is adopted (three different ROMESs have been considered on varying the dimension N_{cal} of the calibration set P_{cal}). The distributions of these errors on varying the ROMs and the ROMESs are represented using the box-plots reported in Figure 3.11.

By combining a ROM with a ROMES, built with the functional kriging method, we recover the same accuracy obtained with an uncorrected ROM with larger dimensions, as we can observe by comparing the results for the errors on the uncorrected output with the corrected ones in Figure 3.11.

3.5 Conclusions

In this Chapter we have presented ROM error surrogates based on kriging interpolation for both real- and functional-valued outputs. In the real-valued case the numerical tests show that the effectivity of the ROMES is almost 1 for every ROMs, which means that the ROMES is able to well approximate the output error. Moreover, in the functional-valued case we are able to improve the error on the output from the 10% to the 50% in the consider test case. Regarding the computational times, the kriging-based ROMES affects only the *offline* phase where additional full-order solutions are computed for each element in the calibration set. However, the online evaluation of the surrogate model is negligible with respect to the ROM one: only the solution of a system of dimension $(N_{cal}+1) \times (N_{cal}+1)$ is required with respect to the N_t linear system of dimension $n \times n$ required by the ROM.
In the next Chapters, we take advantage of this improved accuracy given by a ROMES coupled with the efficiency of a small dimensional ROM to develop efficient uncertainty quantification and inversion procedures.

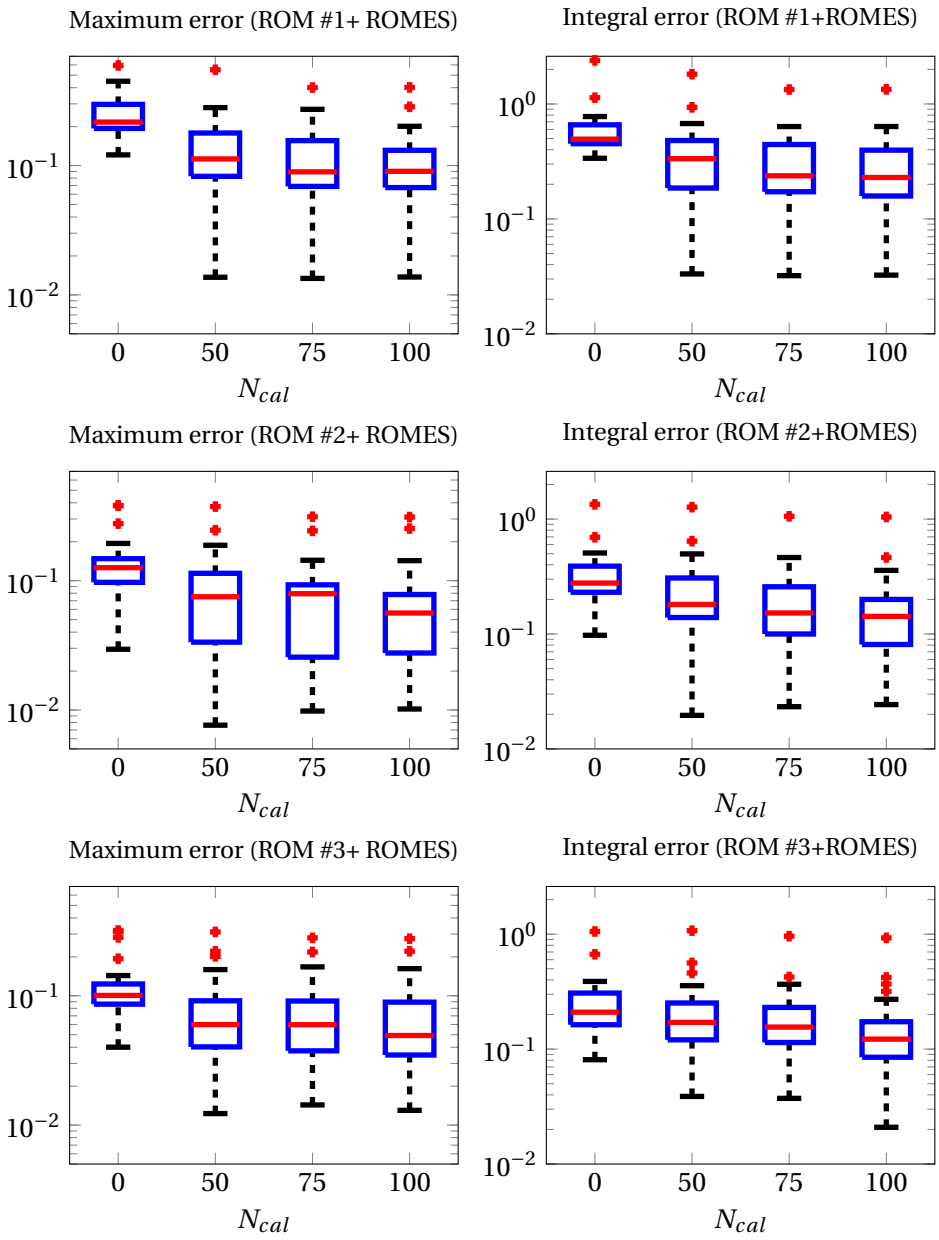

Figure 3.11 – Maximum error and integral error on varying the considered ROMs and the number of parameters vector used for the ROMESs construction. The functional kriging ROMES reduces the error in all cases, in particular the best improvements are related to ROM #1.

Part II

Uncertainty quantification and parameter estimation

4 | Forward uncertainty quantification

In this Chapter we show how to take advantage of reduced-order models (ROMs) coupled with cheaply computable ROM error surrogates in order to deal with forward uncertainty quantification problems arising in cardiac electrophysiology.
The chapter opens with an introduction on the uncertainty quantification (UQ) framework and its goal (Section 4.1). Then, we recall the basic concepts of *sensitivity analysis* (a key tool to perform uncertainty characterization) in Section 4.2 and of *uncertainty propagation* in Section 4.3. Reduced-order models for uncertainty quantification are proposed in Section 4.4 with a theoretical analysis of the bias in the UQ introduced by the propagation of the approximation error. The proposed reduced framework is tested on a problem dealing with electrophysiology, presented in Section 4.5, consisting in the analysis of a simplified ECG signal generated from an idealized two-dimensional heart-torso model.

4.1 Uncertainty quantification

The knowledge of the parameters values of cardiac electrophysiology models is considerably limited, due to difficulties in performing *in vivo* and *in vitro* experiments for their estimation [FNC+11]. Moreover, the cardiac model parameters, characterizing both physical and/or geometrical configurations of the system, show a considerable intra- and extra-subject variability. This latter is also reflected on the outputs of the model, making difficult their analysis: for example, we have pointed out that ECG signals present deviations from the standard three waves patterns due to both intra-patient variability and the presence of possible pathologies. In order to minimize misclassification (false negative and false positive), it is crucial to better understand how model parameters and their uncertainties affect the considered outputs.

With this goal, we apply in this Chapter standard uncertainty quantification techniques [Smi13] to cardiac electrophysiology models. Since these techniques are usually based on sampling procedures, they suffer of dramatic computational costs when full-order models are adopted for the approximation of the parametrized PDEs (possibly coupled with ODEs) arising in cardiac electrophysiology. For this reason, UQ techniques have been exploited so far only for parametrized ODE models at the cell level in [JCB+16, PSG+15, NFN+09]. For a recent overview on the state of the art UQ applications in cardiac electrophysiology see e.g. [MPG+16]. In this Chapter, we adopt the reduction framework developed in Chapter 2 and 3 in order to apply for the first time standard uncertainty quantification techniques to the parametrized PDEs coupled with ODEs characterizing cardiac electrophysiology.

In particular, we will focus on:

- *sensitivity analysis* which studies the parameters role and importance with respect to a considered output, through some indices that can be used to rank the model parameters. The combination of these information with available data enables to design optimally the parametrization of a PDE model;
- *uncertainty propagation*, which focuses on how uncertainty in model parameters propagates to the outputs of interest, providing probability distributions (pdf) or simple statistics.

A sketch of the entire framework can be found in Figure 4.1: *uncertainty characterization* and *propagation* are integrated with the input-output evaluation inside a cycle, since the UQ outcomes could give feedbacks about possible modifications of the model parametrization.

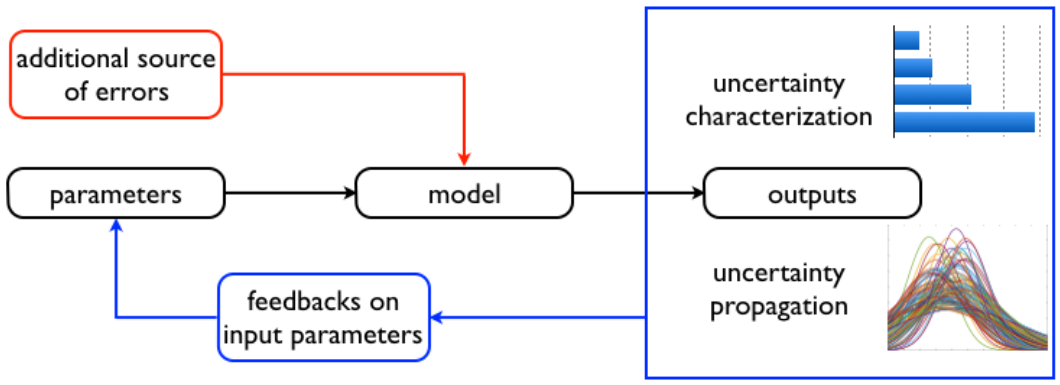

Figure 4.1 – Uncertainty quantification framework

From the mathematical standpoint, we consider the probability space $(\Theta, \mathcal{F}, \mathbb{P})$ and the random function $Y : \Theta \to \mathbb{R}$, whose realization is the full-order output $y_h(\boldsymbol{\mu})$. Given $\boldsymbol{\mu} \in \mathcal{P}$, the input/output mapping

$$\boldsymbol{\mu} \to u_h(t;\boldsymbol{\mu}) \to y_h(\boldsymbol{\mu}),$$

requires e.g. the numerical approximation of a nonlinear unsteady PDE coupled with an ODE, such as the monodomain equation coupled to the Aliev-Panfilov model. For the sake of notation, we consider all the parameters normalized in $[0,1]$.

In variance-based *sensitivity analysis*, the sensitivities of the output with respect to the parameters are measured by looking at the amount of variance caused by the parameter μ_i, $i = 1,\dots,d$. This requires the calculation of conditional expectation of the random variable Y:

$$\mathbb{E}[Y|\mu_i] = \int_\Theta y_h(\boldsymbol{\mu})\pi(\boldsymbol{\mu}|\mu_i)d\boldsymbol{\mu} \qquad i = 1,\dots,d,$$

where $\pi(\boldsymbol{\mu}|\mu_i)$ is the conditional pdf of $\boldsymbol{\mu}$ given μ_i. In fact, $\boldsymbol{\mu}$ is modeled as a multivariate random variable with pdf $\pi(\boldsymbol{\mu})$. The conditional pdf is defined as

$$\pi(\boldsymbol{\mu}|\mu_i) = \frac{\pi(\boldsymbol{\mu})}{\pi_i(\mu_i)},$$

where $\pi_i(\mu_i)$ is the marginal pdf of μ_i. We need also to compute the variance of this conditional expectation with respect to the parameter μ_i

$$\mathrm{Var}(\mathbb{E}[Y|\mu_i]) = \int_{\mathbb{R}} \left(\mathbb{E}[Y|\mu_i]\right)^2 \pi_i(\mu_i)d\mu_i - \left(\int \mathbb{E}[Y|\mu_i]\pi_i(\mu_i)d\mu_i\right)^2.$$

In *uncertainty propagation* the problem consists instead in finding the probability distribution $\pi(y) : Y \to \mathbb{R}$ of the random variable Y given a probability distribution $\pi(\boldsymbol{\mu}) : \mathscr{P} \to \mathbb{R}$ of the uncertain vector of parameter. Sometimes instead of estimating the full pdf $\pi(y)$, the goal is to estimate the expected value:

$$\mathbb{E}[Y] = \int_\Theta y_h(\boldsymbol{\mu})\pi(\boldsymbol{\mu})d\boldsymbol{\mu},$$

and/or its variance

$$\mathrm{Var}(Y) = \int_\Theta (y_h(\boldsymbol{\mu}) - \mathbb{E}[Y])^2\pi(\boldsymbol{\mu})d\boldsymbol{\mu} = \int_\Theta (y_h(\boldsymbol{\mu}))^2\pi(\boldsymbol{\mu})d\boldsymbol{\mu} - \mathbb{E}[Y]^2.$$

Since the full-order intput/output mapping

$$\boldsymbol{\mu} \to u_h(t;\boldsymbol{\mu}) \to y_h(\boldsymbol{\mu})$$

is highly nonlinear, it is not possible to evaluate the expectation values and the variances in a close form. We rely on Monte Carlo (MC) method which provides an approximation of the mean and of the variance of the quantities of interest by generating a random sample $\{\boldsymbol{\mu}_q\}$, $q = 1,\dots,N_{mc}$ of identically distributed draws from $\pi(\boldsymbol{\mu})$. For example, the expected value $\mathbb{E}[Y]$ is approximated by

$$\mathbb{E}[Y] \sim \frac{1}{N_{mc}} \sum_{q=1}^{N_{mc}} y_h(\boldsymbol{\mu}_q),$$

and the variance by

$$\mathrm{Var}(Y) \sim \frac{1}{N_{mc}} \sum_{q=1}^{N_{mc}} \left(y_h(\boldsymbol{\mu}_q) - \frac{1}{N_{mc}} \sum_{q=1}^{N_{mc}} y_h(\boldsymbol{\mu}_q) \right)^2.$$

Both *sensitivity analysis* and *propagation* are computationally-demanding, since a large number of simulations are needed to generate outputs for each parameter vector in $\{\boldsymbol{\mu}_q\}$, $q = 1,\dots,N_{mc}$ (*many query* problem). To improve the performances we can follow different strategies such as, *(i)* to speedup the input-output evaluation with SMs or ROMs, *(ii)* to improve

sampling procedures [Buc88, Gil08, NT15] or *(iii)* to adopt different stochastic procedures [Sud08, Naj09]. In this Chapter we focus on the first strategy for its ease of implementation and flexibility. Moreover, the proposed reduced framework can be easily adapted also to the other different UQ methods. For example, stochastic Galerkin and stochastic collocation methods [NTW08, BNT+11, BNT07, CLMM09] require the evaluation of the input/output mapping on a suitable set of points (e.g. collocation sparse grid) for the calculation of the previous integrals. This procedure could benefit from the adoption of ROM and ROMES for an efficient and yet accurate input/output evaluation. An example of application based on the stochastic finite elements method for the study of the sensitivity of the torso conductivity field can be found in [GKM08, SGS+11].

4.2 Sensitivity analysis

Sensitivity analysis quantifies the effects of parameters variation on the outputs of interest, providing a criterium to rank the most influential input parameters. A large number of approaches to perform sensitivity analysis can be found in the literature; they can be divided in two main families: local and global methods. Local methods are based on the evaluation of the partial derivatives of the outputs with respect to input parameters. The term local is related to the fact that these derivatives are evaluated in a given parameters vector, providing information related to a neighborhood of that point. Evaluating the partial derivatives of complex models outputs is not straightforward: in the case of time-dependent nonlinear PDEs the computation of the derivatives requires the solution of the so-called backward adjoint equation, which is also computationally demanding. For this motivation, local methods usually explore only a small subset of the parameter space, especially when the parameter vector is high-dimensional.

On the other hand, the global approaches are based on sampling techniques on the entire parameter space. Basic tools for sensitivity analysis are the scatter-plots of the outputs against the input parameters and the regression analysis [CH09]. In this work we consider a variance-based global sensitivity analysis (GSA) which describes the amount of output variance generated from the variation of a single parameter (and also from interactions among the parameters). We refer respectively to [SCS+00] ([SRA+08]) for a complete review of the (global) sensitivity analysis framework.

In the field of cardiac electrophysiology, variance-based GSA has been recently applied for the study of 1D models of the cellular cardiac potential [JCB+16], using Gaussian processes to perform efficiently the input-output evaluation. In this Chapter, we propose a reduced-order variance-based GSA for a simplified ECG signal generated by a two-dimensional heart-torso model, while in Chapter 7 we apply this method to study the action-potential shape given by a three-dimensional model of the left ventricle. We also show how the GSA indices could be relevant in the design of the parametrization of the model. We take advantage of kriging-based surrogate models and projection-based ROMs to perform efficiently this task, showing how ROMs could ensure a considerable accuracy in the results.

4.2.1 Variance-based global sensitivity analysis

Variance-based GSA provides a decomposition of the variance associated to an output $y(\boldsymbol{\mu})$ on varying the input $\boldsymbol{\mu} \in \mathscr{P} \subset \mathbb{R}^d$. The variance of the random variable Y can be decomposed in the sum of the first-order effect and the residual:

$$\mathrm{Var}(Y) = \mathrm{Var}(\mathbb{E}[Y|\mu_i]) + \mathbb{E}[\mathrm{Var}(Y|\mu_i)] \qquad i = 1,\dots,d.$$

The second term is the residual variance, which describes on average (with respect to the parameter μ_i) the information left when μ_i is fixed, while the first term is the explained variance, which describes the reduction of the variance due to the knowledge of μ_i. On the basis of these observations, the first-order sensitivity index of μ_i on Y can be defined as:

$$S_i = \frac{\mathrm{Var}(\mathbb{E}[Y|\mu_i])}{\mathrm{Var}(Y)} \qquad i = 1,\dots,d. \tag{4.1}$$

In other words, S_i enables to determine which parameter μ_i, $i = 1,\dots,d$, leads on average to the greatest reduction in the variance of the output Y. The sum of all S_i should be less (or equal) to one if the model is nonadditive (respectively additive). If the model is nonadditive, the variance can be decomposed through the so-called ANOVA decomposition into main effects and interaction effects, which are used to construct the interaction indices

$$S_{i,j} = \frac{\mathrm{Var}(\mathbb{E}[Y|[\mu_i,\mu_j]^T]) - \mathrm{Var}(\mathbb{E}[Y|\mu_i] - \mathrm{Var}(\mathbb{E}[Y|\mu_j])}{\mathrm{Var}(Y)}, \qquad i = 1,\dots,d.$$

However, the computation of all possible interaction indices $S_{i,j}$ becomes impractical for high-dimensional parameter vectors. Instead of studying all the possible interactions, it is preferable to construct a single index, known as total effect index, given by the sum of first-order effects with all higher-order effects due to interactions:

$$S_{T_i} = S_i + \sum_{j \neq i} S_{i,j} + \dots, \qquad i = 1,\dots,d.$$

To derive a direct formula for this index without computing $S_{i,j}$, we consider the variance decomposition of the random variable Y in the sum of the first-order effect and the residual, both conditioned with respect to all the factors except μ_i (indicated with $\sim i$):

$$\mathrm{Var}(Y) = \mathrm{Var}(\mathbb{E}[Y|\mu_{\sim i}]) + \mathbb{E}[\mathrm{Var}(Y|\mu_{\sim i})] \qquad i = 1,\dots,d.$$

As a consequence, the residual quantity

$$\mathrm{Var}(Y) - \mathrm{Var}(\mathbb{E}[Y|\mu_{\sim i}]), \qquad i = 1,\dots,d, \tag{4.2}$$

is the remaining variance of Y that would be left if we could determine the true values of μ_j for all j different from i. The total effect index is then obtained by dividing the residual quantity (4.2) by the total variance $\mathrm{Var}(Y)$:

$$S_{T_i} = 1 - \frac{\mathrm{Var}(\mathbb{E}[Y|\mu_{\sim i}])}{\mathrm{Var}(Y)} \qquad i = 1,\dots,d. \tag{4.3}$$

The total effect index (4.3) is much more informative than the first-order index (4.1), except when there are no interaction effects, in which case they are equal. High-values correspond to influential parameters for the output of interest; in particular, we have that:

1. the condition $S_{T_i} = 0$ is equivalent to the fact that μ_i is a noninfluential parameter.
2. if S_{T_i} is almost zero, μ_i can be fixed to any value in its range without changing the value of the output variance.

Once we have computed the indices, S_{T_i}, $i = 1, \dots, d$, it is possible to rank the most influential parameters, hence to achieve a model simplification by discarding the non-influential ones [ST02].

The analysis can be enriched using the main effects plots, which show how the conditional expectation $\mathbb{E}(Y|\mu_i)$ changes when μ_i is fixed to some values in its range, while the other parameters are sampled randomly from a Gaussian distribution of mean 0.5 and variance 0.04. The trends of these curves are directly linked to the values of the first-order index S_i, which indeed describes their associated variability.

The standard numerical procedure for computing the first-order and total effect indices is based on Monte-Carlo sampling. Given μ_i and a random sample $\{\boldsymbol{\mu}_q\}$, $q = 1, \dots, N_{mc}$ of identically distributed draws from $\pi(\boldsymbol{\mu}|\mu_i)$, each conditional expected value can be approximated by:

$$\mathbb{E}[Y|\mu_i] \sim \frac{1}{N_{mc}} \sum_{q=1}^{N_{mc}} y_h(\boldsymbol{\mu}_q|_{\mu_i}).$$

By repeating this procedure for each μ_i, randomly sampled from $\pi_i(\mu_i)$, we obtain a Monte Carlo approximation of the explained variance $\mathrm{Var}(\mathbb{E}[Y|\mu_i])$. This procedure is clearly not feasible from the computational point of view. For this reason, two methods have been developed to accelerate the evaluation of the sensitivity indices (4.1)-(4.3): the Fourier Amplitude Sensitivity Test (FAST) and the Sobol' method [HS96]. In the following we will focus on the second one, based on Sobol' sequences of quasi-random numbers. The procedure consists in the following steps:

1. generate two matrices $\mathbf{A}, \mathbf{B} \in \mathbb{R}^{N_s \times d}$ of parameter realizations from a Sobol' quasi-random sequence (obtained e.g. with the `Matlab` function `sobolset`):

$$\mathbf{A} = \begin{bmatrix} \mu_1^1 & \mu_2^1 & \cdots & \mu_{d-1}^1 & \mu_d^1 \\ \vdots & & \vdots & & \\ \mu_1^{N_s} & \mu_2^{N_s} & \cdots & \mu_{d-1}^{N_s} & \mu_d^{N_s} \end{bmatrix} \qquad \mathbf{B} = \begin{bmatrix} \mu_{d+1}^1 & \mu_{d+2}^1 & \cdots & \mu_{2d-1}^1 & \mu_{2d}^1 \\ \vdots & & \vdots & & \\ \mu_{d+1}^{N_s} & \mu_{d+2}^{N_s} & \cdots & \mu_{2d-1}^{N_s} & \mu_{2d}^{N_s} \end{bmatrix};$$

2. construct d matrices of parameter realizations $\mathbf{C}_i \in \mathbb{R}^{N_s \times d}$, $i = 1, \dots, d$, using all columns of $\mathbf{B}$ except the $i-th$ column taken from $\mathbf{A}$:

$$\mathbf{C}_i = \begin{bmatrix} \mu_{d+1}^1 & \cdots & \mu_i^1 & \cdots & \mu_{2d}^1 \\ \vdots & & \vdots & & \\ \mu_{d+1}^{N_s} & \cdots & \mu_i^{N_s} & \cdots & \mu_{2d}^{N_s} \end{bmatrix};$$

3. compute the model output for all the vectors of parameters given by the rows of $\mathbf{A}$, $\mathbf{B}$ and $\mathbf{C}_i$. The results are respectively $d+2$ vectors of model outputs y_A, y_B and y_{C_i} of dimension $N_s \times 1$;

4. the first-order index is computed using the following formula:

$$S_i = \frac{\mathrm{Var}(\mathbb{E}[Y|\mu_i])}{\mathrm{Var}(Y)} = \frac{y_A^T y_{C_i} - \overline{y}_A^2}{y_A^T y_A - \overline{y}_A^2}, \qquad i = 1,\dots,d, \tag{4.4}$$

where $\overline{y}_A$ denotes the sample mean of the vector y_A. On the other hand, the total effect index is given by:

$$S_{T_i} = 1 - \frac{\mathrm{Var}(\mathbb{E}[Y|\mu_{\sim i}])}{\mathrm{Var}(Y)} = 1 - \frac{y_B^T y_{C_i} - \overline{y}_A^2}{y_A^T y_A - \overline{y}_A^2}, \qquad i = 1,\dots,d. \tag{4.5}$$

A complete explanation of (4.4) and (4.5) can be found in [SRA+08]. The principal drawback of this procedure is the computational cost: we need to evaluate the model $(d+1)N_s$ times in order to compute all the indices. Moreover, the accuracy of the computation clearly depends on the number N_s of sample points: N_s should be large enough to minimize the statistical error generated by the sampling.

4.3 Uncertainty propagation

The goal of uncertainty propagation is to quantify the impact of uncertainties related to the input parameters $\boldsymbol{\mu}$ on an output of interest $y_h(\boldsymbol{\mu})$, by computing its distribution or some statistics, such as mean and variance.
Since the knowledge on the parameter values of cardiac electrophysiology models is limited, it is crucial to understand how input uncertainties are propagated to the outputs through the solution of a nonlinear time-dependent system of PDEs (possibly coupled with ODEs). For example, we could be interested in understanding how uncertainties in physical coefficients modify the shape of an ECG signal or how geometry uncertainties modify the solution of the electrophysiology models.

Monte-Carlo (MC) sampling [RC13] is the standard approach for this kind of problems: a large number N_{mc} of independent samples $\{\boldsymbol{\mu}_q\}_{q=1}^{N_{mc}}$ are drawn from a given distribution $\pi(\boldsymbol{\mu}) : \mathbb{R}^d \to \mathbb{R}^+$ and then used to compute $\{\mathbf{y}_h(\boldsymbol{\mu}_q)\}_{q=1}^{N}$, or directly statistics of the outputs, such as expected values:

$$\mathbb{E}[Y] \sim \frac{1}{N_{mc}} \sum_{q=1}^{N_{mc}} y_h(\boldsymbol{\mu}_q),$$

and the output variance

$$\mathrm{Var}(Y) \sim \frac{1}{N_{mc}} \sum_{q=1}^{N_{mc}} \left(y_h(\boldsymbol{\mu}_q) - \frac{1}{N_{mc}} \sum_{q=1}^{N_{mc}} y_h(\boldsymbol{\mu}_q) \right)^2.$$

This approach has been successfully adopted in a variety of applications, but suffers of slow performance in terms of convergence rate, in particular when the parametric dimension grows.

The convergence rate can be improved by considering suitable modifications of the method such as variance reduction techniques [Has70], control variates [RM85] or multi level Monte Carlo [Gil08, NT15]. For completeness, we also mention alternative non-sampling approaches,

which have been proposed to improve the performance of uncertainty propagation: the goal of these methods is to directly compute statistics using projection or interpolation techniques on suitable grids. Among these methods, we mention polynomial chaos expansion [XK02, Naj09], stochastic collocation [BNT07] and stochastic Galerkin [GS03, BNT+11]. However the application of non-sampling methods in cardiac electrophysiology is not straightforward due to the complexity of the electrophysiology models and the large number of uncertain parameters.

In this Chapter, we instead substitute the full-order model (FOM) with a surrogate model (SM) or a reduced-order model (ROM) in order to speed up standard MC samplings. Our aim is to study this reduced UQ framework, by analyzing the advantages and drawbacks of SMs and ROMs, by exploiting MC sampling on the heart-torso coupling and a subject-specific model on left ventricle.

4.4 Reduced-order models for UQ

The Sobol' or the Monte Carlo sampling approaches are typical *many query* problems. To speed up the evaluation of the output given a vector of parameters, it is possible to rely on surrogate models, which provides the input/output mapping

$$\boldsymbol{\mu} \rightarrow y_s(\boldsymbol{\mu}) + \varepsilon_s,$$

where $y_s(\boldsymbol{\mu})$ is the output prediction given by a surrogate model, such as the one developed in Section 3.2. On the other hand, a ROM provides the input/output mapping

$$\boldsymbol{\mu} \rightarrow u_n(t;\boldsymbol{\mu}) \rightarrow y_n(\boldsymbol{\mu}),$$

through the solution of the parametrized PDE (possibly coupled with the ODE) projected onto the reduced space (as described in Chapter 2).

In the reduced framework, the calculation of S_i and S_{T_i}, $i = 1,\dots,d$, through the Sobol' method requires the computation of the reduce output for all the vectors of parameters given by the rows of $\mathbf{A}$, $\mathbf{B}$ and $\mathbf{C}_i$. The resulting vectors $y_{n,A}$, $y_{n,B}$ and y_{n,C_i} are then used in (4.4) and (4.5) instead of y_A, y_B and y_{C_i} for the efficient evaluation of S_i and S_{T_i}, $i = 1,\dots,d$.
On the other hand, the calculation of the quantities of interest related to the *uncertainty propagation* becomes: given a set of random samples $\{\boldsymbol{\mu}_q\}$, $q = 1,\dots,N_{mc}$, compute the reduced expected value

$$\mathbb{E}[Y_n] \sim \frac{1}{N_{mc}} \sum_{q=1}^{N_{mc}} y_n(\boldsymbol{\mu}_q),$$

where Y_n is the random variable describing the reduced output. Then, compute the reduced output variance as:

$$\mathrm{Var}(Y_n) \sim \frac{1}{N_{mc}} \sum_{q=1}^{N_{mc}} \left(y_n(\boldsymbol{\mu}_q) - \frac{1}{N_{mc}} \sum_{q=1}^{N_{mc}} y_n(\boldsymbol{\mu}_q) \right)^2.$$

In an equivalent way, the reduced output could be substituted by a surrogate output, such as kriging interpolation or random forest regression [SSH+09]; for the kriging SM also an analytical approach has been proposed in [OO04].

Clearly, the main problem arising when uncertainty quantification is performed using a SM is the reliability and the accuracy of the results, due to the curse of dimensionality. In this work, we compare the results of uncertainty quantification between SMs with projection-based ROMs in terms of efficiency and accuracy.

4.4.1 Reduction error propagation

A relevant issue, arising when a SM or a ROM is exploited to solve a UQ problem, is related to the propagation of approximation errors (i.e. the error between the FOM and the SM or ROM) in the resulting distribution of the outputs. As a matter of fact, neglecting this additional source of error could lead to biased sensitivity indices or skewed distributions of the outputs. This problem has been consider recently in [PWG16], where a multi-fidelity approach has been proposed for the solution of inverse problems and UQ. This method combines different reduced-order and full-order models to ensure the accuracy of sensitivity analysis and uncertainty propagation results. However, the full-order queries arising in cardiac electrophysiology could be computationally demanding, compromising the overall UQ performance. In this Thesis, instead, we prefer the classical *offline-online* approach, in order to avoid full-order queries each time a sensitivity indices is computed. Moreover, we equip our ROM with surrogate models (ROMESs) developed in Chapter 3 to have a statistical representation of the approximation errors and, as overall goal, to improve the accuracy of our analysis.

In this Section we analyze the effect of the output reduction error $y_h(\boldsymbol{\mu}) - y_n(\boldsymbol{\mu})$ on the UQ quantities of interest. In particular, we analyze the output expected value and variance obtained when dealing with forward propagation. We can decompose the error on the resulting expected value as the sum of:

$$\mathbb{E}[Y] - \frac{1}{N_{mc}} \sum_{m=1}^{N_{mc}} \mathbf{y}_n(\boldsymbol{\mu}_m) = \underbrace{\mathbb{E}[Y - Y_n]}_{\text{approx. error}} + \underbrace{\mathbb{E}[Y_n] - \frac{1}{N_{mc}} \sum_{m=1}^{N_{mc}} \mathbf{y}_n(\boldsymbol{\mu}_m)}_{\text{statistical error}},$$

where $\mathbb{E}[Y - Y_n]$ is the average approximation error (bias in the output) depending on the accuracy of the ROM, while the second term is the statistical error depending exclusively on N_{mc}. If we want to minimize the error on the expected values, without changing the ROM, a suitable statistical ROMES $m_{\text{ROM}}(\boldsymbol{\mu})$ must be adopted to minimize the output reduction error:

$$y_h(\boldsymbol{\mu}) = y_n(\boldsymbol{\mu}) + m_{\text{ROM}}(\boldsymbol{\mu}) + \varepsilon_{\text{ROM}}(\boldsymbol{\mu}) \qquad \forall \boldsymbol{\mu} \in \mathscr{P},$$

where $\varepsilon_{\text{ROM}}(\boldsymbol{\mu})$ is a random variable with zero mean and variance $\sigma^2_{\text{ROM}}(\boldsymbol{\mu})$, representing the estimation error. In particular, if we assume that the error in mean is well captured by the ROMES, i.e. there exists a tolerance $\varepsilon_{tol} > 0$ such that:

$$|\mathbb{E}[Y - Y_n - m_{\text{ROM}}]| \leq \varepsilon_{tol}, \tag{4.6}$$

the overall error of the sampling procedure becomes:

$$\left| \mathbb{E}[Y] - \frac{1}{N_{mc}} \sum_{m=1}^{N_{mc}} (\mathbf{y}_n(\boldsymbol{\mu}_m) + \mathbf{m}_{\text{ROM}}(\boldsymbol{\mu}_m)) \right| \leq \varepsilon_{tol} + \left| \mathbb{E}[Y_n] - \frac{1}{N_{mc}} \sum_{m=1}^{N_{mc}} \mathbf{y}_n(\boldsymbol{\mu}_m) \right|.$$

This results can be easily extended to the conditional means, ensuring that

$$\left|\mathbb{E}[Y|\mu_i] - \frac{1}{N_{mc}}\sum_{m=1}^{N_{mc}}(\mathbf{y}_n(\boldsymbol{\mu}_m|_{\mu_i}) + \mathbf{m}_{\text{ROM}}(\boldsymbol{\mu}_m|\mu_i))\right| \leq \varepsilon_{tol} + \left|\mathbb{E}[Y_n|\mu_i] - \frac{1}{N_{mc}}\sum_{m=1}^{N_{mc}}\mathbf{y}_n(\boldsymbol{\mu}_m|_{\mu_i})\right|.$$

On the other hand, if we consider the variance, we have that:

$$\begin{aligned}\text{Var}(Y) - &\frac{1}{N_{mc}}\sum_{m=1}^{N_{mc}}\left(\mathbf{y}_n(\boldsymbol{\mu}_m) - \frac{1}{N_{mc}}\sum_{m=1}^{N_{mc}}\mathbf{y}_n(\boldsymbol{\mu}_m)\right)^2 \\ &= \underbrace{\text{Var}(Y) - \text{Var}(Y_n)}_{\text{approx. error}} + \underbrace{\text{Var}(Y_n) - \frac{1}{N_{mc}}\sum_{m=1}^{N_{mc}}\left(\mathbf{y}_n(\boldsymbol{\mu}_m) - \frac{1}{N_{mc}}\sum_{m=1}^{N_{mc}}\mathbf{y}_n(\boldsymbol{\mu}_m)\right)^2}_{\text{statistical error}}.\end{aligned}$$

The approximation error can be further decomposed as:

$$\text{Var}(Y) - \text{Var}(Y_n) = \text{Var}(Y - Y_n) + 2\text{Cov}(Y - Y_n, Y_n).$$

If the ROMES shows small prediction variance σ^2_{ROM}, there exists a tolerance $\varepsilon_{tol,2} > 0$ such that:

$$|\text{Var}(Y - Y_n - m_{\text{ROM}} - \varepsilon_{\text{ROM}})| < \varepsilon_{tol,2}. \tag{4.7}$$

Since the covariance is linear with respect to both arguments, the term $\text{Cov}(Y - Y_n, Y_n)$ can be bounded by:

$$|\text{Cov}(Y - Y_n, Y_n)| = |\mathbb{E}[(Y - Y_n)Y_n] - \mathbb{E}[Y - Y_n]\mathbb{E}[Y_n]| \leq |\max(Y_n) - \mathbb{E}[Y_n]||\mathbb{E}[Y - Y_n]|,$$

which means that provided 4.6 is fulfilled:

$$|\text{Cov}(Y - Y_n - m_{\text{ROM}}, Y_n + m_{\text{ROM}})| \leq |\max(Y_n + m_{\text{ROM}}) - \mathbb{E}[Y_n + m_{\text{ROM}}]|\varepsilon_{tol}.$$

Finally, we conclude that the error in approximating the variance can be bounded by

$$\begin{aligned}&\left|\text{Var}(Y) - \frac{1}{N_{mc}}\sum_{m=1}^{N_{mc}}\left((\mathbf{y}_n(\boldsymbol{\mu}_m) - \mathbf{m}_{\text{ROM}}(\boldsymbol{\mu}_m)) - \sum_{m=1}^{N_{mc}}(\mathbf{y}_n(\boldsymbol{\mu}_m) - \mathbf{m}_{\text{ROM}}(\boldsymbol{\mu}_m))\right)^2 - \text{Var}(\varepsilon_{\text{ROM}})\right| \\ &\qquad \leq \varepsilon_{tol,2} + (max(Y_n) - \mathbb{E}[Y_n])\varepsilon_{tol} + \text{Var}(Y_n) - \frac{1}{N_{mc}}\sum_{m=1}^{N_{mc}}\left(\mathbf{y}_n(\boldsymbol{\mu}_m) - \frac{1}{N_{mc}}\sum_{m=1}^{N_{mc}}\mathbf{y}_n(\boldsymbol{\mu}_m)\right)^2.\end{aligned}$$

This analysis can be extended also to both the first-order and the total effect indices, where conditional expectations and variance are considered. We can conclude that when a ROM does not provide an accurate approximation of the output, we need to rely on ROMES correction in order to recover reliable results in the UQ framework. Assumptions (4.6) and (4.7) are crucial for both the *sensitivity analysis* and the *uncertainty propagation*: if one of these two assumptions does not hold, we introduce an additional source of error that affects the results (see Figure 4.1).

4.5 Numerical results: 2D section of the torso

We now apply the proposed reduction framework for UQ to the simplified two-dimensional coupled heart-torso problem, aiming at better understanding how physical parameters and their uncertainties influence the shape of a simplified ECG signal. The resulting insights on the inputs-outputs relationship are useful for a wide range of purposes, including model simplification and uncertainty reduction.

A parametrized two-dimensional model for the description of the electrical activity of the heart and the torso is then considered under some simplificative assumptions: (i) the heart is insulated from the outside and (ii) the isotropic relation $\mathbf{D}_i = \lambda \mathbf{D}_e$ holds. In this way, the bidomain model can be replaced by the monodomain model and the torso can be fully uncoupled from the heart. This choice is motivated by the considerable computational savings in the numerical approximation of the uncoupled formulation with respect to the fully coupled one.

The domain $\Omega = \Omega_H \cup \Omega_T$, represented in Figure 4.2, is given by the union of an idealized heart section (domain Ω_H) with a smooth domain representing the section of the surrounding torso (domain Ω_T). We denote with $\partial\Omega_T$ the outer boundary and with $\partial\Omega_H$ the boundary between Ω_H and Ω_T. Given the assumptions (i) and (ii), we first solve the following parametrized problem: given $\boldsymbol{\mu}_H$, find $u = u(\mathbf{x}, t; \boldsymbol{\mu}_H)$ and $w = w(\mathbf{x}, t; \boldsymbol{\mu}_H)$ such that

$$\begin{cases} A_m \left(C_m \dfrac{\partial u}{\partial t} + I_{ion}(u, w; \boldsymbol{\mu}_H) \right) - \operatorname{div}(\sigma_v \nabla u) = A_m I_{app}(t) & \mathbf{x} \in \Omega_H, t \in (0, T] \\ \frac{\partial w}{\partial t} = g(u, w; \boldsymbol{\mu}_H) & \mathbf{x} \in \Omega_H, t \in (0, T] \\ \nabla u(\mathbf{x}, t; \boldsymbol{\mu}_H) \cdot \mathbf{n}_H = 0 & \mathbf{x} \in \partial\Omega_H, t \in (0, T] \\ u(\mathbf{x}, 0; \boldsymbol{\mu}_H) = w(\mathbf{x}, 0; \boldsymbol{\mu}_H) = 0 & \mathbf{x} \in \partial\Omega_H, \end{cases} \tag{4.8}$$

with current specification (1.2) and $\boldsymbol{\mu}_H = [\sigma_v, K, \varepsilon_0]^T$. To complete the system definition, as done in [AP96], we choose $A_m = C_m = 1$ and $a = 0.15$ to model an adimensionalized action potential u. Finally in the definition of $g(u, w)$ in (1.2) we choose $c_1 = 0.12$ and $c_2 = 0.3$. The extra-cellular potential is then obtained by solving: find $u_e = u_e(\mathbf{x}, t; [\sigma_e, \boldsymbol{\mu}_H]^T)$ such that

$$\begin{cases} -\operatorname{div}((\sigma_i + \sigma_e)\nabla u_e) - \operatorname{div}(\sigma_i \nabla u) = 0 & \mathbf{x} \in \Omega_H, t \in (0, T] \\ (\sigma_i + \sigma_e)\nabla u_e(\mathbf{x}, t; [\sigma_e, \boldsymbol{\mu}_H]^T) \cdot \mathbf{n}_H = \sigma_i \nabla u(\mathbf{x}, t; \boldsymbol{\mu}_H) \cdot \mathbf{n}_H & \mathbf{x} \in \partial\Omega_H, t \in (0, T], \end{cases} \tag{4.9}$$

where $\sigma_i = (1 + \lambda)\sigma_v$ and σ_e are the parametrized conductivities. Finally, the torso potential is obtained by solving: find $u_T = u_T(\mathbf{x}, t; [\sigma_t, \sigma_e, \boldsymbol{\mu}_H]^T)$ such that

$$\begin{cases} \operatorname{div}(\nabla \sigma_T u_T) = 0 & \mathbf{x} \in \Omega_T, t \in (0, T] \\ \sigma_T \nabla u_T(\mathbf{x}, t; [\sigma_t, \sigma_e, \boldsymbol{\mu}_H]^T) \cdot \mathbf{n}_T = 0 & \mathbf{x} \in \partial\Omega_T, t \in (0, T] \\ u_T(\mathbf{x}, t; [\sigma_t, \sigma_e, \boldsymbol{\mu}_H]^T) = u_e(\mathbf{x}, t; [\sigma_e, \boldsymbol{\mu}_H]^T) & \mathbf{x} \in \partial\Omega_H, t \in (0, T]. \end{cases} \tag{4.10}$$

As shown in [PDV09] and in [BCF+10], the uncoupled model (4.8)-(4.9)-(4.10) still allows to recover the most important physiological features of an ECG, such as the QRS-complex and the T wave amplitude. On the other hand, for precise quantitative results on the ECG the coupled problem (1.7) must be adopted.

Regarding the ECG signals, since we are considering the two dimensional problem, we are not able to fully reproduce all the 12 leads, however we can provide a simplified approximation of seven leads. In particular, by defining the central reference as $V_w = 0.5(u_T(\mathbf{x}_{LA}, t; [\sigma_t, \sigma_e, \boldsymbol{\mu}_H]^T) + u_T(\mathbf{x}_{RA}, t; [\sigma_t, \sigma_e, \boldsymbol{\mu}_H]^T)$, we construct the seven signals as reported in Figure 4.2.

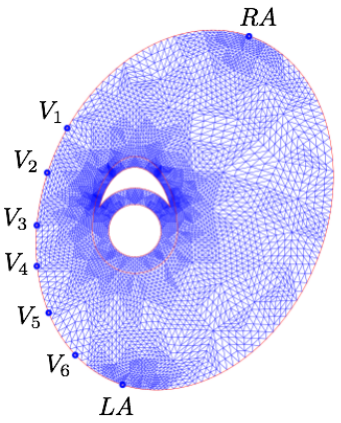

$$I(t) = u_T(t, \mathbf{x}_{LA}) - u_T(t, \mathbf{x}_{RA})$$
$$V_1(t) = u_T(t, \mathbf{x}_{V_1}) - V_w$$
$$V_2(t) = u_T(t, \mathbf{x}_{V_2}) - V_w$$
$$V_3(t) = u_T(t, \mathbf{x}_{V_3}) - V_w$$
$$V_4(t) = u_T(t, \mathbf{x}_{V_4}) - V_w$$
$$V_5(t) = u_T(t, \mathbf{x}_{V_5}) - V_w$$
$$V_6(t) = u_T(t, \mathbf{x}_{V_6}) - V_w$$

Figure 4.2 – ECG signals for the 2D heart-torso coupling

We consider five uncertain physical parameters: the first three describe the conductivity in the cardiac tissue σ_v, the extra-cellular conductivity σ_e and the conductivity of the torso σ_T, while the last two (K and ε_0) affect the depolarization-polarization cycle. We assume that these parameters are uncertain, and that they have a uniform distribution in the ranges of values reported in Table 4.1. For the values of the parameters we have considered [AP96, FSSQ+15, LGT03].

Parameter	Mean	Range
σ_v	3	$[1,5]$
σ_e	3	$[1,5]$
σ_t	0.3	$[0.05,0.55]$
K	8	$[6,10]$
ε_0	0.021	$[0.001,0.041]$

Table 4.1 – Heart-torso parameters and their range.

Once a value of the parameter vector is selected, simplified ECG leads can be computed by solving the forward problem using the finite element method on a mesh formed by 6662 vertices and 12880 elements. Each forward evaluation entails on average more than 52 seconds[1].

On varying the vector of parameter $\boldsymbol{\mu} = [\sigma_v, \sigma_i, \sigma_e, K, \varepsilon_0]$, we get the different curves in Figure 4.3, which show a remarkable variability in both their phase and amplitude.

[1] All the computations of this chapter have been performed on a laptop with 2.4 GHz Intel core i7 processor and 8Gb RAM 1600MHz DDR3.

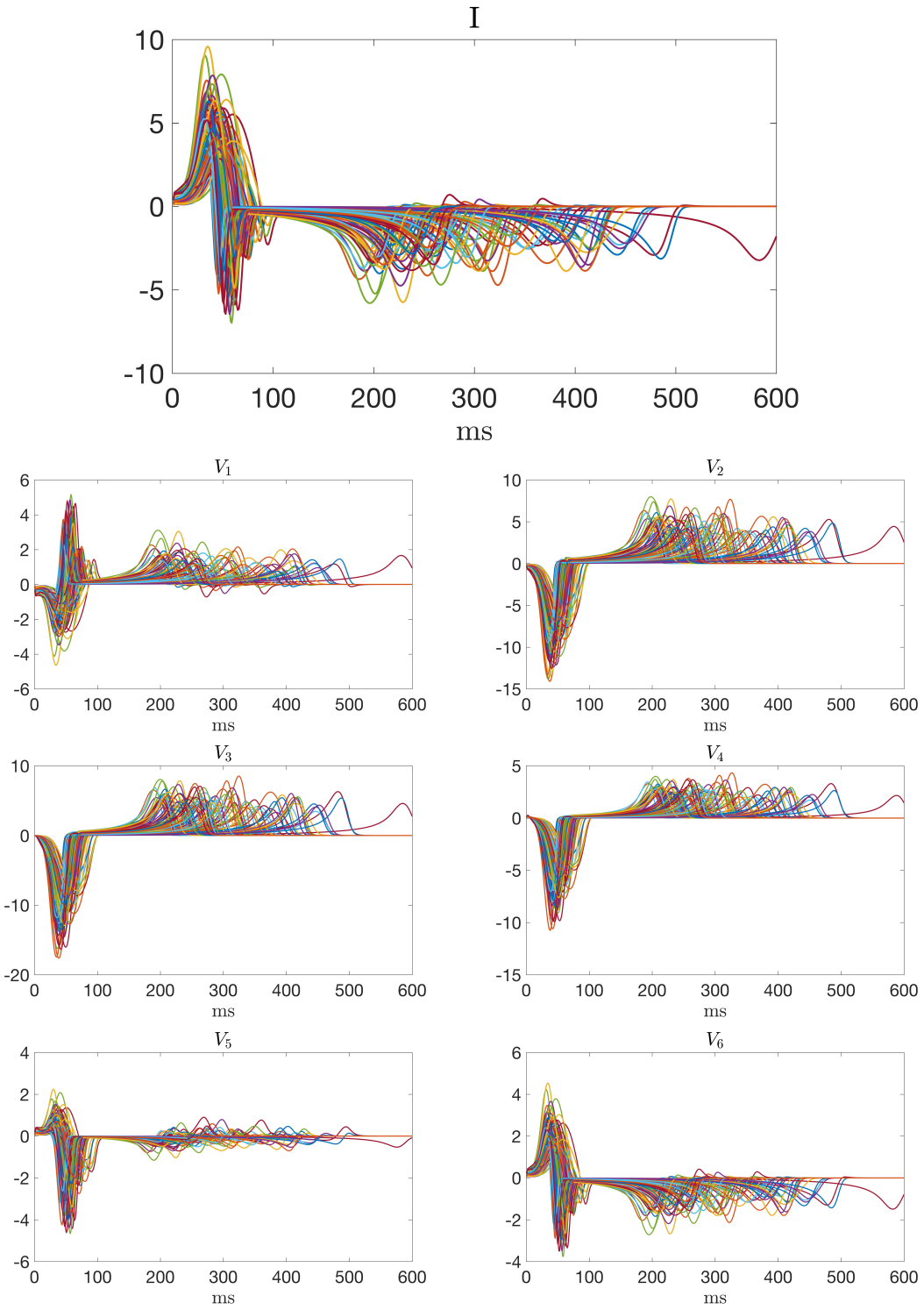

Figure 4.3 – 100 randomly simulated simplified ECGs using a full-order approximation of the uncoupled heart-torso model

By fixing the vector of parameter to $\boldsymbol{\mu} = [4.29, 3.77, 0.21, 9.8, 0.0024]$, we obtain the numerical approximation of the electric potentials $u(t)$, $u_e(t)$ and $u_T(t)$ at different time-steps illustrated in Figure 4.4.

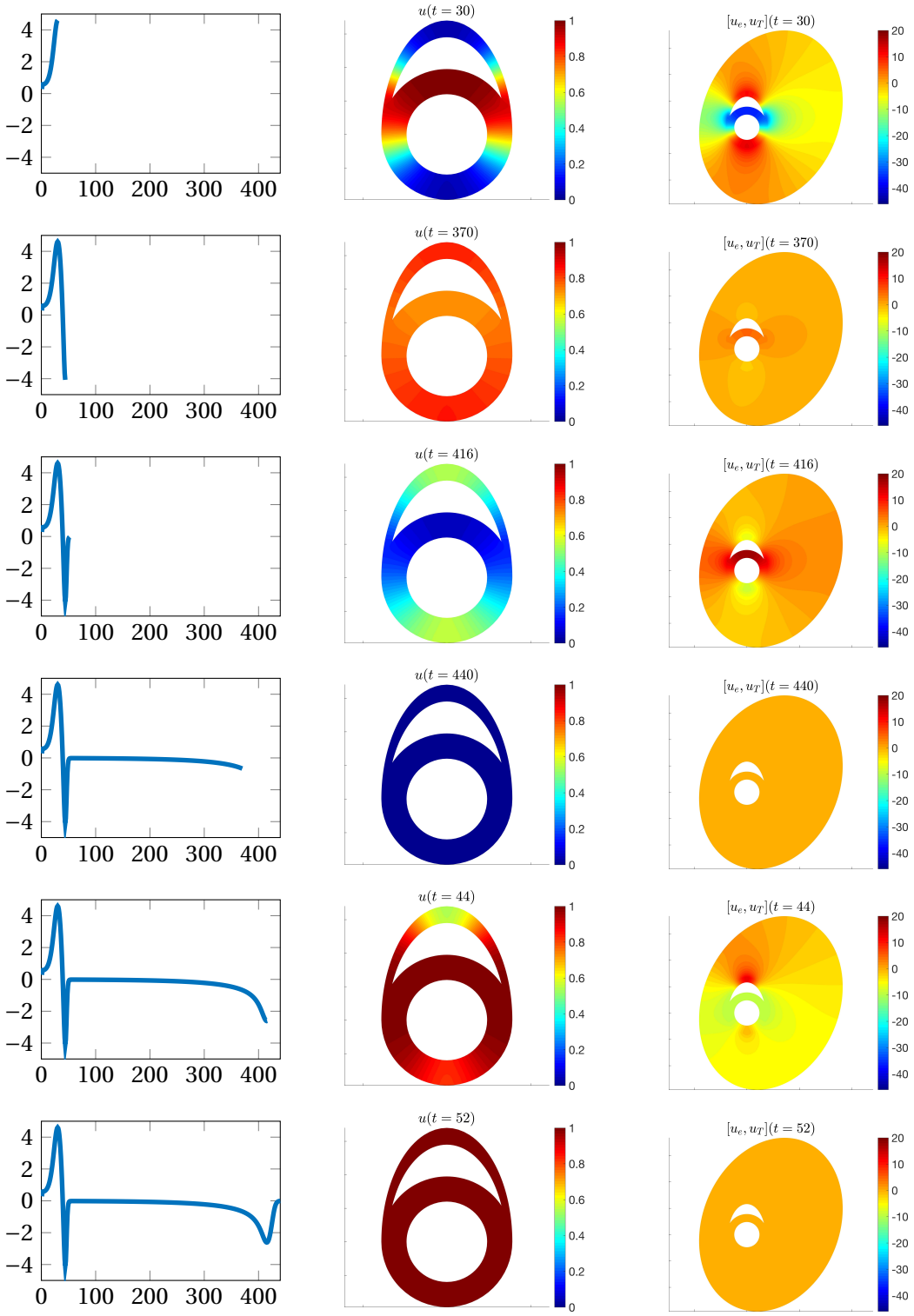

Figure 4.4 – Numerical approximation of heart-torso model at different time steps. From the left to the right: the simplified ECG $I(t)$, the solution $u(t)$ of (4.8) and the solutions $u_e(t)$ of (4.9) and $u_T(t)$ of (4.10), respectively.

The curves show similar patterns corresponding to simplified QRS complex and T wave. The considered model does not take into account the atria, which generate the so-called p-wave of the ECG signal. We have considered this two-dimensional simplified model in order to test the reduction-framework, however the proposed approach can be applied also to more detailed models.

In order to study in details the QRS complex and the T wave, we consider four landmarks $\mathbf{y} = [QRS_{peak}, T_{peak}, t_{QR}, t_{RT}]$, reported in Table 4.2. This four scalar outputs provide an almost complete description of the phenomenon and allow us to study in details how the parameters affect the shape of a simplified ECG signal.

Landmarks	u.m.	physical meaning
QRS_{peak}	mV	QRS maximum amplitude
T_{peak}	mV	T-wave maximum amplitude
t_{QR}	ms	time between stimulation pulse and upstroke
t_{RT}	ms	action potential time from upstroke to resting potential

Table 4.2 – Scalar outputs of interest

4.5.1 Sensitivity analysis

We first perform the varianced-based GSA using both a surrogate model and a projection-based ROM for the efficient evaluation of the map between the vector of parameters $\boldsymbol{\mu}$ and the vector of outputs $\mathbf{y}(\boldsymbol{\mu})$. In particular for both approaches we represent the main effects plots and we compute the sensitivity indices defined in (4.1) and (4.3).

Sensitivity analysis with surrogate model

We build separate kriging SMs for each component of the output vector $\mathbf{y}$ starting from the outputs generated from $N_{train} = 25$ parameter vectors randomly selected. The accuracy is then assessed using a further set of $N_{oob} = 25$ model runs (to which we refer as out-of-bag points), where for each set of inputs the SM outputs are compared with the full-order ones. We recall that the kriging prediction gives also an estimate of the approximation error variance, which can be used to construct confidence intervals. The comparison of the calibration outputs (see Figure 4.5) clearly shows that the confidence in the prediction is rather low for each one of the scalar outputs, especially for t_{QR} and t_{RT}, where also a considerable bias is present for large times. As a consequence, we can expect accurate results from the sensitivity analysis and forward propagation only for the outputs QRS_{peak} and T_{peak}.

We fix the training set to $N_{train} = 25$ in order to compare the SM with the ROM equipped with the ROMES starting from the same amount of information used for the model construction, in order to highlight the additional accuracy provided by a physic-based model with respect to a data-fit model.

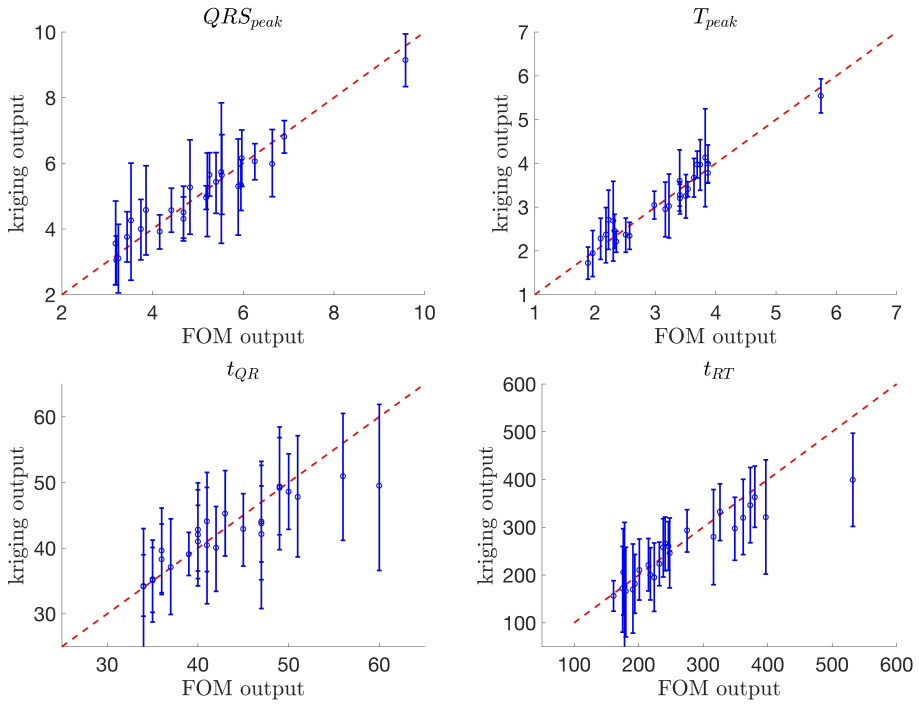

Figure 4.5 – Cross-validation of the kriging prediction with $N_{train} = N_{oob} = 25$. Due to the small number of training parameters the confidence intervals associated to the predictions are very conservative.

The computational costs related to the evaluation of the output using the kriging SM are negligible: for each new vector of parameters $\boldsymbol{\mu} \in \mathscr{P}$ the computation of $\mathbf{y}_s(\boldsymbol{\mu})$ required the solution of four linear systems of dimensions 25×25. This operation is performed on average in 0.0086 seconds, with a consequent speedup of $6104x$ with respect to the FOM.

The main effects plots (see Figure 4.6) show that each output is strongly related to few parameters: the maximum variation of QRS_{peak} and T_{peak} seem to be mostly influenced by σ_e, whereas t_{RT} is strongly related to ε_0, which is the only parameter affecting the recovery equation, and t_{QR} by K. The conductivity σ_v also influences t_{QR}, which is expected since σ_v is related to the velocity of the potential activation front. These plots quantify the effect of each parameter on the output, thus providing a quantitative insight into the physiology and the model behavior.

By looking at the confidence intervals of the main effects plots (Figure 4.7), a lot of variability not explained by the SM: indeed, only the curve relative to σ_e for the QRS_{peak} and K for t_{QR} show a clear trend. On the other hand, all the other curves present considerably large confidence intervals overlapped to the other ones. In conclusion, the main effects plots are not informative on the other parameters in this case.

The first-order sensitivity indices, reported in Table 4.3, and the total effect indices, reported in Table 4.4, confirm that QRS_{peak} and T_{peak} are sensible with respect to variations of the conductivities (especially σ_e), whereas t_{RT} is influenced by ε_0 and t_{QR} equally by σ_v and K.

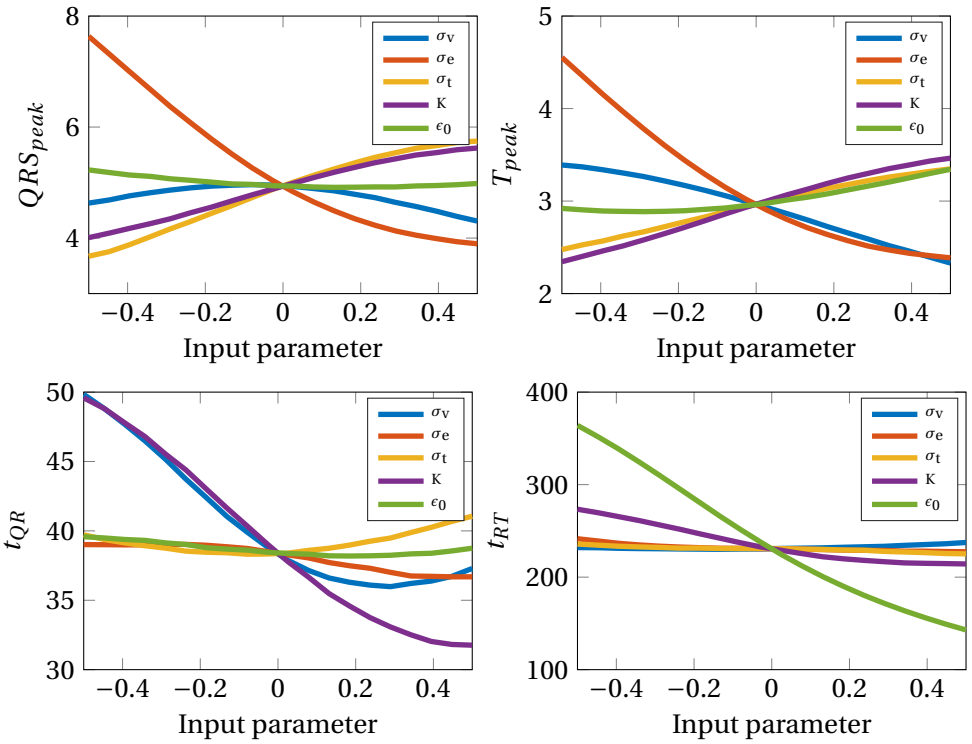

Figure 4.6 – Main effects plots obtained using the kriging-based surrogate model. The curve $\mathbb{E}[QRS_{peak}|\sigma_e]$ and $\mathbb{E}[T_{peak}|\sigma_e]$ are the ones with the highest variations. On the other hand, K and ε_0 most influence the time-related outputs, as expected from the physics of the problem.

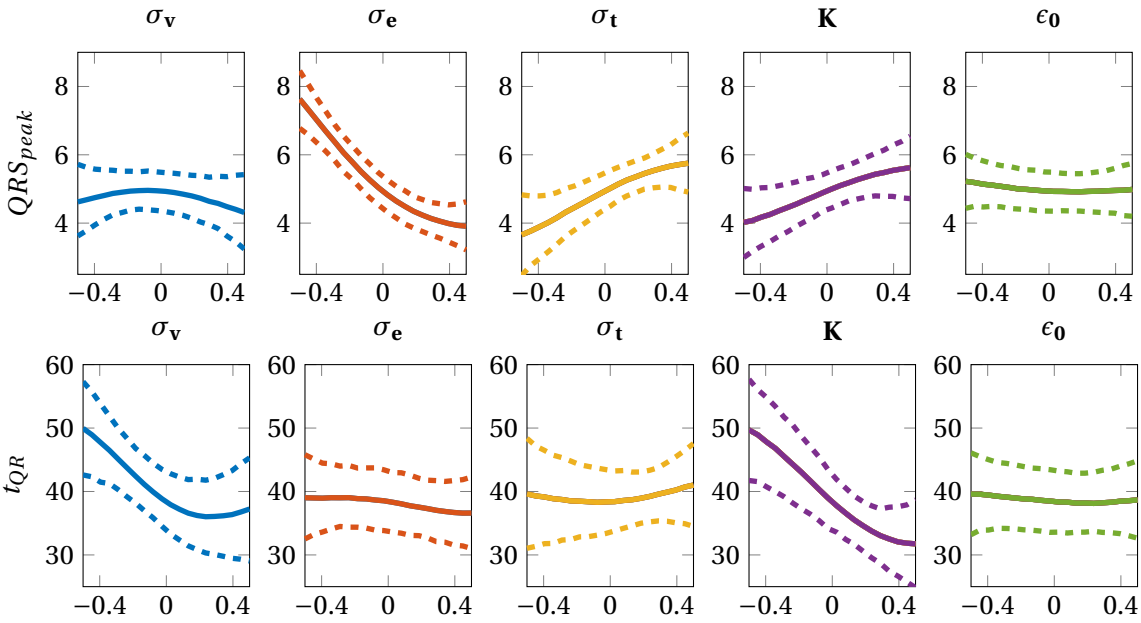

Figure 4.7 – Main effects plots with confidence intervals. The intervals are very conservative in all cases: only the changes of QRS_{peak} when σ_e is fixed are considerable with respect to the width of the confidence band.

Since the output bias shown in Figure 4.5 is non negligible the values of the first-order indices (4.1) and the total-effet indices (4.3) lack of accuracy. In the following we will see how a projection-based ROM will provide more accurate responses when evaluating the outputs compared to this SM.

Output	σ_v	σ_e	σ_t	K	ε_0
QRS_{peak}	0.0248	0.6783	0.1330	0.0978	0.0183
T_{peak}	0.0512	0.7213	0.1242	0.1955	0.0732
t_{QR}	0.4327	0.0044	0.0032	0.4623	0.0018
t_{RT}	0.0314	0.0080	0.0286	0.0384	0.8940

Table 4.3 – First-order indices using the kriging-based surrogate model. The values reflect the trend shown in the main effects plots of Figure 4.7.

Output	σ_v	σ_e	σ_t	K	ε_0
QRS_{peak}	0.1531	0.8637	0.3127	0.0018	0.1584
T_{peak}	0.1698	0.8567	0.2452	0.0084	0.1927
t_{QR}	0.4808	0.0263	0.0502	0.5110	0.0378
t_{RT}	0.0021	0.0032	0.0099	0.0898	0.9590

Table 4.4 – Total effect indices using the kriging-based surrogate model. We can conclude that the physical coefficient K is non-influential for the peak outputs, while all the conductivities do not influence the output t_{RT}. However a complete ECG signal requires all the five parameters to be characterized in a more detailed way.

Sensitivity analysis with projection-based ROM

We build a reduced basis approximation for the problem (4.8)-(4.9)-(4.10) starting from $N_{train} = 10$ parameters randomly selected in the parameter space. The basis functions are computed through the proper orthogonal decomposition (POD) on snapshots matrices formed by $600 \cdot N_{train}$ full-order vectors. The POD approach selects respectively $n = 13$ basis functions for the solution $u(t;\boldsymbol{\mu})$, $n = 10$ basis functions for the solution $u_e(t;\boldsymbol{\mu})$ and also for the solution $u_T(t;\boldsymbol{\mu})$, whereas $m_D = 26$ basis functions are required for the construction of the DEIM approximation of the non-linear term I_{ion}. This low number of basis function is justified by the fact that the only the velocity (and not the direction) of the front propagation is affected by changes in the parameters under consideration.

For each new vector of parameters the evaluation of $\mathbf{y} = [QRS_{peak}, T_{peak}, t_{QR}, t_{RT}]$ requires on average 0.64 seconds, with a consequent speedup of $82x$ with respect to the full-order model. The ROM accuracy can be inferred by considering a further set of $N_{oob} = 25$ model runs, as done previously for the SM (see Figure 4.8). Finally, we have equipped our ROM with a kriging-based ROMES built on the training set formed by the $N_{train} = 10$ parameter vectors used for the basis computation and 15 random parameter vector, in order to minimize the output reduction error. As previously pointed out the ROM and ROMES are constructed from the same number of snapshots used for the SM construction in order to compare the two methodologies.

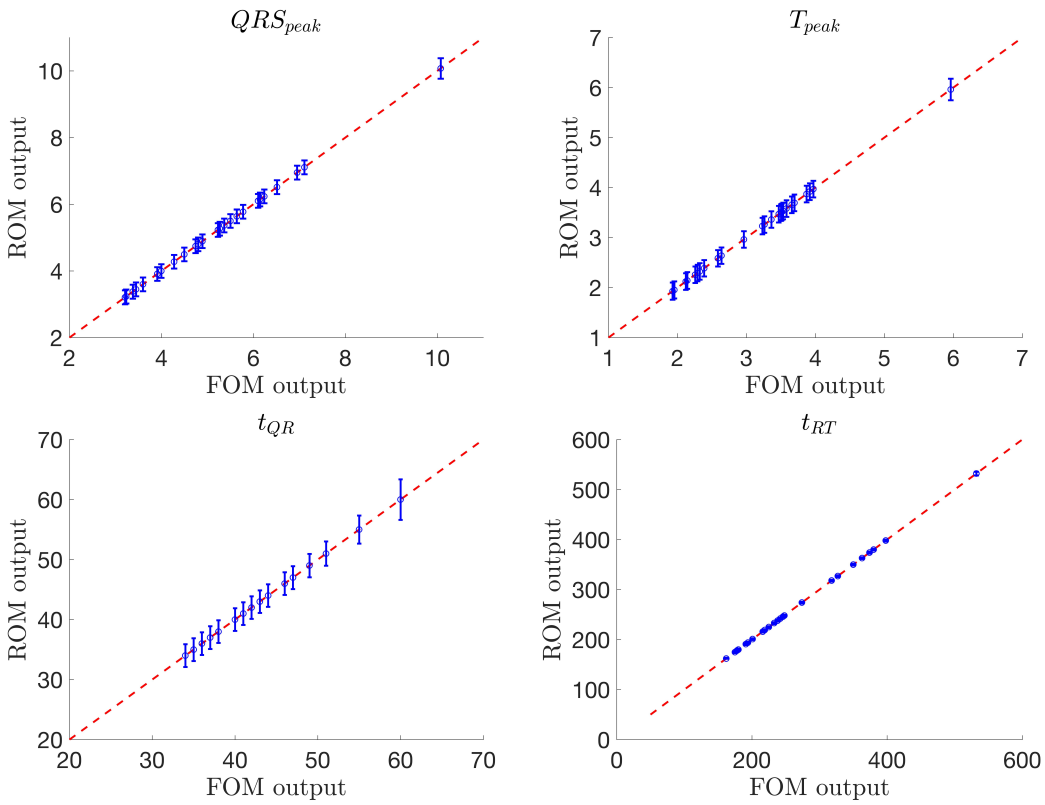

Figure 4.8 – Cross-validation of the ROM prediction with $N_{train} = 10$ and $N_{cal} = 25$. Even with a poor sampling of the parameter space the ROM is able to reproduce the landmarks much more accurately than the kriging model.

The main effects plots (see Figure 4.9) are generally in accordance with the results obtained with the SM. The main differences are relative to the results regarding t_{QR} and t_{RT}, due to the bias of the SM prediction for large values of the outputs (see Figure 4.5). The outputs linked to the QRS complex are clearly influenced by the conductivities σ_v and σ_e, whereas ε_0 affects only t_{RT}.

The reliability of the results obtained with the ROM is clear also by looking at the confidence intervals of the main effects plots (Figure 4.10), which are considerably narrower with respect to the SM case. In fact, the trend of the 5 curves relative to the QRS_{peak} is rather clear.

The evaluation of the first-order and the total effect indices (Table 4.5 and 4.6) provides a parameter ranking or selection: for example, if we are interested only in approximating the QRS complex, we can discard ε_0 (i.e. by fixing its value) and σ_t, whereas, if we are interested only in approximating the T wave, we can discard σ_t and K.

In the following subsection, we will show how to take advantage of this analysis to improve the construction of surrogate or reduced-order models.

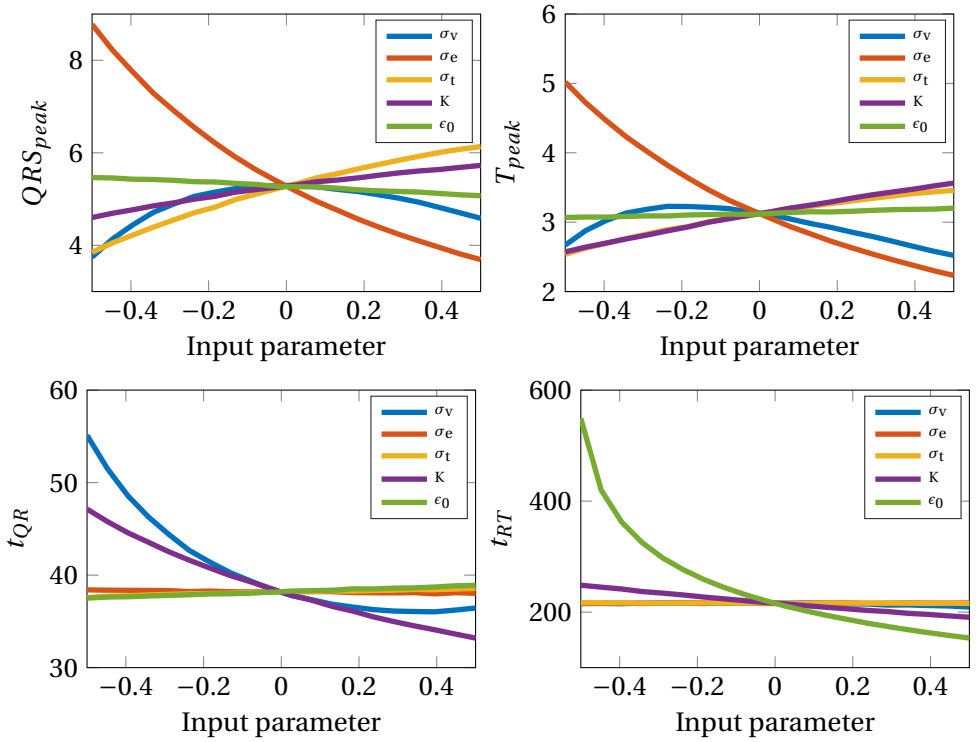

Figure 4.9 – Main effects plots obtained using the RB model. With respect to the results in Figure 4.6, we highlight that the main differences are concentrated when high values of the outputs are investigated.

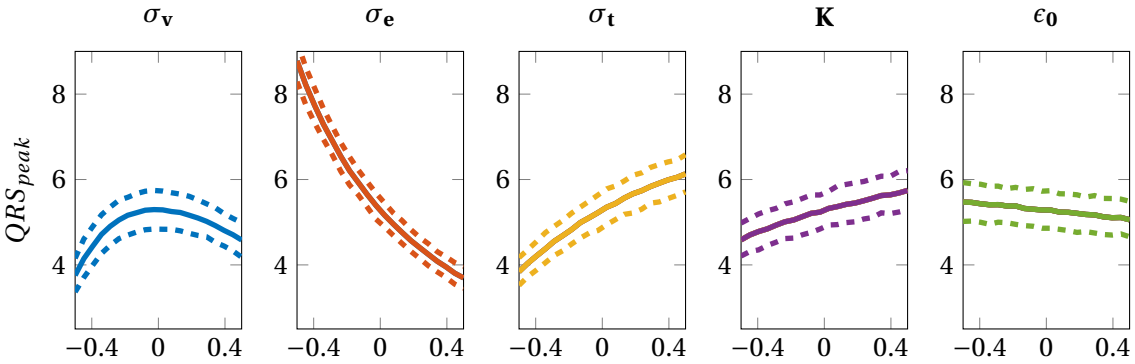

Figure 4.10 – Confidence intervals of the main effects plots for QRS_{peak} computed using the ROM for the input-output evaluation. The width of the confidence intervals is considerably smaller with respect to the variation of the curve: in this way, we are able to distinguish influential (σ_e, σ_v, σ_t and K) and non influential parameters (ε_0).

Output	σ_v	σ_e	σ_t	K	ε_0
QRS_{peak}	0.0413	0.6844	0.1618	0.0445	0.0056
T_{peak}	0.0724	0.6738	0.0878	0.0868	0.0033
t_{QR}	0.5296	0.0184	0.0193	0.4601	0.0329
t_{RT}	0.0117	0.0125	0.0125	0.0362	0.9331

Table 4.5 – Reduced-order first-order indices

Output	σ_v	σ_e	σ_t	K	ε_0
QRS_{peak}	0.0834	0.7308	0.1792	0.0623	0.0094
T_{peak}	0.1169	0.7275	0.0908	0.1236	0.0183
t_{QR}	0.5813	0.0440	0.0480	0.4688	0.0123
t_{RT}	0.0001	0.0008	0.0008	0.0646	0.9633

Table 4.6 – Reduced-order total effect indices. There are clearly non-influential parameters for some outputs of interest, such as the conductivities for t_{RT} and ε_0 for all the other outputs. However, a complete characterization of the ECG signal requires all the five parameters.

GSA post-processing

The previous results can be used for the sake of SM and ROM construction: the total effect indices could help in determining how to correctly explore the input parameters space to better capture the desired features.

Regarding the surrogate model based on kriging, it is possible to incorporate in the prediction the influence on the output of direction dependency by relaxing the assumption of isotropic random field, that is: the variance

$$\mathrm{Var}(Y(\boldsymbol{\mu}_\alpha) - Y(\boldsymbol{\mu}_\beta)) = \gamma(\delta), \qquad \boldsymbol{\mu}_\alpha, \boldsymbol{\mu}_\beta \in \mathscr{P},$$

depends only on the lag $\delta = \|\boldsymbol{\mu}_\alpha - \boldsymbol{\mu}_\beta\|$. The sensitivity analysis has instead highlighted that there are parameters more influential than others. In order to take into account the different influence of the parameters, we can modify with an affine transformation the lag δ, e.g. by properly weighting the different component of the parameter vector:

$$\delta_\omega = \|\boldsymbol{\mu}_1 - \boldsymbol{\mu}_2\|_w = \left(\sum_{j=1}^{d} \omega_j |(\boldsymbol{\mu}_1)_j - (\boldsymbol{\mu}_2)_j|^2 \right)^2.$$

The anisotropic version of the ordinary kriging is then reformulated by assuming that

$$\mathrm{Var}(Y(\boldsymbol{\mu}_\alpha) - Y(\boldsymbol{\mu}_\beta)) = \gamma(\delta_\omega), \qquad \boldsymbol{\mu}_\alpha, \boldsymbol{\mu}_\beta \in \mathscr{P}.$$

The construction of the kriging SM does not change with respect to the one proposed in Section 3.2.2. The only modification is thus given by the different metric used for the evaluation of the semi-variogram. In particular, we propose to use as weights $\{\omega_j\}_{j=1}^d$ the values of the total effect indices $S_{T,i}$, $i = 1, \dots, d$ computed previously. Influential parameters will

correspond to large wights, while non-influential parameters to small weights. The numerical results of Figure 4.11 show that the anisotropic version of the kriging based on the lag δ_ω is more accurate and shows smaller prediction intervals with respect to the isotropic model.

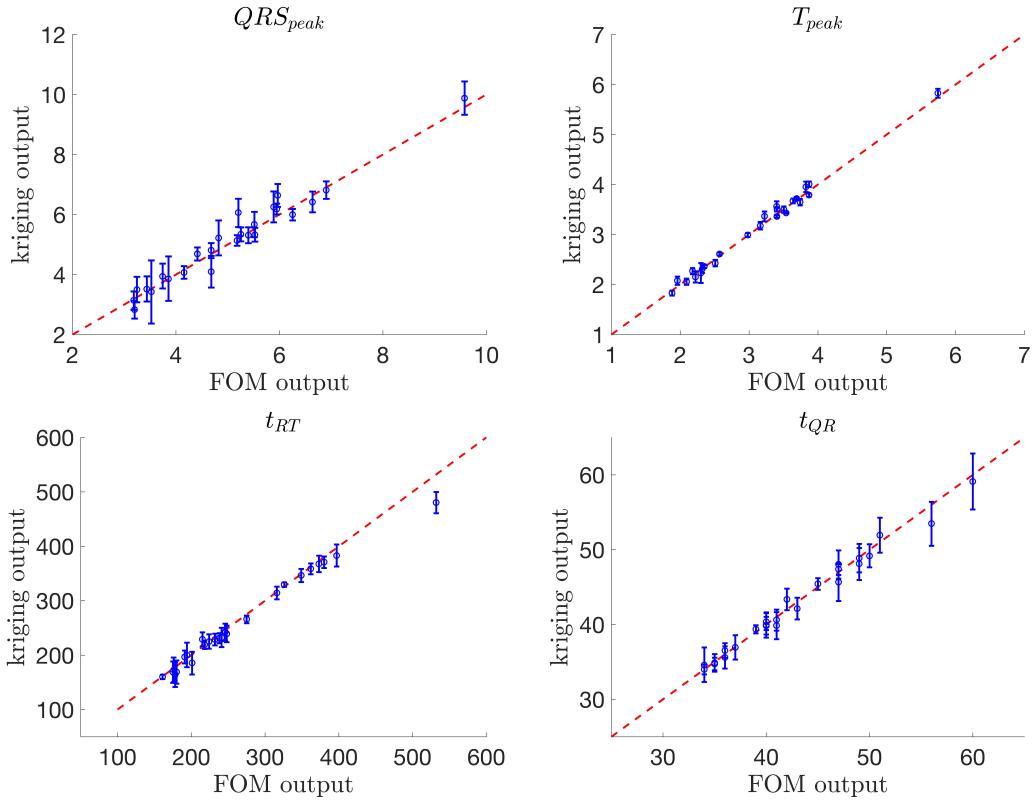

Figure 4.11 – Cross-validation of the modified anisotropic kriging prediction with $N_{train} = 25$. The bias of the model is clearly reduced (i.e. the points are aligned with the bisector line), as well as the width of the confidence intervals.

Regarding the ROM, the information about the parameters influence can be used to better explore the parameter space during the offline phase. We recall that the basis construction can be performed by the POD technique on a snapshots matrix, whose columns are full-order solutions computed for each time-step and for each $\boldsymbol{\mu} \in P_{train}$. Instead of trying to explore randomly the whole space, we can focus on the subspace of parameters yielding a total effect index not close to zero. Here, we take advantage of a sparse grid of 12 elements designed in the two dimensional subspace spanned by the two most influential parameters, and we compare the accuracy in the output obtained with respect to other ROMs trained on different samples $P_{train} \subset \mathscr{P}$.
In particular, we have computed the maximum and the mean of the output errors given on an additional set of parameters (the so-called out-of-bag set). The boxplots in Figure 4.12 represent these two output reduction errors. We have marked with a green circle the error committed by the GSA-driven ROM: in all the cases the error is placed in the lower part of the boxplot, which means that it is smaller than the majority of the errors obtained using ROMs built on different P_{train}. This means that the proposed procedure enables to minimize the

error on the output of interest in the case at hand and to reduce the computational cost of the offline phase, since we are exploring a two-dimensional parameters space instead of the five-dimensional $\mathscr{P}$. Also the design of localized ROMs could take advantage of the results given by the GSA analysis, since the exploration of the parameter space becomes easier.

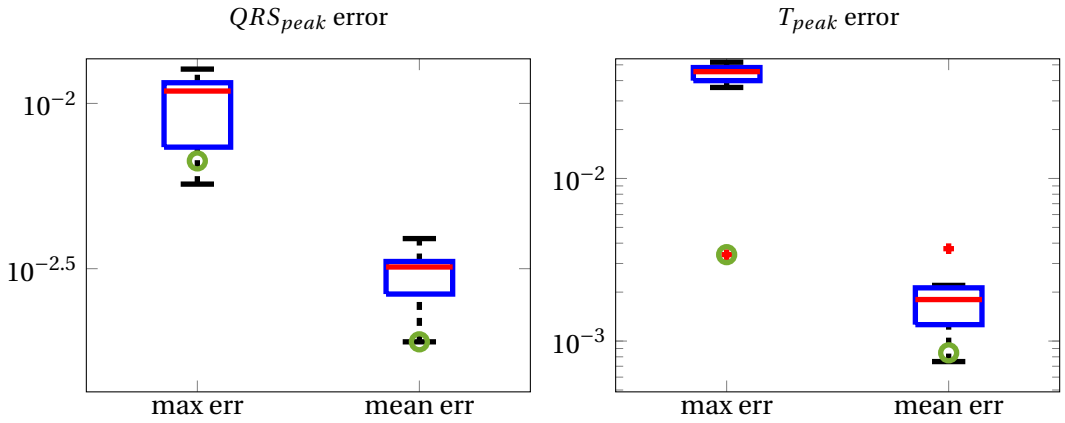

Figure 4.12 – Boxplots of the maximum and mean output error obtained with ROMs built on different training samples P_{train}. The green circles correspond to the GSA-driven ROM errors, which are lower than the ones given by the other tested ROMs.

4.5.2 Uncertainty propagation

We now turn to *uncertainty propagation* on the outputs of interest consisting in four landmarks $\mathbf{y} = [QRS_{peak}, T_{peak}, t_{QR}, t_{RT}]$. We use Monte Carlo sampling based on 5000 evaluations of the SM and the reduced basis ROM equipped with the ROMES. For all the outputs we have firstly considered a uniform distribution with mean 0.5 and a variance 0.04 in normalized units (purple line), then we have progressively augmented the variance for the parameter with the largest total effect index, which is σ_e for QRS_{peak} and T_{peak}, K for t_{QR} and ε_0 for t_{RT}.
We observe that reducing the variance on the input parameters consequently leads to a reduction of the variance on the outputs: this trend can be well highlighted in the case of the reduced-order outputs. Moreover, the propagation of the SM prediction error leads to output distributions with bigger variances with respect to the ROM case. The surrogate model provides a highly efficient way to perform uncertainty propagation, but it generates substantial prediction errors. With respect to the analysis provided in Section 4.4.1, we can conclude that the ROM equipped with ROMES provides more accurate results, without introducing additional source of errors.

4.6 Conclusions

Uncertainty quantification improves our understanding on the role and importance of parameters of the PDE models at hand and estimates the effect of the parameters uncertainties propagation to model outputs. Numerical results show that *sensitivity analysis* and *uncertainty propagation* are crucial to develop a minimal and reliable parametrized model for electrophysiology. In particular, in our test case we have shown that all the parameters included in the

idealized 2D heart-torso model are relevant: some of them are crucial for the approximation of the QRS complex, while others determine the profile of the T wave. This means that if we are interested only in well reproducing just one of this features some parameters could be discarded in order to simplify the model.

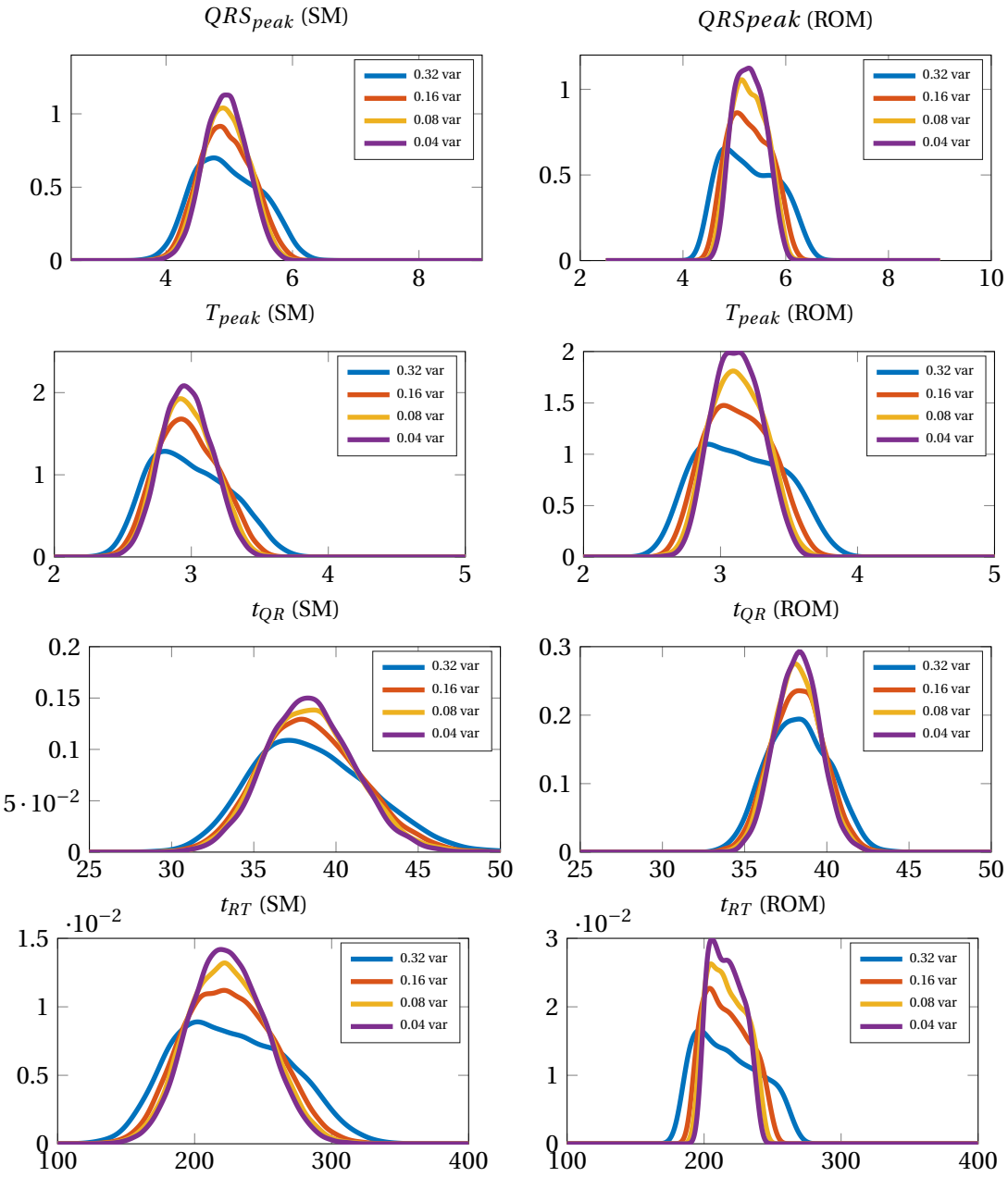

Figure 4.13 – Forward UQ for the four different outputs on varying the variance of most influential parameter (σ_e for QRS_{peak} and T_{peak}, K for t_{QR} and ε_0 for t_{RT}) using SM (left) and ROM (right). The approximation error clearly affects the results obtained with the SM: the resulting variances are much larger than the ones obtained with the ROM.

5 | Bayesian inverse problems

In this Chapter we propose a combined ROM-ROMES strategy for the efficient solution of Bayesian inverse problems in cardiac electrophysiology when real-valued outputs are considered. In particular, we first review in Section 5.1 the basic techniques for the solution of parameter estimation problems in the Bayesian framework. In Section 5.2 we provide a general formulation of the class of problems we are interested in, and in Sect. 5.3 we show how to incorporate the proposed ROM-ROMES strategy into the Bayesian estimator. In Sect. 5.4 we prove some theoretical results related to the consistency of the procedure and the effectivity of the corrections made by the ROMESs. We finally assess the performance of the proposed framework on a numerical example of Bayesian inverse problems governed by parametrized nonlinear unsteady PDEs characterizing 2D heart-torso electrophysiology[1].

5.1 Inverse problems

In the previous Chapters of the Thesis we have presented some numerical techniques for the approximation of the electric potential and of some outputs of interest given a parameters vector $\boldsymbol{\mu} \in \mathscr{P}$, characterizing the inputs of the model (i.e. the geometry, the physical coefficients, the boundary and the initial conditions). In particular, we have focused on the following input-output mapping:

$$\boldsymbol{\mu} \rightarrow \mathbf{u}_h(t;\boldsymbol{\mu}) \rightarrow \mathbf{y}_h(\boldsymbol{\mu}), \tag{5.1}$$

$\mathbf{u}_h(t;\boldsymbol{\mu})$ being the full-order numerical approximation of the electric potential, e.g. the solution of the parametrized monodomain equation (1.4). The real-valued output vector $\mathbf{y}_h(\boldsymbol{\mu})$

[1] The methodology developed in this Chapter is partially based on the published work [MPL16] with A. Manzoni and T. Lassila.

approximates the available clinical measurements, such as ECG landmarks or activation times measured on the endocardium.
In Chapter 2 we have introduced the full-order schemes usually adopted for the numerical approximation of this problem and we have proposed a suitable localized RB framework for an efficient computation of the electric potential. Moreover, in Chapter 3 we have considered suitable statistical ROM error surrogates for the sake of output calibration. Finally in 4, we have performed uncertainty quantification in order to better understand how uncertainties in the model parameters affect the outputs of the numerical simulations. All these problems have required the (partial) knowledge of the input parameters, in order to reproduce the process of interest.

However, the knowledge of input parameters is considerably limited when dealing with cardiac electrophysiology problems, due to the intrinsic difficulty in performing *in vivo* and *in vitro* experiments for their estimation [FNC+11] and because of the multiple sources of error which pollute the measurements of the electric potential. Moreover, the parameters exhibit a spatial heterogeneity in the different regions of the heart [LGA93]. As pointed out in [CBC+11] in the literature there are not clearly defined values for the physical parameters characterizing the electrophysiology models, in particular for the conductivity values, whose importance has been highlighted by the sensitivity analysis performed in Chapter 4. We have shown how homogeneous conductivities greatly affect the shape of an approximated ECG signal and also of the action-potential. A comparison among some values for the conductivities of the bidomain equations reported in the literature can be found e.g. in [SHM05]. The common approach exploited so far is to empirically determine the values of the conductivities by ensuring that the adopted model is able to reproduce some indicators, such as the conductivity velocity (i.e. speed at which an electrochemical impulse propagates in the tissue).

The estimation of the other physical parameters, such as the ones characterizing the Aliev-Panfilov model (e.g. K and ε_0 in (1.2)) or the Mitchell-Schaffer model, is even more complex. In this case, only a tuning with respect to standard action-potential duration (defined as the time during which the potential is larger than its resting values) is usually performed [MS03, AP96, OVV+11]. Furthermore, in this setting, the information coming from sensitivity analysis are necessary to determine how much the parameters selection could affect the results. Non-influential parameters could be fixed to one value in their physiological range, if the sensitivity indices have shown that they do not affect the output of interest.
As pointed out in Chapter 1, there are several possible measurements of the electrical activity of the heart (invasive and noninvasive). Developing efficient and accurate mathematical techniques for the estimation of the model parameters starting from these available noisy measures is crucial for a personalization of the mathematical models. Indeed, the solution of these parameter estimation problems shall also bring, hopefully, to the construction of subject-specific *in silico* models, which could be used to provide additional information on the subject and test the efficiency of some clinical intervention (e.g. ablation [Jac16]).

5.1.1 Problem formulation

Since all the available data are affected by noise, the first step towards the formulation of the Bayesian inverse problems is the construction of a noise model. A popular model is the additive Gaussian noise model, which mimics the effect of many sources of error that occur

in nature. In this framework, the mathematical formulation of a real-valued measurement vector $\mathbf{y} \in \mathbb{R}^{N_y}$ is given by

$$\mathbf{y} = \mathbf{y}_h(\boldsymbol{\mu}) + \boldsymbol{\varepsilon}_{\text{noise}} \qquad \boldsymbol{\varepsilon}_{\text{noise}} \sim \mathcal{N}(\mathbf{0}, \boldsymbol{\Gamma}), \tag{5.2}$$

where $\mathbf{y}_h(\boldsymbol{\mu})$ is the full-order output vector given by (5.1) and $\boldsymbol{\varepsilon}_{\text{noise}}$ is a normally distributed random variable added to the output evaluation. We can associate a Gaussian probability density function $\pi_\varepsilon : Y \to \mathbb{R}_0^+$ to $\boldsymbol{\varepsilon}_{\text{noise}}$. Other additive noise models can be constructed by assuming a different distribution of the random variable $\boldsymbol{\varepsilon}_{\text{noise}}$ (see e.g. [KS06]).

Some *a priori* information on the model parameters could be available, such as the literature values of the coefficients $\boldsymbol{\mu}_{prior}$ and their variability quantified, for instance, through their variance $\mathbf{C}_{prior}$. This additional information about the true underlying structure of the parameters will be crucial to provide more meaningful estimates and for the regularization of the inverse problem.

Given a noisy realization $\mathbf{y}^*$ of the additive noise model (5.2), we are interested in estimating the parameter vectors $\boldsymbol{\mu}^* \in \mathscr{P}$ whose output vector best fits the data in a convenient metric. For the solution of this problem we can adopt two different approaches:

1. solving a *PDE-constrained optimization problem*, which provides an approximation $\hat{\boldsymbol{\mu}}$ of the unknown parameter $\boldsymbol{\mu}^*$ by minimizing a suitable least squares functional, such as

$$\hat{\boldsymbol{\mu}}_{ls} = \arg\min_{\boldsymbol{\mu}\in\mathscr{P}} J(\boldsymbol{\mu}) = \arg\min_{\boldsymbol{\mu}\in\mathscr{P}} \left(\frac{1}{2} \|\mathbf{y}^* - \mathbf{y}_h(\boldsymbol{\mu})\|_{\boldsymbol{\Gamma}}^2 + \frac{1}{2} \|\boldsymbol{\mu} - \boldsymbol{\mu}_{prior}\|_{\mathbf{C}_{prior}}^2 \right),$$

   through an iterative strategy, acting on the parameters vector $\boldsymbol{\mu}$ so that the numerical output $\mathbf{y}_h(\boldsymbol{\mu})$, computed through the numerical approximation of the parametrized PDE, could match the prescribed target $\mathbf{y}^*$. Here, the chosen norms are obtained using as weighting matrices the noise model and the *a priori* covariances. In particular, the gap between the $\mathbf{y}_h(\boldsymbol{\mu})$ and $\mathbf{y}^*$ is weighted by the variability of the noise

$$\|\mathbf{y}^* - \mathbf{y}_h(\boldsymbol{\mu})\|_{\boldsymbol{\Gamma}}^2 = (\mathbf{y}^* - \mathbf{y}_h(\boldsymbol{\mu}))^T \boldsymbol{\Gamma}^{-1} (\mathbf{y}^* - \mathbf{y}_h(\boldsymbol{\mu})),$$

   while the gap between $\boldsymbol{\mu}$ and the *a priori* mean by

$$\|\boldsymbol{\mu} - \boldsymbol{\mu}_{prior}\|_{\mathbf{C}_{prior}}^2 = (\boldsymbol{\mu} - \boldsymbol{\mu}_{prior})^T \mathbf{C}_{prior}^{-1} (\boldsymbol{\mu} - \boldsymbol{\mu}_{prior}),$$

   in order to obtain more informative problem-specific norms;

2. solving a *statistical inverse problem*, which provides a probability distribution $\pi_{post} : \mathscr{P} \times Y \to \mathbb{R}_0^+$, i.e. the probability density function (pdf) of the parameter $\boldsymbol{\mu}$ given the measured value of $\mathbf{y}^*$. By assuming that the *a priori* information is normally distributed with mean $\boldsymbol{\mu}_{prior}$ and covariance matrix $\mathbf{C}_{prior}$, the solution of the statistical inverse problem is given by:

$$\pi_{post}(\boldsymbol{\mu} \,|\, \mathbf{y}^*) \propto \exp\left(-\frac{1}{2} \|\mathbf{y}^* - \mathbf{y}_h(\boldsymbol{\mu})\|_{\boldsymbol{\Gamma}}^2 - \frac{1}{2} \|\boldsymbol{\mu} - \boldsymbol{\mu}_{prior}\|_{\mathbf{C}_{prior}}^2 \right), \tag{5.3}$$

   thanks to *Bayes' theorem* and the chosen Gaussian noise model. Since the input-output map $\boldsymbol{\mu} \mapsto \mathbf{y}_h(\boldsymbol{\mu})$ is nonlinear, the probability distribution of $\pi_{post}(\boldsymbol{\mu} \,|\, \mathbf{y}^*)$ cannot be written in closed form. Instead, it is necessary to sample the posterior pdf by drawing a

sequence of random samples from the (multi-dimensional) distribution given by (5.3). The standard procedures for sampling the posterior distribution belong to the Markov chain Monte Carlo [Gil05, ADFD$^+$03] techniques, which enable a problem specific exploration of the parameter space.

The first approach only provides a deterministic parameters vector $\hat{\boldsymbol{\mu}}_{ls}$, for which the corresponding output $\mathbf{y}_h(\hat{\boldsymbol{\mu}}_{ls})$ matches the measurements $\mathbf{y}^*$ in a least square sense. The second approach, instead, describes a wide range of most likely parameters vectors, whose outcome $\mathbf{y}_h(\boldsymbol{\mu})$ is as near as possible to $\mathbf{y}^*$. Given the assumptions of Gaussian noise model and Gaussian *a priori* distribution of the parameter, the solution of the *PDE-constrained optimization problem* using the weighted norms corresponds to the *maximum a posteriori* (MAP) estimate of the posterior distribution, that is

$$\hat{\boldsymbol{\mu}}_{MAP} = \arg\max_{\boldsymbol{\mu}\in\mathscr{P}} \pi_{post}(\boldsymbol{\mu}\,|\,\mathbf{y}^*) = \hat{\boldsymbol{\mu}}_{ls}.$$

Solving the statistical inverse problems provides indeed much more information with respect to solving the optimization problem: given the posterior pdf $\pi_{post}(\boldsymbol{\mu}\,|\,\mathbf{y}^*)$ we can quantify the variance of the parameters with respect to $\mathbf{y}^*$. In other words, together with point-wise estimators of the most-likely parameters, we provide a measure of the uncertainties on the parameters related to the observed data. The posterior distribution can be analyzed with the classical statistical inference tools, such as confidence (or credible) intervals or quantiles. Moreover, hypothesis testing on the parameters could be performed in order to support decision making.

5.1.2 Applications to cardiac electrophysiology

There are several works dealing with *PDE-constrained optimization problems* and *statistical inverse problems* in cardiac electrophysiology. The first problem of interest has been the identification of physical parameters related to the cardiac cells models (system of ODEs): this problem has been addressed as an optimization problem governed by ODEs, solved using, for instance, gradient-based minimization algorithm in [DL04] or using genetic algorithms in [SVN$^+$05, KMSC16]. The presence of the inter-subject variability in this personalization of the ODE model has been taken into account in [BBOVA$^+$13], by using the basic tools of sensitivity analysis (scatter and correlation plots), and in [GKX$^+$07, FN09] by adopting Markovian models. Recently, uncertainty quantification has been considered in order to provide more detailed a priori information on the parameters for statistical inverse problems in this context [PSG$^+$15, JCB$^+$16]. Even if the cost of solving a parametrized ODE for the cell is negligible with respect to the cost of solving a parametrized coupled PDE-ODE, surrogate models have been exploited in [JCB$^+$16] for an efficient evaluation of the input-output map during Markov chain Monte Carlo samplings.
Once the parameters of the ODE model have been estimated, a simulation at the tissue level requires the estimation of the parameters related to the PDE model. As shown in [CSL$^+$11], the calibration of a ventricular model can take advantage of both deterministic and statistical parameter estimation procedures, performed in sequence at different length-scales. A first optimization-based calibration for a complete electrophysiology model for both atria and ventricles using a population of pre-processed healthy ECG signals has been recently

proposed in [TSC+16]. A great attention has been also paid to the development of models for identification of pathologies such as atrial fibrillation [NK11, KSR+13] and myocardial ischemia [KRC+11, WKM+13, CAAZ+15, ÁAARÁ+12]. An optimization procedure for tuning 3-D ventricles parameters has been introduced in [PKK+14], using ECG and endocardial mapping coming from both healthy patients and patients with Left-Ventricular (LV) conduction disturbances. This methodology has been extended to a complete heart model in [SCG16].

All these procedures featuring macro-scale models have been addressed in the literature using PDE-constrained optimization procedures, which are slightly less computationally demanding than the ones related to statistical inverse problems. An exception is represented by [KRC+11], where a statistical inverse problem of estimating the conductivity field starting from depolarization times has been solved using a simplified Eikonal model for the description of the depolarization mechanism.
Optimization and statistical inverse problems can be characterized as *many-query* problems: efficient reduced-order models, such as the ones proposed in Chapter 2, have a paramount importance in improving their performance. So far, the RB method has been applied in the context of PDE-constrained optimization for the identification of four physical parameters characterizing the bidomain equation in [BSG12]. The development and the application of ROMs in this context is extremely challenging due to the complexity of the underlying phenomena as we have seen in Chapter 2. Moreover, ROM for electrophysiology could represent a breakthrough towards the solution of *statistical inverse problems* in the context of the macro-scale cardiac electrophysiology, which is out of reach at present.
By extending the RB framework presented in [MPL16] to the case of non-linear unsteady PDEs, we show in this Chapter how to take advantage of ROMES to gain a strong computational speedup in the Bayesian computational framework. Moreover, we show how the combination of ROM and ROMES leads to posterior distributions which are unbiased and more reliable than those provided by the ROM alone.

5.2 Bayesian inverse problems governed by PDEs

In this section we introduce the abstract formulation the Bayesian inverse problems governed by PDEs from the mathematical standpoint. In particular, we focus on the estimation of unknown or uncertain parameters related to a PDE model starting from indirect real-valued observations of suitable quantities of interest, such depolarization times or action potential duration. In Chapter 6 we will focus instead on the case of time-dependent outputs.

5.2.1 Bayesian framework

We cast the parameter estimation problem into the Bayesian framework (see e.g. [KS06, Stu10, Tar05]). We model both the observations $\mathbf{y}^*$ and the parameters $\boldsymbol{\mu}$ as random variables, by introducing suitable probability density functions (pdfs). The solution of the inverse problem is given by the *posterior probability* density $\pi_{post} : \mathscr{P} \times Y \to \mathbb{R}_0^+$, i.e. the probability density of the parameter $\boldsymbol{\mu}$ given the measured value of $\mathbf{y}^*$, which can be obtained as

$$\pi_{post}(\boldsymbol{\mu} \,|\, \mathbf{y}^*) = \frac{\pi(\mathbf{y}^* \,|\, \boldsymbol{\mu})\, \pi_{prior}(\boldsymbol{\mu})}{\eta(\mathbf{y}^*)} \tag{5.4}$$

thanks to the *Bayes theorem*. Here $\pi_{prior} : \mathscr{P} \to \mathbb{R}_0^+$ is the *prior probability* density, expressing all available information on $\boldsymbol{\mu}$ independently of the measurements on $\mathbf{y}^*$ that will be considered as data; $\pi : Y \times \mathscr{P} \to \mathbb{R}_0^+$ is the *likelihood function* of $\mathbf{y}^*$ conditionally to $\boldsymbol{\mu}$; finally $\eta(\mathbf{y}^*)$ is a normalization constant, given by

$$\eta(\mathbf{y}^*) = \int_{\mathscr{P}} \pi(\mathbf{y}^* \mid \boldsymbol{\mu})\, \pi_{prior}(\boldsymbol{\mu}).$$

We also denote the likelihood function appearing in (5.4) by highlighting the dependence on the full-order approximation, as

$$\pi(\mathbf{y}^* | \boldsymbol{\mu}) = \pi^h(\mathbf{y}^* | \boldsymbol{\mu}) = \pi_\varepsilon(\mathbf{y}^* - \mathbf{y}_h(\boldsymbol{\mu})) \tag{5.5}$$

so that the expression (5.4) of the full-order posterior pdf can be rewritten as follows:

$$\pi^h_{post}(\boldsymbol{\mu} \,|\, \mathbf{y}^*) = \frac{\pi^h(\mathbf{y}^* | \boldsymbol{\mu})\, \pi_{prior}(\boldsymbol{\mu})}{\eta_h(\mathbf{y}^*)}, \quad \text{being} \quad \eta_h(\mathbf{y}^*) = \int_{\mathscr{P}} \pi^h(\mathbf{y}^* | \boldsymbol{\mu})\, \pi_{prior}(\boldsymbol{\mu}). \tag{5.6}$$

Indeed, the Bayes formula is nothing but the general formulation of problem (5.3). As a matter of fact, the *likelihood function*, under the assumption that the additive noise model is normally distributed with zero mean and covariance $\boldsymbol{\Gamma}$, is such that

$$\pi_\varepsilon(\mathbf{y}^* - \mathbf{y}_h(\boldsymbol{\mu})) \propto \exp\left(-\frac{1}{2}\|\mathbf{y}^* - \mathbf{y}_h(\boldsymbol{\mu})\|^2_{\boldsymbol{\Gamma}}\right).$$

If we also assume that the a priori information is normally distributed with mean $\boldsymbol{\mu}_{prior}$ and covariance matrix $\mathbf{C}_{prior}$, the prior pdf becomes

$$\pi_{prior}(\boldsymbol{\mu})\eta(\mathbf{y}^*) \propto \exp\left(-\frac{1}{2}\|\boldsymbol{\mu} - \boldsymbol{\mu}_{prior}\|^2_{\mathbf{C}_{prior}}\right).$$

Since in the PDE models presented in Chapter 1 the mapping $\boldsymbol{\mu} \mapsto \mathbf{y}(\boldsymbol{\mu})$ is nonlinear, the expression of the likelihood function yields a posterior distribution which cannot be written in closed form, requiring instead an exhaustive exploration of the parameter space. We then need to rely on MCMC techniques to sample the posterior pdf, such as the well-known Metropolis-Hastings or Gibbs sampling techniques [Gil05, ADFD$^+$03, Has70, GG84]. These methods are exploited to draw a sequence of random samples from a (multi-dimensional) pdf which cannot be expressed in closed form. This is meant in order not only to approximate the posterior pdf, but also to compute integrals related to this distribution, such as the posterior expected value and covariance.
However, some key numerical challenges arise when dealing with inverse problems governed by PDEs. These are mainly due to:

(i) *parametric dimension*: the unknown/uncertain quantity to be inferred might be as large as the state of the system in the case of distributed field, while we can rely on few (noisy) observations. This also makes the inverse problem intrinsically ill-posed;

(ii) *many query*: sampling techniques involve a huge amount of PDE approximations for the input/output evaluation;

(iii) *slow MCMC convergence*: sampling accurately the posterior might be unfeasible due to slow convergence rate with respect to the sample size.

In this Chapter we address issue (i) by relying on the sensitivity analysis performed in Chapter 4 and issue (ii) by relying on the reduced-basis method introduced in Chapter 2 for the efficient evaluation of parametrized PDE models. Regarding issue (iii) several techniques have emerged in the last decade to speed up MCMC sampling algorithms [MWB+12, NT15, Gil08]. We point out that the methodologies developed for (i) and (ii) can be extended in a straightforward way also to these modifications of the MCMC.

5.2.2 Identifiability

Determining the identifiable parameters is a key preliminary procedure to improve the estimation capability of the inversion procedure. A parameter vector $\boldsymbol{\mu}$ is said *identifiable* if there is no $\tilde{\boldsymbol{\mu}} \in \mathscr{P}$, $\tilde{\boldsymbol{\mu}} \neq \boldsymbol{\mu}$, such that $\mathbf{y}_h(\boldsymbol{\mu}) = \mathbf{y}_h(\tilde{\boldsymbol{\mu}})$, i.e. the input/output map is bijective (see e.g. the analysis provided in [HCA+15]).
In order to investigate the identifiability of the model parameters related to the heart-torso coupling or the subject-specific left ventricle, we can rely on the global sensitivity analysis performed in Chapter 4. We recall that sensitivity analysis quantifies the effects of parameters variation on the outputs of interest, providing a criterium to rank the most influential input parameters. In global sensitivity analysis this criterium is given by the values of the total-index S_{T_i} $i = 1, \dots, d$, defined in 4.3. In particular we have that the condition $S_{T_i} \approx 0$ is equivalent to the fact that μ_i is a non-influential parameter. We expect that this global property implies non-identifiability, which is a property related to the single parameter vector (and that the opposite implication does not hold).
In alternative, local sensitivity analysis enables the study of local identifiability of the parameters using the so called Fisher Information Matrix, which is indeed the local Hessian matrix of the outputs with respect to parameters variations under the assumption of Gaussian additive noise model [Rot71].

Once the MCMC sampling procedure of the posterior is performed, it is possible to derive some *a posteriori* indicators of the global identifiability. As proposed in [TSR+16], an identifiability index can be found by comparing the posterior marginal variance $\sigma^2(\mu_i \,|\, \mathbf{y}^*)$ and the prior marginal variance $\sigma^2(\mu_i)$ as follows

$$\mathscr{I}_i = 1 - \sqrt{\frac{\sigma^2(\mu_i \,|\, \mathbf{y}^*)}{\sigma^2(\mu_i)}} \qquad i = 1, \dots, d.$$

Parameter components μ_i, $i = 1, \dots, d$, presenting a smaller $\sigma^2(\mu_i \,|\, \mathbf{y}^*)$ with respect to $\sigma^2(\mu_i)$ can be considered to be well-identifiable ($\mathscr{I}_i$ is consequently close to 1). On the other hand, parameter components yielding $\sigma^2(\mu_i \,|\, \mathbf{y}^*) \approx \sigma^2(\mu_i)$, that is $\mathscr{I}_i \approx 0$ are non-identifiable. A more detailed indicator has been derived in [PL15] starting from the Shannon entropy theory [Sha01]. In particular, the gain in information about $\boldsymbol{\mu}$ when the data $\mathbf{y}^*$ is observed is given by

$$G = \int_{\mathscr{P}} \left(\pi_{prior}(\boldsymbol{\mu}) \log\left(\frac{1}{\pi_{prior}(\boldsymbol{\mu})} \right) - \pi_{post}(\boldsymbol{\mu} \,|\, \mathbf{y}^*) \log\left(\frac{1}{\pi_{post}(\boldsymbol{\mu} \,|\, \mathbf{y}^*)} \right) \right) d\boldsymbol{\mu}.$$

In this case large values of G correspond to a large gains in information with respect to the prior distribution and, as a consequence, characterize identifiable parameter components.

Finally, since non-identifiable parameters can be considered as nuisance parameters $\boldsymbol{\zeta}$, we proceed to marginalize them and concentrate only on the identifiable parameters $\boldsymbol{\gamma}$. This leads to computing the conditional marginal distribution

$$\pi^h_{post}(\boldsymbol{\gamma}\,|\,\mathbf{y}^*) = \frac{1}{\eta_h(\mathbf{y}^*)} \int_{\mathscr{P}_\zeta} \pi^h(\mathbf{y}^*|\boldsymbol{\mu})\ \pi_{prior}(\boldsymbol{\gamma},\boldsymbol{\zeta})\ d\boldsymbol{\zeta}. \tag{5.7}$$

for which $\boldsymbol{\mu} = [\boldsymbol{\gamma},\boldsymbol{\zeta}]^T$. MCMC methods are needed to evaluate (possibly) high-dimensional integrals (5.7). These methods involve repeated evaluations of the likelihood function $\pi^h(\mathbf{y}^*|\boldsymbol{\gamma},\boldsymbol{\zeta})$ – and thus repeated evaluations of the forward problem – so that relying on the FOM would be too expensive.

5.3 Reduced-order strategy for Bayesian inverse problems

Projection-based reduced-order models (ROMs), introduced and developed in Chapter 2, can be exploited to speed up the solution of Bayesian inverse problems dealing with parametrized PDEs describing the electrical activity of the heart.
Reduced basis (RB) methods built through greedy algorithms [FMW+10, LMQ+13b, MPL16] or proper orthogonal decomposition (POD) [GFW+10, LSK13, MN09, RAP14] have been already successfully exploited for the solution of statistical inverse problems governed by elliptic and some nonlinear PDEs. Very recently, a possible way to compute snapshots adaptively from the posterior distribution, yielding a data-driven ROM, has been shown in [CMW15]. Proper generalized decomposition has also been combined with stochastic spectral methods to deal with dynamical systems in the presence of stochastic parametric uncertainties [Nou09].

Besides projection-based ROMs, an efficient input/output evaluation could be obtained using surrogate models (SMs), such as the kriging interpolation developed in Chapter 3, or low-fidelity models, built according to simplified physics, coarser discretizations, or multiscale formulations. These latter models can also be equipped with correction functions using global polynomials in term of the stochastic parameters. For instance, non-intrusive polynomial chaos using orthogonal polynomials [GS03] and stochastic collocation using interpolation polynomials [BNT07, XK02] have been developed in conjunction with physics-based low fidelity models [NE12]. See, e.g., [FMW+10] for a detailed discussion on the use of low-fidelity or surrogate models to speed up inverse problems.

Recently, a multi-fidelity approach, based on the proper combination of output evaluations coming from SMs, ROMs and FOMs, has been proposed for the solution of inverse problems (for a complete survey see [PWG16]). However, this approach has been shown to be effective for the solution of simplified problems, such as elliptic PDEs [PWG15]. Due to the high computational costs related to the full-order solution of cardiac electrophysiology models, we prefer the standard offline-online approach in order to ensure a fast solution of the inverse problems and ROMES to guarantee the accuracy in the results.

5.3.1 Reduced-order Bayesian inverse problems

We thus replace the FOM with a computationally less expensive ROM providing an inexpensive output approximation $\mathbf{y}_n(\boldsymbol{\mu})$ to $\mathbf{y}_h(\boldsymbol{\mu})$ (see Chapter 2). Replacing the full-order likelihood

function π^h with its ROM approximation

$$\pi^n(\mathbf{y}^*|\boldsymbol{\mu}) = \pi_\varepsilon(\mathbf{y}^* - \mathbf{y}_n(\boldsymbol{\mu})) \tag{5.8}$$

clearly affects the posterior distribution, which changes as follows:

$$\pi^n_{post}(\boldsymbol{\mu}\,|\,\mathbf{y}^*) = \frac{\pi^n(\mathbf{y}^*|\boldsymbol{\mu})\,\pi_{prior}(\boldsymbol{\mu})}{\eta_n(\mathbf{y}^*)}, \quad \text{being} \quad \eta_n(\mathbf{y}^*) = \int_{\mathscr{P}} \pi^n(\mathbf{y}^*|\boldsymbol{\mu})\,\pi_{prior}(\boldsymbol{\mu}). \tag{5.9}$$

Consequently, the marginal pdf of the identifiable parameters becomes

$$\pi^n_{post}(\boldsymbol{\gamma}\,|\,\mathbf{y}^*) = \frac{1}{\eta_n(\mathbf{y}^*)} \int_{\mathscr{P}_\zeta} \pi^n(\mathbf{y}^*|\boldsymbol{\mu})\ \pi_{prior}(\boldsymbol{\gamma},\boldsymbol{\zeta})\,d\boldsymbol{\zeta}. \tag{5.10}$$

Nevertheless, the output error $\mathbf{y}_h(\boldsymbol{\mu})-\mathbf{y}_n(\boldsymbol{\mu})$ pollutes the evaluation of the likelihood pdf, which means that $\pi^n(\mathbf{y}^*|\boldsymbol{\mu})$ could be skewed with respect to $\pi^h(\mathbf{y}^*|\boldsymbol{\mu})$. It is crucial to correct the reduced likelihood function with suitable error surrogates in order to avoid biased estimates of the parameters.

5.3.2 Error surrogates

Being able to cheaply evaluate the output of a PDE system is essential to speed up the solution of inverse UQ problems within a Bayesian framework. Our goal, once a RB approximation has been built in the offline stage, is to exploit its fast and cheaply computable online queries to speed up the evaluation of the posterior pdf, of related (point or interval) estimates, and of MCMC integrals like (5.7) or (5.10). Not only, by taking into account reduction errors with suitable error surrogates, we can obtain reliable solutions at the end of the inversion process, too. Although ROMs have been exploited to speed up the solution of inverse problems in several works, very few papers have focused on the analysis of reduction error propagation during inversion procedures (see e.g. [LM14a, BPL14]).

With this goal, we highlight the effect of the approximation error generated by the ROM into the additive noise model (5.2):

$$\mathbf{y}(\boldsymbol{\mu}) = \mathbf{y}_n(\boldsymbol{\mu}) + \underbrace{\mathbf{y}_h(\boldsymbol{\mu}) - \mathbf{y}_n(\boldsymbol{\mu})}_{\text{approx. error}} + \boldsymbol{\varepsilon}_{\text{noise}} \qquad \forall\,\boldsymbol{\mu} \in \mathscr{P}. \tag{5.11}$$

In particular, we wish to incorporate a surrogate model into (5.11) in order to avoid the evaluation of the deterministic quantity $\mathbf{y}_h(\boldsymbol{\mu}) - \mathbf{y}_n(\boldsymbol{\mu})$, which would depend on the FOM solution. To this end, we adopt suitable deterministic and statistical reduced-order model error surrogates (ROMESs) $\boldsymbol{\varepsilon}_{\text{ROM}}(\boldsymbol{\mu})$, such that

$$\mathbf{y}(\boldsymbol{\mu}) = \mathbf{y}_n(\boldsymbol{\mu}) + \boldsymbol{\varepsilon}_{\text{ROM}}(\boldsymbol{\mu}) + \boldsymbol{\varepsilon}_{\text{noise}} \qquad \forall\,\boldsymbol{\mu} \in \mathscr{P}. \tag{5.12}$$

The easiest approach to construct a surrogate $\varepsilon_{\text{ROM}}(\boldsymbol{\mu})$ consists in directly approximating the map $\boldsymbol{\mu} \to \mathbf{y}_h(\boldsymbol{\mu}) - \mathbf{y}_n(\boldsymbol{\mu})$ through a gaussian process regression or a kriging interpolation, as done in Chapter 3.
We end up with error indicators which can be either deterministic – that is, $\boldsymbol{\varepsilon}_{\text{ROM}}(\boldsymbol{\mu}) = \mathbf{m}_{\text{ROM}}(\boldsymbol{\mu})$, being $\mathbf{m}_{\text{ROM}}(\boldsymbol{\mu})$ a suitable function of $\boldsymbol{\mu}$ – or expressed through a random variable

$\boldsymbol{\varepsilon}_{\mathrm{ROM}}(\boldsymbol{\mu})$, whose distribution $\pi_{\boldsymbol{\varepsilon}_{\mathrm{ROM}}}$ is characterized by $\mathbb{E}[\boldsymbol{\varepsilon}_{\mathrm{ROM}}(\boldsymbol{\mu})] = \mathbf{m}_{\mathrm{ROM}}(\boldsymbol{\mu})$ and $\mathrm{Cov}[\boldsymbol{\varepsilon}_{\mathrm{ROM}}(\boldsymbol{\mu})] = \boldsymbol{\Gamma}_{\mathrm{ROM}}(\boldsymbol{\mu})$. Correspondingly, we end up with a *corrected* reduced-order likelihood

$$\tilde{\pi}^n(\mathbf{y}^*|\boldsymbol{\mu}) = \begin{cases} \pi_{\boldsymbol{\varepsilon}}(\mathbf{y}^* - \mathbf{y}_n(\boldsymbol{\mu}) - \mathbf{m}_{\mathrm{ROM}}(\boldsymbol{\mu})) & \text{deterministic ROMES} \\ \pi_{\tilde{\boldsymbol{\delta}}}(\mathbf{y}^* - \mathbf{y}_n(\boldsymbol{\mu}) - \mathbf{m}_{\mathrm{ROM}}(\boldsymbol{\mu})) & \text{statistical ROMES} \end{cases} \tag{5.13}$$

being $\tilde{\boldsymbol{\delta}}(\boldsymbol{\mu}) = \boldsymbol{\varepsilon}_{\mathrm{ROM}}(\boldsymbol{\mu}) + \boldsymbol{\varepsilon}_{\mathrm{noise}}$ and $\mathrm{Cov}[\tilde{\boldsymbol{\delta}}(\boldsymbol{\mu})] = \boldsymbol{\Gamma} + \boldsymbol{\Gamma}_{\mathrm{ROM}}(\boldsymbol{\mu})$, by assuming that ROM errors and measurement noise are independent. Correspondingly, we obtain the following *corrected* reduced-order posterior pdf

$$\tilde{\pi}^n_{post}(\boldsymbol{\mu}\,|\,\mathbf{y}^*) = \frac{\tilde{\pi}^n(\mathbf{y}^*|\boldsymbol{\mu})\,\pi_{prior}(\boldsymbol{\mu})}{\tilde{\eta}_n(\mathbf{y}^*)}, \quad \text{being} \quad \tilde{\eta}_n(\mathbf{y}^*) = \int_{\mathscr{P}} \tilde{\pi}^n(\mathbf{y}^*|\boldsymbol{\mu})\,\pi_{prior}(\boldsymbol{\mu}), \tag{5.14}$$

yielding to a similar correction in the marginal pdf of the identifiable parameters (5.10).

5.3.3 Proposed inversion procedure

Let us now summarize the whole numerical procedure we use to solve a Bayesian inverse problem in the case of real-valued outputs. A first *offline* stage (Algorithm 5) consists in the computation of the POD-DEIM basis functions and construction of the reduced arrays. Then the calibration procedure consists in evaluating the difference between the ROM output $\mathbf{y}_n(\boldsymbol{\mu})$ and the full-order output $\mathbf{y}_h(\boldsymbol{\mu})$ for each parameter in the calibration set P_{cal}. Finally, the ROMES construction is performed accordingly to the procedure described in Sect. 3.3.
During the *online* stage (Algorithm 6), the *posterior* distribution is sampled through a Metropolis–Hastings algorithm, which generates a sequence of sample values, whose distribution converges to the desired corrected distribution $\tilde{\pi}^n_{post}$. Each MCMC iteration entails an *online* query, which is performed in an efficient way by the ROM and the ROMES. The quality of the sampling sequence is finally improved by performing a subsequent *burn-in* and *thinning*, in order to reduce the autocorrelation between the sampled points; see e.g. [Gil05, Jac00, ADFD$^+$03] for further details.

5.4 Effectivity of ROM error surrogates

Let us now analyze the effectivity of the *corrections* made on the reduced-order likelihood function thanks to the proposed ROMES. In particular, we aim at stating some conditions to be fulfilled by the ROMES corrections in order to guarantee that the corresponding posterior pdf $\tilde{\pi}_n$ is closer to the full-order pdf π_h than the reduced-order pdf π_n without corrections.
To this end, let us recall the notion of Kullback-Leibler (KL) divergence, which is a non-symmetric measure of the difference between two probability distributions π_A and π_B:

$$D_{KL}(\pi_A||\pi_B) = \int \pi_A(z) \log\left(\frac{\pi_A(z)}{\pi_B(z)}\right) dz. \tag{5.15}$$

Clearly, $D_{KL}(\pi_A||\pi_B) \geq 0$ whereas $D_{KL}(\pi_A||\pi_B) = 0$ if $\pi_A = \pi_B$ almost surely. This notion has already been used to compare approximations of posterior distributions obtained through generalized polynomial chaos representations, see e.g. [MX09, BPL14] for further details.

Algorithm 5 Standard POD-DEIM procedure

procedure [ROM ARRAYS] = OFFLINE(FOM ARRAYS, P_{train}, ϵ_{tol})
  Full-order matrices:
  $\{\beta_j^M(\boldsymbol{\mu}), \mathbf{M}_j\} \leftarrow$ affine decomposition of $\mathbf{M}(\boldsymbol{\mu})$
  $\{\beta_j^A(\boldsymbol{\mu}), \mathbf{A}_j\} \leftarrow$ affine decomposition of $\mathbf{A}(\boldsymbol{\mu})$
  $\{\beta_j^{app}(\boldsymbol{\mu})\mathbf{I}_{app,j}\} \leftarrow$ affine decomposition of $\mathbf{I}_{app}$
  for $\boldsymbol{\mu} \in P_{train}$ **do**
    for $\ell = 1, \dots, N_t$ **do**
      $\mathbf{y}_u = [\mathbf{y}_u, \mathbf{u}_h^{(\ell)}(\boldsymbol{\mu})]$;
      $\mathbf{y}_I = [\mathbf{y}_I, \mathbf{I}_{ion}(\mathbf{u}_h^{(\ell)}, \mathbf{w}_h^{(\ell)}; \boldsymbol{\mu})]$;
    end for
  end for
  $\mathbf{V} \leftarrow POD(\mathbf{y}_u, \epsilon_{tol})$;
  $\mathbf{U} \leftarrow POD(\mathbf{y}_I, \epsilon_{tol})$;
  $\mathbf{P} \leftarrow DEIMindices(\mathbf{U})$;
  Reduced-order matrices:
  $\{\mathbf{M}_{n,j}, \mathbf{A}_{n,j}, (\mathbf{I}_{app,n})_j\} \leftarrow$ projection of the full order matrices onto $\mathbf{V}$
end procedure

procedure [ROMES ARRAYS] = ROMES CALIBRATION(FOM ARRAYS, ROM ARRAYS, P_{cal})
  for j = 1 : N_{cal} **do**
    $\mathbf{y}_h(\boldsymbol{\mu}_j) \leftarrow$ FOM query($\boldsymbol{\mu}_j$)
    $\mathbf{y}_n(\boldsymbol{\mu}_j) \leftarrow$ ROM query($\boldsymbol{\mu}_j$)
    $\mathbf{err}(j) \leftarrow \mathbf{y}_h(\boldsymbol{\mu}_j) - \mathbf{y}_n(\boldsymbol{\mu}_j)$
  end for
  compute ROMES
end procedure

Remark 2. *We assume the following consistency property for the considered ROM: for any RB dimension $n = 1, \dots, N_h$ and DEIM dimension $m_D = 1, \dots, N_h$, there exists $\epsilon^{(\ell)}(n, m_D) > 0$ such that*

$$\|\mathbf{u}_h^{(\ell)}(\boldsymbol{\mu}) - \mathbf{V}\mathbf{u}_n^{(\ell)}(\boldsymbol{\mu})\| \leq \epsilon^{(\ell)}(n, m_D), \qquad \forall \ell = 0, \dots, N_t \ \ \forall \boldsymbol{\mu} \in \mathscr{P}$$

and $\epsilon^{(\ell)}(n, m_D) \to 0$ for $n, m_D \to N_h$. Moreover, if the output is linear with respect to the solution $\mathbf{u}_h$ we have that there exist $\epsilon_y(n, m_D) > 0$

$$\|\mathbf{y}_h(\boldsymbol{\mu}) - \mathbf{y}_n(\boldsymbol{\mu})\| \leq \epsilon_y(n, m_D), \qquad \epsilon_y(n, m_D) \to 0 \text{ for } n, m_D \to N_h.$$

5.4.1 Consistency result

Before comparing our ROMESs and showing their effect on the reduced-order posterior pdfs, we prove that the reduced-order posterior function π_{post}^n approximates the full-order one π_{post}^h in a *consistent* way, as long as the ROM dimension increases:

Algorithm 6 Online procedure

procedure METROPOLIS SAMPLING
  $\boldsymbol{\mu}^{(1)} \leftarrow$ initial value
  sampling loop:
  for cont = 2 : K **do**
    $\bar{\boldsymbol{\mu}} \leftarrow$ random walk
    $[\mathbf{y}_n(\bar{\boldsymbol{\mu}})] \leftarrow$ ROM query($\boldsymbol{\mu}$)
    $\mathbf{m}_{\mathrm{ROM}}(\bar{\boldsymbol{\mu}}) \leftarrow$ evaluate ROMES prediction($\boldsymbol{\mu}$)
    if ROMES is *deterministic* **then**
      $\tilde{\pi}^n \leftarrow \pi_\varepsilon(\mathbf{y}^* - \mathbf{y}_n(\bar{\boldsymbol{\mu}}) - \mathbf{m}_{\mathrm{ROM}}(\bar{\boldsymbol{\mu}}))$
    end if
    if ROMES is *statistical* **then**
      $\Sigma_{\mathrm{ROM}}(\bar{\boldsymbol{\mu}}) \leftarrow$ evaluate ROMES covariance matrix
      $\tilde{\pi}^n \leftarrow \pi_{\tilde{\boldsymbol{\delta}}}(\mathbf{y}^* - \mathbf{y}_n(\bar{\boldsymbol{\mu}}) - \mathbf{m}_{\mathrm{ROM}}(\bar{\boldsymbol{\mu}}))$
    end if
    $\tilde{\pi}^n_{post}(\bar{\boldsymbol{\mu}}|\mathbf{y}^*) \leftarrow$ Bayes' formula
    $\gamma \leftarrow \tilde{\pi}^n_{post}(\bar{\boldsymbol{\mu}}|\mathbf{y}^*)/\tilde{\pi}^n_{post}(\boldsymbol{\mu}^{(k)}|\mathbf{y}^*)$
    $y \leftarrow$ random sampling from $U(0,1)$
    if $y < \gamma$ **then**
      $\boldsymbol{\mu}^{(k+1)} \leftarrow \bar{\boldsymbol{\mu}}$; $k \leftarrow k+1$
    end if
    burn-in:
    eliminate first M simulations ~~$\boldsymbol{\mu}^{(1:M)}$~~
    thinning:
    keep every d-th draw of the chain $\boldsymbol{\mu}^{(1:d:end)}$
  end for
end procedure

Proposition 2. *Let us consider a Gaussian noise model and the RB approximation* $\mathbf{y}_n(\boldsymbol{\mu})$ *of the output* $\mathbf{y}_h(\boldsymbol{\mu})$ *defined by a consistent ROM. Then, for any* $\boldsymbol{\mu} \in \mathscr{P}$*, we have:*

$$\lim_{n \to N_h} D_{KL}(\pi^h_{post} || \pi^n_{post}) \to 0.$$

Proof. When an additive Gaussian noise model is considered, the following relationship holds for any $\boldsymbol{\mu} \in \mathscr{P}$:

$$D_{KL}(\pi^h || \pi^n) = \int_{\mathbb{R}^s} \pi^h(\mathbf{y}|\boldsymbol{\mu}) \log\left(\frac{\pi^h(\mathbf{y}|\boldsymbol{\mu})}{\pi^n(\mathbf{y}|\boldsymbol{\mu})}\right) d\mathbf{y} = \sum_{j=1}^{s} \frac{1}{2\sigma_j^2} (y_h^j(\boldsymbol{\mu}) - y_n^j(\boldsymbol{\mu}))^2, \tag{5.16}$$

thanks to the definition (5.15) of Kullback-Leibler divergence. For the consistency of the selected ROM we have that:

$$\lim_{n \to N_h} D_{KL}(\pi^h || \pi^n) \to 0.$$

Moreover, by applying the KL-divergence to the Bayes formula, we have:

$$\begin{aligned} D_{KL}(\pi^h_{post}||\pi^n_{post}) = & \int_{\mathscr{P}} \frac{\pi^h(\mathbf{y}^*|\boldsymbol{\mu})\pi_{prior}(\boldsymbol{\mu})}{\eta_h(\mathbf{y}^*)} \log\left(\frac{\pi^h(\mathbf{y}^*|\boldsymbol{\mu})}{\pi^n(\mathbf{y}^*|\boldsymbol{\mu})}\frac{\eta_n(\mathbf{y}^*)}{\eta_h(\mathbf{y}^*)}\right) d\boldsymbol{\mu} \\ = & \log\left(\frac{\eta_n(\mathbf{y}^*)}{\eta_h(\mathbf{y}^*)}\right) + \int_{\mathscr{P}} \frac{\pi^h(\mathbf{y}^*|\boldsymbol{\mu})\pi_{prior}(\boldsymbol{\mu})}{\eta_h(\mathbf{y}^*)} \log\left(\frac{\pi^h(\mathbf{y}^*|\boldsymbol{\mu})}{\pi^n(\mathbf{y}^*|\boldsymbol{\mu})}\right) d\boldsymbol{\mu}. \end{aligned} \tag{5.17}$$

By using the definition of π^h and π^n, and the Lipschitz-continuity of $\exp(-\mathbf{y})$ for $\mathbf{y} \geq \mathbf{0}$ (that is, $|e^{-\mathbf{y}} - e^{-\mathbf{t}}| \leq \Lambda|\mathbf{y}-\mathbf{t}|$ for any $\mathbf{y},\mathbf{t} > \mathbf{0}$, with $\Lambda = 1$), we obtain

$$\begin{aligned} \left|\pi^h(\mathbf{y}^*|\boldsymbol{\mu}) - \pi^n(\mathbf{y}^*|\boldsymbol{\mu})\right| &= \prod_{j=1}^{s} \frac{1}{\sqrt{2\pi\sigma_j^2}} \left| \exp\left(-\frac{(y_j^* - y_n^j(\boldsymbol{\mu}))^2}{2\sigma_j^2}\right) - \exp\left(-\frac{(y_j^* - y_h^j(\boldsymbol{\mu}))^2}{2\sigma_j^2}\right)\right| \\ &\leq \prod_{j=1}^{s} \frac{1}{\sqrt{2\pi\sigma_j^2}} \left| -\frac{(y_j^* - y_n^j(\boldsymbol{\mu}))^2}{2\sigma_j^2} + \frac{(y_j^* - y_h^j(\boldsymbol{\mu}))^2}{2\sigma_j^2}\right| \\ &\leq \prod_{j=1}^{s} \frac{1}{\sqrt{2\pi\sigma_j^2}2\sigma_j^2} \left|y_n^j(\boldsymbol{\mu}) - y_h^j(\boldsymbol{\mu})\right| \left|2s_j^* - y_h^j(\boldsymbol{\mu}) - y_n^j(\boldsymbol{\mu})\right| \end{aligned}$$

so that, for any $\boldsymbol{\mu} \in \mathscr{P}$, $\left|\pi^h(\mathbf{y}^*|\boldsymbol{\mu}) - \pi^n(\mathbf{y}^*|\boldsymbol{\mu})\right| \to 0$ when $n \to N_h$ because for the consistency of the ROM we have $|y_h^j(\boldsymbol{\mu}) - y_n^j(\boldsymbol{\mu})| \to 0$ for any $j = 1,\dots,s$. In the same way, $|\eta_n(\mathbf{y}^*) - \eta_h(\mathbf{y}^*)| = \left|\int_{\mathscr{P}}(\pi^h(\mathbf{y}^*|\boldsymbol{\mu}) - \pi^n(\mathbf{y}^*|\boldsymbol{\mu}))\pi_{prior}(\boldsymbol{\mu})d\boldsymbol{\mu}\right| \to 0$ for any given $\mathbf{y}^* \in \mathbb{R}^s$. Thus, both terms in the second line of (5.17) vanish for $n \to N_h$. □

5.4.2 A result of effectivity

Since we are mainly interested in the case where the ROM dimension n is fixed (and possibly small) we want to show that performing a correction according to a ROMES improves the quality of the reduced posterior (in terms of the KL divergence). We first prove a result dealing with the ROM-ROMES approximation of the likelihood function:

Proposition 3. *Under the assumptions of Proposition 2, if for any $j = 1,\dots,s$ there exists $C_j < 1$ such that*

$$|y_h^j(\boldsymbol{\mu}) - y_n^j(\boldsymbol{\mu}) - m^j_{ROM}(\boldsymbol{\mu})| \leq C_j|y_h^j(\boldsymbol{\mu}) - y_n^j(\boldsymbol{\mu})| \qquad \forall \boldsymbol{\mu} \in \mathscr{P} \tag{5.18}$$

then

$$D_{KL}(\pi^h||\tilde{\pi}^n) \leq (\max_{j=1,\dots,s} C_j^2) D_{KL}(\pi^h||\pi^n) \tag{5.19}$$

provided that the correction is made according to a deterministic ROMES.

Proof. In analogy with relation (5.16), a correction operated by means of a deterministic ROMES affects just $\mathbb{E}[\mathbf{s}^*|\boldsymbol{\mu}]$, so that

$$D_{KL}(\pi^h||\tilde{\pi}^n) = \sum_{j=1}^{s} \frac{1}{2\sigma_j^2}(y_h^j(\boldsymbol{\mu}) - y_n^j(\boldsymbol{\mu}) - m^j_{\mathrm{ROM}}(\boldsymbol{\mu}))^2. \tag{5.20}$$

Thus, under condition (5.18), (5.19) directly follows. □

By means of (5.18), we require that the correction provided by a ROMES is *effective*, that is, it yields a reduction in the KL divergence between the reduced-order and the full-order posterior pdfs, when in the former case a correction through a deterministic ROMES is considered. Instead, when relying on a statistical ROMES $\boldsymbol{\varepsilon}_{\text{ROM}}$, the correction could be modeled as a random variable, with mean $\mathbf{m}_{\text{ROM}}$ and covariance matrix $(\Sigma_{\text{ROM}})_{ij} = (\sigma_j^{ROM})^2\delta_{ij}$. As a consequence we would obtain

$$D_{KL}(\pi^h||\tilde{\pi}^n) = \frac{1}{2}\sum_{j=1}^{s}\left(\frac{(y_h^j(\boldsymbol{\mu}) - y_n^j(\boldsymbol{\mu}) - \tilde{\varepsilon}^j(\boldsymbol{\mu}))^2}{\sigma_j^2 + (\sigma_j^{ROM})^2} + \frac{\sigma^2}{\sigma_j^2 + (\sigma_j^{ROM})^2} - 1 - \log\left(\frac{\sigma_j^2}{\sigma_j^2 + (\sigma_j^{ROM})^2}\right)\right) \tag{5.21}$$

instead of (5.20). Thus, in order to ensure that a relation like (5.19) still holds, we need to further require that $(\sigma_j^{ROM})^2$ is sufficiently small compared to σ_j^2, $j = 1,\dots,s$. We remark that it is always possible to construct a ROMES such that this assumption is fulfilled, by considering a sufficient large calibration set S_{cal} during the offline phase.

Let us now turn to evaluate how the corrections introduced by a ROMES impact on the posterior pdfs. First of all, let us remark that, by taking the expectation of the KL divergence between $\pi^h(\mathbf{y}^*|\boldsymbol{\mu})$ and $\pi^n(\mathbf{y}^*|\boldsymbol{\mu})$, and changing the order of integration, we obtain

$$\mathbb{E}[D_{KL}(\pi^h||\pi^n)] = \int_{\mathscr{P}} D_{KL}(\pi^h||\pi^n)\pi_{prior}(\boldsymbol{\mu})d\boldsymbol{\mu}. \tag{5.22}$$

Moreover, thanks to the positivity of the KL divergence and relation (5.19), we get

$$\mathbb{E}[D_{KL}(\pi^h||\tilde{\pi}^n)] \leq \left(\max_{j=1,\dots,s} C_j^2\right)\mathbb{E}[D_{KL}(\pi^h||\pi^n)]. \tag{5.23}$$

The average distance between the corrected reduced likelihood function and the full-order one is bounded by the average distance between the uncorrected reduced likelihood function and the full-order one with a constant depending on the effectivity of the ROMES.

5.4.3 Posterior comparison for fixed n

We now want to compare the KL divergences between the full-order and the corrected/uncorrected posterior pdfs for a (possibly small) fixed ROM dimensions n and m_D. We can show the following

Proposition 4. *Under the assumptions of Proposition 3 and provided that $\eta_n(\mathbf{y}) \sim \eta_h(\mathbf{y})$ for $n, m_D \to N_h$, for any $\mathbf{y} \in \mathbb{R}^s$, we have that*

$$\mathbb{E}[D_{KL}(\pi_{post}^h||\tilde{\pi}_{post}^n)] \leq \mathbb{E}[D_{KL}(\pi_{post}^h||\pi_{post}^n)] \tag{5.24}$$

if the correction is made according to a deterministic ROMES.

Proof. Let us express the right-hand side of (5.24) as

$$\mathbb{E}[D_{KL}(\pi^h_{post}||\pi^n_{post})] = \int_{\mathbb{R}^s}\left(\log\left(\frac{\eta_n(\mathbf{y})}{\eta_h(\mathbf{y})}\right)+\int_{\mathscr{P}}\frac{\pi^h(\mathbf{y}|\boldsymbol{\mu})\pi_{prior}(\boldsymbol{\mu})}{\eta_h(\mathbf{y})}\log\left(\frac{\pi^h(\mathbf{y}|\boldsymbol{\mu})}{\pi^n(\mathbf{y}|\boldsymbol{\mu})}\right)d\boldsymbol{\mu}\right)\eta_h(\mathbf{y})d\mathbf{y}. \tag{5.25}$$

In the same way, the left-hand side of (5.24) becomes

$$\mathbb{E}[D_{KL}(\pi^h_{post}||\tilde{\pi}^n_{post})] = \int_{\mathbb{R}^s}\left(\log\left(\frac{\tilde{\eta}_n(\mathbf{y})}{\eta_h(\mathbf{y})}\right)+\int_{\mathscr{P}}\frac{\pi^h(\mathbf{y}|\boldsymbol{\mu})\pi_{prior}(\boldsymbol{\mu})}{\eta_h(\mathbf{y})}\log\left(\frac{\pi^h(\mathbf{y}|\boldsymbol{\mu})}{\tilde{\pi}^n(\mathbf{y}|\boldsymbol{\mu})}\right)d\boldsymbol{\mu}\right)\eta_h(\mathbf{y})d\mathbf{y}. \tag{5.26}$$

We proceed by analyzing separately the two terms of the right-hand side of (5.25). The second term coincides with (5.22), i.e.

$$\begin{aligned}&\int_{\mathbb{R}^s}\left(\int_{\mathscr{P}}\frac{\pi^h(\mathbf{y}|\boldsymbol{\mu})\pi_{prior}(\boldsymbol{\mu})}{\eta_h(\mathbf{y})}\log\left(\frac{\pi^h(\mathbf{y}|\boldsymbol{\mu})}{\pi^n(\mathbf{y}|\boldsymbol{\mu})}\right)d\boldsymbol{\mu}\right)\eta_h(\mathbf{y})d\mathbf{y} = \\ &\quad=\int_{\mathscr{P}}\left(\int_{\mathbb{R}^s}\pi^h(\mathbf{y}|\boldsymbol{\mu})\log\left(\frac{\pi^h(\mathbf{y}|\boldsymbol{\mu})}{\pi^n(\mathbf{y}|\boldsymbol{\mu})}\right)d\mathbf{y}\right)\pi_{prior}(\boldsymbol{\mu})d\boldsymbol{\mu} = \mathbb{E}[D_{KL}(\pi^h||\pi^n)].\end{aligned}$$

In the same way, the second term of the right-hand side of (5.26) is such that

$$\int_{\mathbb{R}^s}\left(\int_{\mathscr{P}}\frac{\pi^h(\mathbf{y}|\boldsymbol{\mu})\pi_{prior}(\boldsymbol{\mu})}{\eta_h(\mathbf{y})}\log\left(\frac{\pi^h(\mathbf{y}|\boldsymbol{\mu})}{\tilde{\pi}^n(\mathbf{y}|\boldsymbol{\mu})}\right)d\boldsymbol{\mu}\right)\eta_h(\mathbf{y})ds = \mathbb{E}[D_{KL}(\pi^h||\tilde{\pi}^n)].$$

On the other hand, by developing the first term of (5.25) with a Taylor expansion, we obtain

$$\begin{aligned}\int_{\mathbb{R}^s}\log\left(\frac{\eta_n(\mathbf{y})}{\eta_h(\mathbf{y})}\right)\eta_h(\mathbf{y})ds &= \int_{\mathbb{R}^s}\left(\left(\frac{\eta_n(\mathbf{y})}{\eta_h(\mathbf{y})}-1\right)-\frac{1}{2}\left(\frac{\eta_n(\mathbf{y})}{\eta_h(\mathbf{y})}-1\right)^2+\mathscr{O}\left(\frac{\eta_n(\mathbf{y})}{\eta_h(\mathbf{y})}-1\right)^3\right)\eta_h(\mathbf{y})d\mathbf{y} \\ &=\int_{\mathbb{R}^s}(\eta_n(\mathbf{y})-\eta_h(\mathbf{y}))d\mathbf{y}-\int_{\mathbb{R}^s}\frac{1}{2}\left(\frac{\eta_n(\mathbf{y})^2}{\eta_h(\mathbf{y})}-2\eta_n(\mathbf{y})+\eta_h(\mathbf{y})\right)d\mathbf{y}+\int_{\mathbb{R}^s}\mathscr{O}\left(\frac{\eta_n(\mathbf{y})}{\eta_h(\mathbf{y})}-1\right)^3\eta_h(\mathbf{y})d\mathbf{y}.\end{aligned}$$

The first term of the last sum can be rewritten as

$$\int_{\mathbb{R}^s}(\eta_n(\mathbf{y})-\eta_h(\mathbf{y}))ds = \int_{\mathscr{P}}\left(\int_{\mathbb{R}^s}\pi^n(\mathbf{y}|\boldsymbol{\mu})d\mathbf{y}\right)\pi_{prior}(\boldsymbol{\mu})d\boldsymbol{\mu}-\int_{\mathscr{P}}\left(\int_{\mathbb{R}^s}\pi^h(\mathbf{y}|\boldsymbol{\mu})d\mathbf{y}\right)\pi_{prior}(\boldsymbol{\mu})d\boldsymbol{\mu}, \tag{5.27}$$

and it is vanishing, since

$$\int_{\mathscr{P}}\left(\int_{\mathbb{R}^s}\pi^h(\mathbf{y}|\boldsymbol{\mu})d\mathbf{y}\right)\pi_{prior}(\boldsymbol{\mu})d\boldsymbol{\mu} = \int_{\mathscr{P}}\left(\int_{\mathbb{R}^s}\pi^n(\mathbf{y}|\boldsymbol{\mu})d\mathbf{y}\right)\pi_{prior}(\boldsymbol{\mu})d\boldsymbol{\mu} = \int_{\mathscr{P}}\pi_{prior}(\boldsymbol{\mu})d\boldsymbol{\mu} = 1.$$

In this way

$$\int_{\mathbb{R}^s}\log\left(\frac{\eta_n(\mathbf{y})}{\eta_h(\mathbf{y})}\right)\eta_h(\mathbf{y})d\mathbf{y} = -\frac{1}{2}\int_{\mathbb{R}^s}\left(\frac{\eta_n(\mathbf{y})^2}{\eta_h(\mathbf{y})}-1\right)d\mathbf{y}+\int_{\mathbb{R}^s}\mathscr{O}\left(\frac{\eta_n(\mathbf{y})}{\eta_h(\mathbf{y})}-1\right)^3\eta_h(\mathbf{y})d\mathbf{y},$$

considering the integral of the ROMESainder term of the Taylor expansion to be sufficient small when $\eta_n \sim \eta_h$. Similarly, the first term of the right-hand side of (5.26) is negligible, so that

$$\begin{aligned}\mathbb{E}[D_{KL}(\pi^h_{post}||\tilde{\pi}^n_{post})] &= -\frac{1}{2}\int_{\mathbb{R}^s}\left(\frac{\tilde{\eta}_n(\mathbf{y})^2}{\eta_h(\mathbf{y})}-1\right)d\mathbf{y}+\mathbb{E}[D_{KL}(\pi^h||\tilde{\pi}^n)]+\int_{\mathbb{R}^s}\mathscr{O}\left(\frac{\tilde{\eta}_n(\mathbf{y})}{\eta_h(\mathbf{y})}-1\right)^3\eta_h(\mathbf{y})d\mathbf{y} \\ \mathbb{E}[D_{KL}(\pi^h_{post}||\pi^n_{post})] &= -\frac{1}{2}\int_{\mathbb{R}^s}\left(\frac{\eta_n(\mathbf{y})^2}{\eta_h(\mathbf{y})}-1\right)d\mathbf{y}+\mathbb{E}[D_{KL}(\pi^h||\pi^n)]+\int_{\mathbb{R}^s}\mathscr{O}\left(\frac{\eta_n(\mathbf{y})}{\eta_h(\mathbf{y})}-1\right)^3\eta_h(\mathbf{y})d\mathbf{y}.\end{aligned}$$

In conclusion, by using (5.23), inequality (5.24) follows under the following condition:

$$\frac{1}{2}\int_{\mathbb{R}^s}\left(\frac{\eta_n(\mathbf{y})^2}{\eta_h(\mathbf{y})}-\frac{\tilde{\eta}_n(\mathbf{y})^2}{\eta_h(\mathbf{y})}\right)d\mathbf{y}+\int_{\mathbb{R}^s}\mathscr{O}\left(\frac{\tilde{\eta}_n(\mathbf{y})}{\eta_h(\mathbf{y})}-1\right)^3\eta_h(\mathbf{y})d\mathbf{y}$$
$$\leq\left(1-\max_{j=1,\dots,s}C_j^2\right)\mathbb{E}[D_{KL}(\pi^h||\pi^n)]+\int_{\mathbb{R}^s}\mathscr{O}\left(\frac{\eta_n(\mathbf{y})}{\eta_h(\mathbf{y})}-1\right)^3\eta_h(\mathbf{y})d\mathbf{y},$$

which can be seen as a robustness condition on the correction entailed by the ROMES. □

Remark 3. *According to* (5.6), (5.9), $\eta_n \sim \eta_h$ *as soon as the likelihood functions* π^h *and* π^n *are very close to each other, that is,* $D_{KL}(\pi^h||\pi^n) < \varepsilon$ *for any given, small* $\varepsilon > 0$.

5.5 Numerical results

We now apply the proposed reduced method for the solution of a Bayesian inverse problem based on the simplified 2-D coupled heart-torso problem presented in Section 4.5 and a noisy observation of a simplified ECG signal. Our goal is to show how the combination of ROM and ROMES surrogates leads to an efficient and accurate estimation of the posterior probability distribution of the parameters.

5.5.1 2D heart-torso model

We consider the fully uncoupled heart-torso model based on the monodomain equation and the Aliev-Panfilov ionic model: given $\boldsymbol{\mu}_H = [\sigma_v, K, \varepsilon_0]^T$, find $u = u(\mathbf{x},t;\boldsymbol{\mu}_H)$ and $w = w(\mathbf{x},t;\boldsymbol{\mu}_H)$ such that

$$\begin{cases} A_m\left(C_m\dfrac{\partial u}{\partial t}+I_{ion}(u,w;\boldsymbol{\mu}_H)\right)-\operatorname{div}(\sigma_v\nabla u)=A_m I_{app}(t) & \mathbf{x}\in\Omega_H, t\in(0,T] \\ \frac{\partial w}{\partial t}=g(u,w;\boldsymbol{\mu}_H) & \mathbf{x}\in\Omega_H, t\in(0,T] \\ \nabla u(\mathbf{x},t;\boldsymbol{\mu}_H)\cdot\mathbf{n}_H=0 & \mathbf{x}\in\partial\Omega_H, t\in(0,T] \\ u(\mathbf{x},0;\boldsymbol{\mu}_H)=w(\mathbf{x},0;\boldsymbol{\mu}_H)=0 & \mathbf{x}\in\partial\Omega_H, \end{cases} \tag{5.28}$$

with current specification (1.2). The extra-cellular potential is then obtained by solving: find $u_e = u_e(\mathbf{x},t;[\sigma_e,\boldsymbol{\mu}_H]^T)$ such that

$$\begin{cases} -\operatorname{div}((\sigma_i+\sigma_e)\nabla u_e)-\operatorname{div}(\sigma_i\nabla u)=0 & \mathbf{x}\in\Omega_H, t\in(0,T] \\ (\sigma_i+\sigma_e)\nabla u_e(\mathbf{x},t;[\sigma_e,\boldsymbol{\mu}_H]^T)\cdot\mathbf{n}_H=\sigma_i\nabla u(\mathbf{x},t;\boldsymbol{\mu}_H)\cdot\mathbf{n}_H & \mathbf{x}\in\partial\Omega_H, t\in(0,T]. \end{cases} \tag{5.29}$$

Finally, the torso potential is obtained by solving: find $u_T = u_T(\mathbf{x},t;[\sigma_t,\sigma_e,\boldsymbol{\mu}_H]^T)$ such that

$$\begin{cases} \operatorname{div}(\sigma_T\nabla u_T)=0 & \mathbf{x}\in\Omega_T, t\in(0,T] \\ \sigma_T\nabla u_T(\mathbf{x},t;[\sigma_t,\sigma_e,\boldsymbol{\mu}_H]^T)\cdot\mathbf{n}_T=0 & \mathbf{x}\in\partial\Omega_T, t\in(0,T] \\ u_T(\mathbf{x},t;[\sigma_t,\sigma_e,\boldsymbol{\mu}_H]^T)=u_e(\mathbf{x},t;[\sigma_e,\boldsymbol{\mu}_H]^T) & \mathbf{x}\in\partial\Omega_H, t\in(0,T]. \end{cases} \tag{5.30}$$

In this case, we consider as output of interest the landmark $\mathbf{y}_h(\boldsymbol{\mu}) = t_{QR}(\boldsymbol{\mu})$, i.e. the time between the stimulation pulse and the upstroke of the simplified ECG $I(t;\boldsymbol{\mu})$:

$$t_{QR}(\boldsymbol{\mu})=\arg\max_{t\in(0,T)}I(t;\boldsymbol{\mu})=\arg\max_{t\in(0,T)}(u_T(\mathbf{x}_{LA},t;[\sigma_t,\sigma_e,\boldsymbol{\mu}_H]^T)-u_T(\mathbf{x}_{RA},t;[\sigma_t,\sigma_e,\boldsymbol{\mu}_H]^T).$$

We assume that the measurement of the output $y_h(\boldsymbol{\mu}) = t_{QR}(\boldsymbol{\mu})$ is affected by noise, which is modeled with the additive noise model:

$$y = t_{QR}(\boldsymbol{\mu}) + \varepsilon_{\text{noise}} \qquad \varepsilon_{\text{noise}} \sim \mathcal{N}(0, 0.5).$$

The goal of the Bayesian inverse problem is to identify the parameters $\boldsymbol{\gamma} = [\sigma_v, K]^T$ by observing the output y in presence of three nuisance parameters $\boldsymbol{\zeta} = [\sigma_t, \sigma_e, \varepsilon_0]^T$. This choice is motivated by the results obtained from the global sensitivity analysis reported in Section 4.5. The total effect indices S_{T_i}, $i = 1, \dots, 5$, reported in Table 5.1, clearly classify $\boldsymbol{\zeta}$ as non-influential parameters for the output t_{QR}. We expect indeed that $\boldsymbol{\zeta}$ is also a vector of non-identifiable parameters for the case at hand. We suppose that the target value y^* corresponds to a noisy observation of the full order output $y_h(\boldsymbol{\mu}^*)$ evaluated for $\boldsymbol{\gamma}^* = [1.63, 6.92]$ and a random value of $\boldsymbol{\zeta}^*$.

As we have seen in 4.5, the FOM for the approximation of (5.28)-(5.29)-(5.30) can be built using the FE method (with linear $\mathbb{P}^1$ finite elements) on a mesh formed by 6662 vertices and 12880 elements. We consider a reduced basis POD-DEIM model starting from $N_{train} = 10$ parameters randomly selected in the parameter space (the snapshots matrix is consequently of dimensions $6662 \times 10N_t$, with $N_t = 600$). For each new vector of parameters the evaluation of $y_n(\boldsymbol{\mu})$ requires on average in 0.64 seconds, with a speedup of $82x$ with respect to the FOM. The reduced output evaluation $y_n(\boldsymbol{\mu})$ can be corrected using a kriging-based ROMES, built starting from the output errors computed for $N_{cal} = N_{train} + 15$ parameter vectors. The corrected output evaluation becomes:

$$y(\boldsymbol{\mu}) = \begin{cases} y_n(\boldsymbol{\mu}) + m_{\text{ROM}}(\boldsymbol{\mu}) + \varepsilon_{noise} & \text{deterministic ROMES} \\ y_n(\boldsymbol{\mu}) + \varepsilon_{\text{ROM}}(\boldsymbol{\mu}) + \varepsilon_{noise} & \text{statistical ROMES} \end{cases}$$

Finally we also compare the ROM with a surrogate model (SM) constructed on a set of $N_{train} = 25$ outputs (for further details see Section 3.2). In this case the output measurement becomes

$$y(\boldsymbol{\mu}) = \begin{cases} y_n(\boldsymbol{\mu}) + y_s(\boldsymbol{\mu}) + \varepsilon_{noise} & \text{deterministic SM} \\ y_n(\boldsymbol{\mu}) + y_s(\boldsymbol{\mu}) + \varepsilon_s(\boldsymbol{\mu}) + \varepsilon_{noise} & \text{statistical SM} \end{cases}$$

The MCMC algorithm is then exploited for the estimation of the unknown parameters values $\boldsymbol{\gamma}$, by starting from a normal prior distribution on the identifiable parameters of mean $[3, 8]^T$ and covariance matrix $C_{prior} = (0.65)\mathbf{I}$. The mean values are the ones proposed in [AP96], while the covariance matrix is in accordance with the ranges used in the previous Chapter. Instead, we assume a uniform prior distribution on the non-identifiable parameters $\boldsymbol{\zeta}$.

We observe that the marginal posterior distribution of σ_v obtained with the ROM is close to the one obtained with the FOM, while the marginal posterior of K is not (see Figure 5.1). This could be caused by the propagation of the approximation error during the inversion procedure. This bias is even bigger when we consider a low-fidelity SM instead of the ROM. The marginal posterior distributions of σ_v and K obtained with the ROM equipped with the ROMES are close to the ones obtained with the FOM (see Figure5.2), if compared with the ones given by the uncorrected ROM (see Figure 5.1). The error estimation provided by the ROMES enables to minimize the propagation of the reduction error during the inversion procedure. On the other hand, considering the prediction variance of the error in the SM prediction,

defined as statistical SM, does not improve the results: the marginal posterior pdf σ_v is even more far from the FOM posterior pdf with respect to the deterministic SM in Figure 5.1.

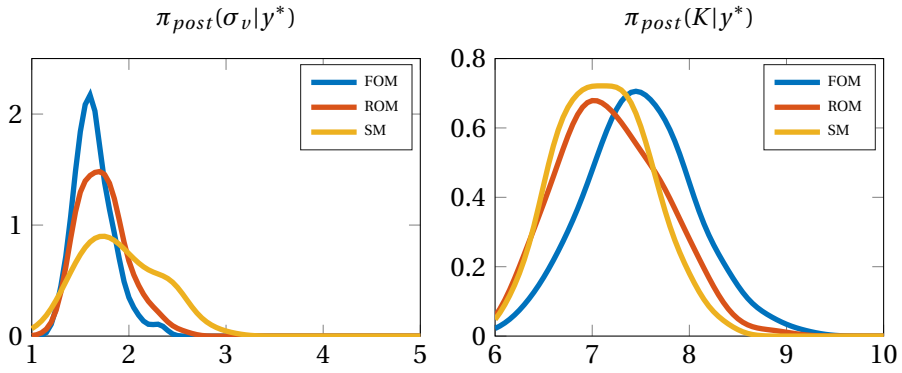

Figure 5.1 – Marginal posterior distributions of the identifiable parameters $\boldsymbol{\gamma} = [\sigma_v, K]^T$ given the noisy observation y^*. The comparison between the FOM marginal posteriors and the ones obtained with the SM and the ROM clearly shows the effect of approximation errors propagation on the results of the inversion procedure.

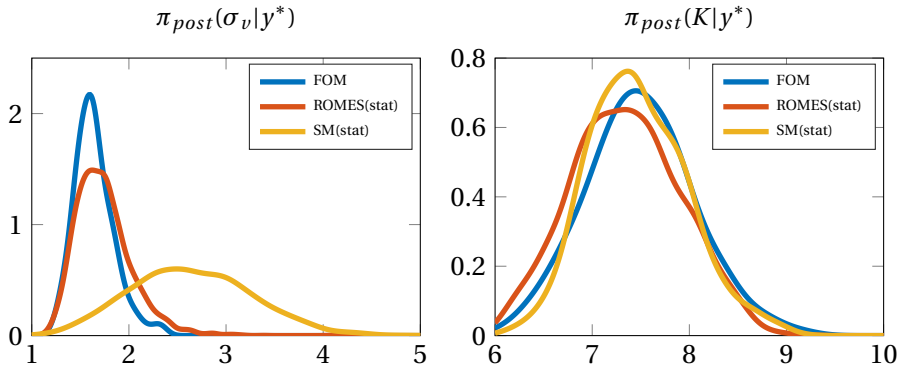

Figure 5.2 – Marginal posterior distributions of the identifiable parameters $\boldsymbol{\gamma} = [\sigma_v, K]^T$ given the noisy observation y^*. The marginal posteriors obtained by combining the ROM with the ROMES are closer to the ones given by the FOM than the uncorrected ROM posterior pdfs. Instead, considering the statistical SM does not improve the results.

A visual representation of the information gain between the prior and the posterior distributions is presented in Figure 5.3, where two random samples from both distributions are reported when FOM, ROM and ROM corrected with ROMES are considered. Moreover, the identifiability indices of Section 5.2.2, whose evaluations on the case at hand are reported in Table 5.1, confirm the a priori ranking of the parameters given by the global sensitivity analysis. However, σ_v is clearly more identifiable than K, as we can also deduced by looking at the variances of the two marginal posterior distributions ($\sigma^2(\sigma_v|y^*)$ is smaller than $\sigma^2(K|y^*)$). As expected, the non-influential parameters $\boldsymbol{\zeta}$ are also non-identifiable.

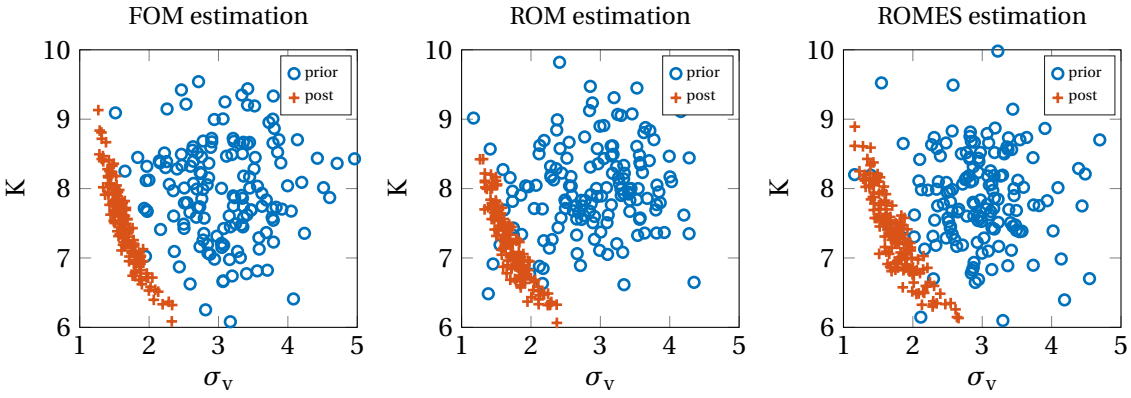

Figure 5.3 – Marginal posterior distributions of the identifiable parameters $\boldsymbol{\gamma}$ given the noisy observation y^* in the case the FOM (left), the ROM (center) and the ROM corrected with the ROMES (right) are used.

Finally, as a validation of the theoretical results presented in Sect. 5.4, we report in Table 5.2 the maximum a-posteriori (MAP) estimate and the KL- divergences for the different models adopted. In this case, we are able to verify the relation between the ROMES corrections and the KL divergence stated in Proposition 4.

Output	σ_v	σ_e	σ_t	K	ε_0
Total effect index S_{T_i}	0.5813	0.0440	0.0480	0.4688	0.0123
Variance reduction $\mathscr{I}_i$	0.6902	0.0608	0.0634	0.1534	0.1112
Entropy index G_i	1.1622	0.0549	0.0544	0.1165	0.0159

Table 5.1 – Total effect indices S_{T_i}, variance reduction indices $\mathscr{I}_i$ and entropy index G_i for $i = 1, \ldots = 5$.

Output	$\hat{\sigma}_v$	$\hat{K}$	KL div σ_v	KL div K
FOM	1.60	7.45		
ROM	1.70	7.45	0.0858	0.1315
SM	1.75	0.3922	0.4593	0.3922
ROM+ROMES(stat)	1.62	7.34	0.0846	0.0412
SM(stat)	2.49	7.37	1.8459	0.0231

Table 5.2 – MAP parameter estimates of the identifiable parameters σ_v and K with the KL divergences between the posterior FOM distribution and the other distributions obtained using the ROM and the SM.

5.6 Conclusions

The combined use of ROMs and ROMESs allows to speed up the solution of Bayesian inverse problems dealing with nonlinear time-dependent PDEs describing the electrical activity of the heart, without affecting the accuracy of the posterior distribution.
The ROM enables to perform the inversion procedure in less than a day with respect to the several days required by a full-order model. Moreover, the inexpensive ROMES evaluation is instrumental to minimize the bias in the resulting posterior distributions. The numerical results finally confirm the theoretical ones proved in this Chapter.

6 | Ensemble Kalman Filter

In this Chapter we develop an ensemble Kalman filter (EnKF) technique that combines reduced-order models (ROM) and ROM error surrogates (ROMES) to solve state/parameter estimation problems governed by nonlinear dynamical systems arising from the discretization of nonlinear time-dependent PDEs.
In particular, we first review in Section 6.1 the state of the art techniques for the solution of Bayesian inverse problems, namely state/parameter estimation problems, when time-dependent outputs are considered. In Section 6.2 we provide a general formulation of the Bayesian filtering, whereas in Section6.3 we introduce the ensemble Kalman filter algorithm. In Section 6.4 we develop the reduced basis EnKF, providing some theoretical results on the quality of the state/parameter estimation given by the RB-EnKF with respect to the full-order EnKF algorithm. In Section 6.5 we show how to integrate the time-dependent ROMES developed in Chapter 3 into the RB-EnKF in order to improve the accuracy in the estimation. Finally, the RB-EnKF equipped with ROMES is tested in Section 6.6 for the identification of three unknown parameters of the FitzHugh-Nagumo ODE system[1].

6.1 Bayesian inverse problems with time-dependent outputs

The estimation of the model parameters, when noisy time-dependent output are considered, can be performed by relying on sequential procedures, such as filtering and data-assimilation techniques, much more reliable than the Markov chain Monte Carlo techniques.
Sequential procedures are currently widely exploited to merge noisy measures or images with the state solution and/or parameters of a PDE model in order to improve the model accuracy

[1] The methodology developed in this Chapter and the numerical results are based upon the work [PMQ16] submitted for publishing.

in reproducing the phenomenon of interest. Although the main applications of sequential state/parameter estimation techniques first arise in weather forecasting [Eve97, DUS+11, Kal03] and hydrology [RME02, HSF+98], several instances of parameter estimation problems have been recently considered in the modeling of cardiovascular applications [DBW+12, LMN16, BMG12].
Typically, the term data-assimilation techniques refers to the estimation of the state of the system, such as the solution of a PDE model, from available data when the model inputs, such as physical coefficients and initial and boundary conditions, are unknown. In this case, the numerical model is exploited to propagate previous information to the current time; then, the data-assimilation procedure corrects the state of the system merging the numerical results with available observations of the phenomenon of interest.
Parameter estimation on the other hand aims at reconstructing the unknown model parameters that lead to a match between numerical outputs and observed sequential data. In this Chapter, we focus on this latter class of problem, by developing a sequential procedure based on the ROM-ROMES framework.

6.1.1 Variational and sequential estimation

We first introduce the state of the art procedures for the solution of state and/or parameter estimation problems from the observation of noisy measurements time-series.
As in the case of real-valued outputs, an additive Gaussian noise model $\boldsymbol{\varepsilon}^{(k)}_{\text{noise}}$ can be adopted to mimic the effect of the source of errors at each time-step:

$$\mathbf{y}^{(k)} = \mathbf{y}^{(k)}_h(\boldsymbol{\mu}) + \boldsymbol{\varepsilon}^{(k)}_{\text{noise}} \qquad \boldsymbol{\varepsilon}^{(k)}_{\text{noise}} \sim \mathcal{N}(\mathbf{0}, \boldsymbol{\Gamma}^{(k)}). \tag{6.1}$$

where $\boldsymbol{\varepsilon}_{\text{noise}}$ is a Gaussian random process with zero mean and covariance $\Gamma^{(k)}$, $k = 1, \dots, N_\tau$.

We divided the interval $(0, T)$ in N_τ windows $(\tau^{(k)}, \tau^{(k+1)})$ of length $\Delta\tau = K\Delta t$, with $k = 0, \dots, N_\tau - 1$ and $K > 1$ (a sketch is reported in Fig. 6.1), on which the data are acquired.

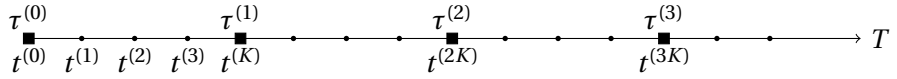

Figure 6.1 – Example of partition of the time interval in windows of length $\Delta\tau = K\Delta t$, $K = 4$.

Given a sequence of noisy realizations $\{\mathbf{y}^{(k)}\}_{k=1}^{N_\tau}$ of (6.1) for the unknown vector $\boldsymbol{\mu}^*$, we can adopt the following approaches for its estimation:

1. *variational methods*, which look at the problem as a PDE-constrained optimization problem, minimizing a least-squared criterion that measures the discrepancy between the observed data $\mathbf{y}^{(k)}$ and the output $\mathbf{y}^{(k)}_h(\boldsymbol{\mu})$ of the numerical model. The problem can be formulated as follows: find the estimate $\hat{\boldsymbol{\mu}}$ of the unknown parameter $\boldsymbol{\mu}^*$ by minimizing a suitable cost functional, such as

$$\hat{\boldsymbol{\mu}} = \arg\min_{\boldsymbol{\mu}\in\mathscr{P}} \sum_{k=1}^{N_\tau} J^{(k)}(\boldsymbol{\mu}) = \arg\min_{\boldsymbol{\mu}\in\mathscr{P}} \left(\frac{1}{2} \sum_{k=1}^{N_\tau} \|\mathbf{y}^{(k)} - \mathbf{y}^{(k)}_h(\boldsymbol{\mu})\|^2_{\boldsymbol{\Gamma}^{(k)}} + \frac{\alpha}{2} \|\boldsymbol{\mu} - \boldsymbol{\mu}_{prior}\|^2_{\mathbf{C}_{prior}} \right),$$

through an iterative strategy. In order to reach a good estimate of the parameters, we need to perform several iterations requiring the numerical approximation of the underlying parametrized PDE model. Here, α is the penalization coefficient of the additional regularization term based on the confidence in the PDE model given by the available *a priori* information (see Section 5.1). For further details see [LDT86, DMP+12].

2. *sequential methods*, which update the state and/or parameters at each instant $\tau^{(k)}$, $k = 1, \dots, N_t$, by properly weighting the discrepancy between the measured data $\mathbf{y}^{(k)}$ and the numerical output $\mathbf{y}_h^{(k)}(\boldsymbol{\mu})$. When the output is linear with respect to the state and the parameters, the Kalman filter (KF) [Kal60] leads to the same results of the variational methods previously introduced with $\alpha = 1$. Suitable modifications of the method have been considered in order to deal with nonlinear models, among which we mention the extended KF, the unscented KF and the ensemble KF (for a complete review on filtering methods see, e.g., [HRW12, Sim06]). In this Thesis, we will refer to this group of method as *approximated* KFs.

   Adopting the approach presented in [LSZ15], we can formulate the filtering problem in the Bayesian framework as follows: given an additive Gaussian noise model and a Gaussian *a priori* distribution of the parameters, the probability distribution $\pi_{post}^{(k)}$, $k = 1, \dots, N_t$, can be approximated as follows

$$\pi_{post}^{(k)}(\boldsymbol{\mu} \,|\, \mathbf{y}^{(1:k)}) \propto \exp\left(-\frac{1}{2}\|\mathbf{y}^{(k)} - \mathbf{y}_h^{(k)}(\boldsymbol{\mu})\|^2_{\boldsymbol{\Gamma}^{(k)}} - \frac{1}{2}\|\boldsymbol{\mu} - \bar{\boldsymbol{\mu}}^{(k-1)}\|^2_{\mathbf{C}^{(k-1)}}\right), \tag{6.2}$$

   where $\bar{\boldsymbol{\mu}}^{(k)}$ and $\mathbf{C}^{(k-1)}$ are, respectively, the mean and the covariance associated to $\pi_{post}^{(k-1)}$. For the sake of completeness, we also cite the Luenberger feedbacks [Lue71], which are filters based on the dissipative properties of the PDE system and the direct observation of both input and outputs quantities.

These methodologies are recently widely exploited for the personalization of electromechanical models starting from clinical MRI data [CWH+16, SMC+06, MCLT09]: in particular we mention the variational approaches [SMCC+06, DBW+12], the unscented KF [MDS+13b, NBG+13] and the Luenberger feedbacks [MCLT08, SCC+11]. However, applying these procedures to cardiac models is a very challenging task due to considerable computational costs related to the PDEs approximation.

ROMs can be exploited to reduce: *(i)* the model complexity, enabling a computationally efficient evaluation of the input/output map (see e.g. [DH16, HK09, HK07, NCD+15]) or *(ii)* the dimensionality of the uncertainty space, enabling a computationally efficient sequential estimation of the quantities of interest (see e.g. [SCH+16, MC11, Sim06, LM14b]). Both strategies lead to reduced-order formulation of the filtering methods. Usually there is no clear distinction in their definition, even if they are considerably different. As a matter of fact, the former could be not consistent, i.e. it is affected by the reduction error, while the latter might lack of stability [MC11].

When a FOM is replaced by a ROM, the propagation of the reduced-order approximation errors during the inversion procedure could lead to biased estimates of the unknown state/parameter [MPL16, CGM+13]. Moreover, the ROM dimension can grow quite dramatically to ensure the achievement of a prescribed accuracy. Consequently, this entails a dramatic loss of computational efficiency. With respect to already existing approaches, we integrate the ROM-ROMES framework into the ensemble Kalman filter to address directly the model complexity.

This choice is motivated by the fact that the EnKF is shown to better handle large dimensional state/parameters vectors and nonlinear errors evolution, characterizing electrophysiology models, with respect to the variational methods and the other approximated KFs [Eve09].

6.2 Problem formulation

In this section we introduce some basic notions on the problem formulation and on the Bayesian filtering instrumental to set up the whole framework.

6.2.1 Forward problem

We focus on the dynamical system arising from the discretization of the system of PDEs that models cardiac electrophysiology, such as the monodomain equation (1.4) coupled with a ionic model. We consider the state vector $\mathbf{u}_h^{(\ell)}(\boldsymbol{\mu}) \in \mathbb{R}^{N_h}$, $\ell = 1,\dots,N_t$, as the solution of the unsteady nonlinear dynamical system

$$\begin{cases} \left(\dfrac{\mathbf{M}(\boldsymbol{\mu})}{\Delta t} + \mathbf{A}(\boldsymbol{\mu})\right)\mathbf{u}_h^{(\ell+1)} = \dfrac{\mathbf{M}(\boldsymbol{\mu})}{\Delta t}\mathbf{u}_h^{(\ell)} + \mathbf{I}_{app}^{(\ell+1)}(\boldsymbol{\mu}) - \mathbf{I}_{ion}(\mathbf{u}_h^{(\ell)}, \mathbf{w}_h^{(\ell)}; \boldsymbol{\mu}) & \ell = 0,\dots,N_t-1 \\ \mathbf{u}_h^{(0)} = \mathbf{u}_0(\boldsymbol{\mu}) & \\ \mathbf{w}_h^{(\ell+1)} = \mathbf{w}_h^{(\ell)} + g(\mathbf{u}_h^{(\ell)}, \mathbf{w}_h^{(\ell)}; \boldsymbol{\mu}) & t \in (0,T) \\ \mathbf{w}_h^{(0)} = \mathbf{w}_0(\boldsymbol{\mu}), & \end{cases} \tag{6.3}$$

given the value of the time-invariant parameter vector $\boldsymbol{\mu} \in \mathscr{P}$.

We considers as numerical output of the model over each window $(\tau^{(k)}, \tau^{(k+1)})$ the values

$$\mathbf{y}_h^{(k+1)}(\boldsymbol{\mu}) = \int_{\tau^{(k)}}^{\tau^{(k+1)}} \mathbf{H}\mathbf{u}_h(t;\boldsymbol{\mu})\,dt \simeq \Delta t \mathbf{H} \sum_{\ell=Kk}^{K(k+1)} \omega_\ell \mathbf{u}_h(t^{(\ell)};\boldsymbol{\mu}), \qquad k = 0,\dots,N_\tau - 1, \tag{6.4}$$

where ω_ℓ, $\ell = Kk,\dots,K(k+1)$ are weights depending on the chosen quadrature formula over $(\tau^{(k)}, \tau^{(k+1)})$ and $\mathbf{H}$ is a matrix arising from the discretization of the observation operator. In this way, we end up with a vector of scalar values on each window consistent with the formulation of the noisy measurements process (6.1).

Remark 4. *For the case at hand data are generated from the numerical scheme, hence they are available at each time step. The output* (6.4) *contains $K > 1$ observations of the solution, one for each time-step of the assimilation window $(\tau^{(k)}, \tau^{(k+1)})$. A possible alternative would be to consider as outputs only the measured values at each $t = \tau^{(k+1)}$, i.e.*

$$\mathbf{y}_h^{(k+1)}(\boldsymbol{\mu}) = \mathbf{H}\mathbf{u}_h(\tau^{(k+1)};\boldsymbol{\mu}) \qquad k = 0,\dots,N_\tau - 1, \tag{6.5}$$

however providing less information than (6.4).

6.2.2 Bayesian data assimilation

We formulate the problem of estimating $\boldsymbol{\mu} \in \mathscr{P} \subset \mathbb{R}^d$ and $\mathbf{u}_h \in X_h$ from noisy data $\{\mathbf{y}^{(k)}\}_{k=1}^{N_\tau} \in \mathbb{R}^{N_\tau \times s}$ as a Bayesian data assimilation problem. Following the approach proposed in [AA99, Ham06], the solution of this problem at iteration $k = 1,\dots,N_\tau$, is given by a multivariate

probability density function (pdf) $\pi_{post} : \mathscr{P} \times X_h \to \mathbb{R}_0^+$ of the parameters $\boldsymbol{\mu}$ and the state $\mathbf{u}_h$ given the noisy data $\mathscr{Y}^{(k)} = \{\mathbf{y}^{(i)}\}_{i=1}^{k}$. Thanks to the *Bayes theorem*, we can express π_{post} as

$$\pi_{post}\left([\boldsymbol{\mu}, \mathbf{u}_h^{(k)}]^T \,\middle|\, \mathscr{Y}^{(k)} \right) = \frac{1}{\eta(\mathbf{y})} \pi\left(\mathscr{Y}^{(k)} \,\middle|\, [\boldsymbol{\mu}, \mathbf{u}_h^{(k)}]^T \right) \pi_{\text{prior}}\left([\boldsymbol{\mu}, \mathbf{u}_h^{(k)}]^T \right), \tag{6.6}$$

where $\pi_{\text{prior}} : \mathscr{P} \times X_h \to \mathbb{R}_0^+$ is the *prior* pdf of the parameters/state vector, $\pi : \mathbb{R}^{k \times s} \to \mathbb{R}_0^+$ the *likelihood* function and $\eta(\mathbf{s})$ a suitable normalization constant, which does not affect the inversion step [Tar05, LSZ15]. We consider an additive noise model: given $\boldsymbol{\mu} = \boldsymbol{\mu}^*$, set

$$\mathbf{y}^{(k)} = \mathbf{y}_h^{(k)}(\boldsymbol{\mu}^*) + \boldsymbol{\varepsilon}_{\text{noise}} \qquad \forall k = 1, \dots, N_\tau \tag{6.7}$$

where we assume that the noise is independent from a time step to another and is modeled by a gaussian random variable $\boldsymbol{\varepsilon}_{\text{noise}}^{(k)} \sim \mathcal{N}(\mathbf{0}, \boldsymbol{\Gamma}^{(k)})$, with covariance matrix $\Gamma^{(k)} \in \mathbb{R}^{s \times s}$. Under these assumptions, the likelihood function can be expressed as:

$$\pi\left(\mathscr{Y}^{(k)} \,\middle|\, [\boldsymbol{\mu}, \mathbf{u}_h^{(k)}]^T \right) = \pi\left(\mathbf{y}^{(k)} \,\middle|\, [\boldsymbol{\mu}, \mathbf{u}_h^{(k)}]^T \right) \pi\left(\mathscr{Y}^{(k-1)} \,\middle|\, [\boldsymbol{\mu}, \mathbf{u}_h^{(k)}]^T \right),$$

and, consequently, (6.6) becomes

$$\begin{aligned} \pi_{post}\left([\boldsymbol{\mu}, \mathbf{u}_h^{(k)}]^T \,\middle|\, \mathscr{Y}^{(k)} \right) &= \frac{1}{\eta(\mathbf{y})} \pi\left(\mathbf{y}^{(k)} \,\middle|\, [\boldsymbol{\mu}, \mathbf{u}_h^{(k)}]^T \right) \pi\left(\mathscr{Y}^{(k-1)} \,\middle|\, [\boldsymbol{\mu}, \mathbf{u}_h^{(k)}]^T \right) \pi_{\text{prior}}\left([\boldsymbol{\mu}, \mathbf{u}_h^{(k)}]^T \right) \\ &= \frac{1}{\eta(\mathbf{y})} \pi\left(\mathbf{y}^{(k)} \,\middle|\, [\boldsymbol{\mu}, \mathbf{u}_h^{(k)}]^T \right) \pi_{post}\left([\boldsymbol{\mu}, \mathbf{u}_h^{(k)}]^T \,\middle|\, \mathscr{Y}^{(k-1)} \right). \end{aligned} \tag{6.8}$$

Equation (6.8) expresses the sequential updating of the posterior pdf of $[\boldsymbol{\mu}, \mathbf{u}_h]^T$ given the measurement vectors $\mathscr{Y}^{(k)}$. Under the assumption that $\boldsymbol{\varepsilon}_{\text{noise}}$ is normally distributed, we have that

$$\pi\left(\mathbf{y}^{(k)} \middle| [\boldsymbol{\mu}, \mathbf{u}_h^{(k)}]^T \right) = \frac{1}{(2\pi)^{(s/2)} |\boldsymbol{\Gamma}^{(k)}|^{\frac{1}{2}}} \exp\left\{ -\frac{1}{2} \|\mathbf{y}^{(k)} - \mathbf{y}_h^{(k)}(\boldsymbol{\mu})\|^2_{\boldsymbol{\Gamma}^{(k)}} \right\}, \tag{6.9}$$

where the weighted norm $\|\cdot\|_{\boldsymbol{\Gamma}}$ is such that $\|\mathbf{v}\|^2_{\boldsymbol{\Gamma}} = \mathbf{v}^T \boldsymbol{\Gamma}^{-1} \mathbf{v}$, $\mathbf{v} \in \mathbb{R}^s$. For the sake of notation we will use the shorthand $\pi^{(k)}$ and $\pi_{post}^{(k)}$ to denote $\pi(\mathbf{y}^{(k)} | [\boldsymbol{\mu}, \mathbf{u}_h^{(k)}]^T)$ and $\pi_{post}([\boldsymbol{\mu}, \mathbf{u}_h^{(k)}]^T | \mathscr{S}^{(k)})$, respectively.

We observe that in principle the posterior updates $\{\pi_{post}^{(k)}\}_{k=1}^{N_\tau}$ can be approximated by adopting a sampling technique, such as the Markov chain Monte Carlo (MCMC). However, the computationally expensive solution of the nonlinear dynamical system, required to evaluate $\mathbf{y}_h(\boldsymbol{\mu})$, would make MCMC-based approximation extremely inefficient.
In order to efficiently update $\{\pi_{post}^{(k)}\}_{k=1}^{N_\tau}$, we would prefer to update only the posterior mean of the state/parameter vector and its covariance using suitable updating formula. Since the map $\boldsymbol{\mu} \to \mathbf{y}_h(\boldsymbol{\mu})$ is highly nonlinear, it is not possible to adopt the standard KF, but we need to rely on *approximated* Gaussian filters, such as the unscented KF or the ensemble KF (ensemble-based assimilation techniques are indeed well suited in situations where linearity and gaussianity assumptions are not matched).
In this work, we consider the *ensemble Kalman filter*, which takes advantage of a randomly generated sample to successively approximate the distribution of $\{\pi_{post}^{(k)}\}_{k=1}^{N_\tau}$ through the sample mean and covariance of the state/parameter vector. In the following section we recall the basic features of this technique; a more detailed overview can be found e.g. in [Eve97, ILS13].

6.3 Ensemble Kalman filter

The ensemble Kalman filter (EnKF) is a recursive filter, based on the idea of updating an *ensemble* of particles using the prediction/analysis procedure introduced in the previous section [Eve03, HM01, RER+15]. In our case, by *ensemble* of particle we mean a sample of N_e parameter vectors

$$\mathscr{P}_h^{(k)} = \{\boldsymbol{\mu}_{h,q}^{(k)}\}_{q=1}^{N_e}, \qquad k = 1, \dots, N_\tau,$$

where $\boldsymbol{\mu}_{h,q}^{(k)}$ denotes the value of a parameter vector $\boldsymbol{\mu}_{h,q}$ at the $k-th$ iteration, and the associated ensemble of N_e state solutions

$$\mathscr{U}_h^{(k)} = \{\mathbf{u}_h^{(k)}(\boldsymbol{\mu}),\ \boldsymbol{\mu} \in \mathscr{P}_h^{(k)}\}, \qquad k = 1, \dots, N_\tau.$$

Moreover, let us introduce, for any $k = 1, \dots, N_\tau$, the sample mean vectors

$$\overline{\mathbf{u}}_h^{(k)} = \frac{1}{N_e} \sum_{\boldsymbol{\mu} \in \mathscr{P}_h^{(k-1)}} \mathbf{u}_h^{(k)}(\boldsymbol{\mu}), \qquad \overline{\mathbf{y}}_h^{(k)} = \frac{1}{N_e} \sum_{\boldsymbol{\mu} \in \mathscr{P}_h^{(k-1)}} \mathbf{y}_h^{(k)}(\boldsymbol{\mu}), \qquad \overline{\boldsymbol{\mu}}_h^{(k)} = \frac{1}{N_e} \sum_{\boldsymbol{\mu} \in \mathscr{P}_h^{(k)}} \boldsymbol{\mu}, \tag{6.10}$$

the sample covariance of the output

$$\mathbf{C}_{y_h y_h}^{(k)} = \frac{1}{N_e - 1} \sum_{\boldsymbol{\mu} \in \mathscr{P}_h^{(k-1)}} (\mathbf{y}_h^{(k)}(\boldsymbol{\mu}) - \overline{\mathbf{y}}_h^{(k)})(\mathbf{y}_h^{(k)}(\boldsymbol{\mu}) - \overline{\mathbf{y}}_h^{(k)})^T \in \mathbb{R}^{s \times s} \tag{6.11}$$

and the sample cross-covariances

$$\mathbf{C}_{\mu_h y_h}^{(k)} = \frac{1}{N_e - 1} \sum_{\boldsymbol{\mu} \in \mathscr{P}_h^{(k-1)}} (\boldsymbol{\mu} - \overline{\boldsymbol{\mu}}^{(k-1)})(\mathbf{y}_h^{(k)}(\boldsymbol{\mu}) - \overline{\mathbf{y}}_h^{(k)})^T \in \mathbb{R}^{d \times s}, \tag{6.12}$$

$$\mathbf{C}_{u_h y_h}^{(k)} = \frac{1}{N_e - 1} \sum_{\boldsymbol{\mu} \in \mathscr{P}_h^{(k-1)}} (\mathbf{u}_h^{(k)}(\boldsymbol{\mu}) - \overline{\mathbf{u}}_h^{(k)})(\mathbf{y}_h^{(k)}(\boldsymbol{\mu}) - \overline{\mathbf{y}}_h^{(k)})^T \in \mathbb{R}^{N_h \times s}. \tag{6.13}$$

Hence, starting from the initial ensemble $\{\mathscr{P}_h^{(0)}, \mathscr{U}_h^{(0)}\}$ sampled from the prior distribution, and the given data $\mathbf{y}^{(k)}$, $k = 1, \dots, N_\tau$, the *prediction-analysis* procedure of the EnKF is given by the following two stages recursion:

1. *prediction stage*: at each time-step k
   - compute the solution $\mathbf{u}_h^{(k+1)}(\boldsymbol{\mu})$ of the forward problem over $[\tau^{(k)}, \tau^{(k+1)})$ by solving (6.3) with initial datum $\mathbf{u}_h^{(k)}(\boldsymbol{\mu}) \in \mathscr{U}^{(k)}$, and evaluate the noisy measurement (6.1) given the output $\mathbf{y}_h^{(k+1)}(\boldsymbol{\mu})$ for each $\boldsymbol{\mu} \in \mathscr{P}_h^{(k)}$;
   - compute the sample means $\overline{\mathbf{u}}_h^{(k+1)}$, $\overline{\mathbf{y}}_h^{(k+1)}$ and $\overline{\boldsymbol{\mu}}^{(k)}$;
   - compute the sample covariance $\mathbf{C}_{y_h y_h}^{(k+1)} \in \mathbb{R}^{s \times s}$ and the cross-covariances $\mathbf{C}_{\mu_h y_h}^{(k+1)} \in \mathbb{R}^{d \times s}$ and $\mathbf{C}_{u_h y_h}^{(k+1)} \in \mathbb{R}^{N_h \times s}$.
2. *analysis stage*: update the state/parameters ensemble by taking advantage of the new information computed during the prediction stage, through the following *KF updating*

formula:

$$\begin{bmatrix} \boldsymbol{\mu}_{h,q}^{(k+1)} \\ \mathbf{u}_h^{(k+1)}(\boldsymbol{\mu}_{h,q}^{(k+1)}) \end{bmatrix} = \begin{bmatrix} \boldsymbol{\mu}_{h,q}^{(k)} \\ \mathbf{u}_h^{(k+1)}(\boldsymbol{\mu}_{h,q}^{(k)}) \end{bmatrix} + \underbrace{\begin{bmatrix} \mathbf{C}_{\mu_h y_h}^{(k+1)} \\ \mathbf{C}_{u_h y_h}^{(k+1)} \end{bmatrix} (\boldsymbol{\Gamma}^{(k)} + \mathbf{C}_{y_h y_h}^{(k+1)})^{-1}}_{\text{Kalman gain}} (\mathbf{y}_q^{(k+1)} - \mathbf{y}_h^{(k+1)}(\boldsymbol{\mu}_{h,q}^{(k)})), \tag{6.14}$$

for each $q = 1, \dots, N_e$, where N_e realizations of the noise $\boldsymbol{\varepsilon}_q^{(k+1)}$, $q = 1, \dots, N_e$, are added to the data to generate $\mathbf{y}_q^{(k+1)} = \mathbf{y}_h^{(k+1)}(\boldsymbol{\mu}^*) + \boldsymbol{\varepsilon}_q^{(k+1)}$.

Then, at each iteration we estimate the unknown parameter vector by computing the sample mean $\hat{\boldsymbol{\mu}}_h = \overline{\boldsymbol{\mu}}_h$; we also compute the sample covariance matrix

$$\mathbf{C}_{\mu_h \mu_h}^{(k+1)} = \frac{1}{N_e - 1} \sum_{\boldsymbol{\mu} \in \mathscr{P}_h^{(k+1)}} (\boldsymbol{\mu} - \overline{\boldsymbol{\mu}}^{(k+1)})(\boldsymbol{\mu} - \overline{\boldsymbol{\mu}}^{(k+1)})^T \in \mathbb{R}^{d \times d}, \tag{6.15}$$

in order to quantify the variability of the resulting parameter ensemble $\mathscr{P}_h^{(k+1)}$. For a formal derivation of the EnKF algorithm see [PMQ16], while for further properties and results, see e.g. [BLL+13, KLS14, ESS14]. A detailed description of the EnKF is reported in Algorithm 7, while a schematic representation of the EnKF loop is presented in Figure 6.2.

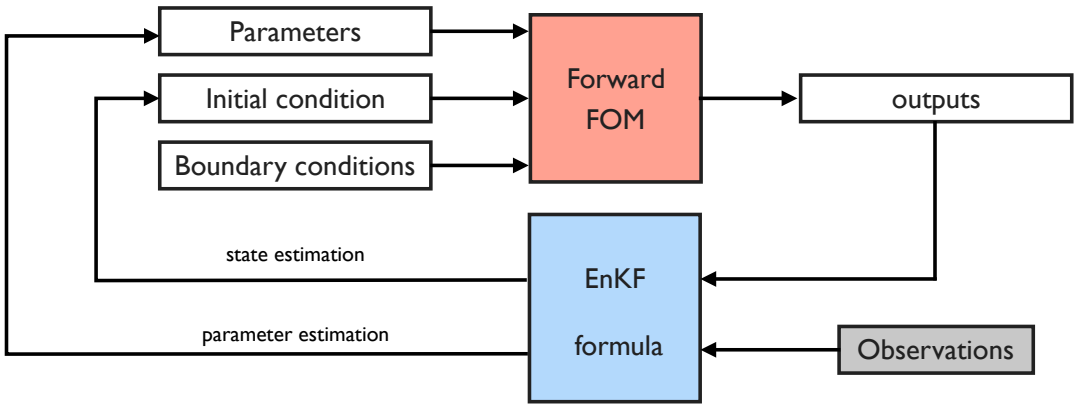

Figure 6.2 – EnKF loop for state-parameter estimation. The state update is used as new initial condition of the forward problem over each time window.

6.4 Reduced basis Ensemble Kalman filter

The sequential update through the EnKF requires, at each step, the solution of the forward problem on the window $[\tau^{(k)}, \tau^{(k+1)})$ for each particle in the ensemble. The large size of this latter and the nonlinear nature of the forward problem may involve moderately large computational costs. For these reasons, we rather rely on the RB method for the fast evaluation of the *prediction* stage, implementing a hyper-reduction procedure based on the (discrete) empirical interpolation method for managing nonlinear terms more efficiently.

Algorithm 7 Full-order Ensemble Kalman filter procedure

procedure ENKF
  Initialization
  $\{\mathscr{P}_h^{(0)}, \mathscr{U}_h^{(0)}\} \leftarrow$ sampling N_e particles from π_{prior}
  for $q = 1 : N_e$, $k = 1 : N_\tau$ **do**
    $\mathbf{y}_q^{(k)} \leftarrow \mathbf{y}_h^{(k)}(\boldsymbol{\mu}^*) + \boldsymbol{\varepsilon}_q^{(k)}$
  end for
  for $k = 0 : N_\tau - 1$ **do**
    Prediction stage:
    for $q = 1 : N_e$ **do**
      $\mathbf{u}_h^{(k+1)}(\boldsymbol{\mu}_{h,q}^{(k)}) \leftarrow$ solve forward problem (6.3) with initial datum $\mathbf{u}_h^{(k)}(\boldsymbol{\mu}_{h,q}^{(k)})$
    end for
    compute means $\overline{\mathbf{u}}_h^{(k+1)}, \overline{\mathbf{y}}_h^{(k+1)}$, and $\overline{\boldsymbol{\mu}}_h^{(k)}$ by (6.10)
    compute covariance $\mathbf{C}_{y_h y_h}^{(k+1)}$ by (6.11)
    compute cross-covariances $\mathbf{C}_{u_h y_h}^{(k+1)}$ and $\mathbf{C}_{\mu_h y_h}^{(k+1)}$ by (6.12)
    Update stage:
    for $q = 1 : N_e$ **do**
      update each state/parameters particle in $\{\mathscr{P}_h^{(k)}\}$ using (6.14)
    end for
  end for
end procedure

Given a suitable ROM for approximating the solution of the forward problem, a reduced EnKF can be obtained by replacing the full-order output evaluation with the reduced-order one. Since we have adopted the RB method, we will refer to the resulting procedure as to the reduced basis ensemble Kalman filter (RB-EnKF). We define the ensemble of N_e parameters as

$$\mathscr{P}_n^{(k)} = \{\boldsymbol{\mu}_{n,q}^{(k)}\}_{q=1}^{N_e}, \qquad k = 0, \dots, N_\tau,$$

and the associated ensemble of reduced state solution

$$\mathscr{U}_n^{(k)} = \{\mathbf{u}_n(\boldsymbol{\mu}),\ \boldsymbol{\mu} \in \mathscr{P}_n^{(k)}\}, \qquad k = 0, \dots, N_\tau.$$

Here, we denote the particles with the subscript n in order to remark the dimension of the state vector and the fact that each particle follows the reduced-order dynamics, which is only an approximation of the full-order one.

We also compute the means (6.10), the covariance (6.11) and the cross-covariances (6.12)–(6.13) by relying on the reduced-order quantities. Hence, starting from the initial ensemble $\{\mathscr{P}_n^{(0)}, \mathscr{U}_n^{(0)}\}$, sampled from the prior distribution of the state and parameters vector, the RB-EnKF can be built with a two-stage recursion, similarly to what we did in Section 6.3:

1. *prediction stage*: at each step k
   - compute the reduced solution $\mathbf{u}_n^{(k+1)}$ of the forward ROM (obtained by projecting (6.3) on the reduced space) on the window $[\tau^{(k)}, \tau^{(k+1)})$ with initial datum $\mathbf{u}_n^{(k)}(\boldsymbol{\mu}) \in \mathscr{U}_n^{(k)}$, and the relative output $\mathbf{y}_n^{(k+1)}$ for each $\boldsymbol{\mu} \in \mathscr{P}_n^{(k)}$;

- compute the sample means $\overline{\mathbf{u}}_n^{(k+1)}$, $\overline{\mathbf{y}}_n^{(k+1)}$ and $\overline{\boldsymbol{\mu}}_n^{(k)}$;
- compute the sample covariance $\mathbf{C}_{y_n y_n}^{(k+1)} \in \mathbb{R}^{s\times s}$ and the cross-covariance matrices $\mathbf{C}_{\mu_n y_n}^{(k)} \in \mathbb{R}^{d\times s}$ and $\mathbf{C}_{u_n y_n}^{(k+1)} \in \mathbb{R}^{n\times s}$, using formulas (6.11)–(6.13) by replacing $\mathbf{y}_h$, $\mathbf{u}_h$ and $\mathscr{P}_h^{(k-1)}$ with $\mathbf{y}_n$, $\mathbf{u}_n$ and $\mathscr{P}_n^{(k-1)}$, respectively;

2. *analysis stage*: update the state/parameters ensemble through the following *reduced KF updating formula*:

$$\begin{bmatrix} \boldsymbol{\mu}_{n,q}^{(k+1)} \\ \mathbf{u}_n^{(k+1)}(\boldsymbol{\mu}_{n,q}^{(k+1)}) \end{bmatrix} = \begin{bmatrix} \boldsymbol{\mu}_{n,q}^{(k)} \\ \mathbf{u}_n^{(k+1)}(\boldsymbol{\mu}_{n,q}^{(k)}) \end{bmatrix} + \underbrace{\begin{bmatrix} \mathbf{C}_{\mu_n y_n}^{(k+1)} \\ \mathbf{C}_{u_n y_n}^{(k+1)} \end{bmatrix} (\boldsymbol{\Gamma}^{(k)} + \mathbf{C}_{y_n y_n}^{(k+1)})^{-1}}_{\text{reduced Kalman gain}} (\mathbf{y}_q^{(k+1)} - \mathbf{y}_n^{(k+1)}(\boldsymbol{\mu}_{n,q}^{(k)})), \tag{6.16}$$

for each $q = 1,\dots,N_e$.

In this way, we are neglecting the error between the ROM and the FOM, which nevertheless might introduce a bias in the whole estimation procedure, as shown in the following section.

6.4.1 Effectivity of the RB-EnKF

We now want to prove that the solution of the state/parameter estimation given by the RB-EnKF algorithm converges, as long as the ROM dimension n increases, to the one which would have been obtained by relying on the full-order EnKF. With this aim, we compare the resulting state/parameters ensemble $\{\mathscr{P}^{(N_\tau)}, \mathscr{U}^{(N_\tau)}\}$ generated by the full-order EnKF with the reduced one $\{\mathscr{P}_n^{(N_\tau)}, \mathscr{U}_n^{(N_\tau)}\}$, for any dimension n, generated by the RB-EnKF. With this goal, let us denote by

$$\mathbf{e}^{(k)} = \begin{bmatrix} \mathbf{e}_\mu^{(k)} \\ \mathbf{e}_u^{(k)} \end{bmatrix} = \begin{bmatrix} \hat{\boldsymbol{\mu}}_h^{(k)} \\ \hat{\mathbf{u}}_h^{(k)} \end{bmatrix} - \begin{bmatrix} \hat{\boldsymbol{\mu}}_n^{(k)} \\ \mathbf{V}\hat{\mathbf{u}}_n^{(k)} \end{bmatrix}, \qquad k = 1,\dots,N_\tau - 1,$$

the error between the means $[\hat{\boldsymbol{\mu}}_n^{(k)}, \mathbf{V}\hat{\boldsymbol{u}}_n^{(k)}]^T$ and $[\hat{\boldsymbol{\mu}}_h^{(k)}, \hat{\boldsymbol{u}}_h^{(k)}]^T$ computed over the respective ensembles. Then, let us denote by

$$\gamma_h^{(k)} = \|(\boldsymbol{\Gamma}^{(k)} + \mathbf{C}_{y_h y_h}^{(k)})^{-1}\| \qquad \gamma_n^{(k)} = \|(\boldsymbol{\Gamma}^{(k)} + \mathbf{C}_{y_n y_n}^{(k)})^{-1}\|.$$

being $\|\cdot\|$ the Euclidean norm (from now on, in this chapter we will use the following notation). Then, at each step $k = 1,\dots,N_t$ we can bound the error $\mathbf{e}^{(k)}$ as stated in the following:

Proposition 5. *For any* $0 < n < N_h$, $k = 1,\dots,N_\tau$, *the following relationships hold:*

$$\|\mathbf{e}_\mu^{(k)}\| \le \|\mathbf{e}_\mu^{(k-1)}\| + c_{\mu,1}^{(k)}\|\overline{\mathbf{y}}_h^{(k)} - \overline{\mathbf{y}}_n^{(k)}\| + c_{\mu,2}^{(k)}\|\mathbf{C}_{\mu_h y_h}^{(k)} - \mathbf{C}_{\mu_n y_n}^{(k)}\| + c_{\mu,3}^{(k)}\|\mathbf{C}_{y_h y_h}^{(k)} - \mathbf{C}_{y_n y_n}^{(k)}\|, \tag{6.17}$$

$$\|\mathbf{e}_u^{(k)}\| \le \|\mathbf{e}_u^{(k-1)}\| + c_{u,1}^{(k)}\|\overline{\mathbf{y}}_h^{(k)} - \overline{\mathbf{y}}_n^{(k+1)}\| + c_{u,2}^{(k)}\|\mathbf{C}_{u_h y_h}^{(k)} - \mathbf{V}\mathbf{C}_{u_n y_n}^{(k)}\| + c_{u,3}^{(k)}\|\mathbf{C}_{y_h y_h}^{(k)} - \mathbf{C}_{y_n y_n}^{(k)})\|, \tag{6.18}$$

where

$$c_{\mu,1}^{(k)} = \gamma_h^{(k)}\|\mathbf{C}_{\mu_h y_h}^{(k)}\|, \qquad c_{u,1}^{(k)} = \gamma_h^{(k)}\|\mathbf{C}_{u_h y_h}^{(k)}\|,$$

$$c_{\mu,2}^{(k)} = c_{u,2}^{(k)} = \gamma_h^{(k)}\|\mathbf{y}^{(k)} - \overline{\mathbf{y}}_n^{(k)}\|,$$

$$c_{\mu,3}^{(k)} = \gamma_n^{(k)}\gamma_h^{(k)}\|\mathbf{C}_{\mu_n y_n}^{(k)}\|_{\mathbb{R}^{d\times s}}\|\mathbf{y}^{(k)} - \overline{\mathbf{y}}_n^{(k)}\|, \qquad c_{u,3}^{(k)} = \gamma_n^{(k)}\gamma_h^{(k)}\|\mathbf{V}\mathbf{C}_{u_n y_n}^{(k)}\|\|\mathbf{y}^{(k)} - \overline{\mathbf{y}}_n^{(k)}\|.$$

Proof. By averaging (6.14) over the sample $\mathscr{P}^{(k-1)}$, we obtain the following update equation for the estimate $[\hat{\boldsymbol{\mu}}_h, \hat{\boldsymbol{u}}_h]^T$

$$\begin{bmatrix} \hat{\boldsymbol{\mu}}_h^{(k)} \\ \hat{\mathbf{u}}_h^{(k)} \end{bmatrix} = \begin{bmatrix} \hat{\boldsymbol{\mu}}_h^{(k-1)} \\ \hat{\mathbf{u}}_h^{(k-1)} \end{bmatrix} + \begin{bmatrix} \mathbf{C}_{\mu_h y_h}^{(k)} \\ \mathbf{C}_{u_h y_h}^{(k)} \end{bmatrix} (\boldsymbol{\Gamma}^{(k)} + \mathbf{C}_{y_h y_h}^{(k)})^{-1} (\mathbf{y}^{(k)} - \overline{\mathbf{y}}_h^{(k)}); \tag{6.19}$$

by doing the same on (6.16) we have instead

$$\begin{bmatrix} \hat{\boldsymbol{\mu}}_n^{(k)} \\ \hat{\mathbf{u}}_n^{(k)} \end{bmatrix} = \begin{bmatrix} \hat{\boldsymbol{\mu}}_n^{(k-1)} \\ \hat{\mathbf{u}}_n^{(k-1)} \end{bmatrix} + \begin{bmatrix} \mathbf{C}_{\mu_n y_n}^{(k)} \\ \mathbf{C}_{u_n y_n}^{(k)} \end{bmatrix} (\boldsymbol{\Gamma}^{(k)} + \mathbf{C}_{y_n y_n}^{(k)})^{-1} (\mathbf{y}^{(k)} - \overline{\mathbf{y}}_n^{(k)}). \tag{6.20}$$

By subtracting (6.20) from (6.19), we can express $\mathbf{e}^{(k)} = \mathbf{e}^{(k-1)} + \mathbf{e}_I^{(k)} + \mathbf{e}_{II}^{(k)}$, being

$$\mathbf{e}_I^{(k)} = \begin{bmatrix} \mathbf{C}_{\mu_h y_h}^{(k)} \\ \mathbf{C}_{u_h y_h}^{(k)} \end{bmatrix} (\boldsymbol{\Gamma}^{(k)} + \mathbf{C}_{y_h y_h}^{(k)})^{-1} (\overline{\mathbf{y}}_n^{(k)} - \overline{\mathbf{y}}_h^{(k)}),$$

$$\mathbf{e}_{II}^{(k)} = \left(\begin{bmatrix} \mathbf{C}_{\mu_h y_h}^{(k)} \\ \mathbf{C}_{u_h y_h}^{(k)} \end{bmatrix} (\boldsymbol{\Gamma}^{(k)} + \mathbf{C}_{y_h y_h}^{(k)})^{-1} - \begin{bmatrix} \mathbf{C}_{\mu_n y_n}^{(k)} \\ \mathbf{V}\mathbf{C}_{u_n y_n}^{(k)} \end{bmatrix} (\boldsymbol{\Gamma}^{(k)} + \mathbf{C}_{y_n y_n}^{(k)})^{-1} \right) (\mathbf{y}^{(k)} - \overline{\mathbf{y}}_n^{(k)}). \tag{6.21}$$

Then, the following error estimates hold

$$\|\mathbf{e}_{I,\mu}^{(k)}\| \leq c_{\mu,1}^{(k)} \|\overline{\mathbf{y}}_n^{(k)} - \overline{\mathbf{y}}_h^{(k)}\|, \qquad c_{\mu,1}^{(k)} = \gamma_h^{(k)} \|\mathbf{C}_{\mu_h y_h}^{(k)}\|, \tag{6.22}$$

$$\|\mathbf{e}_{I,u}^{(k)}\| \leq c_{u,1}^{(k)} \|\overline{\mathbf{y}}_n^{(k)} - \overline{\mathbf{y}}_h^{(k)}\|, \qquad c_{u,1}^{(k)} = \gamma_h^{(k)} \|\mathbf{C}_{u_h y_h}^{(k)}\|, \tag{6.23}$$

respectively. On the other hand, by adding and subtracting in (6.21) the quantity

$$\begin{bmatrix} \mathbf{C}_{\mu_n y_n}^{(k)} \\ \mathbf{V}\mathbf{C}_{u_n y_n}^{(k)} \end{bmatrix} (\boldsymbol{\Gamma}^{(k)} + \mathbf{C}_{y_h y_h}^{(k)})^{-1} (\mathbf{y}^{(k)} - \overline{\mathbf{y}}_n^{(k)})$$

and rewriting the expression (6.21) as $\mathbf{e}_{II}^{(k)} = \mathbf{e}_i^{(k)} + \mathbf{e}_{ii}^{(k)}$, with

$$\mathbf{e}_i^{(k)} = \left(\begin{bmatrix} \mathbf{C}_{\mu_h y_h}^{(k)} \\ \mathbf{C}_{u_h y_h}^{(k)} \end{bmatrix} - \begin{bmatrix} \mathbf{C}_{\mu_n y_n}^{(k)} \\ \mathbf{V}\mathbf{C}_{u_n y_n}^{(k)} \end{bmatrix} \right) (\boldsymbol{\Gamma}^{(k)} + \mathbf{C}_{y_h y_h}^{(k)})^{-1} (\mathbf{y}^{(k)} - \overline{\mathbf{y}}_n^{(k)}),$$

$$\mathbf{e}_{ii}^{(k)} = \begin{bmatrix} \mathbf{C}_{\mu_n y_n}^{(k)} \\ \mathbf{V}\mathbf{C}_{u_n y_n}^{(k)} \end{bmatrix} \left((\boldsymbol{\Gamma}^{(k)} + \mathbf{C}_{y_n y_n}^{(k)})^{-1} - (\boldsymbol{\Gamma}^{(k)} + \mathbf{C}_{y_h y_h}^{(k)})^{-1} \right) (\mathbf{y}^{(k)} - \overline{\mathbf{y}}_n^{(k)}),$$

we find

$$\begin{aligned} \|\mathbf{e}_{i,\mu}^{(k)}\| &\leq c_{\mu,2}^{(k)} \|\mathbf{C}_{\mu_h y_h}^{(k)} - \mathbf{C}_{\mu_n y_n}^{(k)}\| \qquad c_{\mu,2}^{(k)} = \gamma_h^{(k)} \|(\mathbf{y}^{(k)} - \overline{\mathbf{y}}_n^{(k)})\|, \\ \|\mathbf{e}_{i,u}^{(k)}\| &\leq c_{u,2}^{(k)} \|\mathbf{C}_{u_h y_h}^{(k)} - \mathbf{V}\mathbf{C}_{u_n y_n}^{(k)}\| \qquad c_{u,2}^{(k)} = \gamma_h^{(k)} \|(\mathbf{y}^{(k)} - \overline{\mathbf{y}}_n^{(k)})\|. \end{aligned} \tag{6.24}$$

By applying the Sherman-Morrison-Woodbury Formula (see, e.g., Sect. 2.4 in [GVL12]) we have that

$$(\boldsymbol{\Gamma}^{(k)} + \mathbf{C}_{y_n y_n}^{(k)})^{-1} - (\boldsymbol{\Gamma}^{(k)} + \mathbf{C}_{y_h y_h}^{(k)})^{-1} = (\boldsymbol{\Gamma}^{(k)} + \mathbf{C}_{y_n y_n}^{(k)})^{-1} (\mathbf{C}_{y_h y_h}^{(k)} - \mathbf{C}_{y_n y_n}^{(k)}) (\boldsymbol{\Gamma}^{(k)} + \mathbf{C}_{y_h y_h}^{(k)})^{-1},$$

and, consequently,

$$\|(\mathbf{\Gamma}^{(k)}+\mathbf{C}^{(k)}_{y_n y_n})^{-1}-(\mathbf{\Gamma}^{(k)}+\mathbf{C}^{(k)}_{y_h y_h})^{-1}\| \leq \gamma_n^{(k+1)}\gamma_h^{(k)}\|\mathbf{C}^{(k)}_{y_h y_h}-\mathbf{C}^{(k)}_{y_n y_n}\|,$$

whence the following bounds hold for $\mathbf{e}^{(k)}_{ii}$

$$\|\mathbf{e}^{(k)}_{ii,\mu}\| \leq c^{(k)}_{\mu,3}\|\mathbf{C}^{(k)}_{y_h y_h}-\mathbf{C}^{(k)}_{y_n y_n}\|, \qquad \|\mathbf{e}^{(k)}_{ii,u}\| \leq c^{(k)}_{u,3}\|\mathbf{C}^{(k)}_{y_h y_h}-\mathbf{C}^{(k)}_{y_n y_n}\|. \tag{6.25}$$

Finally, by combining (6.22), (6.23), (6.24) and (6.25), we obtain (6.17)–(6.18). □

In order to obtain accurate state/parameters estimates when employing the proposed RB-EnKF, we thus require the ROM to be able to generate similar means $\overline{\mathbf{y}}^{(k)}_n(\boldsymbol{\mu}) \approx \overline{\mathbf{y}}^{(k)}_h(\boldsymbol{\mu})$ and similar covariance matrices $\mathbf{C}^{(k)}_{y_n y_n} \approx \mathbf{C}^{(k)}_{y_h y_h}$ and $\mathbf{C}^{(k)}_{\mu_n y_n} \approx \mathbf{C}^{(k)}_{\mu_h y_h}$, for each $k = 1,\dots,N_\tau$, to the ones which would have been provided by the FOM.
As a matter of fact, from the previous proposition we can also state an *asymptotic consistency* property, ensuring that the state/parameters estimated through the RB-EnKF procedure converge to the ones that would be estimated estimated by the full-order EnKF, as soon as the approximation error induced by the reduction and the hyper-reduction procedures becomes negligible when $n, m_D \to N_h$.

Corollary 1. *Assume that for each ROM dimension $n = 1,\dots,N_h$ and DEIM dimension $m_D = 1,\dots,N_h$, there exists $\epsilon^{(\ell)}(n,m_D) > 0$ such that*

$$\|\mathbf{u}^{(\ell)}_h(\boldsymbol{\mu}) - \mathbf{V}\mathbf{u}^{(\ell)}_n(\boldsymbol{\mu})\| \leq \epsilon^{(\ell)}(n,m_D), \qquad \forall \ell = 0,\dots,N_t \;\; \forall \boldsymbol{\mu} \in \mathscr{P}$$

and $\epsilon^{(\ell)}(n,m_D) \to 0$ for $n, m_D \to N_h$. Then it follows that

$$\|\hat{\boldsymbol{\mu}}_n - \hat{\boldsymbol{\mu}}_h\| \to 0 \qquad \|\mathbf{V}\hat{\mathbf{u}}_n - \hat{\mathbf{u}}_h\| \to 0 \qquad \text{for } n, m_D \to N_h.$$

Proof. Since the outputs $\mathbf{y}_h(\boldsymbol{\mu})$ ($\mathbf{y}_n(\boldsymbol{\mu})$) is linear with respect to the solution $\mathbf{u}_h(x,t;\boldsymbol{\mu})$ ($\mathbf{u}_n(x,t;\boldsymbol{\mu})$) of the dynamical system, it follows that, for any $\boldsymbol{\mu} \in \mathscr{P}$,

$$\|\mathbf{y}^{(k)}_h(\boldsymbol{\mu}) - \mathbf{y}^{(k)}_n(\boldsymbol{\mu})\| \leq \Delta t \|\mathbf{H}\| \sum_{K(k-1)\leq \ell \leq K(k)} \epsilon^{(\ell)}(n,m_D) \qquad \forall k = 1,\dots,N_\tau. \tag{6.26}$$

Then, since the means and the covariance matrices of the quantities of interest are evaluated on different subsets $\mathscr{P}^{(k)}_h$ and $\mathscr{P}^{(k)}_n$ for each $k = 1,\dots,N_\tau$, let us denote by

$$(\overline{\mathbf{y}}^{(k)}_n)_{\mathscr{P}_h} = \frac{1}{N_e}\sum_{\boldsymbol{\mu}\in\mathscr{P}^{(k-1)}_h} \mathbf{y}^{(k)}_n(\boldsymbol{\mu}),$$

$$(\mathbf{C}^{(k)}_{y_n y_n})_{\mathscr{P}_h} = \frac{1}{N_e - 1}\sum_{\mu\in\mathscr{P}^{(k-1)}_h} (\mathbf{y}^{(k)}_n(\boldsymbol{\mu}) - (\overline{\mathbf{y}}^{(k)}_n)_{\mathscr{P}_h})(\mathbf{y}^{(k)}_n(\boldsymbol{\mu}) - (\overline{\mathbf{y}}^{(k)}_n)_{\mathscr{P}_h})^T$$

the mean and the covariance of the reduced output over the full-order ensemble $\mathscr{P}_h$, respectively. Then, we can control the difference between the output means as

$$\|\overline{\mathbf{y}}^{(k)}_h - \overline{\mathbf{y}}^{(k)}_n\| \leq \|\overline{\mathbf{y}}^{(k)}_h - (\overline{\mathbf{y}}^{(k)}_n)_{\mathscr{P}_h}\| + \|(\overline{\mathbf{y}}^{(k)}_n)_{\mathscr{P}_h} - \overline{\mathbf{y}}^{(k)}_n\|, \tag{6.27}$$

so that, by averaging (6.26) over $\mathscr{P}_h$, we bound the first term of (6.27) as

$$\|\overline{\mathbf{y}}_h^{(k)} - (\overline{\mathbf{y}}_n^{(k)})_{\mathscr{P}_h}\| \le \Delta t \|\mathbf{H}\| \sum_{K(k-1)\le \ell \le K(k)} \epsilon^{(\ell)}(n, m_D) \qquad \forall k = 1, \dots, N_\tau.$$

Similarly, the difference between the covariance matrices can be bounded as

$$\|\mathbf{C}_{y_h y_h}^{(k)} - \mathbf{C}_{y_n y_n}^{(k)}\| \le \|\mathbf{C}_{y_h y_h}^{(k)} - (\mathbf{C}_{y_n y_n}^{(k)})_{\mathscr{P}_h}\| + \|(\mathbf{C}_{y_n y_n}^{(k)})_{\mathscr{P}_h} - \mathbf{C}_{y_n y_n}^{(k)})\|;$$

the first term can be bounded as

$$\|\mathbf{C}_{y_h y_h}^{(k)} - (\mathbf{C}_{y_n y_n}^{(k)})_{\mathscr{P}_h}\| \le c_{ss}^{(k)} \sum_{K(k-1)\le \ell \le K(k)} \epsilon^{(\ell)}(n, m_D) \qquad \forall k = 1, \dots, N_\tau,$$

where

$$c_{ss}^{(k)} = 4\Delta t \max_{\boldsymbol{\mu} \in \mathscr{P}^{(k-1)}} (\|\mathbf{y}_h^{(k)}(\boldsymbol{\mu}) - \overline{\mathbf{y}}_h^{(k)}\| + \|\mathbf{y}_n^{(k)}(\boldsymbol{\mu}) - \overline{\mathbf{y}}_n^{(k)}\|).$$

Indeed, for any couple of random vectors $\mathbf{x} = [\mathbf{x}_1, \mathbf{x}_2], \mathbf{y} = [\mathbf{y}_1, \mathbf{y}_2]$,

$$\|C_{\mathbf{x}_1\mathbf{y}_1} - C_{\mathbf{x}_2\mathbf{y}_2}\| \le (\|\mathbf{y}_1 - \overline{\mathbf{y}}_1\| + \|\mathbf{x}_2 - \overline{\mathbf{x}}_2\|)(\|\mathbf{x}_1 - \mathbf{x}_2\| + \|\overline{\mathbf{x}}_1 - \overline{\mathbf{x}}_2\| + \|\mathbf{y}_1 - \mathbf{y}_2\| + \|\overline{\mathbf{y}}_1 - \overline{\mathbf{y}}_2\|),$$

where $C_{\mathbf{xy}}$ denotes the cross-covariance matrix between $\mathbf{x}$ and $\mathbf{y}$; see e.g. [ESS14].
Provided that $\mathscr{P}_h^{(0)} = \mathscr{P}_n^{(0)}$ and assuming that $\epsilon^{(\ell)}(n, m_D) \to 0$ for $n, m_D \to N_h$, we have that

$$\|\overline{\mathbf{y}}_h^{(k)} - (\overline{\mathbf{y}}_n^{(k)})_{\mathscr{P}_h}\| \to 0, \qquad \|\mathbf{C}_{y_h y_h}^{(k)} - (\mathbf{C}_{y_n y_n}^{(k)})_{\mathscr{P}_h}\| \to 0, \qquad k = 1, \dots, N_\tau$$

and, consequently,

$$\|(\overline{\mathbf{y}}_n^{(k)})_{\mathscr{P}_h} - \overline{\mathbf{y}}_n^{(k)}\| \to 0, \qquad \|(\mathbf{C}_{y_n y_n}^{(k)})_{\mathscr{P}_h} - \mathbf{C}_{y_n y_n}^{(k)})\| \to 0, \qquad k = 1, \dots, N_\tau.$$

In the same way, we can conclude that $\|\mathbf{C}_{u_h y_h}^{(k+1)} - \mathbf{C}_{u_n y_n}^{(k+1)})\|$ and $\|\mathbf{C}_{\mu_h y_h}^{(k+1)} - \mathbf{C}_{\mu_n y_n}^{(k+1)})\|$ are also controlled by $\epsilon^{(\ell)}(n, m_D)$, $\ell = Kk, \dots, K(k+1)$; hence, the right-hand sides of both (6.17) and (6.18) tend to zero for $n, m_D \to N_h$. □

6.5 Corrected RB-EnKF

Using a ROM to evaluate the output of the forward PDE system greatly reduces the cost entailed by the solution of the entire Bayesian inverse problem. Indeed, by simply rewriting the additive error noise model (6.1), we get

$$\mathbf{y}^{(k)} = \mathbf{y}_n^{(k)}(\boldsymbol{\mu}) + \left(\mathbf{y}_h^{(k)}(\boldsymbol{\mu}) - \mathbf{y}_n^{(k)}(\boldsymbol{\mu}^*)\right) + \boldsymbol{\varepsilon}_{\text{noise}}^{(k)}, \qquad \forall k = 1, \dots, N_\tau; \tag{6.28}$$

hence, if the reduction error $\mathbf{y}_h^{(k)}(\boldsymbol{\mu}) - \mathbf{y}_n^{(k)}(\boldsymbol{\mu})$ is not negligible with respect to $\boldsymbol{\varepsilon}_{\text{noise}}$, the RB-EnKF might yield biased estimates.
The reduction error can be seen as an additional epistemic uncertainty affecting the input/output evaluation. In the EnKF literature, this kind of problems arises when real observations are compared with simulated outputs [MHP02, HMD09]. Two standard techniques for taking into account this additional error source are inflation and localization. The former consists in augmenting the variance of the additive noise model, whereas the latter properly modifies the prior ensemble to reduce filtering errors and avoid filter divergence (for further details

on both techniques see e.g. [And07, HZ16]). The approach proposed in this Chapter can be seen as a direct way to correct the input/output evaluation coupled with the inflation of the covariance matrix to ensure the accuracy of the results. We indeed directly quantify this additional uncertainty using the kriging-based ROM error surrogates developed in Section 3.4. Therefore, we introduce a ROMES for the time-dependent reduction error $\boldsymbol{\varepsilon}^{(k)}_{\text{ROM}}(\boldsymbol{\mu})$, over each window $k = 1,\dots,N_\tau$, such that (6.28) can be replaced by

$$\mathbf{y}^{(k)} = \mathbf{y}^{(k)}_n(\boldsymbol{\mu}^*) + \boldsymbol{\varepsilon}^{(k)}_{\text{ROM}}(\boldsymbol{\mu}^*) + \boldsymbol{\varepsilon}_{\text{noise}} \qquad \forall\, k = 1,\dots,N_\tau. \tag{6.29}$$

In this way the evaluation of the deterministic quantity $\mathbf{y}^{(k)}_h(\boldsymbol{\mu}) - \mathbf{y}^{(k)}_n(\boldsymbol{\mu})$, which would depend on the FOM solution, can be avoided.
We briefly show how to construct the ROMES in this case, following the approach developed in Section 3.4. We assume each component $\{\chi_{t,j}(\boldsymbol{\mu})\}$, $j = 1,\dots,s$, of the output reduction error

$$\boldsymbol{\chi}_t(\boldsymbol{\mu}) = (\mathbf{H}(\mathbf{u}_h(x,t;\boldsymbol{\mu}) - \mathbf{u}_n(x,t;\boldsymbol{\mu})) \in \mathbb{R}^s, \qquad t \in (0,T)$$

to be a second-order stationary and isotropic functional random field.
Given the calibration set $P_{cal} = \{\boldsymbol{\mu}_1,\dots,\boldsymbol{\mu}_{N_{cal}}\}$ (with $P_{train} \subset P_{cal}$), we compute during the *offline* phase the error $\boldsymbol{\chi}_t(\boldsymbol{\mu})$ for each $\boldsymbol{\mu} \in P_{train}$. Then, for any new $\boldsymbol{\mu}_0 \in \mathscr{P}$, the kriging interpolation of the error is given by:

$$\hat{\chi}_{t,j}(\boldsymbol{\mu}_0) = \sum_{q=1}^{N_{cal}} \lambda_q^{(j)}(\boldsymbol{\mu}_0)\chi_{t,j}(\boldsymbol{\mu}_q), \qquad \boldsymbol{\mu}_0 \in \mathscr{P}, \quad j = 1,\dots,s,$$

where the set of weights $\{\lambda_q^{(j)}(\boldsymbol{\mu}_0)\}_{q=1}^{N_{cal}}$ is the solution of the linear system (3.13) as derived in Section 3.4.

Since we are interested in embedding the ROMES into the KF updating formula for the sequential update of the ensemble on each window $[\tau^{(k)},\tau^{(k+1)})$, we need to integrate $\hat{\chi}_{t,j}(\boldsymbol{\mu}_0)$ over $[\tau^{(k-1)},\tau^{(k)})$ to obtain a correction for each component of the output error $\mathbf{y}_h(\boldsymbol{\mu}_0) - \mathbf{y}_n(\boldsymbol{\mu}_0)$. In particular, we end up with the ROMES prediction:

$$\boldsymbol{m}^{(k)}_{\text{ROM}}(\boldsymbol{\mu}_0) \,:\, m^{(k)}_{\text{ROM},j}(\boldsymbol{\mu}_0) = \int_{\tau^{(k-1)}}^{\tau^{(k)}} \hat{\chi}_t^{(j)}(\boldsymbol{\mu}_0)\,dt. \tag{6.30}$$

The corresponding trace-variances

$$\hat{\sigma}^2_{\text{ROM},j}(\boldsymbol{\mu}_0) = \sum_{q=1}^{N_{cal}} \lambda_q^{(j)}(\boldsymbol{\mu}_0) \int_{\tau^{(k-1)}}^{\tau^{(k)}} \gamma_t(\|\boldsymbol{\mu}_i - \boldsymbol{\mu}_0\|) - \eta$$

allow to define the (diagonal) covariance matrix

$$\boldsymbol{\Gamma}^{(k)}_{\text{ROM}}(\boldsymbol{\mu}_0) \,:\, (\boldsymbol{\Gamma}^{(k)}_{\text{ROM}}(\boldsymbol{\mu}_0))_{jj} = \hat{\sigma}^2_{\text{ROM},j}(\boldsymbol{\mu}_0). \tag{6.31}$$

This latter takes automatically into account the error committed by the ROMES in approximating the reduction error. The proposed ROMES thus yields an output correction $\varepsilon^{(k)}_{\text{ROM}}$ and an additional contribution $\boldsymbol{\Gamma}^{(k)}_{\text{ROM}}$ to the Kalman gain – which have indeed to be evaluated for

each $k = 1, \dots, N_\tau$ and upon each ensemble particle – thus leading to the following *corrected KF updating formula* to update the ensemble $\mathscr{P}_c^{(k)}$:

$$\begin{bmatrix} \boldsymbol{\mu}_{c,q}^{(k+1)} \\ \mathbf{u}_c^{(k+1)}(\boldsymbol{\mu}_{c,q}^{(k+1)}) \end{bmatrix} = \begin{bmatrix} \boldsymbol{\mu}_{c,q}^{(k)} \\ \mathbf{u}_c^{(k+1)}(\boldsymbol{\mu}_{c,q}^{(k)}) \end{bmatrix} + \begin{bmatrix} \mathbf{C}_{\mu_c y_c}^{(k+1)} \\ \mathbf{C}_{u_c y_c}^{(k+1)} \end{bmatrix} (\boldsymbol{\Gamma}^{(k)} + \boldsymbol{\Gamma}_{\mathrm{ROM}}^{(k+1)}(\boldsymbol{\mu}_{c,q}^{(k)}) + \mathbf{C}_{y_c y_c}^{(k+1)})^{-1} (\mathbf{y}_q^{(k+1)} - \mathbf{y}_c^{(k+1)}(\boldsymbol{\mu}_{c,q}^{(k)})) \quad (6.32)$$

where $\mathbf{y}_c^{(k)}(\boldsymbol{\mu})$ represents the *corrected output*, i.e.

$$\mathbf{y}_c^{(k)}(\boldsymbol{\mu}) = \mathbf{y}_n^{(k)}(\boldsymbol{\mu}) + \mathbf{m}_{\mathrm{ROM}}^{(k)}(\boldsymbol{\mu}), \qquad \boldsymbol{\mu} \in \mathscr{P}.$$

The sample covariance $\mathbf{C}_{y_c y_c}^{(k)}$ and cross-covariances $\mathbf{C}_{\mu_c y_c}^{(k)}$, $\mathbf{C}_{u_c y_c}^{(k)}$ are computed as in equations (6.11), (6.12) and (6.13) by substituting $\mathbf{y}_h$, $\mathbf{u}_h$ and $\mathscr{P}_h^{(k-1)}$ with $\mathbf{y}_c$, $\mathbf{u}_c$ and $\mathscr{P}_c^{(k-1)}$, respectively. The use of the ROMES during the RB-EnKF thus only requires, at each iteration of the filtering procedure, to solve s linear systems (see equation (3.13)) of small dimension $(N_{cal}+1)\times(N_{cal}+1)$, to get the weights $\{\lambda_q^{(j)}\}_{q=1}^{N_{cal}}$ for each output component $j = 1, \dots, s$. Each linear system requires to fit the so-called semi-variogram function γ_t on the calibration set, as described in Section 3.4. A detailed description of the *corrected RB-EnKF* algorithm is finally reported in Algorithm 8, while the schematic representation of the *corrected RB-EnKF* loop is presented in Figure 6.3.

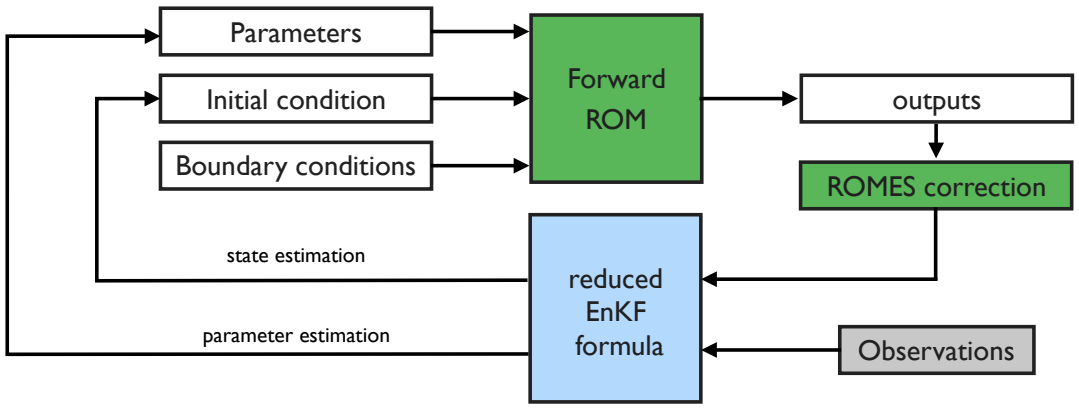

Figure 6.3 – Corrected RB-EnKF loop for state/parameter estimation. The reduced state update is used as new initial condition of the forward problem over each time window.

6.5.1 Effectivity of ROMESs

We point out that the reduction error directly affects the likelihood function (6.9) from which the KF updating formula is derived (see e.g. [PMQ16]). Under the assumption that the noise process is Gaussian, the reduced likelihood could be defined as

$$\pi_n^{(k)} = \pi_n\left(\mathbf{s}^{(k+1)} \middle| [\boldsymbol{\mu}, \mathbf{V}\mathbf{u}_n^{(k+1)}]^T\right) = (2\pi)^{(-\frac{s}{2})} |\boldsymbol{\Gamma}|^{-\frac{1}{2}} \exp\left\{-\frac{1}{2}\|\mathbf{s}^{(k+1)} - \mathbf{s}_n^{(k+1)}\|_{\boldsymbol{\Gamma}}\right\},$$

and the corrected likelihood as

$$\pi_c^{(k)} = (2\pi)^{(-\frac{s}{2})} |\boldsymbol{\Gamma} + \hat{\boldsymbol{\Gamma}}_{\mathrm{ROM}}^{(k)}|^{-\frac{1}{2}} \exp\left\{-\frac{1}{2}\|\mathbf{s}^{(k+1)} - \mathbf{s}_c^{(k+1)}\|_{\boldsymbol{\Gamma}+\hat{\boldsymbol{\Gamma}}_{\mathrm{ROM}}^{(k+1)}}\right\}.$$

Algorithm 8 Corrected reduced basis ensemble Kalman filter procedure

procedure RB-EnKF(+ROMES)
  Initialization
  $\{\mathscr{P}_c^{(0)}, \mathscr{U}_c^{(0)}\} \leftarrow$ sampling N_e vectors from π_{prior}
  for $q = 1 : N_e$, $k = 1 : N_\tau$ **do**
    $\mathbf{y}_q^{(k)} \leftarrow \mathbf{y}_h^{(k)}(\boldsymbol{\mu}^*) + \boldsymbol{\varepsilon}_q^{(k)}$
  end for
    for $k = 0 : N_\tau - 1$ **do**
      for j=1 : s **do**
        sample the empirical semi-variogram $\{(\delta_m, \hat{\gamma}(\delta_m))\}_{m=1}^M$,
        fit the parametric semi-variogram model on the sample $\{(\delta_m, \hat{\gamma}(\delta_m))\}_{m=1}^M$
      end for
      Prediction stage:
      for $q = 1 : N_e$ **do**
        $\mathbf{u}_c^{(k+1)}(\boldsymbol{\mu}_{c,q}) \leftarrow$ solve ROM related to pb. (6.3) with initial datum $\mathbf{u}_c^{(k)}(\boldsymbol{\mu}_{c,q})$
        for j=1 : s **do**
          $\boldsymbol{\varepsilon}_{\text{ROM}}^{(k+1)}(\boldsymbol{\mu}_{c,q}) \leftarrow$ solve ROMES linear system
          $(\boldsymbol{\Gamma}_{\text{ROM}}^{(k+1)})_{jj}(\boldsymbol{\mu}_{c,q}) \leftarrow$ evaluate (3.15)
        end for
        $\mathbf{y}_c^{(k+1)}(\boldsymbol{\mu}_{c,q}) = \mathbf{y}_n^{(k+1)}(\boldsymbol{\mu}_{c,q}) + \boldsymbol{\varepsilon}_{\text{ROM}}^{(k+1)}(\boldsymbol{\mu}_{c,q})$
      end for
      compute means $\overline{\mathbf{y}}_c^{(k+1)}$, $\overline{\mathbf{u}}_c^{(k+1)}$, $\overline{\boldsymbol{\mu}}_c^{(k+1)}$
      compute covariance $\mathbf{C}_{y_c y_c}^{(k+1)}$
      compute cross-covariances $\mathbf{C}_{\mu_c y_c}^{(k+1)}, \mathbf{C}_{u_c y_c}^{(k+1)}$
      Update stage:
      for $q = 1 : N_e$ **do**
        update each state/parameters particle using (6.32)
      end for
    end for
  end procedure

We can rely on the analysis provided in Section 5.4 on the Kullback-Leibler (KL) divergence (5.15) between the likelihood functions $\pi^{(k)}$, $\pi_n^{(k)}$ and $\pi_c^{(k)}$ at each *prediction-analysis* step $k = 1, \dots, N_\tau$.
In this case, we would obtain

$$D_{KL}(\pi^{(k)} || \pi_n^{(k)}) = \frac{1}{2} \sum_{j=1}^{s} \left(\frac{(\mathbf{y}_h^{(k+1)}(\boldsymbol{\mu}) - \mathbf{y}_n^{(k+1)}(\boldsymbol{\mu}))_j^2}{{\boldsymbol{\Gamma}^{(k)}}_{jj}} \right)$$

and

$$D_{KL}(\pi^{(k)} || \pi_c^{(k)}) = \frac{1}{2} \sum_{j=1}^{s} \left(\frac{(\mathbf{y}_h^{(k+1)}(\boldsymbol{\mu}) - \mathbf{y}_n^{(k+1)}(\boldsymbol{\mu}) - \boldsymbol{\varepsilon}_{\text{ROM}}^{(k+1)}(\boldsymbol{\mu}))_j^2}{{\boldsymbol{\Gamma}^{(k)}}_{jj} + ({\boldsymbol{\Gamma}^{(k)}}_{\text{ROM}}^{(k+1)})_{jj}(\boldsymbol{\mu})} + \frac{{\boldsymbol{\Gamma}^{(k)}}_{jj}}{{\boldsymbol{\Gamma}^{(k)}}_{jj} + (\boldsymbol{\Gamma}_{\text{ROM}}^{(k+1)})_{jj}(\boldsymbol{\mu})} - 1 - \log\left(\frac{{\boldsymbol{\Gamma}^{(k)}}_{jj}}{{\boldsymbol{\Gamma}^{(k)}}_{jj} + (\boldsymbol{\Gamma}_{\text{ROM}}^{(k+1)})_{jj}(\boldsymbol{\mu})} \right) \right).$$

Thus, in order to ensure that the KL divergence $D_{KL}(\pi^{(k)}||\pi_c^{(k)})$ is smaller than $D_{KL}(\pi^{(k)}||\pi_n^{(k)})$, we require that:

1. the ROMES correction is effective, that is

$$\mathbb{E}[\|\mathbf{y}_h^{(k)}(\boldsymbol{\mu}) - \mathbf{y}_c^{(k)}(\boldsymbol{\mu})\|] \leq \mathbb{E}[\|\mathbf{y}_h^{(k)}(\boldsymbol{\mu}) - \mathbf{y}_n^{(k)}(\boldsymbol{\mu})\|] \qquad \forall k = 1,\dots,N_\tau, \tag{6.33}$$

2. $(\boldsymbol{\Gamma}_{\text{ROM}}^{(k+1)})_{jj}$ is sufficiently small compared to $\boldsymbol{\Gamma}_{jj}^{(k)}$, $j = 1,\dots,s$.

Note that by construction $\mathbf{y}_h^{(k)}(\boldsymbol{\mu}) - \mathbf{y}_c^{(k)}(\boldsymbol{\mu}) = \mathbf{0}$ and $\boldsymbol{\Gamma}_{\text{ROM}}(\boldsymbol{\mu}) = \mathbf{0}$ for each $\boldsymbol{\mu} \in P_{cal}$. Since the noise is prescribed with a fixed covariance, the ROM and the ROMES construction can be suitably performed in order to ensure both the previous assumptions.

Remark 5. *Since the EnKF is based on a finite ensemble of particles, the distributions π, π_n and $\tilde{\pi}_n$ are only approximated in the EnKF updating formula* (6.14)*.* (6.16) *and* (6.32)*, respectively. It is sufficient to consider a large ensemble in order to avoid the propagation of additional sources of error.*

Note that the updating formula (6.32) could be derived using the corrected likelihood distribution $\pi_c^{(k)}$ instead of $\pi^{(k)}$. As a consequence, the ensemble updated through (6.32) provides a good approximation of (6.14) if the REM is effective. Moreover, under the two previous assumptions the corrected particle ensemble $\mathscr{P}_c^{(k)}$ (and respectively $\mathscr{U}_c^{(k)}$) is considerably closer to $\mathscr{P}_h^{(k)}$ ($\mathscr{U}_h^{(k)}$) than $\mathscr{P}_n^{(k)}$ ($\mathscr{U}_n^{(k)}$). If we assume, at each step $k = 1,\dots,N_\tau$, to use as prior the full-order ensemble $\mathscr{P}_h^{(k)}$ ($\mathscr{U}_h^{(k)}$), it is possible to prove that

$$\mathbb{E}[D_{KL}(\pi_{post}^{(k)}||\pi_{post,c}^{(k)})] < \mathbb{E}[D_{KL}(\pi_{post}^{(k)}||\pi_{post,n}^{(k)})],$$

where $\pi_{post}^{(k)}$, $\pi_{post,n}^{(k)}$ and $\pi_{post,c}^{(k)}$ denote respectively the full-order, the reduced-order and the corrected posterior distributions obtained by substituting the respective likelihood functions $\pi^{(k)}$, $\pi_n^{(k)}$ and $\pi_c^{(k)}$ in (6.8); for further details see Section 5.4.
As a matter of fact, $\boldsymbol{\varepsilon}_{\text{ROM}}$ and $\boldsymbol{\Gamma}_{\text{ROM}}$ depend on either the number of basis functions and the calibration set dimension. For this reason, in the numerical results we compare the errors $\|\hat{\boldsymbol{\mu}}_h - \hat{\boldsymbol{\mu}}_n\|$ and $\|\hat{\boldsymbol{\mu}}_h - \hat{\boldsymbol{\mu}}_c\|$ between the sample means and the ones between the relative covariance matrices $\|(\mathbf{C}_{\boldsymbol{\mu}_h,\boldsymbol{\mu}_h})^{1/2} - (\mathbf{C}_{\boldsymbol{\mu}_n,\boldsymbol{\mu}_n})^{1/2}\|$ and $\|(\mathbf{C}_{\boldsymbol{\mu}_h,\boldsymbol{\mu}_h})^{1/2} - (\mathbf{C}_{\boldsymbol{\mu}_c,\boldsymbol{\mu}_c})^{1/2}\|$ over the ensemble obtained with the full-order Kalman filter ($\mathscr{P}_h$), the RB-EnKF ($\mathscr{P}_n$) and the corrected RB-EnKF ($\mathscr{P}_c$) on varying the number of basis functions and the calibration set dimension.

6.6 Numerical results

We present some numerical results [2] exploiting the proposed RB-EnKF procedure for the identification of unknown parameters using as forward model the FitzHugh-Nagumo (FN) equations, which model the activation/deactivation dynamics of an excitable cardiac cell. In particular, we study a parametrized version of the test case proposed in [CS10]: given the

[2] All the computations of this chapter have been performed on a laptop with 2.4 GHz Intel core i7 processor and 8Gb RAM 1600MHz DDR3.

parameter vector $\boldsymbol{\mu} = [\mu_1, \mu_2, \mu_3]^T$, $\forall\, t \in (0,T)$, find the couple $[u(x,t;\boldsymbol{\mu}), w(x,t;\boldsymbol{\mu})]$, $x \in \Omega = (0,1)$, such that:

$$\begin{cases} \sigma_v(x;\boldsymbol{\mu})u_t(x,t;\boldsymbol{\mu}) = \sigma_v^2(x;\boldsymbol{\mu})u_{xx}(x,t;\boldsymbol{\mu}) + I_{ion}(u(x,t;\boldsymbol{\mu}), w(x,t;\boldsymbol{\mu})) + \mu_2 & x \in \Omega,\ t \in (0,T) \\ w_t(x,t;\boldsymbol{\mu}) = \mu_1 u(x,t;\boldsymbol{\mu}) - \gamma u(x,t;\boldsymbol{\mu}) + \mu_2 & x \in \Omega,\ t \in (0,T) \\ u_x(x,t;\boldsymbol{\mu}) = -50000\, t^3 e^{-15t} & x = 0,\ t \in (0,T) \\ u_x(x,t;\boldsymbol{\mu}) = 0 & x = 1,\ t \in (0,T) \\ u(x,0;\boldsymbol{\mu}) = w(x,0;\boldsymbol{\mu}) = 0 & x \in \Omega; \end{cases} \tag{6.34}$$

here the cubic nonlinear term is defined as $I_{ion}(u,w) = u(u-0.1)(1-u) - w$, the coefficient $\gamma = 2$ and we prescribe a non-homogeneous conductivity field:

$$\sigma_v(\mathbf{x};\boldsymbol{\mu}) = 0.015(1-\mu_3)\exp\left(-\frac{(x-0.6)^2}{0.04}\right).$$

The parameter μ_3 describes the lack of conductivity centered in $x = 0.6$; μ_1 influences instead the time between the depolarization and the polarization phase, while μ_2 is an applied constant current, which enables the mechanism of self excitation of the cell.
The semi-discretized FE approximation of problem (6.34) is based on a partition of the computational domain Ω into 1024 elements and linear finite elements. By considering a time discretization based on $N_t = 800$ time-steps and the implicit Euler method, we obtain the dynamical system under the form (6.3). Then, we consider as output the vector

$$\mathbf{y}_h^{(k+1)} = \begin{bmatrix} \int_{\tau^{(k)}}^{\tau^{(k+1)}} \mathbf{u}_h(x,t;\boldsymbol{\mu})|_{x=0}\, dt \\ \int_{\tau^{(k)}}^{\tau^{(k+1)}} \mathbf{u}_h(x,t;\boldsymbol{\mu})|_{x=1}\, dt \end{bmatrix} \in \mathbb{R}^2 \qquad \forall\, k = 0,\dots,N_\tau - 1.$$

The goal of the Bayesian inverse problem is to estimate the unknown parameters vector $\boldsymbol{\mu}^*$ from a sequence of noisy output measurements $\mathbf{y}^{(k)} = \mathbf{y}_h^{(k)}(\boldsymbol{\mu}^*) + \boldsymbol{\varepsilon}_{noise}^{(k)}$, $k = 1,\dots,N_\tau$, with $\boldsymbol{\varepsilon}_{\text{noise}}^{(k)} \sim \mathcal{N}(0,\sigma^2 I)$. We take a Gaussian prior, so that $\boldsymbol{\mu}^{(0)} \in \mathcal{N}(\boldsymbol{\mu}_{\text{prior}}, \Sigma_{\text{prior}})$, with

$$\boldsymbol{\mu}_{\text{prior}} = \begin{bmatrix} 0.7 \\ 0.07 \\ 0.76 \end{bmatrix}, \qquad \Sigma_{\text{prior}} = \begin{bmatrix} 0.0004 & 0 & 0 \\ 0 & 0.00009 & 0 \\ 0 & 0 & 0.004 \end{bmatrix}.$$

The discretized solution $[\mathbf{u}_h, \mathbf{w}_h]^T$ of the forward problem for the choice

$$\boldsymbol{\mu}^* = [0.6331, 0.0985, 0.7197]^T$$

is represented in Fig. 6.4.
We consider hereon $\boldsymbol{\mu}^*$ as the *true* parameter vector value, which generates the measurements $\mathbf{y}_q^{(k)}$ through N_e random realizations of the additive noise model (6.1).
We first solve the inverse problem with the *full-order* EnKF starting from output measurements (6.1) with different noise standard deviations, in particular by considering $\sigma = 5\sigma_0$ and $\sigma = \sigma_0$, with $\sigma_0 = 0.033$. By looking at the behavior of the estimate $\hat{\boldsymbol{\mu}}_h$ in Fig. 6.5 for each component of the parameter vector, we observe that a faster convergence of the estimate to the *true* parameter value during the inversion procedure is achieved in the case of a smaller standard deviation (σ_0 with respect to $5\sigma_0$) on the noise.

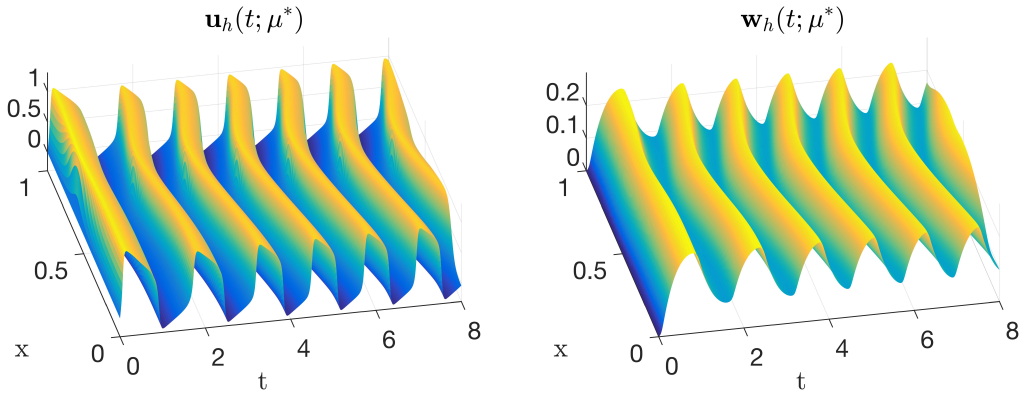

Figure 6.4 – FE approximation of the forward problem for $\boldsymbol{\mu} = \boldsymbol{\mu}^*$.

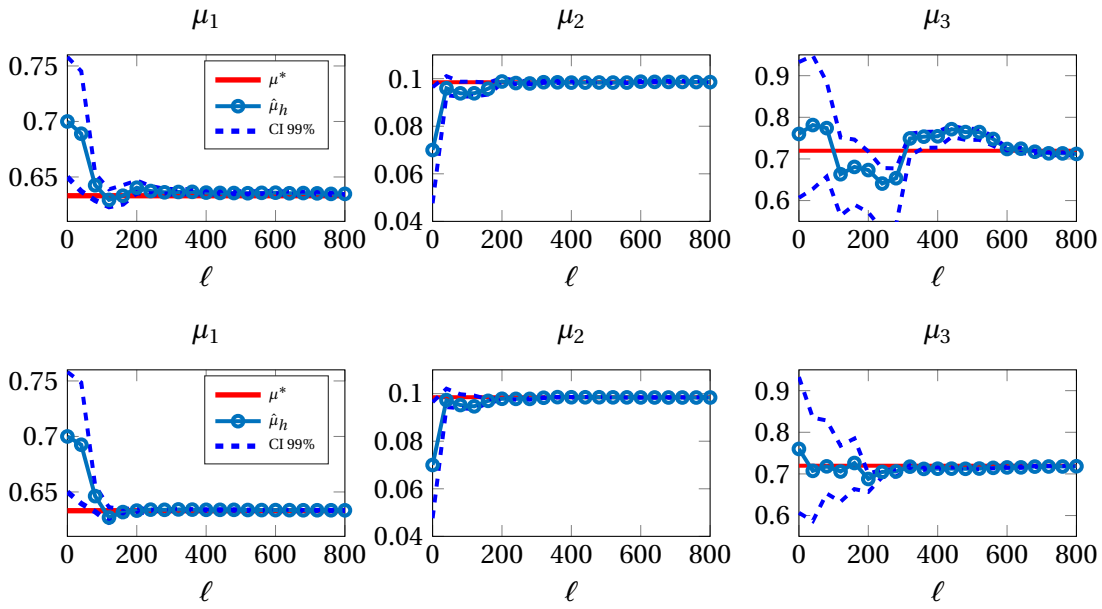

Figure 6.5 – Comparison between $\boldsymbol{\mu}^*$ and $\{\hat{\boldsymbol{\mu}}_h^{(k)}\}_{k=1}^{N_\tau}$ for $\sigma = 5\sigma_0$ (first row) $\sigma = \sigma_0$ (second row), using $N_e = 500$ particles. The lower the noise level, the faster the convergence to $\boldsymbol{\mu}^*$ during the state/parameter estimation procedure (see e.g. the figures on the third column, related to the component μ^3).

Next, we compare the solution of the state/parameter estimation problem obtained by varying the window length $\Delta\tau$, the noise standard deviation and the ensemble size N_e (see Fig. 6.6) taking $m_D = 15$ DEIM elements and $n = [7, 11, 15]$ basis function on the RB approximation. As expected, the estimates improve if both the noise $\boldsymbol{\epsilon}_{\text{noise}}$ and $\Delta\tau$ decrease. While the former is a datum of the problem, the latter can be properly tuned (and reduced) to improve the estimation of the quantities of interest by slightly increasing the whole computational costs. In Figure 6.7 we also study the state estimation with respect to the number of ROM basis functions: the reduction error clearly affects the estimation of this quantity.

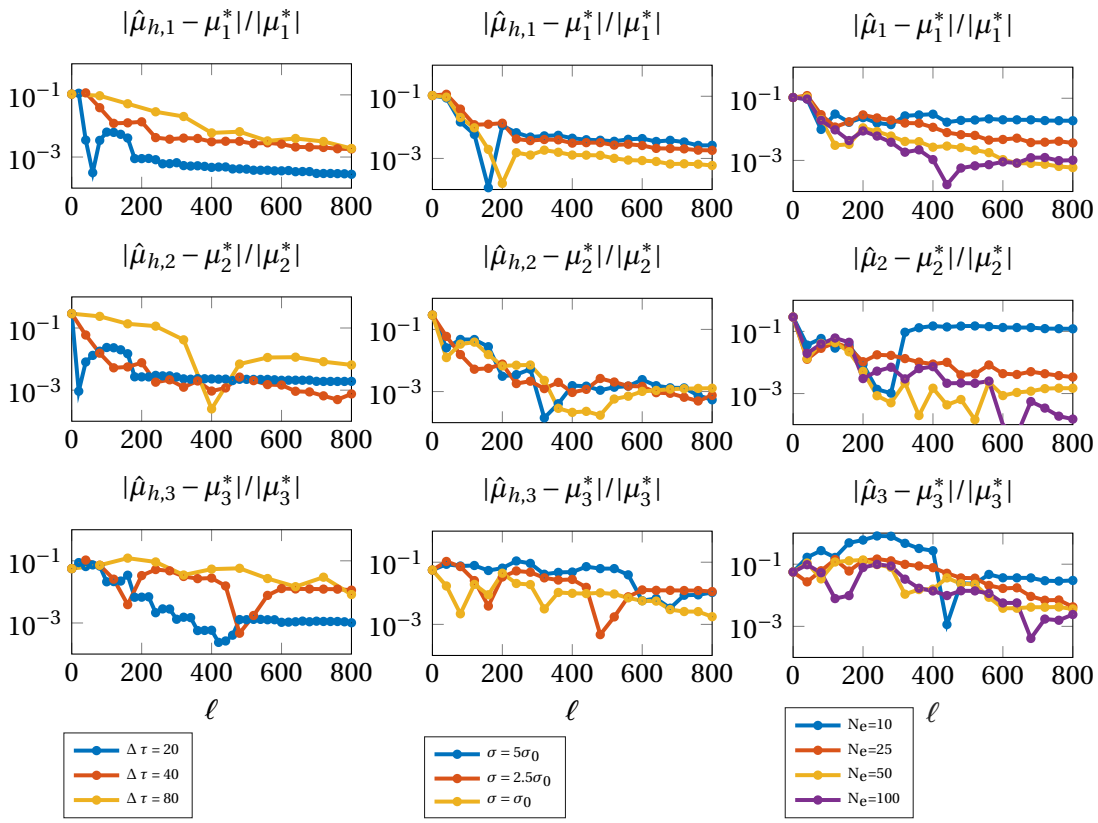

Figure 6.6 – Relative error on estimated parameter components $|\mu^* - \hat{\mu}_h^{(k)}|/|\mu^*|$ with respect to the updating time-discretization length $\Delta\tau$ (left), the noise standard deviation (center) and the ensemble size (right).

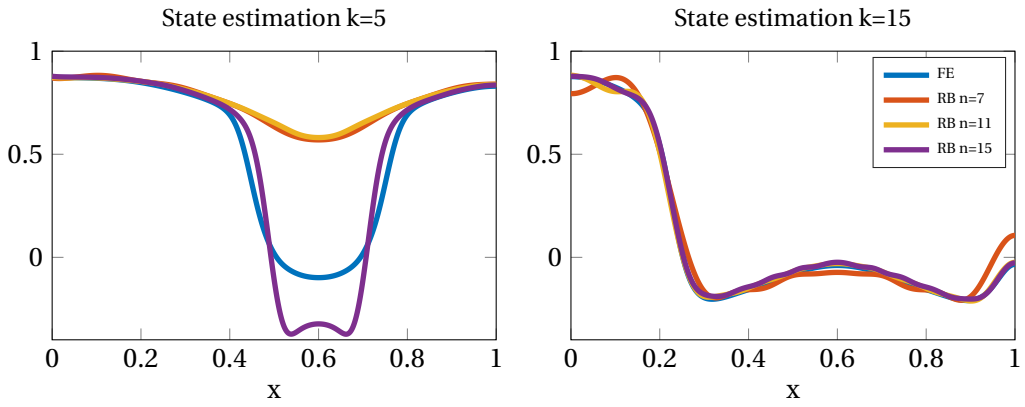

Figure 6.7 – State estimation versus RB dimension n, at two different iterations ($k = 5$, left; $k = 15$, right) of the RB-EnKF.

Then, we turn to the comparison between the RB-EnKF algorithm and its corrected version, in order to assess the effect of the proposed ROMES in reducing the bias in the parameter estimation as a function of the noise variance σ.

In the case $\sigma = 5\sigma_0$ (first row of Figure 6.9), the results of the RB-EnKF for $n = 15$ are comparable with the ones of the full-order EnKF, meaning that the reduction error (see e.g. Figure 6.8) is negligible with respect to the noise. This is not true when the RB dimension is set to $n = 7, 11$. In these two cases, there is a bias in the first two components of the parameter vector estimate. On the other hand, for a lower noise variance, such as in the case $\sigma = \sigma_0$ (second row of Figure 6.9), we observe that the reduction error affects the parameter estimate for all RB dimensions $n = 7, 11, 15$.

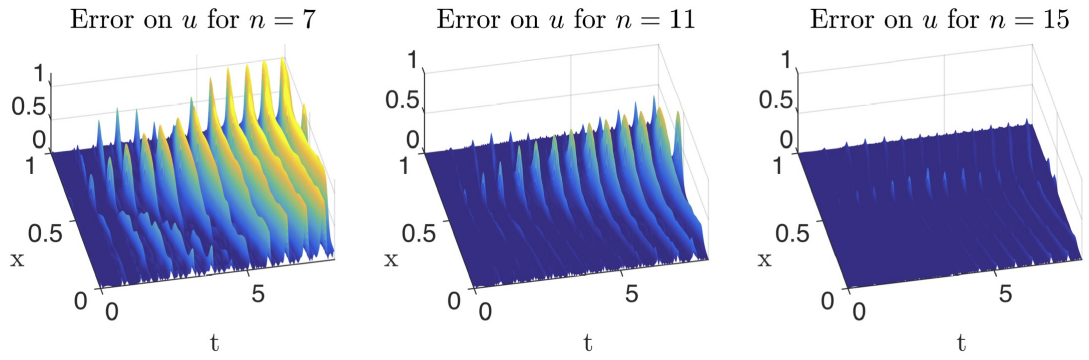

Figure 6.8 – Error $|\mathbf{u}_h(t;\boldsymbol{\mu}^*) - \mathbf{u}_n(t;\boldsymbol{\mu}^*)|$ between the FOM and the ROM for different choices of the RB dimension $n = 7, 11, 15$.

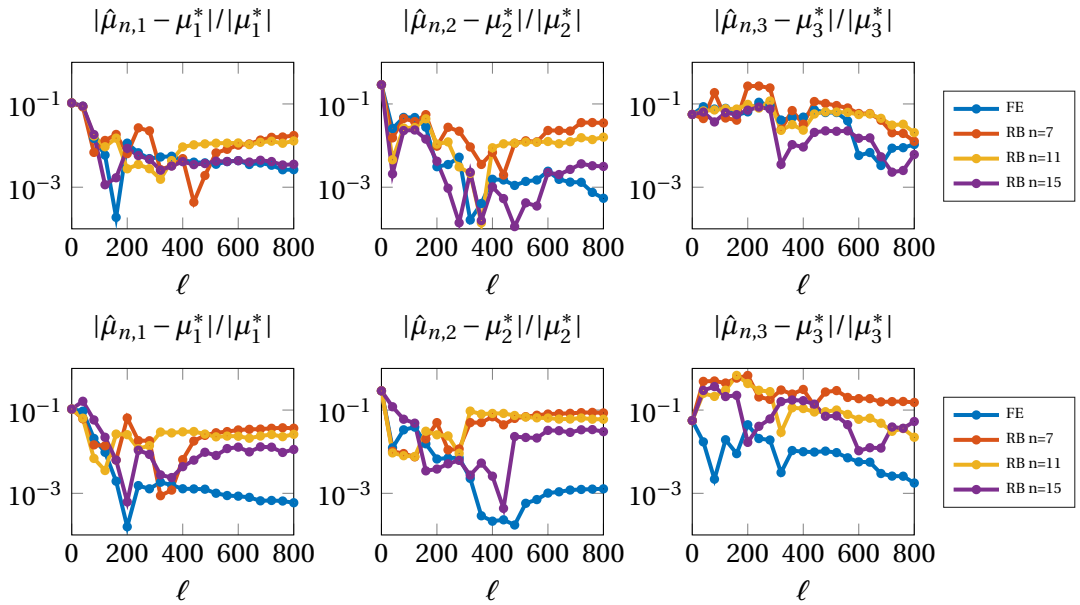

Figure 6.9 – Relative error on estimated parameter components $|\mu^* - \hat{\mu}_n^{(k)}|/|\mu^*|$ versus the RB dimension n for the RB-EnKF when different noise variances $\sigma = 5\sigma_0$ (first row) and $\sigma = \sigma_0$ (second row) are considered.

For both values of the noise variance, the ROMES is therefore essential to improve the accuracy of the RB-EnKF estimates: as a matter of fact, the proposed ROMES based on curve kriging

improves (by minimizing the propagation of the reduction error) the parameter estimation in our RB-EnKF up to two orders of magnitude in some cases, as we can grasp by comparing Fig. 6.9 with Fig. 6.10.

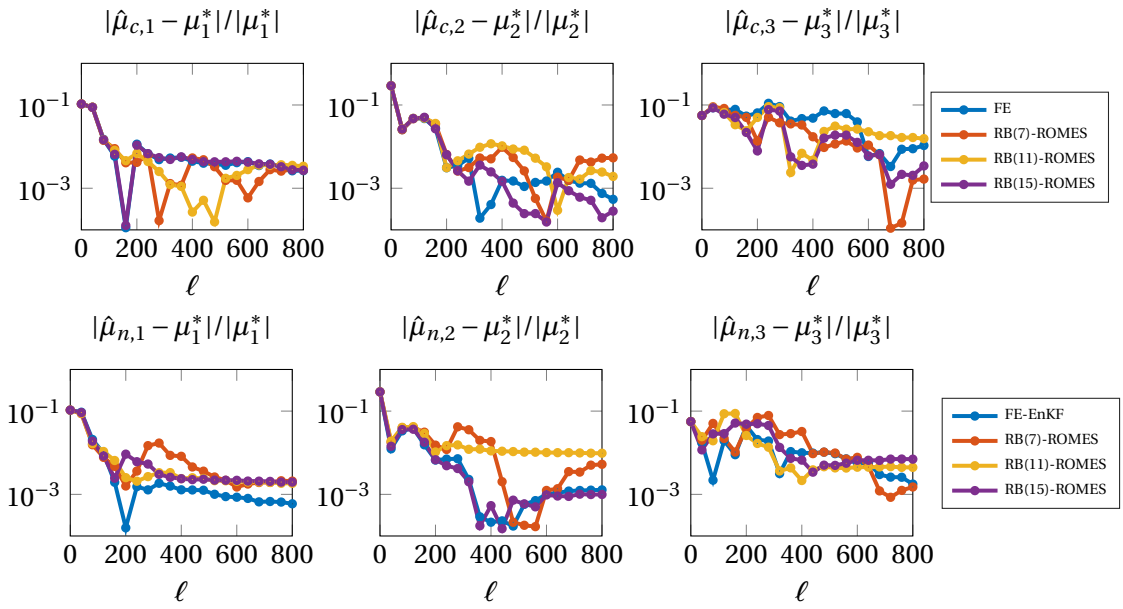

Figure 6.10 – Relative error on estimated parameter components $|\mu^* - \hat{\mu}_n^{(k)}|/|\mu^*|$ versus the RB dimension n for the corrected RB-EnKF when different noise variances $\sigma = 5\sigma_0$ (first row) and $\sigma = \sigma_0$ (second row) are considered.

More detailed results can be found in Table 6.1: for a noise level $\sigma = \sigma_0$, the ROM affects the accuracy of the identification for every choice of n, while for higher noise levels the estimation error can be much smaller at least for larger RB dimensions (see e.g. the results obtained for $n = 15$). This is motivated by the fact that the reduction error for $n = 15$ is considerably small, as we can observe in Fig. 6.8.

	σ	$n=7$	$n=11$	$n=15$
	$5\sigma_0$	$0.0442\ (1.49\cdot10^{-4})$	$0.0365\ (2.01\cdot10^{-4})$	$0.0054\ (3.11\cdot10^{-5})$
RB-EnKF	$2.5\sigma_0$	$0.1594\ (6.11\cdot10^{-5})$	$0.0488\ (2.37\cdot10^{-4})$	$0.0070\ (3.47\cdot10^{-5})$
	σ_0	$0.1779\ (4.09\cdot10^{-5})$	$0.0708\ (2.59\cdot10^{-5})$	$0.0613(2.04\cdot10^{-5})$
	$5\sigma_0$	$0.0148\ (3.37\cdot10^{-4})$	$0.0265\ (1.01\cdot10^{-3})$	$0.0073\ (2.25\cdot10^{-4})$
RB-EnKF(+ROMES)	$2.5\sigma_0$	$0.0175\ (1.24\cdot10^{-4})$	$0.0226\ (9.63\cdot10^{-4})$	$0.0117\ (2.84\cdot10^{-4})$
	σ_0	$0.0058\ (1.95\cdot10^{-4})$	$0.0108\ (5.85\cdot10^{-4})$	$0.0059\ (2.82\cdot10^{-4})$

Table 6.1 – Comparison of the error $\|\hat{\boldsymbol{\mu}}_h - \hat{\boldsymbol{\mu}}_n\|$ ($\|(\mathbf{C}^{(N_\tau)}_{\boldsymbol{\mu}_h,\boldsymbol{\mu}_h})^{1/2} - (\mathbf{C}^{(N_\tau)}_{\boldsymbol{\mu}_n,\boldsymbol{\mu}_n})^{1/2}\|$) and $\|\hat{\boldsymbol{\mu}}_h - \hat{\boldsymbol{\mu}}_c\|$ ($\|(\mathbf{C}^{(N_\tau)}_{\boldsymbol{\mu}_h,\boldsymbol{\mu}_h})^{1/2} - (\mathbf{C}^{(N_\tau)}_{\boldsymbol{\mu}_c,\boldsymbol{\mu}_c})^{1/2}\|$) versus the dimension n of the RB space and noise variance σ. Our ROMES considerably improves the accuracy of the estimated parameter: $\|\hat{\boldsymbol{\mu}}_h - \hat{\boldsymbol{\mu}}_n\|$ decreases by an order of magnitude for $n = 7$ whereas the error on the covariance matrices $\|(\mathbf{C}^{(N_\tau)}_{\boldsymbol{\mu}_h,\boldsymbol{\mu}_h})^{1/2} - (\mathbf{C}^{(N_\tau)}_{\boldsymbol{\mu}_n,\boldsymbol{\mu}_n})^{1/2}\|$ is still negligible with respect to the error $\|\hat{\boldsymbol{\mu}}_h - \hat{\boldsymbol{\mu}}_n\|$.

We recall that ROMES construction is performed only once after the ROM has been built during the *offline* phase. Given the reduction error $\boldsymbol{\chi}_t(\boldsymbol{\mu})$ for each $\boldsymbol{\mu} \in S_{cal}$, we check the assumption that the random field is second-order stationary and isotropic.

As shown in Figure 6.11 for the case $N_{train} = 80$ and $n = 11$, the correlation between errors shows a dependence on the parameter location: parameters with small lag present a smaller variability with respect to parameters with a larger lag. Then, we estimated the empirical semi-variogram $\{\hat{\gamma}(\delta_1), \dots, \hat{\gamma}(\delta_8)\}$ using (3.8) at 8 discrete lags $\{\delta_1, \dots, \delta_8\}$ for each component of the output and on each window $(\tau^{(k)}, \tau^{(k+1)})$. Through these estimated values the spherical semi-variogram model (3.6) is fitted and then used to compute the corresponding matrix of the linear system (3.3). An example of empirical semi-variograms and relative semi-variograms model is presented in Figure 6.11.

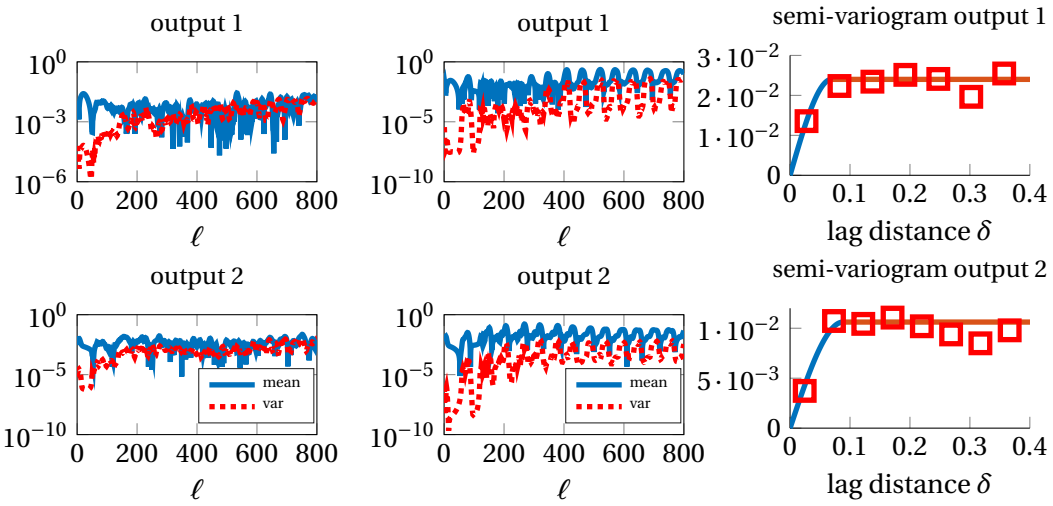

Figure 6.11 – Sample means and covariances of the errors on both output components evaluated over samples $N(\delta_1)$ (left), $N(\delta_2)$ (right), $\delta_1 \ll \delta_2$. Estimated semi-variogram $\{\hat{\gamma}(\delta_1), \dots, \hat{\gamma}(\delta_8)\}$ (red squares) and fitted spherical model γ for the two output components on the time interval $(a, b) = (0, T)$.

The quality of the ROMES yields significant improvements not only on the estimated mean $\hat{\boldsymbol{\mu}}_c$, but also on the covariance matrix of the parameter ensemble $\mathbf{C}_{\mu\mu}^{(N_\tau)}$. If we compare the errors $\|\hat{\boldsymbol{\mu}}_h - \hat{\boldsymbol{\mu}}_n\|$ and $\|\hat{\boldsymbol{\mu}}_h - \hat{\boldsymbol{\mu}}_c\|$ between the estimates obtained with the full-order EnKF ($\hat{\boldsymbol{\mu}}_h$), the RB-EnKF ($\hat{\boldsymbol{\mu}}_n$) and the corrected RB-EnKF ($\hat{\boldsymbol{\mu}}_c$), we find that $\|\hat{\boldsymbol{\mu}}_h - \hat{\boldsymbol{\mu}}_c\|$ is smaller than $\|\hat{\boldsymbol{\mu}}_h - \hat{\boldsymbol{\mu}}_n\|$ in all the considered cases, differing in some cases by more than two orders of magnitude. Even more, also the error $\|(\mathbf{C}_{\boldsymbol{\mu}_h,\boldsymbol{\mu}_h}^{(N_\tau)})^{1/2} - (\mathbf{C}_{\boldsymbol{\mu}_c,\boldsymbol{\mu}_c}^{(N_\tau)})^{1/2}\|$ between the square roots of the covariance matrices is considerably smaller than the error on the mean $\|\hat{\boldsymbol{\mu}}_h^{(N_\tau)} - \hat{\boldsymbol{\mu}}_c^{(N_\tau)}\|$, as we can observe in Table 6.2. In other words, the correction introduced by the ROMES is able to correct the bias yielded by the propagation of the reduction error, without substantially modifying the distribution of the ensemble particles. This means that the ensemble $\mathscr{P}_c^{(N_\tau)}$ resulting from the application of the corrected RB-EnKF is closer to $\mathscr{P}_h^{(N_\tau)}$, the one given by the full-order EnKF, than $\mathscr{P}_n^{(N_\tau)}$, the ensemble given by the RB-EnKF, as we have proven in Sect. 6.5.1.

		$N_{cal}=0$	$N_{cal}=24$	$N_{cal}=80$	$N_{cal}=240$
$N_{train}=24$	$n=7$	0.6669	0.1490	0.0250	0.0361
	$n=11$	0.0465	0.0337	0.0152	0.0140
	$n=15$	0.0385	0.0118	0.0161	0.0082
$N_{train}=80$	$n=7$	0.1594	–	0.0218	0.0175
	$n=11$	0.0488	–	0.0398	0.0226
	$n=15$	0.0070	–	0.0075	0.0117

Table 6.2 – Comparison of the error $\|\boldsymbol{\mu}^* - \hat{\boldsymbol{\mu}}_c\| / \|\hat{\boldsymbol{\mu}}\|$ on varying the dimension $N_{train} = |S_{train}|$, $N_{cal} = |S_{cal}|$ of the training set and of the calibration set. The error decreases as soon as the calibration and the training sample have a large dimension. The case with $N_{cal} < N_{train}$ is meaningless, since we would ignore part of the already computed data within the training set.

As we can observe in Table 6.3, building a RB approximation of small dimension n over a training set with dimension $N_{cal} = 24$ (resp. $N_{cal} = 80$) requires an *offline* CPU time of 16 min (resp 53 min), which is small compared to the CPU time of 387 min needed by the full-order EnKF procedure. In this test case, the calibration of the ROMES over sets of comparable dimension ($N_{cal} = 24$ and $N_{cal} = 80$) can be performed in few seconds. On the other hand, considering a calibration sample of large dimension $N_{cal} = 240$ yields better results in terms of estimation accuracy, however entailing a remarkable increase of the calibration costs.
The solution of the state/parameter estimation problem using the corrected RB-EnKF entails only 11 min: by comparing the whole procedures, in the worst case scenario we are saving 219 min, i.e. more than the 55% of the total computational cost. We also pointed out that the computational saving is even larger if more than one state/parameter estimation problem has to be solved, for instance on varying the noisy data $\mathbf{y}$: in this case the basis computation and the calibration need not to be run again, the only additional costs being those involved by the filtering procedure.

6.7 Conclusions

The RB-EnKF approach equipped with ROMES developed in this paper enables to speed up the solution of Bayesian inverse problems when time-dependent outputs are considered. The RB methodology provides a quick evaluation of the input/output mapping, leading to a considerable speedup of the whole EnKF procedure. On the other hand the ROMES guarantees with negligible computational costs the accuracy of the output evaluation. In this way, we obtain a corrected EnKF updating formula, whose accuracy has been investigated in the theoretical results provided in Section 6.5. A considerable computational earning is achieved by the RB-EnKF procedure: the computational speedup in performing the filter goes from 55× to 64× with respect to the full-order EnKF.

	RB			FE
	$n = 7$	$n = 11$	$n = 15$	$N_h = 1024$
dof reduction	99.3%	98.9%	98.5%	0%
Forward solution	0.6 s	0.7 s	0.8 s	40 s
$\|S_{train}\| = 24$				
ROM construction	16 min	16 min	16 min	
ROMES cal. $N_{cal} = 24$	15.1 s	17.4 s	18.73 s	
ROMES cal. $N_{cal} = 80$	37 min	37.1 min	37.3 min	
ROMES cal. $N_{cal} = 240$		139.2 min	139.3 min	139.4 min
$\|S_{train}\| = 80$				
ROM construction	53 min	53 min	53 min	
ROMES cal. $N_{cal} = 24$	15.1 s	17.4 s	18.73 s	
ROMES cal. $N_{cal} = 80$	49.8 s	53.8 s	59.7 s	
ROMES cal. $N_{cal} = 240$		103.3 min	103.4 min	103.5 min
Inverse problem				
EnKF time	6 min	6.3 min	6.9 min	387 min
EnKF ROMES $N_{cal} = 24$	7.7 min	8.2 min	8.6 min	
EnKF ROMES $N_{cal} = 80$	8.9 min	9 min	9.4 min	
EnKF ROMES $N_{cal} = 240$	10.9 min	11.1 min	11.4 min	

Table 6.3 – Computational performances of the proposed framework (offline construction and online inversion stages) and comparison with the FOM case.

Part III

Integrating data within models

7 | Three-dimensional subject-specific left ventricle

In this Chapter we apply the sensitivity analysis and uncertainty propagation developed in Chapter 4 to study the dependence of the action-potential shape from the physical and geometrical parameters on a three-dimensional left ventricle. Using the results of this analysis we simplify the parametric dependence in order to apply the Markov chain Monte Carlo (MCMC) developed in Chapter 5. After introducing the forward problem and its full-order numerical approximation in Section 7.1, we construct in Section 7.2 a state-based localized reduced-order model (ROM) and a GP-based ROM error surrogate. These latter are mandatory to perform the analysis presented in this Chapter due to the unfeasible computational costs arising from the full-order numerical model.
In Section 7.3 we first perform a sensitivity analysis revealing the role of the parameters with respect to the action-potential shape. Then, we further investigate the influence of geometrical parameters through an uncertainty propagation analysis. Finally, model personalization of the identifiable parameters is performed in Section 7.4. Our goal is to show the potential of the whole strategy in view of future more realistic applications.

7.1 Forward problem

We consider a parametrized system to describe the behavior of the cardiac potential on a three dimensional left ventricle in physiological conditions. We assume an isotropic conductivity tensor $\mathbf{D}_0 = \sigma_v \mathbf{I}$, being σ_v a parameter of the model. We describe the electrical activity of the left ventricle using the Monodomain model (1.4) with the Aliev-Panfilov model for the ionic term I_{ion} and the recovery term g (1.2). The model consists of the following parabolic

nonlinear PDE coupled with a nonlinear ODE: given $\boldsymbol{\mu} = [K, a, c_1, c_2, \varepsilon_0, \sigma_v, t_1, t_2]^T$, find $u = u(\mathbf{x}, t; \boldsymbol{\mu})$ such that:

$$\begin{cases} A_m \left(C_m \dfrac{\partial u}{\partial t} + K u(u-a)(u-1) + wu \right) - \operatorname{div}(\mathbf{D}_0 \nabla u) = A_m I_{app}(\mathbf{x}, t) & \mathbf{x} \in \Omega,\ t \in (0,T) \\ \dfrac{\partial w}{\partial t} = \left(\varepsilon_0 + \dfrac{c_1 w}{c_2 + u} \right) (-w - Ku(u-a-1)) & \mathbf{x} \in \Omega,\ t \in (0,T) \\ \nabla u(\mathbf{x}, t; \boldsymbol{\mu}) \cdot \mathbf{n} = 0 & \mathbf{x} \in \partial\Omega,\ t \in (0,T) \\ u(\mathbf{x}, 0; \boldsymbol{\mu}) = 0 & \mathbf{x} \in \partial\Omega, \end{cases} \tag{7.1}$$

where A_m and C_m are both fixed to 1. The applied current is given by two different stimuli located in $\mathbf{p}_1^a$ and $\mathbf{p}_2^a$, respectively:

$$I_{app}(t) = C_1 \exp\left(\frac{(\mathbf{x} - \mathbf{p}_1^a)^2}{0.6} \right) \mathbb{1}_{[t_1, t_1 + \Delta t]}(t) + C_2 \exp\left(\frac{(\mathbf{x} - \mathbf{p}_2^a)^2}{0.6} \right) \mathbb{1}_{[t_2, t_2 + \Delta t]}(t),$$

where t_1 and t_2 are different pacing times and $\mathbb{1}$ the indicator function, defined as

$$\mathbb{1}_{(a,b)}(t) = \begin{cases} 0 & \text{if } t \notin (a,b) \\ 1 & \text{if } t \in (a,b). \end{cases}$$

In order to take into account possible intra-subject variability of the left ventricle geometry, we introduce a suitable shape parametrization of the computational domain based on radial basis functions (RBFs) (see e.g. [Buh00]). In particular, we define a set of admissible shapes obtained as diffeomorphic images $\Omega(\boldsymbol{\mu}^g)$ of the reference domain Ω through a parametrized map $T(\cdot; \boldsymbol{\mu}^g)$ depending on eight parameters $\boldsymbol{\mu}^g = [\mu_1^g, \dots, \mu_8^g]$; these latter represent the displacement of eight control points in the normal direction to the left ventricle surface ($\mathbf{n}_{ext}$). Here we denote the deformed position $\mathbf{p}_k$ of each control point as

$$\mathbf{p}_k = \mathbf{p}_k^0 + \mu_k^g \mathbf{n}_{ext} \qquad k = 1, \dots, 8,$$

where $\mathbf{p}_1^0, \dots, \mathbf{p}_8^0 \subset \mathbb{R}^3$ denote the positions of the control points in the unperturbed reference configuration Ω. The parametric map $T(\cdot; \boldsymbol{\mu}^g) : \Omega \to \Omega(\boldsymbol{\mu}^g)$ is thus given by

$$T(\mathbf{x}; \boldsymbol{\mu}^g) = \mathbf{x} + \mathbf{W}^T \mathbf{s}(\mathbf{x}),$$

where $\mathbf{s}(\mathbf{x}) = [\phi(\|\mathbf{x} - \mathbf{p}_1^0\|), \dots, \phi(\|\mathbf{x} - \mathbf{p}_8^0\|)]$, ϕ is the Gaussian RBF function and $\mathbf{W} \in \mathbb{R}^{3 \times 8}$ the weights matrix satisfying the interpolation constrains (for further details see e.g. [MQR12]). In particular, by choosing $\mu_k^g = \{-1, 1\}$, $k = 1, \dots, 8$, we obtain the configurations reported in Figure 7.1. In this way, we are able to describe a wide range of different geometrical configurations, thus enabling to explore a variety of subject-specific geometries.

In conclusion, we end up with eight physical parameters characterizing the PDEs and the ODE of the monodomain model (7.1) and eight additional geometrical parameters, characterizing the left ventricle shape. A complete list of all the considered physical parameters and their range is presented in Table 7.1. The mean values have been chosen accordingly to [AP96].

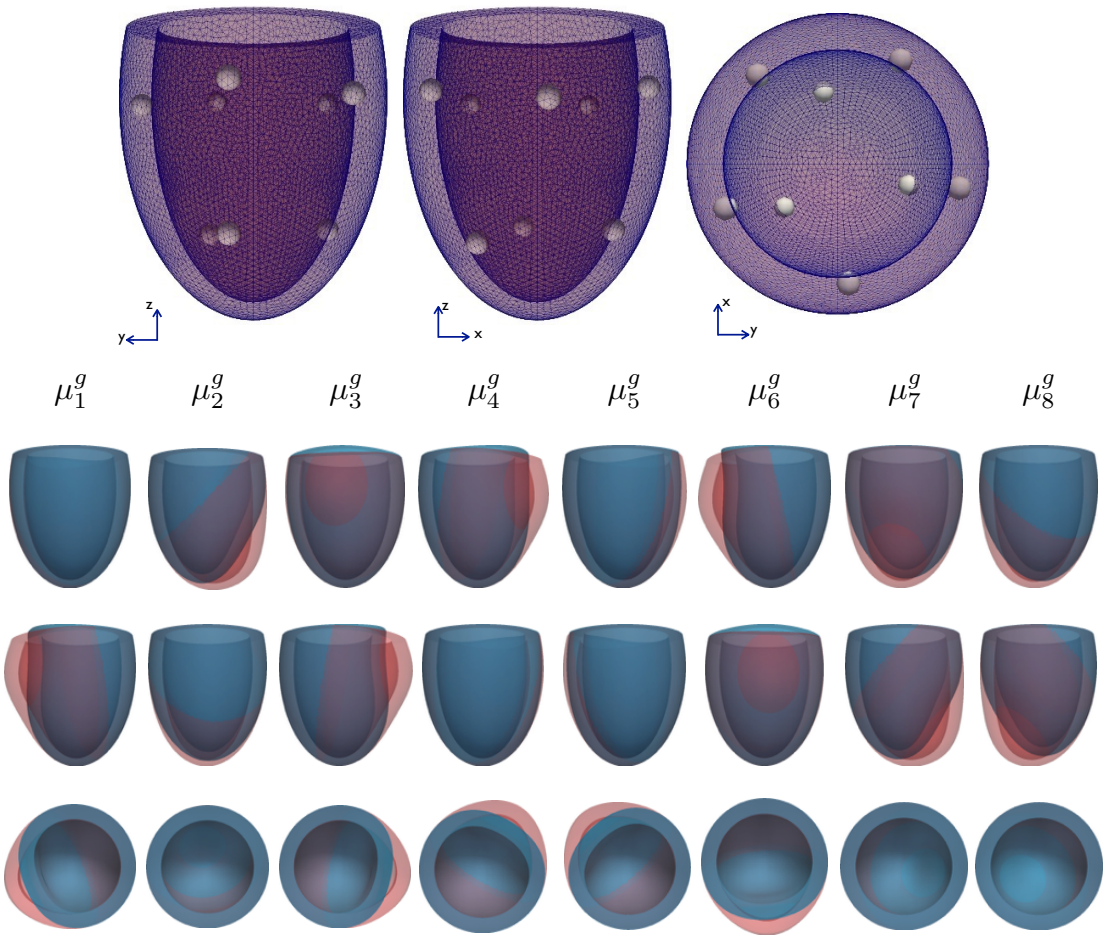

Figure 7.1 – Position of the control points in the unperturbed reference configuration Ω (top) and geometrical deformations of the reference domain Ω obtained by varying the eight geometrical parameters $\boldsymbol{\mu}^g$ (bottom)

Parameter	Mean	Range
K	8	[7,9]
ε_0	0.021	[0.001,0.041]
c_1	0.1	[0.05,0.15]
c_2	0.3	[0.25,0.35]
σ_v	0.35	[0.1,0.6]
a	0.15	[0.1,0.2]
t_1	10	[5,15]
t_2	25	[0.1,0.2]

Table 7.1 – Physical parameters of the left ventricle model and their range

A representation of different depolarization (activation) and polarization (deactivation) times is provided in Figure 7.2 for four different random values of the physical and geometrical parameters.

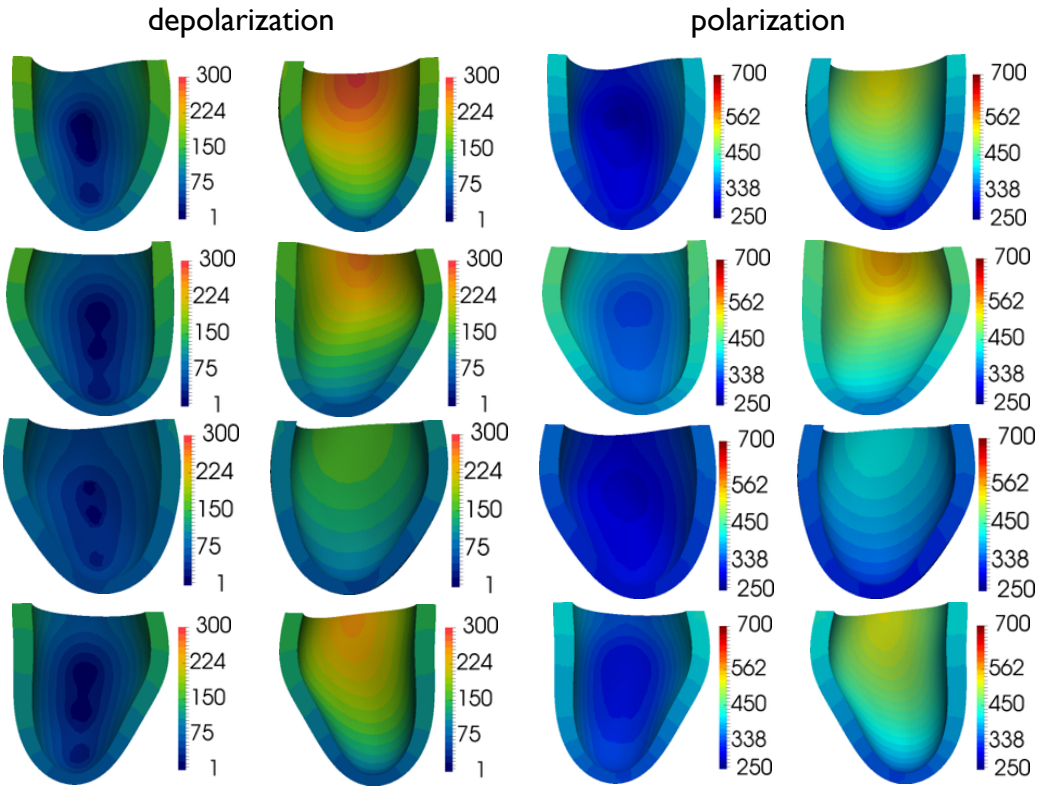

Figure 7.2 – Depolarization and polarization times [ms] for four different values of the parameter vector $\boldsymbol{\mu}$. The physical parameters greatly affect the propagation velocity of the front, while the geometrical ones are responsible of the change in the front profile.

Due to the high-dimensionality of the parameter space, a sensitivity analysis of the outputs with respect to the parameters is mandatory to simplify our model. Moreover, we focus on the inverse problem of identifying the physical parameters (for model personalization) starting from noisy measurements of the potential and considering the geometrical parameters as nuisance parameters, as happens e.g. when image registration is performed (see e.g. [SRSO$^+$05, SMC$^+$06, AHC$^+$15, AHC$^+$17]).

With this aim, we consider as output the action-potential:

$$\mathbf{y}_h(t;\boldsymbol{\mu}) = \mathbf{u}_h(t;\boldsymbol{\mu})\big|_{\mathbf{x}=\mathbf{x}_c},$$

computed at a selected point $\mathbf{x}_c$ of the left ventricle (a random sample of this output evaluations is reported in Figure 7.3). In this way, we can use the proposed reduced UQ framework to study how parameters modify the computed electric potential.

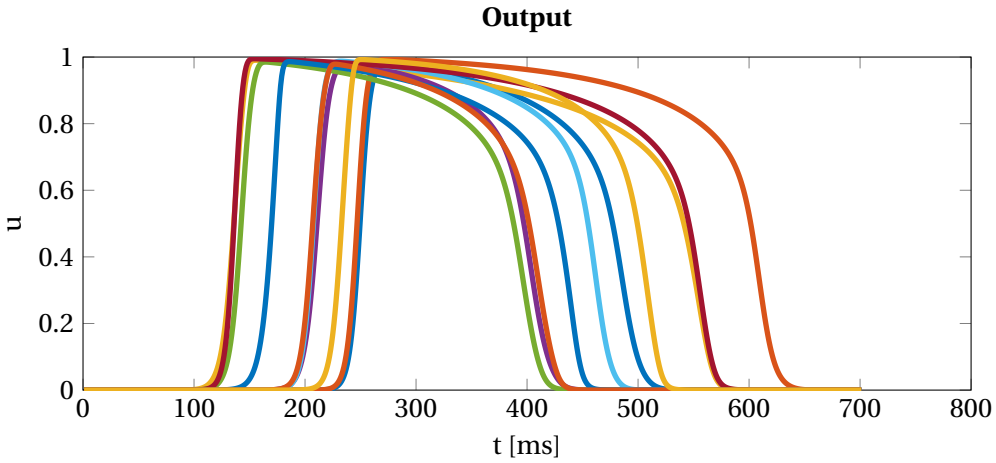

Figure 7.3 – Action-potential $\mathbf{y}_h(t;\boldsymbol{\mu})$ computed for random values of the parameters

As done in the previous numerical test, we describe these functions through three landmarks, reported in Table 7.2.
The forward problem is first approximated using linear finite elements on a mesh formed by $N_h = 15592$ vertices and 63802 elements. We consider the semi-implicit Euler scheme for time-advancing on a subdivision of $N_t = 800$ time-steps of length $\Delta t = 1ms$. This forward query entails on average 14 minutes and 30 seconds.

Landmarks	u.m.	physical meaning
t_{MRRU}	ms	time of upstroke rise max rate
t_S	ms	time of the stimulation pulse
t_{AP}	ms	action potential time from upstroke to resting potential

Table 7.2 – Considered scalar outputs for the description of the action-potential

7.2 Reduced-order model

In order to improve the computational performance of the input-output evaluation we rely on ROMs. However, constructing a ROM in this setting is a very challenging problem, due to the large number of parameters and to the problem complexity. For these reasons, we also do not consider a kriging-based SM, but we only rely on a state-based localized ROM equipped with a ROMES based on GP regression. Our localized-reduced basis approximation is built starting from $N_{train} = 25$ parameters randomly selected in the parameter space. In this case, the dimensions of the solution and nonlinear term snapshot matrices are $N_h \times 25N_t$.

We choose $N_c = 6$ clusters of the solution snapshots matrix and we compute the relative centroids using the *k-means* clustering technique. Then, for each cluster we compute the basis functions for the solution and the nonlinear term of the monodomain equation by means of

the POD technique with tolerance $2.5 \cdot 10^{-2}$. The resulting number of basis functions for each cluster is reported in Table 7.3. In this setting, the reduced solution is computed in 21 seconds on average, providing a speed up of $41x$ in the input-output evaluation with respect to the full-order FE approximation.

	#1	#2	#3	#4	#5	#6
solution	5	16	32	9	15	21
nonlinear term	66	80	77	47	47	78

Table 7.3 – Number of basis functions of the solution and the nonlinear term for each cluster

We also equip the constructed localized-ROM with a GP-based ROMES built over a calibration set of $N_{cal} = 40$ parameter vectors. By looking at the scatter-plots of the components of the reduced output vector versus the full-order ones (Figure 7.4), we can highlight that there is a simple dependence between the full- and the reduced-order outputs. For each component a GP regression is fitted, providing a way to efficiently approximate the output error. In this way, we avoid the curse of dimensionality, which could affect a kriging-based ROMES due to the large number of parameters.

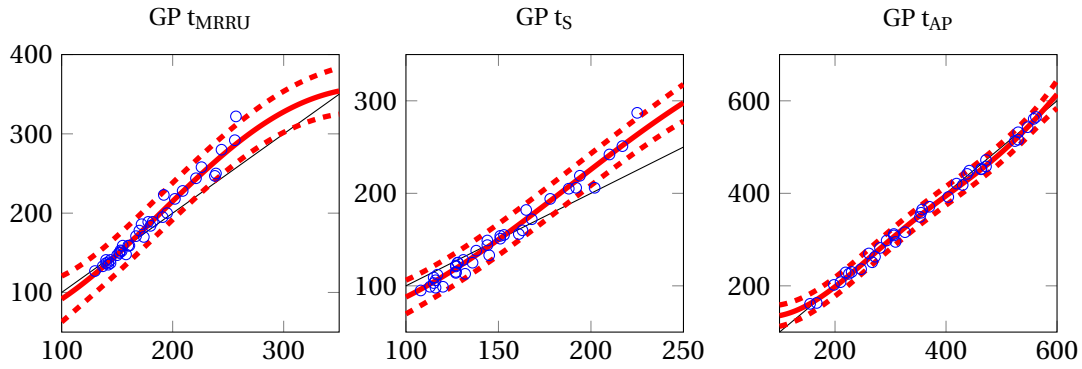

Figure 7.4 – GP-based ROMES for the approximation error on the outputs in Table 7.2. The stochastic dependence between the reduced and full-order model enables the construction of this ROMES whose complexity is independent from the parameters space.

The accuracy in the output given by the ROM equipped with the ROMES is tested on a third subset of the parameters space of dimension $N_{oob} = 25$ (see Figure 7.5). The bias in the ROM output is successfully corrected by the ROMES without introducing a large additional uncertainty in the prediction.

7.3 Uncertainty quantification

In view of a personalization of this model, that is the need of identifying the parameters related to a specific subject, we exploit the UQ framework previously introduced in order to better understand the main features of this model.

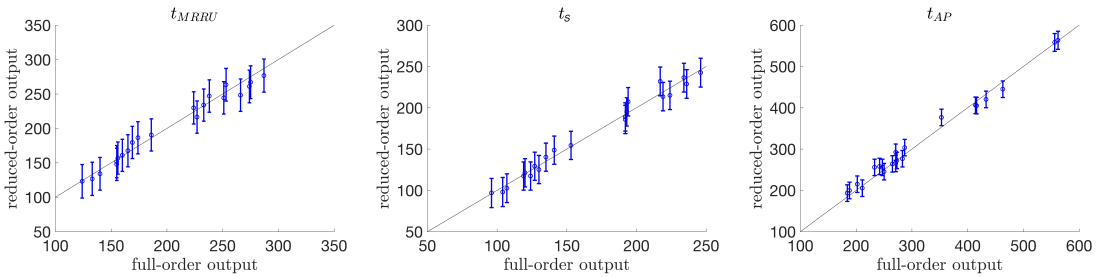

Figure 7.5 – Cross-validation of the ROM output equipped with GP-ROMES with $N_{train} = 25$, $N_{cal} = 40$ and $N_{oob} = 25$.

Sensitivity analysis

The main effects plots (see Figure 7.6) show that there are influential parameters among the physical ones: in particular the conductivity σ_v and the physical coefficient a clearly affect the maximum time t_{MRRU} of upstroke rise and the time t_S of the stimulation pulse, while the recovery coefficients ε_0 and c_1 and the physical coefficient a the time t_{AP} from upstroke to resting potential. These dependences are not surprising since the first two outputs are related to the depolarization phase, while the third one to the polarization phase.
On the other hand, we observe that variations of main effect curves are negligible when we consider a geometrical parameter μ_i^g. This is motivated by the fact that local changes (around the selected control point $\mathbf{p}_i^0$) in the domain do not considerably affect the wave propagation (and consequently t_S and t_{MRRU}).

The reliability of the results obtained with the ROM model, is clear also by looking at the confidence intervals of the main effects plots (Figure 7.7), all showing a small width.
The main effect indices S_i and $S_{T,i}$ (Table 7.4 and 7.5) confirm the results from main effects plots and highlight that K, c_2, t_1 and t_2 are non-influential for the considered outputs and could be fixed to any value in their range to simplify the model.

Output	K	ε_0	c_1	c_2	σ_v	a	t_1	t_2
t_{MRRU}	0.0456	0.0248	0.0225	0.0072	0.6380	0.2069	0.0069	0.0049
t_S	0.0507	0.0140	0.0104	0.0089	0.7136	0.1756	0.0069	0.0068
t_{AP}	0.0109	0.3554	0.2064	0.0169	0.0097	0.3000	0.0168	0.0185

Table 7.4 – Reduced-order first-order indices

Output	K	ε_0	c_1	c_2	σ_v	a	t_1	t_2
t_{MRRU}	0.0534	0.0315	0.0390	0.0040	0.7250	0.2301	0.0023	0.0067
t_S	0.0435	0.0136	0.0037	0.0014	0.7519	0.1938	0.0011	0.0011
t_{AP}	0.0150	0.4830	0.2680	0.0043	0.0152	0.3544	0.0017	0.0016

Table 7.5 – Reduced-order total effect indices

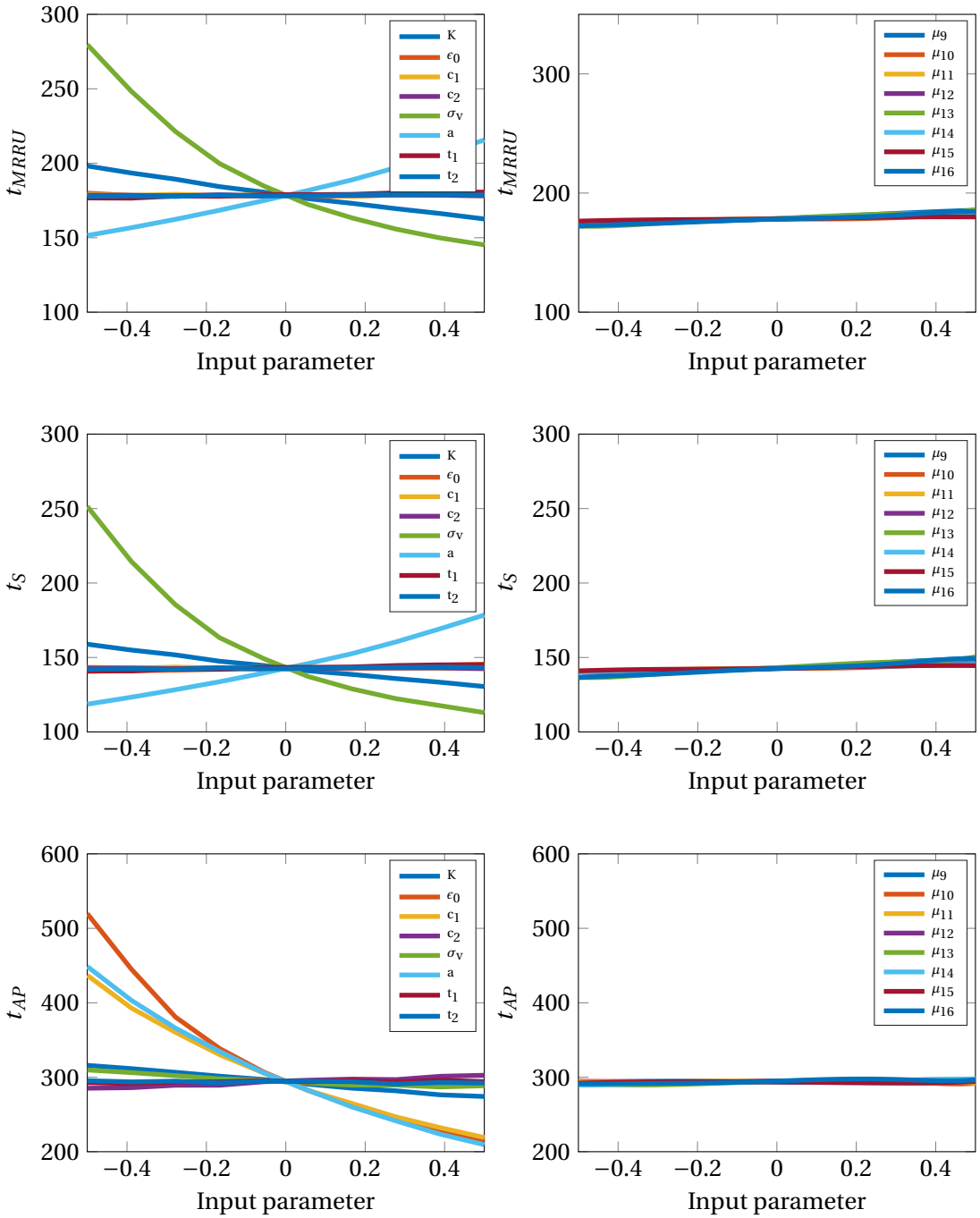

Figure 7.6 – Main effects plots obtained with the ROM equipped with the GP-ROMES. In this case, the role of the geometrical parameters is negligible with respect to the physical ones.

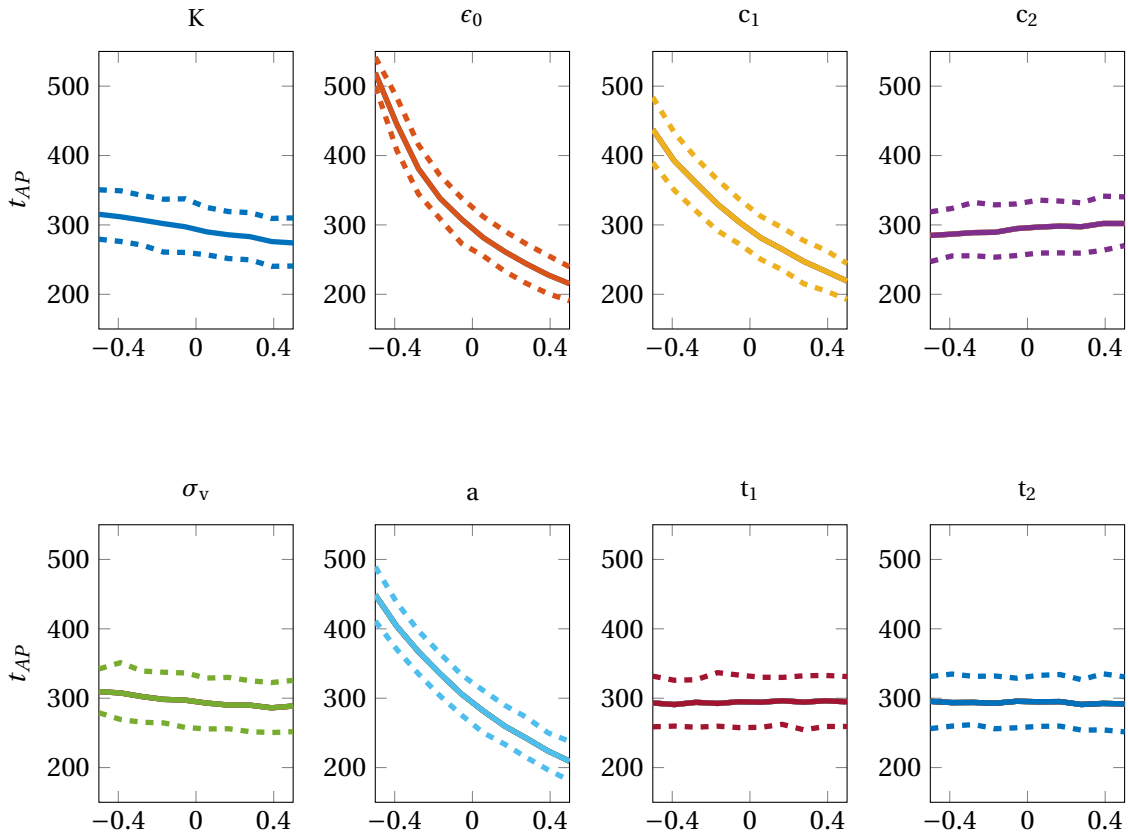

Figure 7.7 – Outputs variation with confidence intervals

Uncertainty propagation

Finally, we perform *uncertainty propagation* for the three-dimensional problem (7.1): in particular, we are interested in better understanding the role of the geometrical parameters with respect to the outputs.

From the sensitivity analysis, we have deduced that it is possible to neglect geometrical parameters without considerably compromising the accuracy in reproducing the output of interest. In order to verify this conclusion, we propagate the uncertainties in the geometrical parameters on the outputs starting from samplings with different variances. In particular, we test the case in which the geometrical parameters are sampled uniformly from the whole range $[-1,1]$, and on the ranges $[-0.5,0.5]$ and $[-0.04,0.04]$ (see Figure 7.8).

We notice that for t_{MRRU} and t_{AP} the additional variance introduced when large ranges of the geometrical parameter are considered is negligible. This conclusion does not hold for t_S, for which we observe a standard deviation on the output ranging from 1.03 to 5.42. This fact can be explained by considering that the time at which the stimulus reach $\mathbf{x}_c$ also depends on the shape of the domain. We can conclude that in order to study some pathologies that affect the action-potential shape it is sufficient to rely on a model where the geometrical configuration is fixed. If we are interested in modeling accurately the velocity of the front, the geometrical parameters should be taken into account. Of course, more detailed models, such as the bidomain system of equations, could provide even better insights.

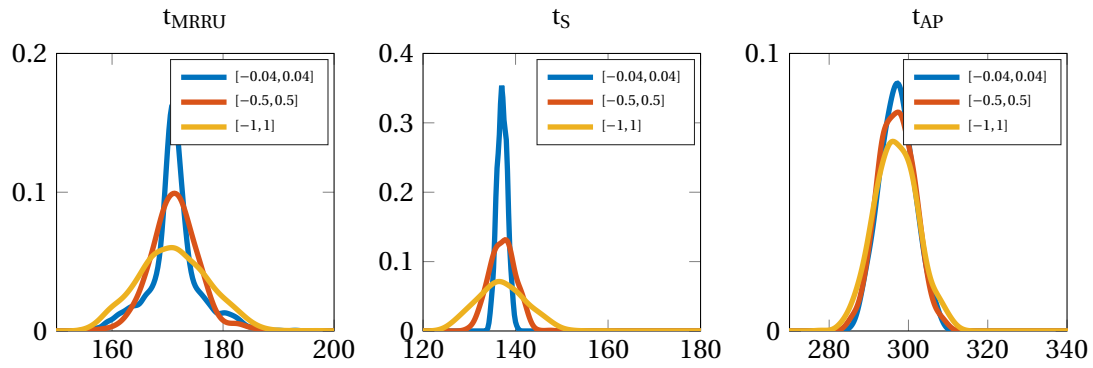

Figure 7.8 – Output probability densities obtained by a forward propagation of the uncertainties in the input parameters. The variance of each physical parameter is equal to 0.04 in normalized units, while we vary the range of the geometrical parameters from $[-1,1]$ to $[-0.04,0.04]$. Only for the output t_S we observe a considerable increase in the output variance, when the parameter variance changes.

7.4 Parameter estimation

We now solve a Bayesian inverse problem for the monodomain equation with Aliev-Panfilov ionic model for the three-dimensional personalized left ventricle presented in Section 7.1. The sensitivity analysis performed in Section 7.3 has shown that between the sixteen uncertain parameters (eight physical and eight geometrical) only $\boldsymbol{\gamma} = [a, c_1, \varepsilon_0, \sigma_v]^T$ are influential for the output vector

$$\mathbf{y}_h(\boldsymbol{\mu}) = [t_{MRRU}(\boldsymbol{\mu}), t_S(\boldsymbol{\mu}), t_{AP}(\boldsymbol{\mu})]^T,$$

whose components are the landmarks of the function $\mathbf{u}_h(t;\boldsymbol{\mu})\big|_{\mathbf{x}=\mathbf{x}_c}$. In particular, we consider

1. the time of upstroke rise max rate t_{MRRU},
2. time of the stimulation pulse t_S,
3. action potential time from upstroke to resting potential t_{AP}.

In this case, the Bayesian inverse problem consists in identifying the posterior distributions of $\boldsymbol{\gamma} = [a, c_1, \varepsilon_0, \sigma_v]^T$ in presence of the 12 nuisance parameters $\boldsymbol{\zeta}$ (formed by the others four physical parameters and the eight geometrical ones), from a noisy observation of the outputs vector:

$$\mathbf{y}^* = \mathbf{y}_h([\boldsymbol{\gamma}^*, \boldsymbol{\zeta}^*]) + \boldsymbol{\varepsilon}_{\text{noise}}$$

with $\boldsymbol{\gamma}^* = [0.017, 0.090, 0.147, 0.151]$ and $\boldsymbol{\zeta}^*$ randomly selected. Moreover, we assume that $\boldsymbol{\varepsilon}_{\text{noise}}$ is distributed as a multivariate Gaussian random variabile with zero mean and covariance:

$$\Gamma = \begin{bmatrix} 1.56 & 0 & 0 \\ 0 & 1 & 0 \\ 0 & 0 & 6.25 \end{bmatrix}.$$

We compare the results of the Bayesian inverse problem using a full-order model based on the finite element method and a state-based localized-ROM using a GP-based ROMES correction (for further details on the construction of these models see Section 7.2). The resulting posterior

pdfs using the different models are presented in Figure 7.9. In this case, we highlight that the ROMES correction is mandatory to improve the results of the Bayesian inversion: the marginal uncorrected ROM posterior pdfs for a and σ_v are completely different from the FOM ones.

The identifiability indices, reported in Table 7.6, confirm also in this case the connection between influential parameters, determined by the sensitivity analysis performed in Section 7.3, and identifiability. Starting from a uniform prior distribution on the parameters, we obtain marginal posterior distributions with small variances: as a matter of fact, the variance reduction indices $\mathscr{I}_i$ are greater than 0.6 in all cases and the values of the entropy index G are considerably large.

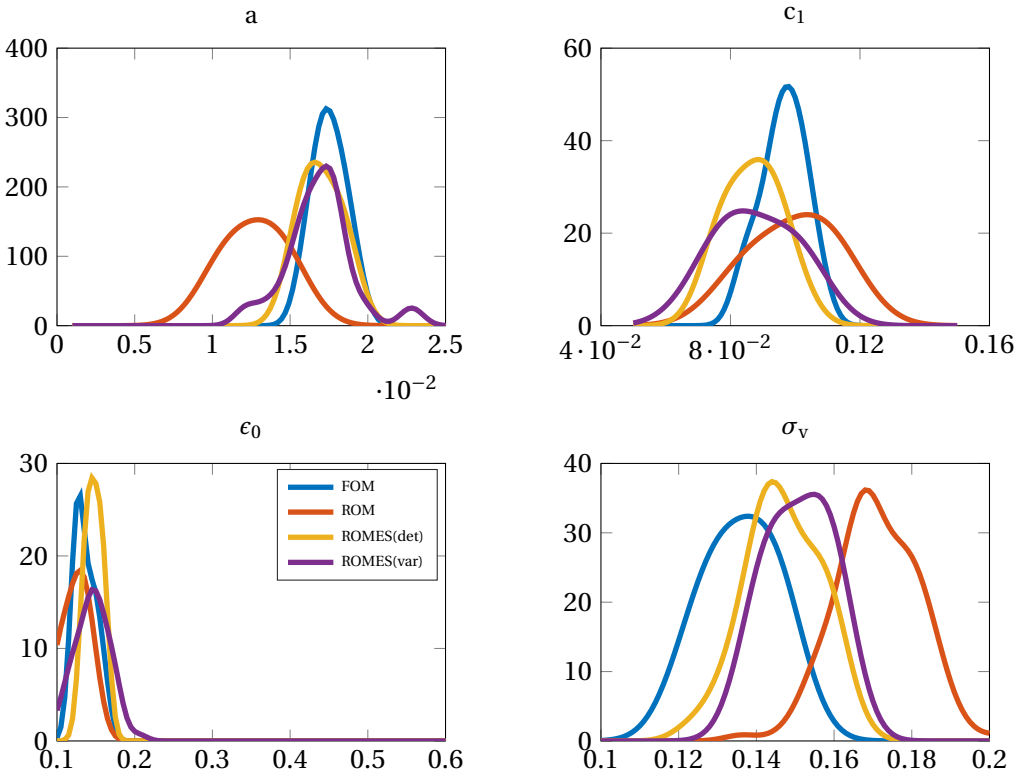

Figure 7.9 – Marginal posterior distributions of the identifiable parameters $\boldsymbol{\gamma} = [a, c_1, \varepsilon_0, \sigma_v]^T$ given the noisy observation y^*. The marginal posteriors obtained by combining the ROM with the (both deterministic and statical) ROMES are closer to the ones given by the FOM with respect to the uncorrected ROM posterior pdfs. Instead, considering the statistical SM prediction does not improve the results.

Finally, in order to verify the theoretical results presented in Sect. 5.4, we show in Table 7.7 the evaluations of the KL-divergences between the marginal FOM posteriors and the ROM ones when different correction strategies (deterministic and statistical GP-based ROMES) are considered. In this case, we highlight the effect of the deterministic ROMES correction in the marginal posterior distributions of a and σ_v, where the KL divergence goes from 2.37 (5.01) to 0.12 (0.52).

Output	a	c_1	ε_0	σ_v
Variance reduction $\mathscr{I}_i$	0.82	0.74	0.89	0.61
Entropy index G_i	1.56	1.17	2.09	0.78

Table 7.6 – Variance reduction indices $\mathscr{I}_i$ and entropy index G_i for $i = 1, \ldots = 5$

Output	a	c_1	ε_0	σ_v
ROM	2.37	0.42	0.29	5.01
ROM+ROMES(det)	0.12	0.49	0.30	0.52
ROM+ROMES(stat)	0.24	0.47	0.39	1.05

Table 7.7 – KL divergences between the posterior FOM distribution and the ROM one featuring ROMES correction.

7.5 Conclusions

The personalization of electrophysiology models is a rather involved procedure which requires the identification of the model geometry starting from imaging and the estimation of physical coefficients characterizing the mathematical model. The uncertainty arising during this procedure severely affects the estimation process, preventing its application in more realistic scenarios. Not only, such a process is extremely time consuming, because of the very large number of forward model queries. Moreover, this number could dramatically increase with respect to the number of parameters and the way they influence the output of interest. Selecting the most relevant parameters to be identified has thus a great impact on the whole personalization procedure. Our ROM/ROMES strategy makes *sensitivity analysis* and *uncertainty propagation* affordable even in such a complex case. In particular, we have reduced the number of parameters from sixteen to four when analyzing the impact of possible pathologies on the action-potential curve.

The parametrization of the geometry, which is an essential step towards a more realistic model, needs to be further improved in order to enhance the accuracy of the results. A higher number of RBFs could be considered also to address variations of the wall thickness. From the modeling perspective, the bidomain model could be considered in spite of its higher computational costs.
Although the validity of the test case is limited by the simplifying assumptions, the reliability of the whole strategy, demonstrated though the numerical results, is promising for a future application in a more realistic scenario.

8 | Myocardial ischemia detection

In this Chapter we apply the corrected reduced-basis ensemble Kalman filter (EnKF) developed in Chapter 6 to estimate the location and the shape of myocardial ischemic regions on a patient-specific left ventricle. An efficient solution of this rather involved test is obtained by combining the numerical methodologies developed in this Thesis, such as the localized reduced-order model (ROM) of Chapter 2, the ROM error surrogate of Chapter 3 and the EnKF of Chapter 6.
After introducing the full-order numerical approximation of the forward problem, we construct in Section 8.2 a state-based localized reduced-order model (ROM) taking advantage of the analysis carried out in Chapter 2. In Section 8.3 we formulate the state/parameter estimation problem related with ischemia detection, by focusing on the definition of different prior distributions modeling the most common locations of artery blocks. Three ROMs of different dimensions are considered in order to show the trade-off between the accuracy in solving the state/parameter estimation problem and the computational resources required by the whole procedure. In Section 8.4 and 8.5 we finally present the numerical results achieved with the RB-EnKF and its ROMES corrected version, showing the reliability of this procedure in detecting myocardial ischemia. This test case represents a preliminary step towards an efficient data-model integration in a clinical scenario.

8.1 Forward problem

In this last test case we consider the monodomain model (1.4) with Aliev-Panfilov current specification (1.2) on a realistic left ventricle aiming at estimating the presence of ischemic regions. As done in [KRC+11], an ischemic region is described as a lack of the conductivity field. In particular, we adopt a description of the non-homogeneous parametrized diffusion

coefficient $\sigma_v = \sigma_v(\mathbf{x};\boldsymbol{\mu})$ relying on a set of radial basis functions to take into account local variation of the conductivity field:

$$\sigma_v(\mathbf{x},\boldsymbol{\mu}) = \frac{1}{\nu_m(\mathbf{x})}\sum_{i=1}^{d}\mu_i \exp\left(-\frac{\|\mathbf{x}-\mathbf{x}_i\|^2}{\sigma^2}\right) \qquad \nu_m(\mathbf{x}) = \sum_{i=1}^{d}\exp\left(-\frac{\|\mathbf{x}-\mathbf{x}_i\|^2}{\sigma^2}\right),$$

where $\mu_i \in [0.01, 1]$, $1 \le i \le d = 20$ are the unknown parameters, ν_m a normalization term and $\mathbf{x}_1, \mathbf{x}_2, \ldots, \mathbf{x}_d$ are the centers of the radial basis functions, represented in Figure 8.1 covering all the domain. In this way, a healthy configuration is obtained when all the parameters are close to 1, while for μ_i close to 0.01 we have a lack of conductivity located around the corresponding center $\mathbf{x}_i$.

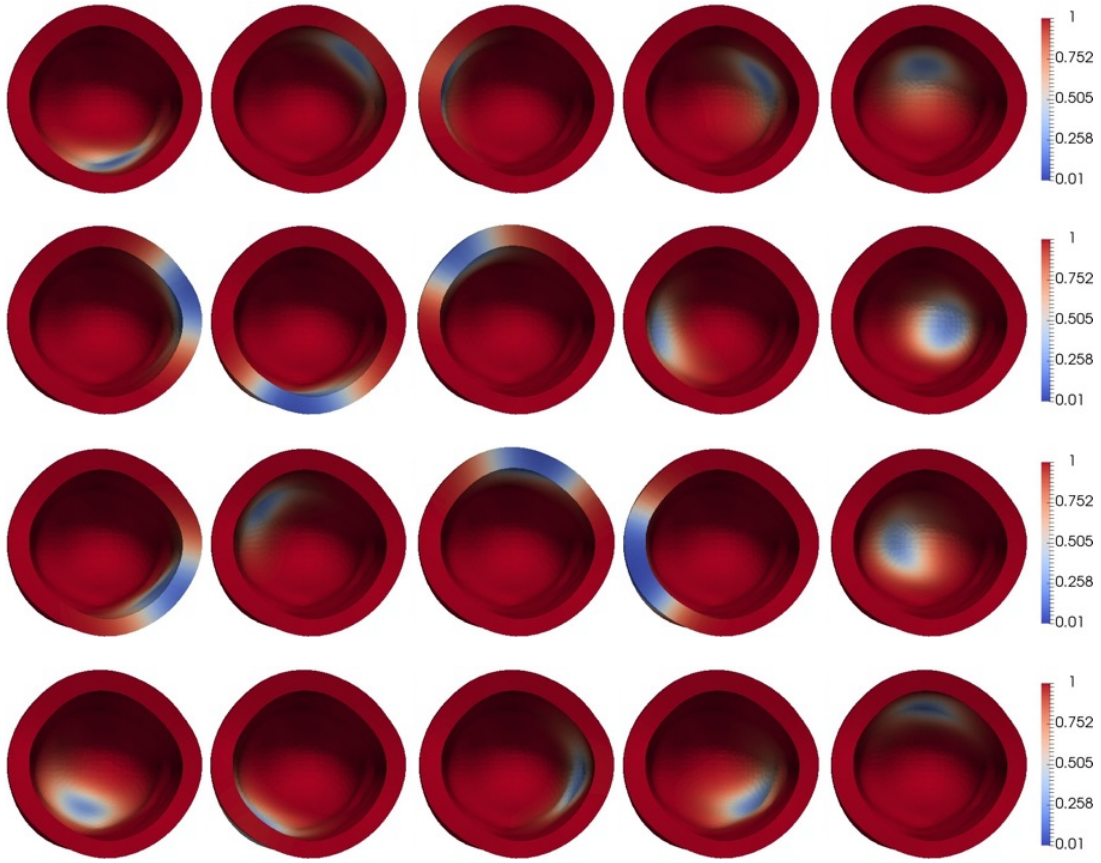

Figure 8.1 – Diffusion coefficient $\sigma_v(\mathbf{x};\boldsymbol{\mu})$ for $\boldsymbol{\mu} = \mathbf{e}_i$, $i = 1, \ldots, 20$, being $\mathbf{e}_i = \delta_i$ in the Kronecker notation

The model is completed by considering the non-homogeneous parametrized ionic current:

$$I_{ion} = \sigma_v(\mathbf{x};\boldsymbol{\mu})(Ku(u-a)(u-1) + uw).$$

An alternative representations of σ_v can be obtained e.g. by introducing a truncated Karhunen-Loève expansion [GS03] of the Gaussian random field $v \sim \mathcal{N}(\mathbf{0}, C)$, where C is a covariance matrix describing the spatial smoothness of the random field σ_v. Despite we have already

adopted this approach in [PMQ16], for the test case at hand the RBF approach has been chosen because of its capability of yielding a more realistic representation of the conductivity field. This is motivated by the fact that the RBF centers can be arbitrarily located in the regions of the left ventricle mainly affected by an artery occlusion. Two examples of resulting fields and relative depolarization maps are presented in Figure 8.2.

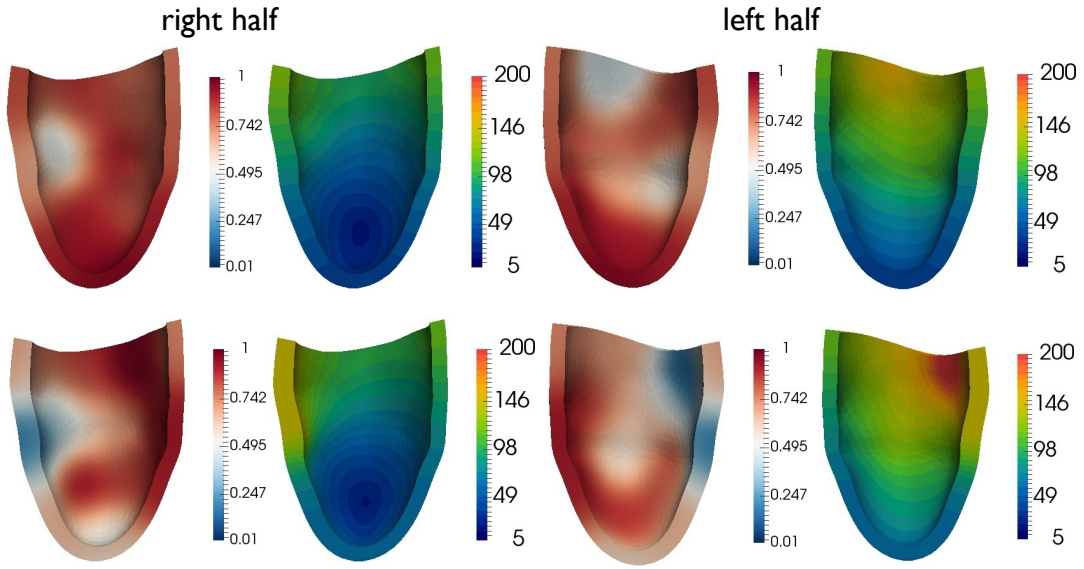

Figure 8.2 – Diffusion coefficient $\sigma_v(\mathbf{x};\boldsymbol{\mu})$ for two different values of $\boldsymbol{\mu}$, and the associated depolarization map, i.e. the times at which $u(\mathbf{x};\boldsymbol{\mu})$ reaches its maximum value for each point $\mathbf{x}$ of the computational mesh

Hence, we are able to characterize both healthy and unhealthy conditions in a specific way: in fact, the RBF model is able to describe local damages due to an occlusion of one of the main arteries (LAD,RCA,LCX). For this reason, solving the data-assimilation problem of estimating the vector of parameters $\boldsymbol{\mu}$ starting from noisy measurements of the electric potential is very interesting from a clinical perspective. On the other hand, the complexity of this problem poses several challenges from the numerical standpoint. The tools developed in the following chapters, such as the localized-ROM and the ROMES for functional-valued output, are thus essential in order to achieve accurate and efficient solutions of the data-assimilation problem.

The full-order approximation of the electrophysiology problem (1.4) with Aliev-Panfilov current specification (1.2) is obtained using the finite element method. We adopt linear finite elements on a computational mesh with $N_h = 6356$ mesh vertices and $N_{el} = 28080$ mesh elements (see Figure 8.3). We underline that more refined meshes together with more detailed models, such as the bidomain system of equations, should be considered in order to provide realistic simulations. However, the methodology developed in this Thesis could be extended also to manage these modifications of the problem.

From the given parametrization, we obtain also an affine decomposition of the diffusion

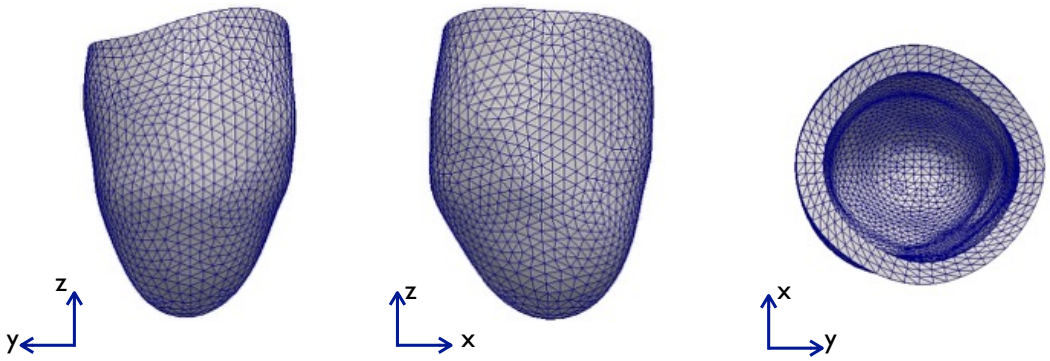

Figure 8.3 – Computational mesh of the patient-specific left ventricle.

matrix $A(\boldsymbol{\mu})$:

$$\mathbf{A}(\boldsymbol{\mu}) = \sum_{j=1}^{20} \mu_j \mathbf{A}^j,$$

where $\mathbf{A}^j$ are $\boldsymbol{\mu}$-independent FE matrices preassembled using the radial basis functions as conductivity coefficients.

By taking a partition of the time interval $(0, T)$ into $N_t = 900$ time-steps ($\Delta t = 0.5$ [ms]) and the semi-implicit Euler method, the forward problem takes the form of the following dynamical system: given $\boldsymbol{\mu} \in \mathscr{P} \subset \mathbb{R}^{20}$ find $\mathbf{u}_h^{(\ell+1)}$ such that

$$\begin{cases} \left(\mathbf{M} + \sum_{j=1}^{20} \mu_j \mathbf{A}^j\right) \mathbf{u}_h^{(\ell+1)} = \mathbf{M}\mathbf{u}_h^{(\ell)} + \Delta t(\mathbf{I}_{app}^{(\ell+1)}(\boldsymbol{\mu}) - \mathbf{I}_{ion}(\mathbf{u}_h^{(\ell)}), \mathbf{w}_h^{(\ell)}; \boldsymbol{\mu}) & \ell = 0, \dots, N_t - 1 \\ \mathbf{u}_h^{(0)} = \mathbf{u}_0(\boldsymbol{\mu}) & \\ \mathbf{w}_h^{(\ell+1)} = \mathbf{w}_h^{(\ell)} + \Delta t\, \mathbf{g}(\mathbf{u}_h^{(\ell)}, \mathbf{w}_h^{(\ell)}; \boldsymbol{\mu}) & \ell = 0, \dots, N_t - 1 \\ \mathbf{w}_h^{(0)} = \mathbf{w}_0(\boldsymbol{\mu}). & \end{cases} \tag{8.1}$$

We consider a vector $\mathbf{y}_h = [y_h^1, \dots, y_h^9]^T$ of nine functional outputs, whose components are defined as:

$$y_h^j(t; \boldsymbol{\mu}) = \int_\Omega \frac{1}{(0.1\pi)^{3/2}} \left(\nabla \exp\left(-\frac{\|\mathbf{x} - \mathbf{x}_j^c\|^2}{2(0.05)^2} \right) \right) \cdot \left(\sigma_v(\mathbf{x}) \nabla u(\mathbf{x}, t; \boldsymbol{\mu}) \right) d\Omega \qquad j = 1, \dots, 9, \tag{8.2}$$

being $\{\mathbf{x}_j^c\}_{j=1}^9$ nine points on the endocardium. Our aim is to approximate local measurements of the extracellular potential given by small electrodes placed in 9 points on the endocardium (formula (8.2) has been constructed adapting the integral expression presented in [GR02]). By considering a higher number of points it is possible to approximate the so-called simultaneous endocardial mapping in the human left ventricle obtained with a non-contact multi-electrode catheter (for further details see [SPD98, ÁAARÁ+12, YFR+05]). In Figure 8.4 we report the locations of the nine chosen points and the relative output components $y_h^j(t; \boldsymbol{\mu})$ computed for twenty random values in the parameters space.

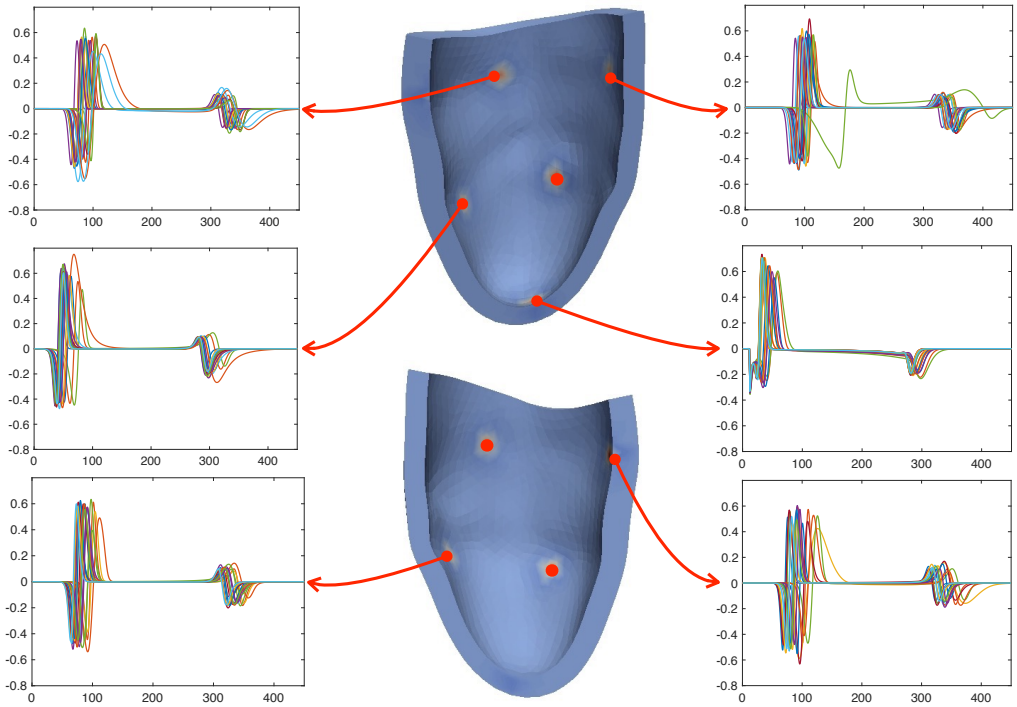

Figure 8.4 – Functional outputs modeling the local measurements of the extracellular potential. The outputs are characterized by a first considerable variation due to the depolarization of the LV (comparable to the QRS complex of a ECG) and a second smaller variation due to the polarization (comparable to to the T wave of a ECG).

Solving the algebraic system (8.1) by the full-order model (FOM) takes almost 9 minutes on average [1] (each evaluation of the nonlinear term requires on average 0.5 seconds, while the solution of the linear system about 0.1 seconds). Even in this simplified setting, the solution of (8.1) is already computationally intensive: as a matter of fact, performing sequentially 160 input/output evaluations using the FOM takes almost one day. Moreover, much more refined meshes are required when the goal is to capture in a detailed way the front velocity, with a consequent increase of the computational costs.

8.2 Reduced-order model

In this Section we consider the task of constructing a ROM for the forward problem (8.1) on a subjet-specific left ventricle. We first show that standard RB techniques are not straightforward for the problem at hand; in this respect, the state-based localized-ROM proposed in Chapter 2 is required in order to improve the computational performances of the input/output evaluation.

To give an insight of the complexity of the parametric dependence in this case, we have computed the singular values of the snapshots matrices of solutions $\mathbf{u}_h$ and of nonlinear terms

[1] All the *online* computations of this chapter have been performed on a laptop with 3.2 GHz Intel core i5 processor and 16Gb RAM.

$\mathbf{I}_{ion}$ in three cases:

1. the parameters vector is fixed to $\boldsymbol{\mu} = \mathbf{1} = [1,\dots,1]^T$, i.e. the solution snapshots matrix is only made by N_t full order vectors $\{\mathbf{u}_h^{(\ell)}(\mathbf{1})\}_{\ell=1}^{N_t}$;
2. only the first component of the parameters vector can vary (we have considered 10 random realizations to built the corresponding snapshots matrix of dimensions $N_h \times (10N_t)$);
3. only the first two components of the parameters vector can change (we have considered 20 random realizations to built the corresponding snapshots matrix of dimensions $N_h \times (20N_t)$).

The decay of the singular values, represented in Figure 8.5, clearly shows that the complexity of the solution manifold dramatically increases when variations in the parameters are considered.

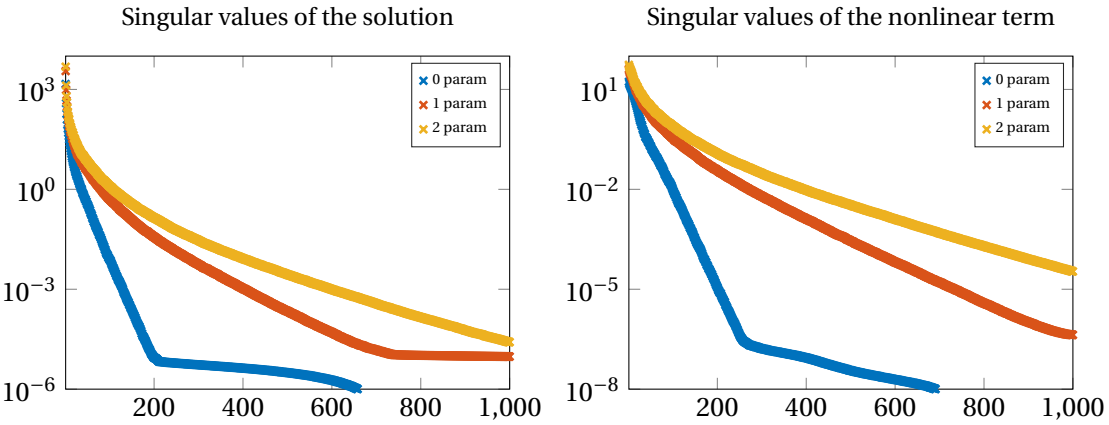

Figure 8.5 – Singular values decay for the case with fixed parameters vector (blue line), and the case where one (red line) and two (yellow line) components of $\boldsymbol{\mu}$ vary. In order to reach a precision of 10^{-2}, 97 basis functions are required in the first case, 268 basis functions in the second and 385 in the third.

As a consequence, classical state of the art RB techniques are not feasible for this application. We thus consider the state-based localized-ROM proposed in Chapter 2 relying on the *k-means* clustering technique for the selection of the local RB subspaces.

The *K-means* clustering aims at partitioning the snapshots matrix $\mathbf{S}_u$ into N_c submatrices $\mathbf{S}_u^1,\dots,\mathbf{S}_u^{N_c}$ in order to minimize the distance between each vector in the cluster and the cluster sample mean. In this application we consider $N_c = 20$ clusters built with respect to the Euclidean metric, with the goal of constructing possibly low-dimensional reduced-order arrays. By looking at the centroids selected by the *k-means* algorithm (see Figure 8.6), we highlight that the cluster subdivision is principally operated with respect to the time variable. Twelve centroids are related to the depolarization phase, showing a sharp traveling front, while only seven centroids are associated to the polarization phase.

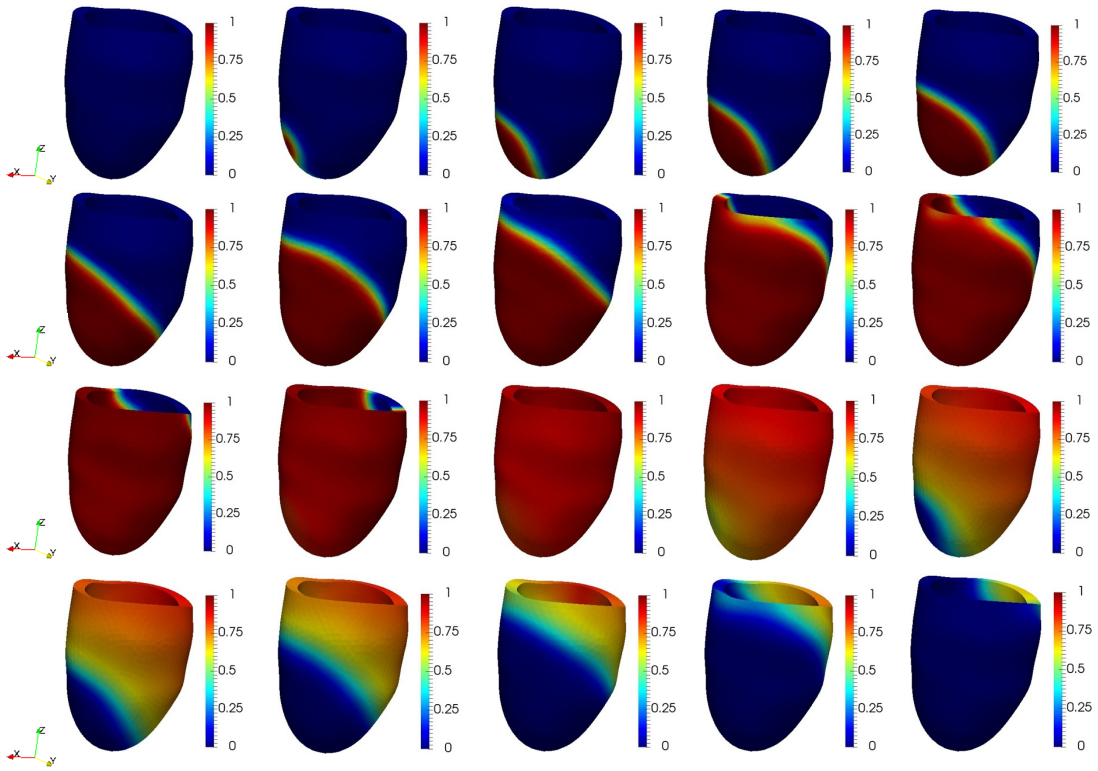

Figure 8.6 – Centroids selected by the *k-means* algorithm. The majority of them are related to the depolarization phase (first twelve subplots from the top left).

The snapshots matrix $\mathbf{S}_u$ of extremely high dimensions $N_h \times 900N_{train}$, with $N_{train} = 300$, is divided in the corresponding 20 submatrices $\mathbf{S}_u^k$, $k = 1,\dots,20$ identified by the *k-means* algorithm. The same operation is repeated also for the nonlinear vector $\mathbf{I}_{ion}$, relying on the state solution as clustering indicator. From each $\mathbf{S}_u^k$, we compute a set of RB basis functions using the proper orthogonal decomposition technique ($tol = 1.2\ 10^{-2}$). After repeating the same procedure for the nonlinear term, we end up with a localized-ROM (denoted in the following as ROM #1), for which the number of basis functions of the solution (nonlinear term) in each cluster varies from a minimum of $n_2 = 32$ ($m_{D,2} = 25$) to a maximum of $n_8 = 205$ ($m_{D,8} = 253$). The numerical approximation of the problem (8.1) given by ROM #1 requires 51 seconds, with a speed up of $10.5x$ if compared to the FOM of Section 8.1.

In order to speedup even more the input/output evaluation, we consider also two additional ROMs:

- ROM #2, built by retaining in each cluster the 60% of ROM #1 basis functions. This reduced model enables to solve the problem in 33 seconds, reaching a speed up of $16.3x$;
- ROM #3, built by retaining in each cluster the 40% of ROM #1 basis functions. This reduced model enables to solve the problem in 29 seconds, reaching a speed up of $18.6x$.

It is not surprising that a better computational performance is associated to a loss of computational accuracy (see Figure 8.7). The error propagation affects mainly ROM #3 for which

different front velocities cause anticipations or delays of the depolarization phase. On the other hand, ROM #2 is affected by a much smaller error than ROM #3. Moreover, the reduction error affects mainly the parts of the left ventricle close to the ischemic regions, which are responsible of the great variability of the solutions. Retaining less basis functions than the ones selected by ROM #1, clearly reduces the ability in reproducing the whole variability of the phenomenon.

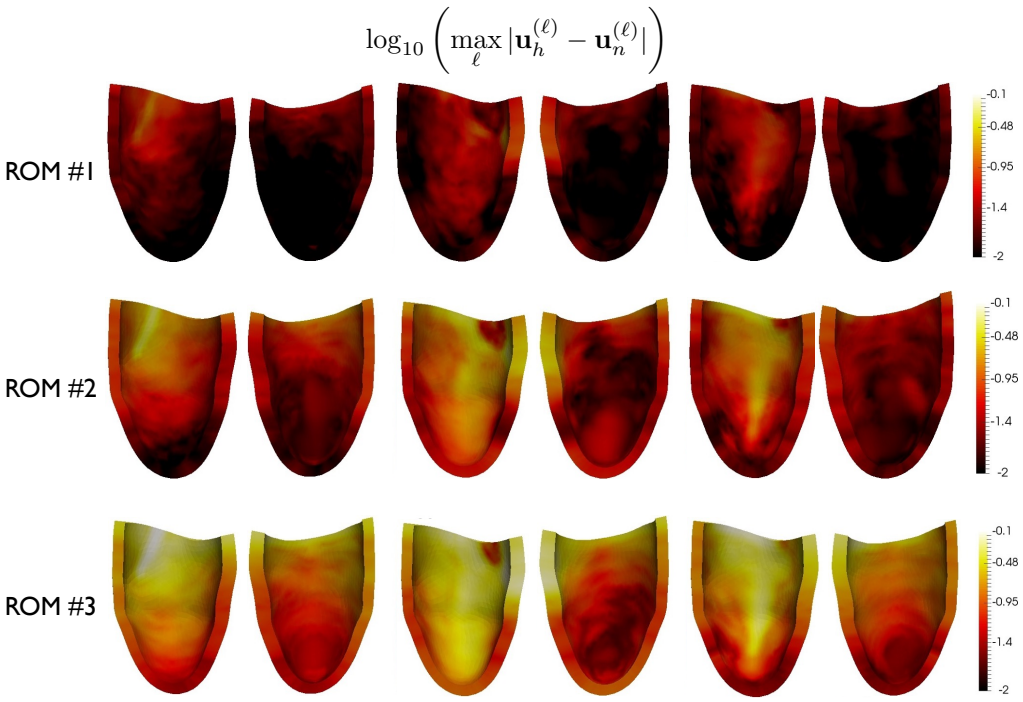

Figure 8.7 – Maximum error in time computed for three different values of the parameters vector and using the three different ROMs presented in this Section. For ROM #1, there is almost no error propagation: the phenomenon is well captured in all the three parameters configurations. For ROM #2 and ROM #3 non negligible errors are observed in correspondence of the ischemic regions.

The comparison of the outputs reported in Figure 8.8 clearly underlines that:

1. the reduced outputs given by ROM #1 almost coincides with the ones obtained using the FOM;
2. ROM #2 and ROM #3 are affected by a non-negligible approximation error, leading to an early depolarization in the ischemic region.

8.3 State-parameter estimation problem

The goal of the inverse problem is to estimate the vector of parameters $\boldsymbol{\mu}^*$ together with the state $\mathbf{u}^*$ from noisy sequential data:

$$\mathbf{y}^{(k)} = \mathbf{y}_h^{(k)}(\boldsymbol{\mu}^*) + \boldsymbol{\varepsilon}_{\text{noise}}^{(k)}, \qquad k = 1, \dots, N_\tau,$$

being $\varepsilon_{\text{noise}}^{(k)} \sim \mathcal{N}(\mathbf{0}, \Gamma)$ a Gaussian process modeling the noise on each window $(\tau^{(k-1)}, \tau^{(k)})$.

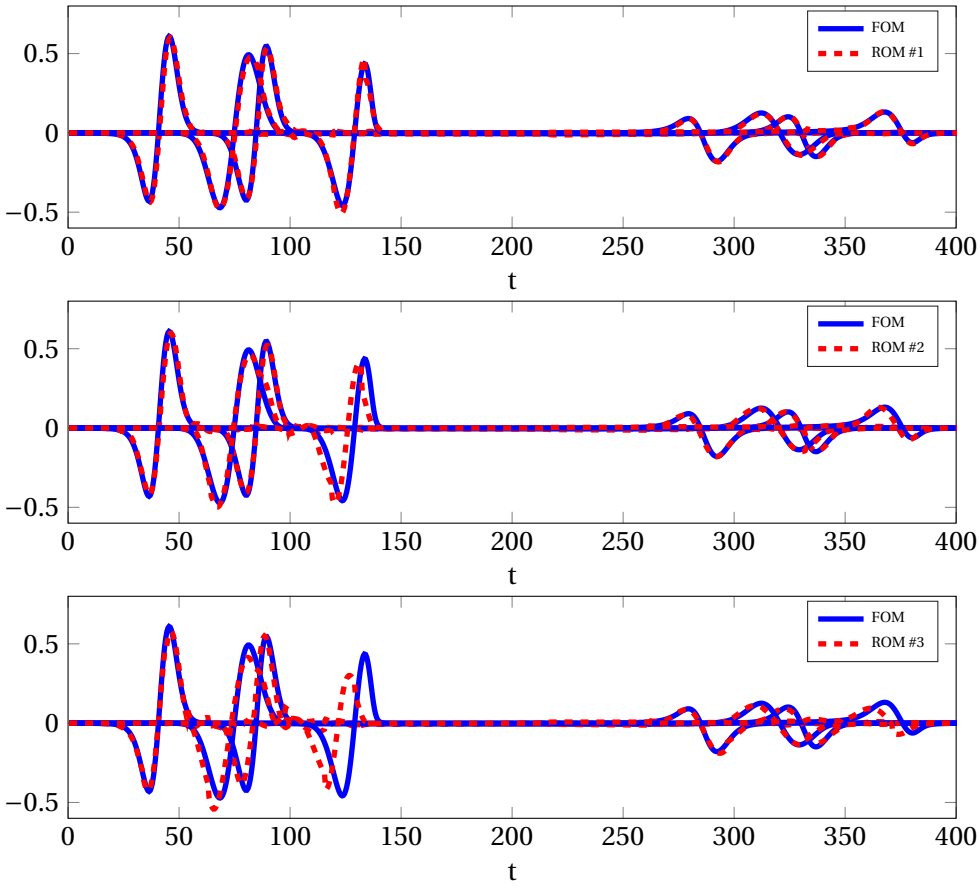

Figure 8.8 – Comparison between ROM and FOM outputs for ROM #1, #2 and #3 from top to the bottom.

In order to generate an initial ensemble of particles $\{\mathscr{P}_h^{(0)}, \mathscr{U}_h^{(0)}\}$ a prior distribution must be provided. In our case, since the initial condition is $\boldsymbol{\mu}$-independent, we are only interested in providing a prior distribution for the parameters vector. In this work we choose four different Gaussian priors, modeling different a priori information about the state of the patient (see Chapter 1 for further details):

1. healthy condition: the left ventricle shows good conductivity properties, which are modeled by choosing as prior mean $\mathbb{E}[(\boldsymbol{\mu}_{prior})_j] = 0.8$, $j = 1,\dots,20$, and as covariance matrix $(\mathbf{C}_{prior})_{jj} = 0.03$ for all $j = 1,\dots,20$;

2. artery block: the tissue is assumed to have a lack of conductivity in the region perfused by the LAD artery and good conductivity properties elsewhere, which are modeled by choosing as prior mean $\mathbb{E}[(\boldsymbol{\mu}_{prior})_j] = 0.5$, $j = 1,\dots,20$, and as covariance matrix $(\mathbf{C}_{prior})_{jj} = 0.05$ for each j such that $\mathbf{x}_j^c$ belongs to the LAD/RCA/LCX region.

This choice of the prior distributions is quite conservative, since we are considering a wide range of possible configurations, in order to not overweight the a-priori information with respect to the ones coming from the measurements. It is possible to design more detailed prior in order to test specific configuration.

From each prior, we sample N_e vectors $\boldsymbol{\mu}_q^{(0)}$, $q = 1,\dots,N_e$ forming the starting ensemble $\mathscr{P}_h^{(0)}$. The resulting four prior ensembles are represented in Figure 8.9, where the conductivity field σ_v has been computed for the sample mean $\overline{\boldsymbol{\mu}}_h^{(0)}$ and two values of the α-quantile $\mathbf{q}_\alpha$ (with $\alpha \in [0,1]$). We define the α-quantile as the vector formed by the values q_α^j such that the ensemble $(\boldsymbol{\mu}_q^{(0)})_j$, $q = 1,\dots,N_e$ is divided in two part proportional to α and characterized by $\mu_q^j \le q_\alpha^j$ and $\mu_q^j > q_\alpha^j$, $j = 1,\dots,d$.

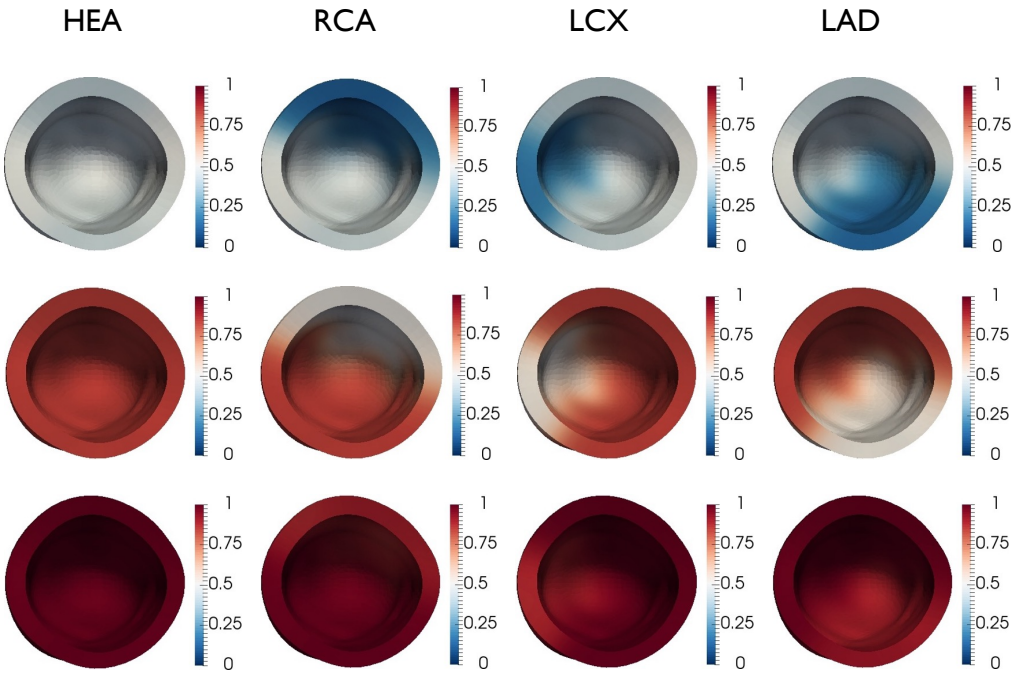

Figure 8.9 – Conductivity field $\sigma_v(\mathbf{x};\boldsymbol{\mu})$ computed from the sample mean estimate $\boldsymbol{\mu} = \overline{\boldsymbol{\mu}}_h^{(0)}$ (center row) and the empirical 0.05 and 0.95-quantiles $\boldsymbol{\mu} = \mathbf{q}_{0.05}$ and $\boldsymbol{\mu} = \mathbf{q}_{0.05}$ (top and bottom rows) of the four prior ensembles $\mathscr{P}_h^{(0)}$.

We test our reduced-framework for the estimation of a local ischemic region obtained by taking $\boldsymbol{\mu} = \boldsymbol{\mu}^*$ such that $\mu_6^* = 0.0760$, $\mu_{14}^* = 0.5096$ and random values $\mu_i^* > 0.7$, $i \neq 6,14$. This reference vector is used to artificially generate the nine noisy measurements of the output $\mathbf{Hu}_h^\ell(\boldsymbol{\mu}^*)$ reported in Figure 8.10.
At each iteration of the EnKF, we measure:

$$\mathbf{y}_h^{(k+1)}(\boldsymbol{\mu}) = \int_{\tau^{(k)}}^{\tau^{(k+1)}} \mathbf{Hu}_h(t;\boldsymbol{\mu})\,dt,$$

where $\mathbf{H}$ is the numerical approximation of (8.2). Each window $(\tau^{(k)},\tau^{(k+1)})$ contains 25 time-steps of the time-advancing scheme (a full simulation of the problem is performed on 36 windows). On each window the Kalman update formula

$$\begin{bmatrix} \boldsymbol{\mu}_q^{(k+1)} \\ \mathbf{u}_h^{(k+1)}(\boldsymbol{\mu}_q^{(k+1)}) \end{bmatrix} = \begin{bmatrix} \boldsymbol{\mu}_q^{(k)} \\ \mathbf{u}_h^{(k+1)}(\boldsymbol{\mu}_q^{(k)}) \end{bmatrix} + \begin{bmatrix} \mathbf{C}_{\mu y_h}^{(k+1)} \\ \mathbf{C}_{u_h y_h}^{(k+1)} \end{bmatrix} (\boldsymbol{\Gamma} + \mathbf{C}_{y_h y_h}^{(k+1)})^{-1} (\mathbf{y}_q^{(k+1)} - \mathbf{y}_h^{(k+1)}(\boldsymbol{\mu}_q^{(k)})),$$

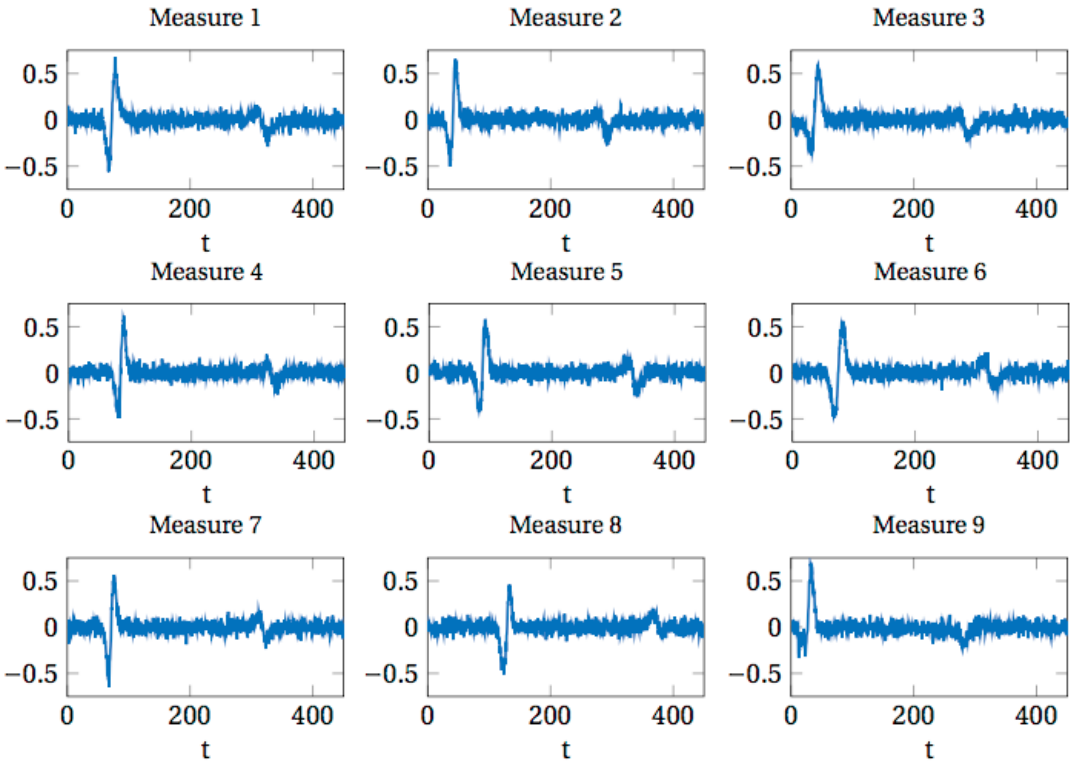

Figure 8.10 – Noisy measurements $\mathbf{H}\mathbf{u}_h^{(\ell)}(\boldsymbol{\mu}^*)$ perturbed with Gaussian random noise (zero mean and standard deviation equal to $(\Gamma)_{jj}^{1/2} = 0.05$).

compares N_e realizations of the noise $\boldsymbol{\varepsilon}_q^{(k+1)}$, $q = 1,\dots,N_e$, with the data coming from the *prediction stage*, where the full-order forward problem is solved for each element $\boldsymbol{\mu}_q^{(k)}$ in the ensemble $\mathscr{P}_h^{(k)}$ with the corresponding initial conditions $\mathbf{u}_h^{(k)}(\boldsymbol{\mu}_q^{(k)})$ contained in $\mathscr{U}_h^{(k)}$. The EnKF sequentially corrects the particle ensembles $\mathscr{P}_h^{(k)}$ and $\mathscr{U}_h^{(k)}$ in order to match the current state estimation with sequentially acquired noisy measurements, as we can observe in Figure 8.11.

8.4 RB-EnKF

We then apply the RB-EnKF in order to estimate the unknown parameters $\boldsymbol{\mu}^*$ characterizing the conductivity properties of the left ventricle when ROMs with different fidelities are exploited. Starting from the prior distribution corresponding to a LAD block, we run the RB-EnKF with $N_e = 200$ particles. When ROM #1 is adopted in the EnKF, the updating procedure of the parameters ensemble leads to a correct identification of the parameters vector, as shown in Figure 8.12. We observe that the ensemble confidence bands (dotted blue lines) become smaller and smaller during the solution of the EnKF, meaning that the knowledge about the parameters increases thanks to the information coming from the assimilated measurements. In particular, the parameters related to the healthy regions ($\mu_i > 0.7$) are well captured after 7 iterations, while more iterations are required for a correct estimation of μ_6.

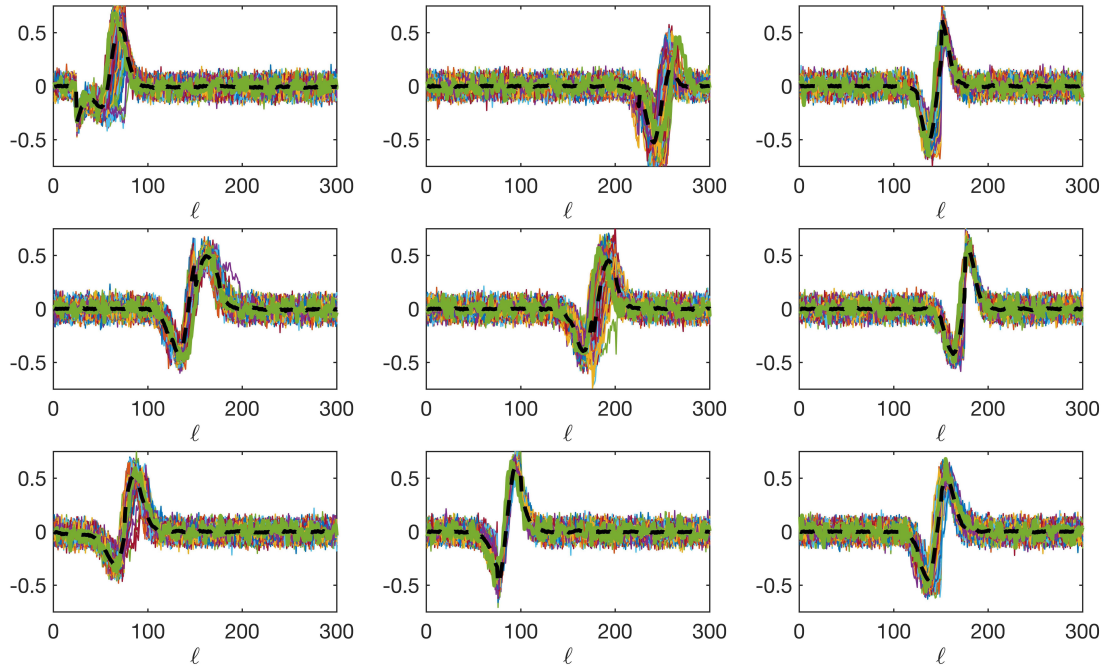

Figure 8.11 – Outputs $\mathbf{Hu}_n^{(\ell)}$ computed for each element in the ensemble $\mathscr{P}_h^{(k)}$ with the corresponding initial datum taken in $\mathscr{U}_h^{(k)}$ on the first twelve windows. We can observe that the means of the outputs (black dotted line) match with the noisy measurements on each window.

At the end of the EnKF procedure, the parameters ensemble $\mathscr{P}_n^{(N_\tau)}$ is a good sample of the posterior pdf of the parameters given the noisy data. Some indicators of the unknown parameter vector are finally computed on $\mathscr{P}_n^{(N_\tau)}$, such as the posterior mean or the maximum a posteriori estimate. The conductivity fields $\sigma_v(\mathbf{x};\hat{\boldsymbol{\mu}})$ obtained with the mean estimates $\hat{\boldsymbol{\mu}} = \overline{\boldsymbol{\mu}}_n^{(N_\tau)}$ are presented in Figure 8.13 on varying the different ROMs exploited for the PDE model approximation. We notice that the propagation of the error, when ROM #2 and #3 are used, leads to biased estimates of the conductivity field. Together with the mean, we also compute the empirical standard deviation of $\sigma_v(\mathbf{x};\boldsymbol{\mu})$, for all $\boldsymbol{\mu} \in \mathscr{P}_n^{(N_\tau)}$ in each point of the computational domain (see bottom part of Figure 8.13). The starting maximum standard deviation of 0.2143 computed on the prior ensemble $\mathscr{P}_n^{(0)}$ is reduced to 0.08 when ROM #2 and #3 are adopted (the uncertainties are mainly concentrated around the non captured ischemic region).

Moreover, on each resulting ensemble $\mathscr{P}_n^{(N_\tau)}$ we compute the probability that $\mu_6 < \eta$, being η a selected threshold (here we take $\eta = 0.4$). We obtain $\mathbb{P}(\mu_6 < \eta) = 0.9960$ using ROM #1, $\mathbb{P}(\mu_6 < \eta) = 0.5280$ with ROM #2 and finally $\mathbb{P}(\mu_6 < \eta) = 0.0240$ with ROM #3. On the basis of these results, we correctly estimate the presence of an ischemic region only when ROM #1 is used in the RB-EnKF. On the other hand, there is a complete misclassification when ROM #3 is used, since we deduce from the numerical results that the tissue is healthy, when instead it is not.

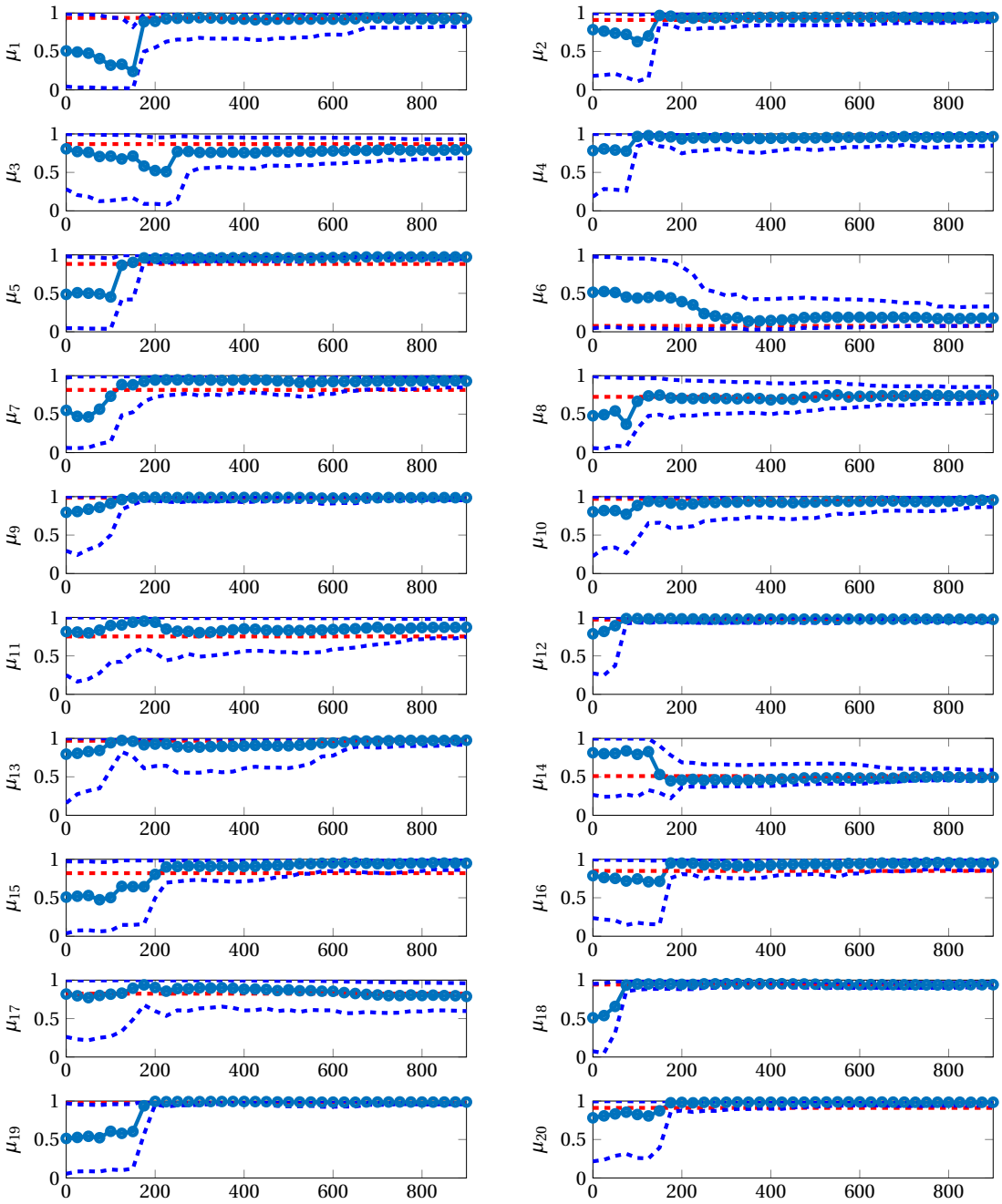

Figure 8.12 – Mean (blue circles) of the parameters ensemble $\mathscr{P}_n^{(k)}$ for $k = 1, \ldots, N_\tau$, together with the 95% confidence bands (dotted blue line). Here, the red dotted lines corresponds to the components of $\boldsymbol{\mu}^*$, the parameter vector used to generate the noisy data. The width of the confidence bands is reduced in time, due to the progressive assimilation of the data.

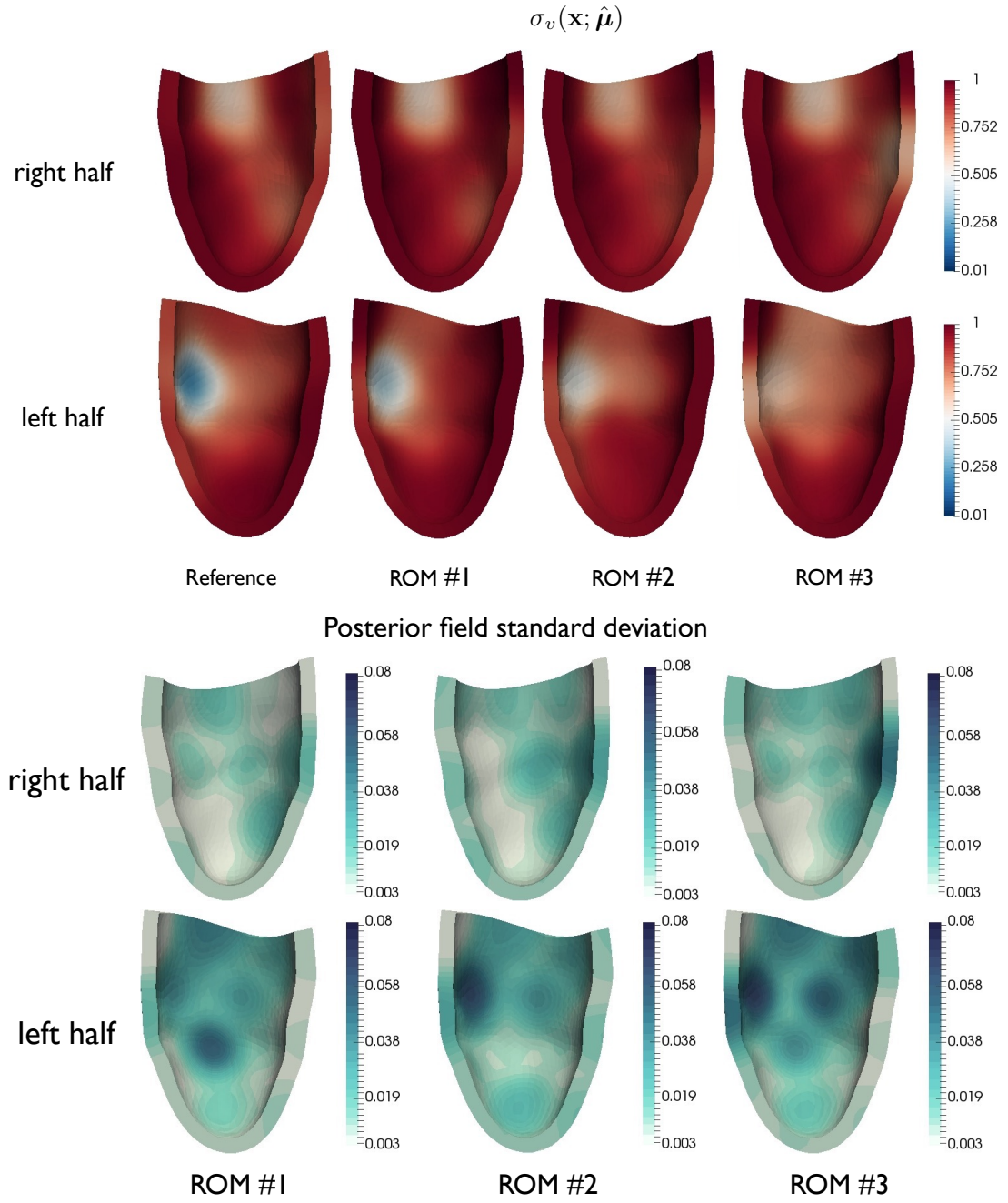

Figure 8.13 – Conductivity fields $\sigma_v(\mathbf{x};\hat{\boldsymbol{\mu}})$, $\hat{\boldsymbol{\mu}} = \overline{\boldsymbol{\mu}}_n^{(N_\tau)}$, given by the RB-EnKF using different ROMs (top) and their standard deviations (bottom). The field is only well captured using ROM #1, which is the most accurate model. In this case the field corresponding to the mean vector estimate is close to the reference one and the standard deviation is lower than 0.06 in each point of the computational domain (and even smaller in all the right half of the left ventricle). When less accurate ROMs are adopted, the mean fields obtained are far from the reference one; additional uncertainties in the estimation (yielding larger standard deviations) arise. Taking into account the approximation error is thus crucial to recover an unbiased estimate.

In Figure 8.14 we represent the field $\sigma_v(\mathbf{x};\mathbf{q}_{0.05})$ and $\sigma_v(\mathbf{x};\mathbf{q}_{0.95})$, being $\mathbf{q}_{0.05}$ and $\mathbf{q}_{0.95}$ the empirical 0.05 and 0.95-quantiles of $\mathscr{P}_n^{(N_r)}$ for the different ROMs. In this way, we can visualize all the range of possible configurations of σ_v. We observe that also the field associated to the quantiles are far from the true solution when ROM #3 is used.

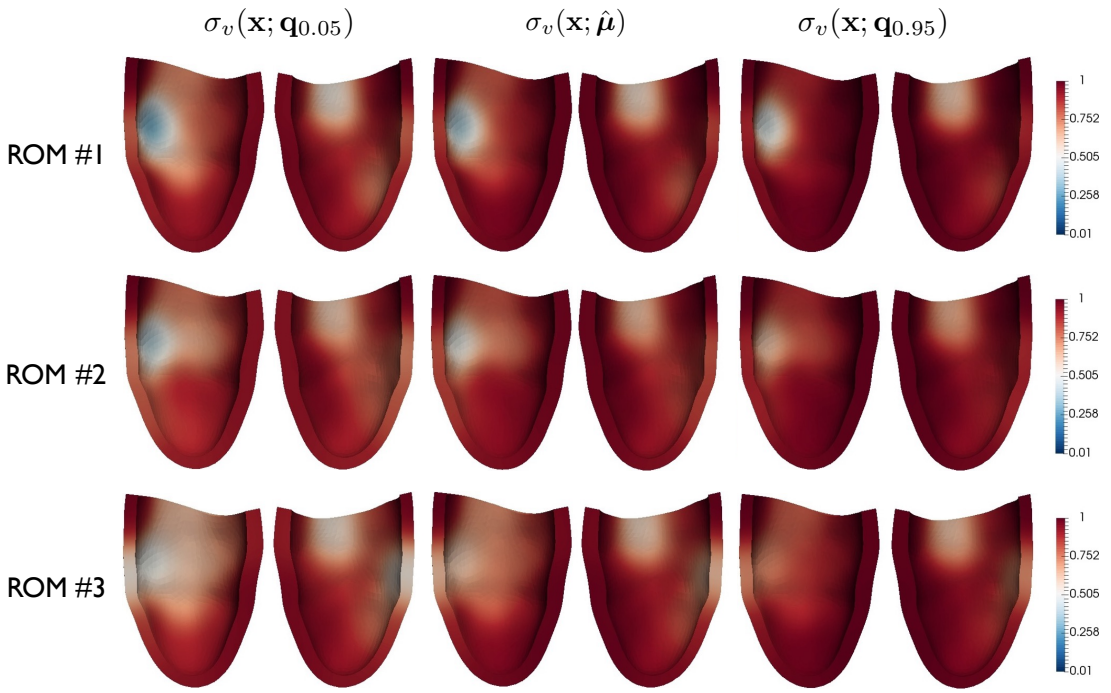

Figure 8.14 – The 0.05 and 0.95-quantiles of the conductivity fields given by the RB-EnKF using ROM #1, #2 and #3 (from the top to the bottom). The fields related to ROM #1 are very close to the reference field. The propagation of approximation error in the case of ROM #3 compromises the estimation procedure leading to biased estimates.

The effect of the error propagation is also clear from the reconstructed state solutions: in the reference solution the traveling front slows down when reaching the ischemic region (see Figure 8.15); this behavior is well captured only when ROM #1 is used, while it is not when ROM #2 and ROM #3 are used (the solution is much more similar to the ones related to healthy patients).

The computational costs of the RB-EnKF using these different ROMs varies considerably: the estimation procedure entails 2 hours and 55 minutes with ROM #1 and 1 hour and 39 minutes with ROM #3. However, the computational earnings obtained with a less accurate ROM correspond to non correct parameter estimates. For this reason, we consider a kriging-based ROMES to minimize the propagation of the reduction error, trying to preserve the computational speedup obtained with ROM #2 and #3.

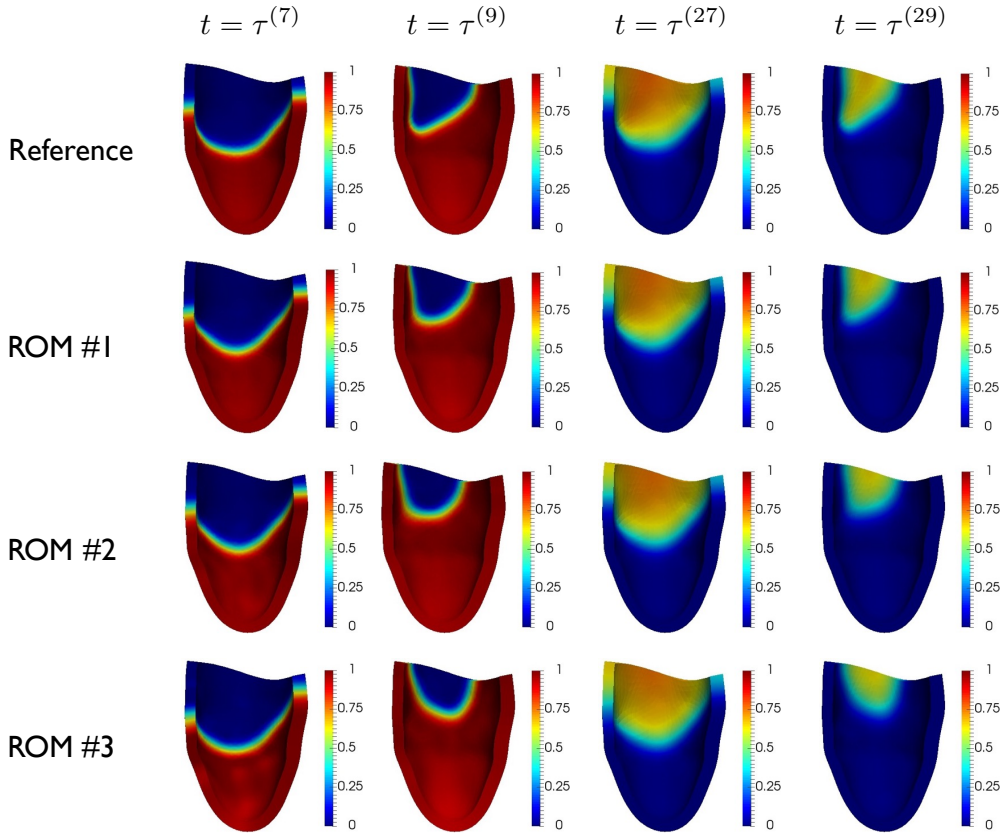

Figure 8.15 – Mean estimates of the state ensemble $\mathbf{u}_n^{(k)}$ for $k = 7, 9, 27, 29$. As observed for the mean estimates of the conductivity field, also the state solutions are similar to the reference ones when an accurate ROM is used.

8.5 Corrected RB-EnKF

In order to construct a corrected version of the RB-EnKF, we build a kriging-based ROMES for functional data on a set of $N_{cal} = 400$ parameters samples. The computational costs related to the solution of the kriging system of dimension 400×400 are still negligible with respect to the costs of solving the ROM on each window. For this reason, adding the ROMES to our RB-EnKF does not affect the overall computational performances.
The corrected RB-EnKF yields more accurate reconstructions of the field with respect to the uncorrected procedure. The errors in approximating the true field:

$$|\sigma_v(\mathbf{x}; \boldsymbol{\mu}^*) - \sigma_v(\mathbf{x}; \overline{\boldsymbol{\mu}}_n^{(N_\tau)})|$$

is reduced when a ROMES is integrated in the RB-EnKF (see Figure 8.16).

Moreover, the probability that an ischemic region is present in the left ventricle becomes $\mathbb{P}(\mu_6 < \eta) = 0.8920$ with ROM #2 and $\mathbb{P}(\mu_6 < \eta) = 0.8050$ with ROM #3. Thanks to the corrected RB-EnKF we avoid the misclassification: in both cases we would correctly identify that the tissue as being affected by the pathology.

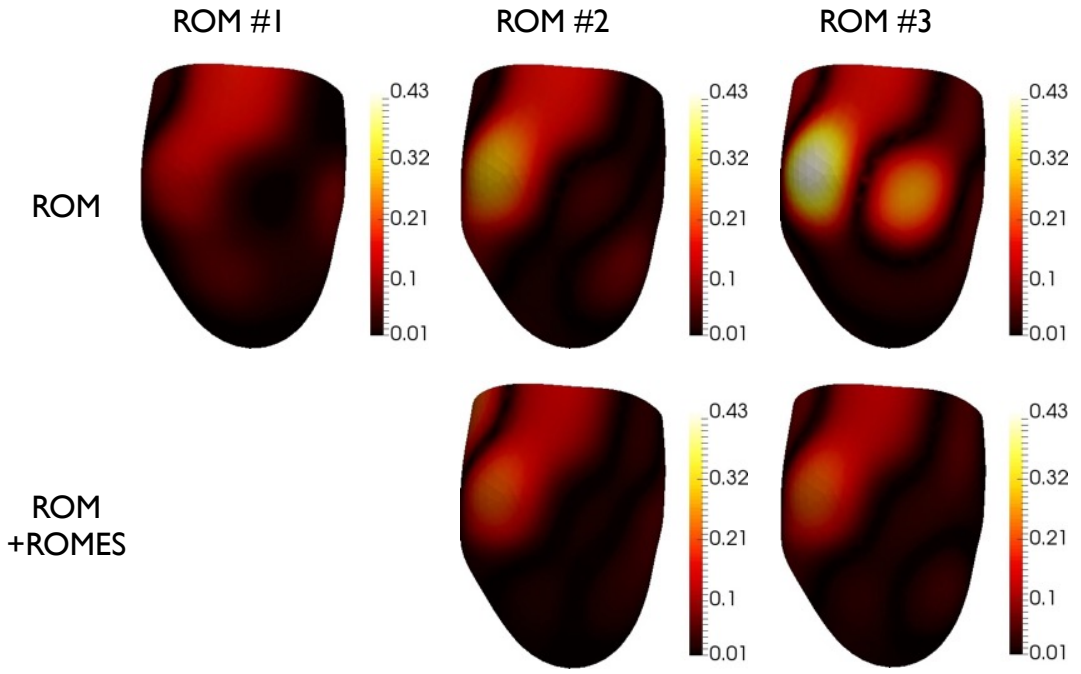

Figure 8.16 – Errors in approximating the true field $\sigma_v(\mathbf{x};\boldsymbol{\mu}^*)$ given by the RB-EnKF using ROM #1 (left), ROM #1 (center) and ROM #3 (right). The field estimation error is reduced in both cases and the results are comparable with the error given by the RB-EnKF equipped with ROM #1.

Finally, we consider also the state solution reconstructed by the corrected RB-EnKF (see Figure 8.17). The results in terms of state estimation are remarkable: even if the ROMs are not particularly accurate, the corrected Kalman updating formula minimizes the estimation error leading to results comparable with the one obtained using ROM #1.

The low computational costs of the corrected RB-EnKF, as well as the improved accuracy in the estimation, clearly motivate the introduction of a ROMES in the solution of these complex parameter estimation problems.

8.6 Prior comparison

We consider the field given by the vector of parameters $\boldsymbol{\mu}^*$ with $\mu^*_{13} = 0.3839$, $\mu^*_4 = 0.4953$, $\boldsymbol{\mu}^*_7 = 0.5348$, $\boldsymbol{\mu}^*_{5,6,14} \sim 0.63$ and random values $\mu^*_i > 0.77$, $i \neq 4,7,13$. By this choice, we localize the region with the major lack of conductivity in the lower part of the left ventricle.

We compare the results of the RB-EnKF based on ROM #1 on varying the different prior parameters ensembles introduced previously in Figure 8.9. Our goal is to study the influence of the prior distribution on the posterior obtained with the RB-EnKF. As a matter of fact, the prior distribution is a key element of the inversion procedure, providing a fast convergence of the filter when the prior pdf is close to the posterior.

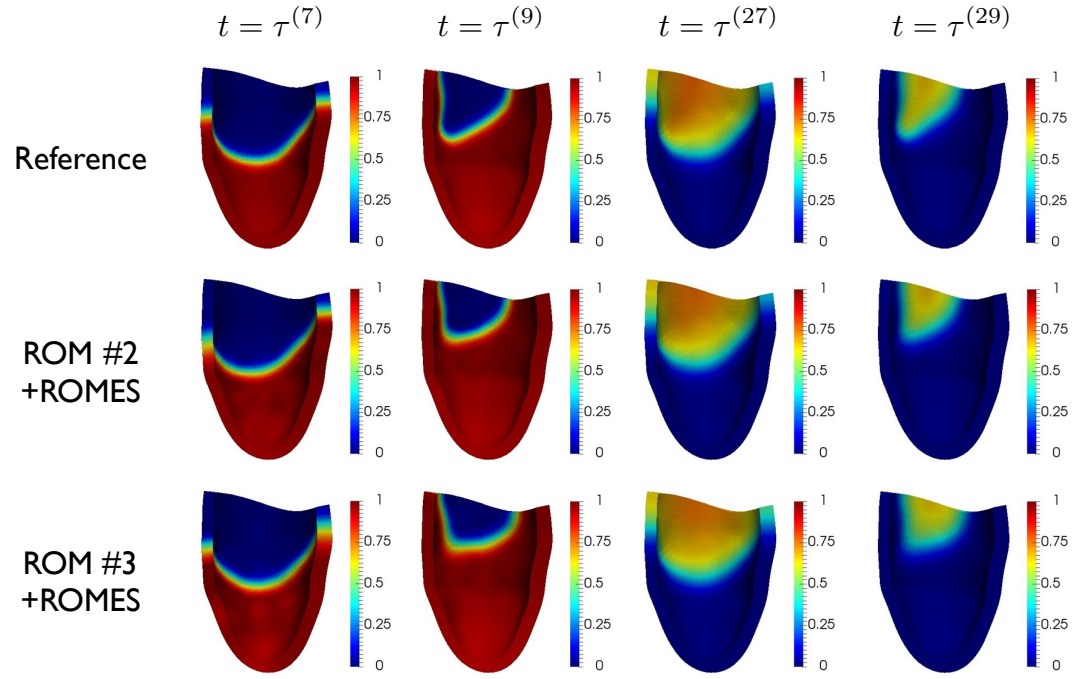

Figure 8.17 – Mean estimate of the state ensemble $\mathbf{u}_n^{(k)}$ for $k = 7, 9, 27, 29$. As observed for the mean estimate of the conductivity field, also the state solution is similar in all cases to the reference one when the ROM/ROMES strategy is used.

In this case, since the major lack of conductivity is localized on the apex, the prior given by assuming a LAD block is the closest to the true conductivity field. As a consequence, we have a fast convergence of the EnKF and the error $|\sigma_v(\mathbf{x};\boldsymbol{\mu}^*) - \sigma_v(\mathbf{x};\overline{\boldsymbol{\mu}}_n^{(N_\tau)})|$ is very small. Moreover, also the fields related to the 0.05 and 0.95 quantiles are very close to the reference one (see Figure 8.18).

Assuming instead a LCX block as prior distribution leads to less accurate results, since this starting information is far from the reference one: in fact, the estimated region with conductivity less than 0.5 is larger (over-estimated) with respect to the reference one. However, even in this worst case, the estimation error $|\sigma_v(\mathbf{x};\boldsymbol{\mu}^*) - \sigma_v(\mathbf{x};\overline{\boldsymbol{\mu}}_n^{(N_\tau)})|$ is small.

In conclusion, for all the four prior distributions the developed RB-EnKF provides estimates of the conductivity field close to the true field with low computational costs.

8.7 Conclusions

The numerical approach developed in this Thesis enables the efficient solution of a rather involved parameter estimation problem for the detection of myocardial ischemia. The state-based localized ROM developed in Chapter 2 yields efficient input/output query, whose accuracy is guaranteed by the ROMES developed in Chapter 3. The integration between this reduction framework and the EnKF has been successfully tested on the problem at hand.

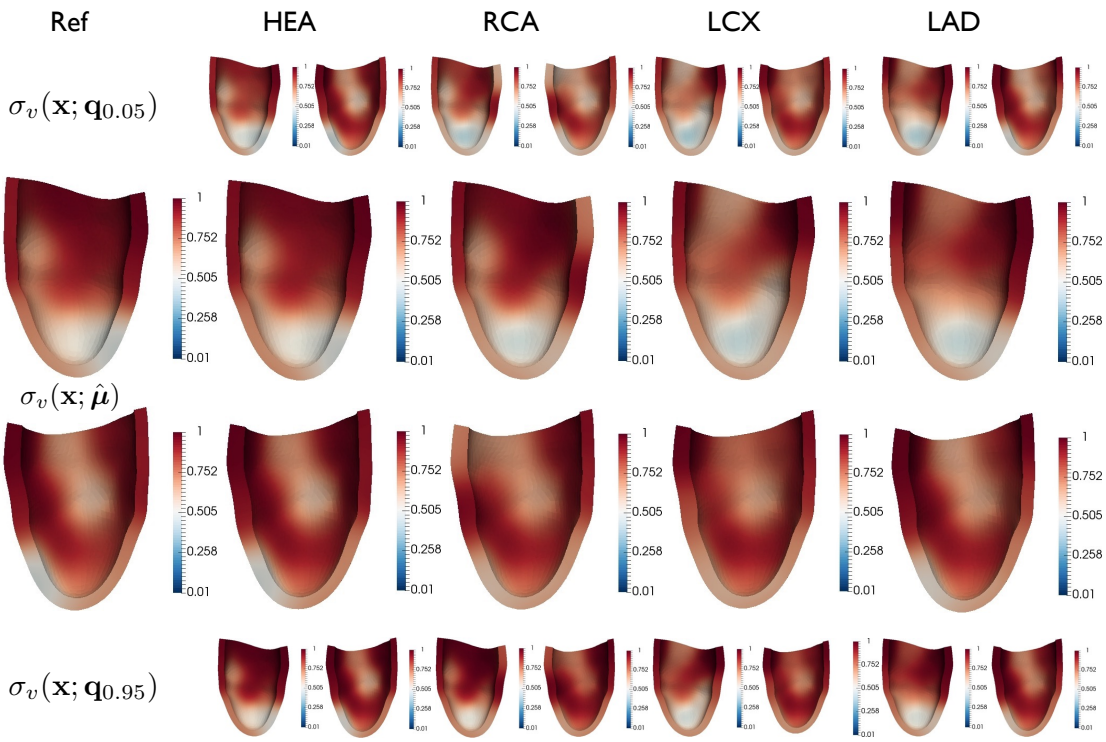

Figure 8.18 – Conductivity field $\sigma_v(\mathbf{x};\boldsymbol{\mu})$ for $\overline{\boldsymbol{\mu}}_n^{(N_\tau)}$ and the 0.05 and 0.95 quantiles obtained starting from different prior ensembles.

These results give preliminary evidence on the potential of the developed methodology to address realistic scenarios. Real local catheter recordings on the endocardium could be affected by several sources of error, such as the limited accuracy of the measurement or the non-perfect positioning of the electrode. The corrected RB-EnKF provides fast estimation of the electrical potential and of the unknown parameters characterizing the model even in a situation where the noise considerably contaminates the data.
At the moment, the simplifying assumptions made on the model and on the computational mesh limit the potential use in a clinical scenario. Future works will consider more realistic meshes and models, using also non-invasive measurements such as ECGs as data.

Conclusion

In this Thesis, we have faced some problems dealing with the integration of data within complex models arising in cardiac electrophysiology. Some methodologies based on reduced-order models (ROMs) have been developed to perform *model calibration and uncertainty quantification* and to solve *inverse and data assimilation problems* in this context. In particular, we have achieved the following results:

1. **Reduced-order models have been extended to cardiac electrophysiology problems using localization strategies**. In Chapter 2 we have developed different strategies to construct localized ROMs, which have been tested for the solution of the monodomain equation featuring the presence of an ischemic region on a two-dimensional domain. Moreover, by comparing the ROMs according to their efficiency, accuracy and low memory consumption, we have identified the state-based localized-ROM, relying on the *k-means* algorithm, as the best option for the case at hand.

   Starting from these promising results, we have applied the state-based localized-ROM methodology for the solution of the monodomain equation coupled with Aliev-Panfilov ionic model on a three-dimensional subject-specific left ventricle (see Chapters 7 and 8). We have shown that our approach enables to speed up the approximation of the solution even when the conductivity field is parametrized using up to twenty terms.

2. **ROM error surrogates have been exploited to estimate the approximation error on the outputs**. In Chapter 3, we have developed kriging-based ROM error surrogates (ROMES) for both real- and functional-valued outputs. Since it is not straightforward to derive efficient and effective error bounds for nonlinear time-dependent PDEs, we have developed unbiased statistical models based on kriging interpolation and Gaussian process regression, which present negligible computational costs with respect to the

ROM approximation. This latter feature is particularly relevant when time-dependent outputs are considered: in this case the approximation of the error on the entire time interval simply requires the solution of a linear system.

In particular, we have shown that reduced-order or surrogate models alone are not sufficient to provide an efficient and accurate approximation of the FOM. The best solution is instead given by a suitable combination of the two approaches, to which we have referred to as ROM/ROMES strategy.

Then, the ROMESs have been integrated within uncertainty quantification (UQ) and inversion procedures in order to minimize the propagation of the error between a FOM and a ROM. The ROMES effectivity for these problems has been confirmed in a broad range of numerical tests in Chapters from 4 to 8, giving a strong evidence of the theoretical results provided in this work.

3. **Uncertainty quantification has been integrated in the developed reduction framework**. The ROM-ROMES strategy has been exploited to speed up sensitivity analysis and uncertainty propagation based on sampling techniques. The insights on the role and the importance of the cardiac model parameters given by these procedures have allowed not only to improve the selection of the forward problem parametrization, but also to construct more efficiently a ROM with an informed exploration of the parameters space.

   Moreover, we have shown the relationship between non-influential parameters, detected by the sensitivity analysis, and their non-identifiability. For this reason, UQ is crucial also in the construction of an inverse problem: the provided information indicate which parameters have to be identified (and which ones have to be marginalized) and enable the construction of suitable priors distribution that regularize the inverse problem.

   The presented numerical test cases related to a simplified ECG signal and the action potential shape are encouraging towards the application of this whole framework for the personalization of cardiac models. The use of detailed full-order models has so far affected considerably the use of such UQ and estimation procedures in more complex and realistic scenarios, mainly due to the unfeasible computational time involved. The ROM/ROMES strategy is shown to be a potential solution to this issue, bringing these approaches to more realistic applications.

4. **Personalization of electrophysiology models and ischemic detection** Finally, these tools have been used for the efficient solution of Bayesian inverse problems, namely state/parameter estimation problems, starting from noisy observations of real-valued or time-dependent outputs. Both the Bayes and the Kalman update formulas have been properly modified with ROM and ROMES to provide efficient and accurate estimations of the quantities of interest. Some theoretical results on the consistency and the effectivity of the developed inversion procedures have been proven in an abstract setting and have also found a validation in the numerical tests of Chapters 5 and 6.

   The final numerical example, presented in Chapter 8, has shown the reliability of the corrected RB-EnFK for the solution of a complex parameter estimation problem, such as the detection of ischemic regions on the myocardium.

The reduction strategy introduced in this Thesis can be further developed to deal with more realistic applications aiming at a model personalization for patient-specific clinical treatments. Moreover, it can provide several perspectives about the development of new methodologies or the improvement of existing ones, such as:

1. testing different classification procedures and statistical learning techniques to enhance data-driven localized-ROMs;
2. constructing new reduction techniques for problems characterized by traveling fronts, problems whose solution features a strong variability (at the limit, different physical behaviors) in the parameter space, and coupled problems;
3. applying the ROM-ROMES strategy to different UQ methodologies, such as polynomial chaos expansion [Sud08] or stochastic Galerkin and stochastic collocation methods [BNT+11];
4. extending the reduction-framework to filtering procedures for the estimation of time-dependent parameters.

Bibliography

[AA99] J. L. Anderson and S. L. Anderson. A Monte Carlo implementation of the nonlinear filtering problem to produce ensemble assimilations and forecasts. *Monthly Weather Review*, 127(12):2741–2758, 1999.

[ÁAARÁ+12] D. Álvarez, F. Alonso-Atienza, J. L. Rojo-Álvarez, A. García-Alberola, and M. Moscoso. Shape reconstruction of cardiac ischemia from non-contact intracardiac recordings: A model study. *Mathematical and Computer Modelling*, 55(5):1770–1781, 2012.

[AAV+15] H. Ashikaga, H. Arevalo, F. Vadakkumpadan, R. C. Blake, R. D. Berger, H. Calkins, N. A. Trayanova, and H. R. Halperin. MRI-based patient-specific virtual electrophysiology laboratory for scar-related ventricular tachycardia. *Circulation*, 124(21), 2015.

[ABT13] R. C. Aster, B. Borchers, and C. H. Thurber, editors. *Parameter Estimation and Inverse Problems*. Academic Press, Boston, second edition, 2013.

[ACC+09] D. Amsallem, J. Cortial, K. Carlberg, and C. Farhat. A method for interpolating on manifolds structural dynamics reduced-order models. *International Journal for Numerical Methods in Engineering*, 80(9):1241–1258, 2009.

[ADFD+03] C. Andrieu, N. De Freitas, A. Doucet, and M. I. Jordan. An introduction to MCMC for machine learning. *Machine learning*, 50(1-2):5–43, 2003.

[AHC+15] L. Asner, M. Hadjicharalambous, R. Chabiniok, D. Peresutti, E. Sammut, J. Wong, G. Carr-White, P. Chowienczyk, J. Lee, A. King, et al. Estimation of passive and active properties in the human heart using 3D tagged MRI. *Biomechanics and Modeling in Mechanobiology*, 15(5):1121–1139, 2015.

[AHC+17] L. Asner, M. Hadjicharalambous, R. Chabiniok, D. Peressutti, E. Sammut, J. Wong, G. Carr-White, R. Razavi, A. King, N. Smith, et al. Patient-specific modeling for left ventricular mechanics using data-driven boundary energies. *Computer Methods in Applied Mechanics and Engineering*, 314:269–295, 2017.

[And07] J. L. Anderson. An adaptive covariance inflation error correction algorithm for ensemble filters. *Tellus A*, 59(2):210–224, 2007.

[AP96] R. R. Aliev and A. V. Panfilov. A simple two-variable model of cardiac excitation. *Chaos, Solitons & Fractals*, 7(3):293–301, 1996.

[ASG01] A. C. Antoulas, D. C. Sorensen, and S. Gugercin. A survey of model reduction methods for large-scale systems. *Contemporary Mathematics*, 280:193–220, 2001.

[AZF12] D. Amsallem, M. J. Zahr, and C. Farhat. Nonlinear model order reduction based on local reduced-order bases. *International Journal for Numerical Methods in Engineering*, 92(10):891–916, 2012.

[BBOVA+13] O. J. Britton, A. Bueno-Orovio, K. Van Ammel, H. R. Lu, R. Towart, D. J. Gallacher, and B. Rodriguez. Experimentally calibrated population of models predicts and explains intersubject variability in cardiac cellular electrophysiology. *Proceedings of the National Academy of Sciences*, 110(23):2098–2105, 2013.

[BCF+10] M. Boulakia, S. Cazeau, M. A. Fernández, J.-F. Gerbeau, and N. Zemzemi. Mathematical modeling of electrocardiograms: a numerical study. *Annals of Biomedical Engineering*, 38(3):1071–1097, 2010.

[BCP09] Y. Bourgault, Y. Coudiere, and C. Pierre. Existence and uniqueness of the solution for the bidomain model used in cardiac electrophysiology. *Nonlinear Analysis: Real World Applications*, 10(1):458–482, 2009.

[BFG+08] M. Boulakia, M. A. Fernández, J.-F. Gerbeau, and N. Zemzemi. A coupled system of PDEs and ODEs arising in electrocardiograms modeling. *Applied Mathematics Research eXpress*, 2008.

[BFI+16] F. Ballarin, E. Faggiano, S. Ippolito, A. Manzoni, A. Quarteroni, G. Rozza, and R. Scrofani. Fast simulations of patient-specific haemodynamics of coronary artery bypass grafts based on a POD–Galerkin method and a vascular shape parametrization. *Journal of Computational Physics*, 315:609–628, 2016.

[BG04] H.-J. Bungartz and M. Griebel. Sparse grids. *Acta Numerica*, 13:147–269, 2004.

[BGW15a] P. Benner, S. Gugercin, and K. Willcox. A survey of projection-based model reduction methods for parametric dynamical systems. *SIAM Review*, 57(4):483–531, 2015.

[BGW15b] J. Biehler, M. Gee, and W. Wall. Towards efficient uncertainty quantification in complex and large scale biomechanical problems based on a Bayesian multi fidelity scheme. *Biomechanics and Modeling in Mechanobiology*, 14(3):489–51, 2015.

[BLL+13] C. Brett, K. F. Lam, K. Law, D. McCormick, M. Scott, and A. Stuart. Accuracy and stability of filters for dissipative PDEs. *Physica D: Nonlinear Phenomena*, 245(1):34–45, 2013.

[BMG12] C. Bertoglio, P. Moireau, and J.-F. Gerbeau. Sequential parameter estimation for fluid–structure problems: Application to hemodynamics. *International Journal for Numerical Methods in Biomedical Engineering*, 28(4):434–455, 2012.

[BMN+04] M. Barrault, Y. Maday, N. C. Nguyen, and A. T. Patera. An empirical interpolation method: application to efficient reduced-basis discretization of partial differential equations. *Comptes Rendus Mathematique*, 339(9):667–672, 2004.

[BMP+12] A. Buffa, Y. Maday, A. T. Patera, C. Prud'homme, and G. Turinici. A priori convergence of the greedy algorithm for the parametrized reduced basis method. *ESAIM: Mathematical Modelling and Numerical Analysis*, 46(3):595–603, 2012.

[BMQ16] D. Bonomi, A. Manzoni, and A. Quarteroni. A matrix discrete empirical interpolation method for the efficient model reduction of parametrized nonlinear PDEs: application to nonlinear elasticity problems. *MOX-Report No. 14/2016*, 2016.

[BNT07] I. Babuška, F. Nobile, and R. Tempone. A stochastic collocation method for elliptic partial differential equations with random input data. *SIAM Journal on Numerical Analysis*, 45(3):1005–1034, 2007.

[BNT+11] J. Bäck, F. Nobile, L. Tamellini, and R. Tempone. Stochastic spectral Galerkin and collocation methods for PDEs with random coefficients: a numerical comparison. In J. Hesthaven and R. Einar, editors, *Spectral and High Order Methods for Partial Differential Equations*, pages 43–62. Springer, 2011.

[BPL14] A. Birolleau, G. Poëtte, and D. Lucor. Adaptive Bayesian inference for discontinuous inverse problems, application to hyperbolic conservation laws. *Communications in Computational Physics*, 16:1–34, 2014.

[BS16] M. J. Budoff and J. S. Shinbane. *Cardiac CT imaging: diagnosis of cardiovascular disease*. Springer, 2016.

[BSG12] M. Boulakia, E. Schenone, and J.-F. Gerbeau. Reduced-order modeling for cardiac electrophysiology. application to parameter identification. *International Journal for Numerical Methods in Biomedical Engineering*, 28(6-7):727–744, 2012.

[BTDW04] T. Bui-Thanh, M. Damodaran, and K. E. Willcox. Aerodynamic data reconstruction and inverse design using proper orthogonal decomposition. *AIAA journal*, 42(8):1505–1516, 2004.

[BTWG08] T. Bui-Thanh, K. Willcox, and O. Ghattas. Parametric reduced-order models for probabilistic analysis of unsteady aerodynamic applications. *AIAA journal*, 46(10):2520–2529, 2008.

[Buc88] C. G. Bucher. Adaptive sampling–an iterative fast Monte Carlo procedure. *Structural Safety*, 5(2):119–126, 1988.

[Buh00] M. D. Buhmann. Radial basis functions. *Acta Numerica 2000*, 9:1–38, 2000.

[CAAZ+15] C. E. Chavez, F. Alonso-Atienza, N. Zemzemi, Y. Coudiere, and D. Alvarez. Inverse localization of ischemia in a 3D realistic geometry: A level set approach. In *Computing in cardiology*, 2015.

[CBB+01] C. P. Cannon, A. Battler, R. G. Brindis, J. L. Cox, S. G. Ellis, N. R. Every, J. T. Flaherty, R. A. Harrington, H. M. Krumholz, M. L. Simoons, F. J. V. D. Werf, W. S. Weintraub, K. R. Mitchell, S. L. Morrisson, R. G. Brindis, H. Anderson, D. S. Cannom, W. C. Jr, J. E. Cigarroa, R. L. Collins-Nakai, S. G. Ellis, R. J. Gibbons, F. L. Grover, P. A. Heidenreich, B. K. Khandheria, S. B. Knoebel, H. L. Krumholz, D. J. Malenka, D. B. Mark, C. R. Mckay, E. R. Passamani, M. J. Radford, R. N. Riner, J. B. Schwartz, R. E. Shaw, R. J. Shemin, D. B. V. Fossen, E. D. Verrier, M. W. Watkins, D. R. Phoubandith, and T. Furnelli. American college of cardiology key data elements and definitions for measuring the clinical management and outcomes of patients with acute coronary syndromes. *Journal of the American College of Cardiology*, 38(7):2114 – 2130, 2001.

[CBC+11] R. Clayton, O. Bernus, E. Cherry, H. Dierckx, F. Fenton, L. Mirabella, A. Panfilov, F. B. Sachse, G. Seemann, and H. Zhang. Models of cardiac tissue electrophysiology: progress, challenges and open questions. *Progress in Biophysics and Molecular Biology*, 104(1):22–48, 2011.

[CD09] J.-P. Chiles and P. Delfiner. *Geostatistics: modeling spatial uncertainty*, volume 497 of *Wiley Series in Probability and Statistics*. John Wiley & Sons, 2009.

[CDQ14] C. M. Colciago, S. Deparis, and A. Quarteroni. Comparisons between reduced order models and full 3D models for fluid–structure interaction problems in haemodynamics. *Journal of Computational and Applied Mathematics*, 265:120–138, 2014.

[CFC+13] K. Carlberg, C. Farhat, J. Cortial, and D. Amsallem. The GNAT method for nonlinear model reduction: effective implementation and application to computational fluid dynamics and turbulent flows. *Journal of Computational Physics*, 242:623–647, 2013.

[CFP04] P. Colli Franzone and L. F. Pavarino. A parallel solver for reaction–diffusion systems in computational electrocardiology. *Mathematical Models and Methods in Applied Sciences*, 14(06):883–911, 2004.

[CFPS14] P. Colli Franzone, L. F. Pavarino, and S. Scacchi. *Mathematical cardiac electrophysiology*, volume 13 of *MS&A*. Springer, 2014.

[CFPT05] P. Colli Franzone, L. Pavarino, and B. Taccardi. Simulating patterns of excitation, repolarization and action potential duration with cardiac bidomain and monodomain models. *Mathematical Biosciences*, 197(1):35–66, 2005.

[CFS02] P. Colli Franzone and G. Savaré. Degenerate evolution systems modeling the cardiac electric field at micro- and macroscopic level. In *Evolution equations, semigroups and functional analysis*, pages 49–78. Springer, 2002.

[CGM+13] D. Chapelle, A. Gariah, P. Moireau, and J. Sainte-Marie. A Galerkin strategy with Proper Orthogonal Decomposition for parameter-dependent problems–analysis, assessments and applications to parameter estimation. *ESAIM: Mathematical Modelling and Numerical Analysis*, 47(06):1821–1843, 2013.

[CGM15] C. Corrado, J.-F. Gerbeau, and P. Moireau. Identification of weakly coupled multiphysics problems. application to the inverse problem of electrocardiography. *Journal of Computational Physics*, 283:271–298, 2015.

[CH09] S. Chatterjee and A. S. Hadi. *Sensitivity analysis in linear regression*, volume 327. John Wiley & Sons, 2009.

[Cha00] A. Chatterjee. An introduction to the proper orthogonal decomposition. *Current Science*, 78(7):808–817, 2000.

[CLM+16] C. Corrado, J. Lassoued, M. Mahjoub, and N. Zemzemi. Stability analysis of the POD reduced order method for solving the bidomain model in cardiac electrophysiology. *Mathematical biosciences*, 272:81–91, 2016.

[CLMM09] T. Crestaux, O. Le Maitre, and J.-M. Martinez. Polynomial chaos expansion for sensitivity analysis. *Reliability Engineering & System Safety*, 94(7):1161–1172, 2009.

[CML+12] R. Chabiniok, P. Moireau, P.-F. Lesault, A. Rahmouni, J.-F. Deux, and D. Chapelle. Estimation of tissue contractility from cardiac cine-MRI using a biomechanical heart model. *Biomechanics and modeling in mechanobiology*, 11(5):609–630, 2012.

[CMW15] T. Cui, Y. M. Marzouk, and K. E. Willcox. Data-driven model reduction for the Bayesian solution of inverse problems. *International Journal for Numerical Methods in Engineering*, 102(5):966–990, 2015.

[Cre15] N. Cressie. *Statistics for spatial data*. John Wiley & Sons, 2015.

[CS10] S. Chaturantabut and D. C. Sorensen. Nonlinear model reduction via discrete empirical interpolation. *SIAM J. Sci. Comp.*, 32(5):2737–2764, 2010.

[CSB01] A. Cimponeriu, C. F. Starmer, and A. Bezerianos. A theoretical analysis of acute ischemia and infarction using ECG reconstruction on a 2-D model of myocardium. *IEEE Transactions on Biomedical Engineering*, 48(1):41–54, 2001.

[CSL+11] O. Camara, M. Sermesant, P. Lamata, L. Wang, M. Pop, J. Relan, M. D. Craene, H. Delingette, H. Liu, S. Niederer, A. Pashaei, G. Plank, D. Romero, R. Sebastian, K. Wong, H. Zhang, N. Ayache, A. Frangi, P. Shi, N. Smith, and G. Wright. Inter-model consistency and complementarity: Learning from ex-vivo imaging and electrophysiological data towards an integrated understanding of cardiac physiology. *Progress in Biophysics and Molecular Biology*, 107(1):122 – 133, 2011.

[CWH+16] R. Chabiniok, V. Wang, M. Hadjicharalambous, L. Asner, J. Lee, M. Sermesant, E. Kuhl, A. Young, P. Moireau, M. Nash, et al. Multiphysics & multiscale modeling, data-model fusion and integration of organ physiology in the clinic: Ventricular cardiac mechanics. *Interface Focus*, 6(2):1–24, 2016.

[DBW+12] H. Delingette, F. Billet, K. C. Wong, M. Sermesant, K. Rhode, M. Ginks, C. A. Rinaldi, R. Razavi, and N. Ayache. Personalization of cardiac motion and contractility from images using variational data assimilation. *IEEE Transactions on Biomedical Engineering*, 59(1):20–24, 2012.

[DC15] M. Drohmann and K. Carlberg. The ROMES method for statistical modeling of reduced-order-model error. *SIAM/ASA Journal on Uncertainty Quantification*, 3(1):116–145, 2015.

[DH16] M. Dihlmann and B. Haasdonk. A reduced basis Kalman filter for parametrized partial differential equations. *ESAIM: Control, Optimisation and Calculus of Variations*, 22(3):625–669, 2016.

[DKD09] A. Der Kiureghian and O. Ditlevsen. Aleatory or epistemic? Does it matter? *Structural Safety*, 31(2):105–112, 2009.

[DL04] S. Dokos and N. H. Lovell. Parameter estimation in cardiac ionic models. *Progress in biophysics and molecular biology*, 85(2):407–431, 2004.

[DMP+12] M. D'Elia, L. Mirabella, T. Passerini, M. Perego, M. Piccinelli, C. Vergara, and A. Veneziani. Applications of variational data assimilation in computational hemodynamics. In D. Ambrosi, A. Quarteroni, and G. Rozza, editors, *Modeling of Physiological Flows*, pages 363–394. Springer, 2012.

[DUS+11] D. Dee, S. Uppala, A. Simmons, P. Berrisford, P. Poli, S. Kobayashi, U. Andrae, M. Balmaseda, G. Balsamo, P. Bauer, et al. The era-interim reanalysis: Configuration and performance of the data assimilation system. *Quarterly Journal of the royal meteorological society*, 137(656):553–597, 2011.

[EB08] M. Ethier and Y. Bourgault. Semi-implicit time-discretization schemes for the bidomain model. *SIAM Journal on Numerical Analysis*, 46(5):2443–2468, 2008.

[EHD+14] C. Eitel, G. Hindricks, N. Dagres, P. Sommer, and C. Piorkowski. Ensite velocity™ cardiac mapping system: a new platform for 3d mapping of cardiac arrhythmias. *Expert review of medical devices*, 2014.

[EPS+08] O. Ecabert, J. Peters, H. Schramm, C. Lorenz, J. von Berg, M. J. Walker, M. Vembar, M. E. Olszewski, K. Subramanyan, G. Lavi, and J. Weese. Automatic model-based segmentation of the heart in CT images. *IEEE Transactions on Medical Imaging*, 27(9):1189–1201, Sept 2008.

[ESS14] O. G. Ernst, B. Sprungk, and H.-J. Starkloff. Bayesian inverse problems and Kalman filters. In S. Dahlke, W. Dahmen, M. Griebel, W. Hackbusch, K. Ritter, R. Schneider, C. Schwab, and H. Yserentant, editors, *Extraction of Quantifiable Information from Complex Systems*, pages 133–159. Springer International Publishing, 2014.

[Eve97] G. Evensen. Advanced data assimilation for strongly nonlinear dynamics. *Monthly Weather Review*, 125(6):1342–1354, 1997.

[Eve03] G. Evensen. The ensemble Kalman filter: Theoretical formulation and practical implementation. *Ocean dynamics*, 53(4):343–367, 2003.

[Eve09] G. Evensen. *Data assimilation: the ensemble Kalman filter*. Springer Science & Business Media, 2009.

[FHT01] J. Friedman, T. Hastie, and R. Tibshirani. *The elements of statistical learning*, volume 1. Springer series in statistics Springer, Berlin, 2001.

[Fit61] R. FitzHugh. Impulses and physiological states in theoretical models of nerve membrane. *Biophysical journal*, 1(6):445–466, 1961.

[FMW+10] M. Frangos, Y. Marzouk, K. Willcox, and B. van Bloemen Waanders. Surrogate and reduced-order modeling: A comparison of approaches for large-scale statistical inverse problems. In L. Biegler, G. Biros, O. Ghattas, M. Heinkenschloss, D. Keyes, B. Mallick, Y. Marzouk, B. van Bloemen Waanders, and K. Willcox, editors, *Large-Scale Inverse Problems and Quantification of Uncertainty*, chapter 7, pages 123–150. John Wiley & Sons, Ltd, 2010.

[FN09] M. Fink and D. Noble. Markov models for ion channels: versatility versus identifiability and speed. *Philosophical Transactions of the Royal Society of London A: Mathematical, Physical and Engineering Sciences*, 367(1896):2161–2179, 2009.

[FNC+11] M. Fink, S. A. Niederer, E. M. Cherry, F. H. Fenton, J. T. Koivumäki, G. Seemann, R. Thul, H. Zhang, F. B. Sachse, D. Beard, et al. Cardiac cell modelling: observations from the heart of the cardiac physiome project. *Progress in biophysics and molecular biology*, 104(1):2–21, 2011.

[FQV10] L. Formaggia, A. Quarteroni, and A. Veneziani. *Cardiovascular Mathematics: Modeling and simulation of the circulatory system*, volume 1 of *MS&A*. Springer-Verlag, 2010.

[FSSQ+15] A. Ferrer, R. Sebastián, D. Sánchez-Quintana, J. F. Rodríguez, E. J. Godoy, L. Martínez, and J. Saiz. Detailed anatomical and electrophysiological models of human atria and torso for the simulation of atrial activation. *PloS one*, 10(11):1–29, 2015.

[FZ10] M. A. Fernández and N. Zemzemi. Decoupled time-marching schemes in computational cardiac electrophysiology and ECG numerical simulation. *Mathematical Biosciences*, 226(1):58–75, 2010.

[GDM11] R. Giraldo, P. Delicado, and J. Mateu. Ordinary kriging for function-valued spatial data. *Environmental and Ecological Statistics*, 18(3):411–426, 2011.

[GFW+10] D. Galbally, K. Fidkowski, K. Willcox, and O. Ghattas. Non-linear model reduction for uncertainty quantification in large-scale inverse problems. *International Journal for Numerical Methods in Engineering*, 81(12):1581–1608, 2010.

[GG84] S. Geman and D. Geman. Stochastic relaxation, Gibbs distributions, and the Bayesian restoration of images. *IEEE Transactions on pattern analysis and machine intelligence*, (6):721–741, 1984.

[Gil05] W. R. Gilks. *Markov chain Monte Carlo*. Wiley Online Library, 2005.

[Gil08] M. B. Giles. Multilevel Monte Carlo path simulation. *Operations Research*, 56(3):607–617, 2008.

[GK09] S. Goktepe and E. Kuhl. Computational modeling of cardiac electrophysiology: a novel finite element approach. *International Journal for Numerical Methods in Engineering*, 79(2):156–178, 2009.

[GKM08] S. E. Geneser, R. M. Kirby, and R. S. MacLeod. Application of stochastic finite element methods to study the sensitivity of ECG forward modeling to organ conductivity. *IEEE Transactions on Biomedical Engineering*, 55(1):31–40, 2008.

[GKX+07] S. E. Geneser, R. M. Kirby, D. Xiu, and F. B. Sachse. Stochastic markovian modeling of electrophysiology of ion channels: Reconstruction of standard deviations in macroscopic currents. *Journal of Theoretical Biology*, 245(4):627 – 637, 2007.

[GL14] J.-F. Gerbeau and D. Lombardi. Approximated Lax pairs for the reduced order integration of nonlinear evolution equations. *Journal of Computational Physics*, 265:246–269, 2014.

[GLS15] J.-F. Gerbeau, D. Lombardi, and E. Schenone. Reduced order model in cardiac electrophysiology with approximated Lax pairs. *Advances in Computational Mathematics*, 41(5):1103–1130, 2015.

[GMN+07] M. A. Grepl, Y. Maday, N. C. Nguyen, and A. T. Patera. Efficient reduced-basis treatment of nonaffine and nonlinear partial differential equations. *ESAIM: Mathematical Modelling and Numerical Analysis*, 41(3):575–605, 2007.

[GP05] M. A. Grepl and A. T. Patera. A posteriori error bounds for reduced-basis approximations of parametrized parabolic partial differential equations. *ESAIM: Mathematical Modelling and Numerical Analysis*, 39(1):157–181, 2005.

[GR02] K. Gima and Y. Rudy. Ionic current basis of electrocardiographic waveforms a model study. *Circulation Research*, 90(8):889–896, 2002.

[GRFW+16] S. Giffard-Roisin, L. Fovargue, J. Webb, R. Molléro, J. Lee, H. Delingette, N. Ayache, R. Razavi, and M. Sermesant. Estimation of purkinje activation from ECG: an intermittent left bundle branch block study. In *Proceedings of the 7th international STACOM workshop (Athens, 17 October 2016)*, 2016.

[GRJF+16] S. Giffard-Roisin, T. Jackson, L. Fovargue, J. Lee, H. Delingette, R. Razavi, N. Ayache, and M. Sermesant. Non-invasive personalisation of a cardiac electrophysiology model from body surface potential mapping. *IEEE Transactions on Biomedical Engineering*, PP(99), 2016.

[GS03] R. G. Ghanem and P. D. Spanos. *Stochastic finite elements: a spectral approach*. Springer New York, 2003.

[GVL12] G. H. Golub and C. F. Van Loan. Matrix computations, 2012.

[Ham06] T. M. Hamill. *Ensemble-based atmospheric data assimilation*, volume Predictability of Weather and Climate, chapter 6, pages 124–156. Cambridge Press, 2006.

[Han10] P. C. Hansen. *Discrete inverse problems: insight and algorithms*, volume 7. Siam, 2010.

[Has70] W. K. Hastings. Monte Carlo sampling methods using Markov chains and their applications. *Biometrika*, 57(1):97–109, 1970.

[Hay04] S. Haykin. *Neural Network - A comprehensive foundation*, volume 2. Prentice Hall, 2004.

[HAZD+12] S. Halliburton, A. Arbab-Zadeh, D. Dey, A. J. Einstein, R. Gentry, R. T. George, T. Gerber, M. Mahesh, and W. G. Weigold. State-of-the-art in CT hardware and scan modes for cardiovascular CT. *Journal of Cardiovascular Computed Tomography*, 6(3):154 – 163, 2012.

[HCA+15] M. Hadjicharalambous, R. Chabiniok, L. Asner, E. Sammut, J. Wong, G. Carr-White, J. Lee, R. Razavi, N. Smith, and D. Nordsletten. Analysis of passive cardiac constitutive laws for parameter estimation using 3D tagged MRI. *Biomechanics and modeling in mechanobiology*, 14(4):807–828, 2015.

[HDO11] B. Haasdonk, M. Dihlmann, and M. Ohlberger. A training set and multiple bases generation approach for parameterized model reduction based on adaptive grids in parameter space. *Mathematical and Computer Modelling of Dynamical Systems*, 17(4):423–442, 2011.

[Hen92] C. S. Henriquez. Simulating the electrical behavior of cardiac tissue using the bidomain model. *Critical Reviews in Biomedical Engineering*, 21(1):1–77, 1992.

[HH52] A. L. Hodgkin and A. F. Huxley. A quantitative description of membrane current and its application to conduction and excitation in nerve. *The Journal of Physiology*, 117(4):500–544, 1952.

[HK07] J. Huttunen and J. Kaipio. Approximation error analysis in nonlinear state estimation with an application to state-space identification. *Inverse Problems*, 23(5):2141—2157, 2007.

[HK09] J. M. Huttunen and J. P. Kaipio. Model reduction in state identification problems with an application to determination of thermal parameters. *Applied Numerical Mathematics*, 59(5):877–890, 2009.

[HM01] P. L. Houtekamer and H. L. Mitchell. A sequential ensemble Kalman filter for atmospheric data assimilation. *Monthly Weather Review*, 129(1):123–137, 2001.

[HMD09] P. Houtekamer, H. L. Mitchell, and X. Deng. Model error representation in an operational ensemble Kalman filter. *Monthly Weather Review*, 137(7):2126–2143, 2009.

[HPK+06] R. C. Hendel, M. R. Patel, C. M. Kramer, M. Poon, J. C. Carr, N. A. Gerstad, L. D. Gillam, J. M. Hodgson, R. J. Kim, J. R. Lesser, et al. ACCF/ACR/SCC/SCMR/ASNC/NASCI/SCAI/SIR 2006 Appropriateness criteria for cardiac computed tomography and cardiac magnetic resonance imaging: A report of the american college of cardiology foundation quality strategic directions committee appropriateness criteria working group, american college of radiology, society of cardiovascular computed tomography, society for cardiovascular magnetic resonance, american society of nuclear cardiology, north american society for cardiac imaging, society for cardiovascular angiography and interventions, and society of interventional radiology. *Journal of the American College of Cardiology*, 48(7):1475–1497, 2006.

[HRS16] J. S. Hesthaven, G. Rozza, and B. Stamm. *Certified reduced basis methods for parametrized partial differential equations*. SpringerBriefs in Mathematics. Springer International Publishing, 2016.

[HRW12] J. Humpherys, P. Redd, and J. West. A fresh look at the Kalman filter. *SIAM review*, 54(4):801–823, 2012.

[HS96] T. Homma and A. Saltelli. Importance measures in global sensitivity analysis of nonlinear models. *Reliability Engineering & System Safety*, 52(1):1–17, 1996.

[HSF+98] P. R. Houser, W. J. Shuttleworth, J. S. Famiglietti, H. V. Gupta, K. H. Syed, and D. C. Goodrich. Integration of soil moisture remote sensing and hydrologic modeling using data assimilation. *Water Resources Research*, 34(12):3405–3420, 1998.

[HW79] J. A. Hartigan and M. A. Wong. Algorithm as 136: A k-means clustering algorithm. *Journal of the Royal Statistical Society. Series C (Applied Statistics)*, 28(1):100–108, 1979.

[HZ16] P. Houtekamer and F. Zhang. Review of the ensemble Kalman filter for atmospheric data assimilation. *Monthly Weather Review*, 144(12):4489–4532, 2016.

[IH88] R. L. Iman and J. C. Helton. An investigation of uncertainty and sensitivity analysis techniques for computer models. *Risk Analysis*, 8(1):71–90, 1988.

[IK05] D. C. Isbell and C. M. Kramer. Cardiovascular magnetic resonance: Structure, function, perfusion, and viability. *Journal of Nuclear Cardiology*, 12(3):324–336, 2005.

[ILS13] M. A. Iglesias, K. J. Law, and A. M. Stuart. Ensemble Kalman methods for inverse problems. *Inverse Problems*, 29(4):045001, 2013.

[Jac00] S. Jackman. Estimation and inference via Bayesian simulation: An introduction to Markov chain Monte Carlo. *American Journal of Political Science*, pages 375–404, 2000.

[Jac16] V. Jacquemet. Lessons from computer simulations of ablation of atrial fibrillation. *The Journal of Physiology*, 594(9):17–30, 2016.

[JCB+16] R. H. Johnstone, E. T. Chang, R. Bardenet, T. P. de Boer, D. J. Gavaghan, P. Pathmanathan, R. H. Clayton, and G. R. Mirams. Uncertainty and variability in models of the cardiac action potential: Can we build trustworthy models? *Journal of Molecular and Cellular Cardiology*, 96:49 – 62, 2016. Special Issue: Computational Modelling of the Heart.

[Joh67] S. C. Johnson. Hierarchical clustering schemes. *Psychometrika*, 32(3):241–254, 1967.

[Kal60] R. E. Kalman. A new approach to linear filtering and prediction problems. *Journal of Fluids Engineering*, 82(1):35–45, 1960.

[Kal03] E. Kalnay. *Atmospheric modeling, data assimilation and predictability*. Cambridge university press, 2003.

[Kat10] A. M. Katz. *Physiology of the Heart*. Lippincott Williams & Wilkins, 2010.

[KC96] A. I. Khuri and J. A. Cornell. *Response surfaces: designs and analyses*, volume 152. CRC press, 1996.

[KGB+07] P. Kligfield, L. S. Gettes, J. J. Bailey, R. Childers, B. J. Deal, E. W. Hancock, G. van Herpen, J. A. Kors, P. Macfarlane, D. M. Mirvis, et al. Recommendations for the standardization and interpretation of the electrocardiogram: part i: the electrocardiogram and its technology a scientific statement from the american heart association electrocardiography and arrhythmias committee, council on clinical cardiology; the american college of cardiology foundation; and the heart rhythm society endorsed by the international society for computerized electrocardiology. *Journal of the American College of Cardiology*, 49(10):1109–1127, 2007.

[KLS14] D. Kelly, K. Law, and A. Stuart. Well-posedness and accuracy of the ensemble Kalman filter in discrete and continuous time. *Nonlinearity*, 27(10):2579, 2014.

[KM13] K. Kunisch and A. Marica. Well-posedness for the Mitchell-Schaeffer model of the cardiac membrane. *SFB-Report No*, 18:2013, 2013.

[KMSC16] T. Krogh-Madsen, E. A. Sobie, and D. J. Christini. Improving cardiomyocyte model fidelity and utility via dynamic electrophysiology protocols and optimization algorithms. *The Journal of Physiology*, 594(9):2525–2536, 2016.

[KO01] M. C. Kennedy and A. O'Hagan. Bayesian calibration of computer models. *Journal of the Royal Statistical Society: Series B (Statistical Methodology)*, 63(3):425–464, 2001.

[KRC+11] E. Konukoglu, J. Relan, U. Cilingir, B. H. Menze, P. Chinchapatnam, A. Jadidi, H. Cochet, M. Hocini, H. Delingette, P. Jaïs, et al. Efficient probabilistic model personalization integrating uncertainty on data and parameters: Application to eikonal-diffusion models in cardiac electrophysiology. *Progress in biophysics and molecular biology*, 107(1):134–146, 2011.

[KS06] J. Kaipio and E. Somersalo. *Statistical and computational inverse problems*, volume 160. Springer Science & Business Media, 2006.

[KSR+13] M. W. Krueger, G. Seemann, K. Rhode, D. U. J. Keller, C. Schilling, A. Arujuna, J. Gill, M. D. O'Neill, R. Razavi, and O. Dossel. Personalization of atrial anatomy and electrophysiology as a basis for clinical modeling of radio-frequency ablation of atrial fibrillation. *IEEE Transactions on Medical Imaging*, 32(1):73–84, 2013.

[KV01] K. Kunisch and S. Volkwein. Galerkin proper orthogonal decomposition methods for parabolic problems. *Numerische Mathematik*, 90(1):117–148, 2001.

[KvBW+04] M. R. Kaus, J. von Berg, J. Weese, W. Niessen, and V. Pekar. Automated segmentation of the left ventricle in cardiac MRI. *Medical Image Analysis*, 8(3):245–254, 2004.

[LDT86] F. X. Le Dimet and O. Talagrand. Variational algorithms for analysis and assimilation of meteorological observations: theoretical aspects. *Tellus*, 38(2):97–110, 1986.

[LGA93] D.-W. Liu, G. A. Gintant, and C. Antzelevitch. Ionic bases for electrophysiological distinctions among epicardial, midmyocardial, and endocardial myocytes from the free wall of the canine left ventricle. *Circulation Research*, 72(3):671–687, 1993.

[LGT03] T. G. Lines, P. Grottum, and A. Tveito. Modeling the electrical activity of the heart: A bidomain model of the ventricles embedded in a torso. *Computing and Visualization in Science*, 5(4):195–213, 2003.

[Lil12] L. S. Lilly. *Pathophysiology of heart disease: a collaborative project of medical students and faculty*. Lippincott Williams & Wilkins, 2012.

[Llo82] S. Lloyd. Least squares quantization in PCM. *IEEE Transactions on Information Theory*, 28(2):129–137, 1982.

[LM14a] J. Li and Y. M. Marzouk. Adaptive construction of surrogates for the Bayesian solution of inverse problems. *SIAM Journal on Scientific Computing*, 36(3):1163–1186, 2014.

[LM14b] B. Lin and D. McLaughlin. Efficient characterization of uncertain model parameters with a reduced-order ensemble Kalman filter. *SIAM Journal on Scientific Computing*, 36(2):198–224, 2014.

[LMN16] R. Lal, B. Mohammadi, and F. Nicoud. Data assimilation for identification of cardiovascular network characteristics. *International Journal for Numerical Methods in Biomedical Engineering*, ahead of print, 2016.

[LMQ+13a] T. Lassila, A. Manzoni, A. Quarteroni, and G. Rozza. Generalized reduced basis methods and n-width estimates for the approximation of the solution manifold of parametric PDEs. In *Analysis and Numerics of Partial Differential Equations*, pages 307–329. Springer, 2013.

[LMQ+13b] T. Lassila, A. Manzoni, A. Quarteroni, and G. Rozza. A reduced computational and geometrical framework for inverse problems in hemodynamics. *International Journal for Numerical Methods in Biomedical Engineering*, 29(7):741–776, 2013.

[LNN+11] P. Lamata, S. Niederer, D. Nordsletten, D. C. Barber, I. Roy, D. Hose, and N. Smith. An accurate, fast and robust method to generate patient-specific cubic hermite meshes. *Medical image analysis*, 15(6):801–813, 2011.

[LSK13] A. Lipponen, A. Seppänen, and J. Kaipio. Electrical impedance tomography imaging with reduced-order model based on proper orthogonal decomposition. *Journal of Electronic Imaging*, 22(2):8–23, 2013.

[LSZ15] K. Law, A. Stuart, and K. Zygalakis. *Data Assimilation: A Mathematical Introduction*. Texts in Applied Mathematics. Springer International Publishing, 2015.

[Lue71] D. Luenberger. An introduction to observers. *IEEE Transactions on Automatic Control*, 16(6):596–602, 1971.

[Man14] A. Manzoni. An efficient computational framework for reduced basis approximation and a posteriori error estimation of parametrized Navier–Stokes flows. *ESAIM: Mathematical Modelling and Numerical Analysis*, 48(4):1199–1226, 2014.

[MBG+16] D. Mozaffarian, E. J. Benjamin, A. S. Go, D. K. Arnett, M. J. Blaha, M. Cushman, S. R. Das, S. de Ferranti, J.-P. Després, H. J. Fullerton, V. J. Howard, M. D. Huffman, C. R. Isasi, M. C. Jiménez, S. E. Judd, B. M. Kissela, J. H. Lichtman, L. D. Lisabeth, S. Liu, R. H. Mackey, D. J. Magid, D. K. McGuire, E. R. Mohler, C. S. Moy, P. Muntner, M. E. Mussolino, K. Nasir, R. W. Neumar, G. Nichol, L. Palaniappan, D. K. Pandey, M. J. Reeves, C. J. Rodriguez, W. Rosamond, P. D. Sorlie, J. Stein, A. Towfighi, T. N. Turan, S. S. Virani, D. Woo, R. W. Yeh, and M. B. Turner. Heart disease and stroke statistics—2016 update. *Circulation*, 133(4):38–360, 2016.

[MC11] P. Moireau and D. Chapelle. Reduced-order unscented Kalman filtering with application to parameter identification in large-dimensional systems. *ESAIM: Control, Optimisation and Calculus of Variations*, 17(2):380–405, 2011.

[MCLT08] P. Moireau, D. Chapelle, and P. Le Tallec. Joint state and parameter estimation for distributed mechanical systems. *Computer methods in applied mechanics and engineering*, 197(6):659–677, 2008.

[MCLT09] P. Moireau, D. Chapelle, and P. Le Tallec. Filtering for distributed mechanical systems using position measurements: perspectives in medical imaging. *Inverse problems*, 25(3):035010, 2009.

[MDS+13a] S. Marchesseau, H. Delingette, M. Sermesant, and N. Ayache. Fast parameter calibration of a cardiac electromechanical model from medical images based on the unscented transform. *Biomechanics and modeling in mechanobiology*, 12(4):815–831, 2013.

[MDS+13b] S. Marchesseau, H. Delingette, M. Sermesant, R. Cabrera-Lozoya, C. Tobon-Gomez, P. Moireau, R. F. i Ventura, K. Lekadir, A. Hernandez, M. Garreau, et al. Personalization of a cardiac electromechanical model using reduced order unscented Kalman filtering from regional volumes. *Medical image analysis*, 17(7):816–829, 2013.

[MF15] A. L. Marsden and J. A. Feinstein. Computational modeling and engineering in pediatric and congenital heart disease. *Current opinion in pediatrics*, 27(5):587–596, 2015.

[MH89] C. E. Miller and C. S. Henriquez. Finite element analysis of bioelectric phenomena. *Critical Reviews in Biomedical Engineering*, 18(3):207–233, 1989.

[MHP02] H. L. Mitchell, P. Houtekamer, and G. Pellerin. Ensemble size, balance, and model-error representation in an ensemble Kalman filter. *Monthly weather review*, 130(11):2791–2808, 2002.

[MMT16] Y. Maday, O. Mula, and G. Turinici. Convergence analysis of the generalized empirical interpolation method. *SIAM Journal on Numerical Analysis*, 54(3):1713–1731, 2016.

[MN09] Y. M. Marzouk and H. N. Najm. Dimensionality reduction and polynomial chaos acceleration of Bayesian inference in inverse problems. *Journal of Computational Physics*, 228(6):1862–1902, 2009.

[MN15] A. Manzoni and F. Negri. Heuristic strategies for the approximation of stability factors in quadratically nonlinear parametrized PDEs. *Advances in Computational Mathematics*, 41(5):1255–1288, 2015.

[MNP+09] Y. Maday, N. C. Nguyen, A. T. Patera, and S. H. Pau. A general multipurpose interpolation procedure: the magic points. *Communications on Pure and Applied Analysis*, 8(1):383–404, 2009.

[MPG+16] G. R. Mirams, P. Pathmanathan, R. A. Gray, P. Challenor, and R. H. Clayton. White paper: uncertainty and variability in computational and mathematical models of cardiac physiology. *The Journal of physiology*, 2016.

[MPL16] A. Manzoni, S. Pagani, and T. Lassila. Accurate solution of Bayesian inverse uncertainty quantification problems combining reduced basis methods and reduction error models. *SIAM/ASA Journal on Uncertainty Quantification*, 4(1):380–412, 2016.

[MQR12] A. Manzoni, A. Quarteroni, and G. Rozza. Model reduction techniques for fast blood flow simulation in parametrized geometries. *International Journal for Numerical Methods in Biomedical Engineering*, 28(6-7):604–625, 2012.

[MS03] C. C. Mitchell and D. G. Schaeffer. A two-current model for the dynamics of cardiac membrane. *Bulletin of Mathematical Biology*, 65(5):767–793, 2003.

[MSDR13] A. Menafoglio, P. Secchi, and M. Dalla Rosa. A universal kriging predictor for spatially dependent functional data of a hilbert space. *Electronic Journal of Statistics*, 7:2209–2240, 2013.

[MVCDB98] N. Maglaveras, F. Van Capelle, and J. De Bakker. Wave propagation simulation in normal and infarcted myocardium: Computational and modelling issues. *Medical Informatics*, 23(2):105–118, 1998.

[MWB+12] J. Martin, L. C. Wilcox, C. Burstedde, and O. Ghattas. A stochastic Newton MCMC method for large-scale statistical inverse problems with application to seismic inversion. *SIAM Journal on Scientific Computing*, 34(3):1460–1487, 2012.

[MX09] Y. Marzouk and D. Xiu. A stochastic collocation approach to Bayesian inference in inverse problems. *Communications in Computational Physics*, 6(4):826–847, 2009.

[Naj09] H. N. Najm. Uncertainty quantification and polynomial chaos techniques in computational fluid dynamics. *Annual Review of Fluid Mechanics*, 41:35–52, 2009.

[NAY62] J. Nagumo, S. Arimoto, and S. Yoshizawa. An active pulse transmission line simulating nerve axon. *Proceedings of the IRE*, 50(10):2061–2070, 1962.

[NBG+13] A. Nagler, C. Bertoglio, M. Gee, and W. Wall. Personalization of cardiac fiber orientations from image data using the unscented Kalman filter. In *International Conference on Functional Imaging and Modeling of the Heart*, pages 132–140. Springer, 2013.

[NCD+15] E. Nadal, F. Chinesta, P. Díez, F. Fuenmayor, and F. Denia. Real time parameter identification and solution reconstruction from experimental data using the proper generalized decomposition. *Computer Methods in Applied Mechanics and Engineering*, 296:113–128, 2015.

[NE12] L. W.-T. Ng and M. Eldred. Multifidelity uncertainty quantification using nonintrusive polynomial chaos and stochastic collocation. In *Proceedings of the 14th AIAA Non-Deterministic Approaches Conference, number AIAA-2012-1852, Honolulu, HI*, volume 43, 2012.

[Neg16] F. Negri. redbKIT Version 1.0. http://redbkit.github.io/redbKIT/, 2016.

[NFN+09] S. Niederer, M. Fink, D. Noble, and N. Smith. A meta-analysis of cardiac electrophysiology computational models. *Experimental physiology*, 94(5):486–495, 2009.

[NHS08] D. Nordsletten, P. Hunter, and N. Smith. Conservative and non-conservative arbitrary lagrangian–eulerian forms for ventricular flows. *International journal for numerical methods in fluids*, 56(8):1457–1463, 2008.

[NK09] M. L. Neal and R. Kerckhoffs. Current progress in patient-specific modeling. *Briefings in bioinformatics*, 2009.

[NK11] C. Nagaiah and K. Kunisch. Higher order optimization and adaptive numerical solution for optimal control of monodomain equations in cardiac electrophysiology. *Applied numerical mathematics*, 61(1):53–65, 2011.

[NKB+11] S. A. Niederer, E. Kerfoot, A. P. Benson, M. O. Bernabeu, O. Bernus, C. Bradley, E. M. Cherry, R. Clayton, F. H. Fenton, A. Garny, et al. Verification of cardiac tissue electrophysiology simulators using an n-version benchmark. *Phil. Trans. R. Soc. A*, 369(1954):4331–4351, 2011.

[NLT07] B. F. Nielsen, M. Lysaker, and A. Tveito. On the use of the resting potential and level set methods for identifying ischemic heart disease: An inverse problem. *Journal of Computational Physics*, 220(2):772–790, 2007.

[NMA15] F. Negri, A. Manzoni, and D. Amsallem. Efficient model reduction of parametrized systems by matrix discrete empirical interpolation. *Journal of Computational Physics*, 303:431–454, 2015.

[NMK+11] D. Nordsletten, M. McCormick, P. Kilner, P. Hunter, D. Kay, and N. Smith. Fluid–solid coupling for the investigation of diastolic and systolic human left ventricular function. *International Journal for Numerical Methods in Biomedical Engineering*, 27(7):1017–1039, 2011.

[NNN+11] D. Nordsletten, S. Niederer, M. Nash, P. Hunter, and N. Smith. Coupling multi-physics models to cardiac mechanics. *Progress in Biophysics and Molecular Biology*, 104(1):77–88, 2011.

[Nob62] D. Noble. A modification of the Hodgkin–Huxley equations applicable to purkinje fibre action and pacemaker potentials. *The Journal of Physiology*, 160(2):317–352, 1962.

[Nou09] A. Nouy. Recent developments in spectral stochastic methods for the numerical solution of stochastic partial differential equations. *Archives of Computational Methods in Engineering*, 16(3):251–285, 2009.

[NRL+07] B. F. Nielsen, T. S. Ruud, G. T. Lines, and A. Tveito. Optimal monodomain approximations of the bidomain equations. *Applied Mathematics and Computation*, 184(2):276–290, 2007.

[NT15] F. Nobile and F. Tesei. A multi level Monte Carlo method with control variate for elliptic PDEs with log-normal coefficients. *Stochastic Partial Differential Equations: Analysis and Computations*, 3(3):398–444, 2015.

[NTW08] F. Nobile, R. Tempone, and C. G. Webster. A sparse grid stochastic collocation method for partial differential equations with random input data. *SIAM Journal on Numerical Analysis*, 46(5):2309–2345, 2008.

[OO04] J. E. Oakley and A. O'Hagan. Probabilistic sensitivity analysis of complex models: a Bayesian approach. *Journal of the Royal Statistical Society: Series B (Statistical Methodology)*, 66(3):751–769, 2004.

[OR15] M. Ohlberger and S. Rave. Reduced basis methods: Success, limitations and future challenges. *arXiv preprint arXiv:1511.02021*, 2015.

[OVV+11] T. O'Hara, L. Virág, A. Varró, and Y. Rudy. Simulation of the undiseased human cardiac ventricular action potential: Model formulation and experimental validation. *PLoS Comput Biol*, 7(5):1–29, 05 2011.

[PBW+14] B. Peherstorfer, D. Butnaru, K. Willcox, and H.-J. Bungartz. Localized discrete empirical interpolation method. *SIAM Journal on Scientific Computing*, 36(1):168–192, 2014.

[PCB05] A. J. Pullan, L. K. Cheng, and M. L. Buist. *Mathematically modelling the electrical activity of the heart: From cell to body surface and back again*. World Scientific, 2005.

[PDR+06] M. Potse, B. Dubé, J. Richer, A. Vinet, and R. M. Gulrajani. A comparison of monodomain and bidomain reaction-diffusion models for action potential propagation in the human heart. *IEEE Transactions on Biomedical Engineering*, 53(12):2425–2435, 2006.

[PDV09] M. Potse, B. Dubé, and A. Vinet. Cardiac anisotropy in boundary-element models for the electrocardiogram. *Medical & Biological Engineering & Computing*, 47(7):719–729, 2009.

[PHS16] S. Pezzuto, J. Hake, and J. Sundnes. Space-discretization error analysis and stabilization schemes for conduction velocity in cardiac electrophysiology. *International Journal for Numerical Methods in Biomedical Engineering*, 32(10):2040–7947, 2016.

[PKK+14] M. Potse, D. Krause, W. Kroon, R. Murzilli, S. Muzzarelli, F. Regoli, E. Caiani, F. W. Prinzen, R. Krause, and A. Auricchio. Patient-specific modelling of cardiac electrophysiology in heart-failure patients. *Europace*, 16(suppl 4):iv56–iv61, 2014.

[PL15] S. Pant and D. Lombardi. An information-theoretic approach to assess practical identifiability of parametric dynamical systems. *Mathematical biosciences*, 268:66–79, 2015.

[PLdS+07] G. Plank, M. Liebmann, R. W. dos Santos, E. J. Vigmond, and G. Haase. Algebraic multigrid preconditioner for the cardiac bidomain model. *IEEE Transactions on Biomedical Engineering*, 54(4):585–596, 2007.

[PMQ16] S. Pagani, A. Manzoni, and A. Quarteroni. A reduced basis ensemble Kalman filter for state/parameter identification in large-scale nonlinear dynamical systems. *MOX-Report No. 24/2016*, 2016.

[PRV+02] C. Prud'homme, D. V. Rovas, K. Veroy, L. Machiels, Y. Maday, A. T. Patera, and G. Turinici. Reliable real-time solution of parametrized partial differential equations: Reduced-basis output bound methods. *Journal of Fluids Engineering*, 124(1):70–80, 2002.

[PSA+14] A. Prakosa, M. Sermesant, P. Allain, N. Villain, C. A. Rinaldi, K. Rhode, R. Razavi, H. Delingette, and N. Ayache. Cardiac electrophysiological activation pattern estimation from images using a patient-specific database of synthetic image sequences. *IEEE Transactions on Biomedical Engineering*, 61(2):235–245, 2014.

[PSCF05] M. Pennacchio, G. Savaré, and P. Colli Franzone. Multiscale modeling for the bioelectric activity of the heart. *SIAM Journal on Mathematical Analysis*, 37(4):1333–1370, 2005.

[PSG+15] P. Pathmanathan, M. S. Shotwell, D. J. Gavaghan, J. M. Cordeiro, and R. A. Gray. Uncertainty quantification of fast sodium current steady-state inactivation for multi-scale models of cardiac electrophysiology. *Progress in Biophysics and Molecular Biology*, 117(1):4 – 18, 2015. Multi-scale Systems Biology.

[PWG15] B. Peherstorfer, K. Willcox, and M. Gunzburger. Optimal model management for multifidelity Monte Carlo estimation. *Technical report 15–2, Aerospace Computational Design Laboratory, MIT*, 2015.

[PWG16] B. Peherstorfer, K. Willcox, and M. Gunzburger. Survey of multifidelity methods in uncertainty propagation, inference, and optimization. *ACDL Technical Report TR16-1*, 2016.

[QHS+05] N. V. Queipo, R. T. Haftka, W. Shyy, T. Goel, R. Vaidyanathan, and P. K. Tucker. Surrogate-based analysis and optimization. *Progress in Aerospace Sciences*, 41(1):1–28, 2005.

[QLR+16] A. Quarteroni, T. Lassila, S. Rossi, and R. Ruiz-Baier. Integrated heart–coupling multiscale and multiphysics models for the simulation of the cardiac function. *Computer Methods in Applied Mechanics and Engineering*, 2016.

[QMN16] A. Quarteroni, A. Manzoni, and F. Negri. Reduced basis methods for partial differential equations. La Matematica per il 3+2. Springer International Publishing, 2016.

[Qua15] A. Quarteroni. *Modeling the Heart and the Circulatory System*, volume 14 of *MS&A*. Springer, 2015.

[RAP14] O. Roderick, M. Anitescu, and Y. Peet. Proper orthogonal decompositions in multifidelity uncertainty quantification of complex simulation models. *International Journal of Computer Mathematics*, 91(4):748–769, 2014.

[RC13] C. Robert and G. Casella. *Monte Carlo statistical methods*. Springer Science & Business Media, 2013.

[RCS+11] J. Relan, P. Chinchapatnam, M. Sermesant, K. Rhode, M. Ginks, H. Delingette, C. A. Rinaldi, R. Razavi, and N. Ayache. Coupled personalization of cardiac electrophysiology models for prediction of ischaemic ventricular tachycardia. *Interface Focus*, 1(3):396–407, 2011.

[RER+15] M. Rochoux, C. Emery, S. Ricci, B. Cuenot, and A. Trouvé. Towards predictive data-driven simulations of wildfire spread–part ii: Ensemble Kalman filter for the state estimation of a front-tracking simulator of wildfire spread. *Natural Hazards and Earth System Science*, 15(8):1721–1739, 2015.

[RHP08] G. Rozza, D. B. P. Huynh, and A. T. Patera. Reduced basis approximation and a posteriori error estimation for affinely parametrized elliptic coercive partial differential equations. *Archives of Computational Methods in Engineering*, 15(3):229–275, 2008.

[RM85] R. Y. Rubinstein and R. Marcus. Efficiency of multivariate control variates in Monte Carlo simulation. *Operations Research*, 33(3):661–677, 1985.

[RME02] R. H. Reichle, D. B. McLaughlin, and D. Entekhabi. Hydrologic data assimilation with the ensemble Kalman filter. *Monthly Weather Review*, 130(1):103–114, 2002.

[Rot71] T. J. Rothenberg. Identification in parametric models. *Econometrica: Journal of the Econometric Society*, pages 577–591, 1971.

[RW06] C. Rasmussen and C. Williams. *Gaussian Processes for Machine Learning*. Adaptative computation and machine learning series. University Press Group Limited, 2006.

[SCC+11] M. Sermesant, R. Chabiniok, P. Chinchapatnam, T. Mansi, F. Billet, P. Moireau, J. Peyrat, K. Wong, J. Relan, K. Rhode, et al. Patient-specific electromechanical models of the heart for the prediction of pacing acute effects in crt: A preliminary clinical validation. *Medical image analysis*, 2011.

[SCG16] E. Schenone, A. Collin, and J.-F. Gerbeau. Numerical simulation of electrocardiograms for full cardiac cycles in healthy and pathological conditions. *International Journal for Numerical Methods in Biomedical Engineering*, 32(5):27–44, 2016.

[SCH+16] A. Solonen, T. Cui, J. Hakkarainen, and Y. Marzouk. On dimension reduction in Gaussian filters. *Inverse Problems*, 32(4):045003, 2016.

[SCS+00] A. Saltelli, K. Chan, E. M. Scott, et al. *Sensitivity analysis*, volume 1. Wiley New York, 2000.

[SdVM+11] N. Smith, A. de Vecchi, M. McCormick, D. Nordsletten, O. Camara, A. F. Frangi, H. Delingette, M. Sermesant, J. Relan, N. Ayache, M. W. Krueger, W. H. W. Schulze, R. Hose, I. Valverde, P. Beerbaum, C. Staicu, M. Siebes, J. Spaan, P. Hunter, J. Weese, H. Lehmann, D. Chapelle, and R. Rezavi. euheart: personalized and integrated cardiac care using patient-specific cardiovascular modelling. *Interface Focus*, 2011.

[SGS+11] D. J. Swenson, S. E. Geneser, J. G. Stinstra, R. M. Kirby, and R. S. MacLeod. Cardiac position sensitivity study in the electrocardiographic forward problem using stochastic collocation and boundary element methods. *Annals of biomedical engineering*, 39(12):2900–2910, 2011.

[Sha01] C. E. Shannon. A mathematical theory of communication. *ACM SIGMOBILE Mobile Computing and Communications Review*, 5(1):3–55, 2001.

[SHM05] J. G. Stinstra, B. Hopenfeld, and R. S. MacLeod. On the passive cardiac conductivity. *Annals of biomedical engineering*, 33(12):1743–1751, 2005.

[Sim06] D. Simon. *Optimal state estimation: Kalman, H infinity, and nonlinear approaches*. John Wiley & Sons, 2006.

[SLC+07] J. Sundnes, G. T. Lines, X. Cai, B. F. Nielsen, K.-A. Mardal, and A. Tveito. *Computing the electrical activity in the heart*, volume 1. Springer Science & Business Media, 2007.

[SLT05] J. Sundnes, G. T. Lines, and A. Tveito. An operator splitting method for solving the bidomain equations coupled to a volume conductor model for the torso. *Mathematical Biosciences*, 194(2):233–248, 2005.

[SMC+06] M. Sermesant, P. Moireau, O. Camara, J. Sainte-Marie, R. Andriantsimiavona, R. Cimrman, D. L. Hill, D. Chapelle, and R. Razavi. Cardiac function estimation from MRI using a heart model and data assimilation: Advances and difficultiesmri using a heart model and data assimilation: advances and difficulties. *Medical Image Analysis*, 10(4):642–656, 2006.

[SMCC+06] J. Sainte-Marie, D. Chapelle, R. Cimrman, and M. Sorine. Modeling and estimation of the cardiac electromechanical activity. *Computers & structures*, 84(28):1743–1759, 2006.

[Smi13] R. C. Smith. *Uncertainty quantification: theory, implementation, and applications*, volume 12. SIAM, 2013.

[SNC+04] N. Smith, D. Nickerson, E. Crampin, and P. Hunter. Multiscale computational modelling of the heart. *Acta Numerica*, 13:371–431, 2004.

[SPD98] R. J. Schilling, N. S. Peters, and D. W. Davies. Simultaneous endocardial mapping in the human left ventricle using a noncontact catheter comparison of contact and reconstructed electrograms during sinus rhythm. *Circulation*, 98(9):887–898, 1998.

[SR97] R. M. Shaw and Y. Rudy. Electrophysiologic effects of acute myocardial ischemia: a theoretical study of altered cell excitability and action potential duration. *Cardiovascular Research*, 35(2):256–272, 1997.

[SRA+08] A. Saltelli, M. Ratto, T. Andres, F. Campolongo, J. Cariboni, D. Gatelli, M. Saisana, and S. Tarantola. *Global sensitivity analysis: the primer*. John Wiley & Sons, 2008.

[SRSO+05] M. Sermesant, K. Rhode, G. I. Sanchez-Ortiz, O. Camara, R. Andriantsimiavona, S. Hegde, D. Rueckert, P. Lambiase, C. Bucknall, E. Rosenthal, et al. Simulation of cardiac pathologies using an electromechanical biventricular model and XMR interventional imaging. *Medical image analysis*, 9(5):467–480, 2005.

[ŞS16] R. Ştefănescu and A. Sandu. Efficient approximation of sparse jacobians for time-implicit reduced order models. *International Journal for Numerical Methods in Fluids*, 2016.

[SSH+09] C. B. Storlie, L. P. Swiler, J. C. Helton, and C. J. Sallaberry. Implementation and evaluation of nonparametric regression procedures for sensitivity analysis of computationally demanding models. *Reliability Engineering & System Safety*, 94(11):1735–1763, 2009.

[ST02] A. Saltelli and S. Tarantola. On the relative importance of input factors in mathematical models: safety assessment for nuclear waste disposal. *Journal of the American Statistical Association*, 97(459):702–709, 2002.

[Stu10] A. M. Stuart. Inverse problems: a Bayesian perspective. *Acta Numerica*, 19:451–559, 2010.

[Sud08] B. Sudret. Global sensitivity analysis using polynomial chaos expansions. *Reliability Engineering & System Safety*, 93(7):964–979, 2008.

[Sul15] T. J. Sullivan. *Introduction to uncertainty quantification*, volume 63. Springer, 2015.

[SVN+05] Z. Syed, E. Vigmond, S. Nattel, and L. Leon. Atrial cell action potential parameter fitting using genetic algorithms. *Medical and Biological Engineering and Computing*, 43(5):561–571, 2005.

[SWN13] T. J. Santner, B. J. Williams, and W. I. Notz. *The design and analysis of computer experiments*. Springer Science & Business Media, 2013.

[Tar05] A. Tarantola. *Inverse problem theory and methods for model parameter estimation: SIAM*. Society for Industrial and Applied Mathematics, 2005.

[TAW07] K. Thygesen, J. S. Alpert, and H. D. White. Universal definition of myocardial infarction. *Journal of the American College of Cardiology*, 50(22):2173–2195, 2007.

[TDQ15] A. Tagliabue, L. Dede, and A. Quarteroni. Fluid dynamics of an idealized left ventricle: the extended Nitsche's method for the treatment of heart valves as mixed time varying boundary conditions. *MOX-Report No. 61/2015*, 2015.

[TMD+13] H. Talbot, S. Marchesseau, C. Duriez, M. Sermesant, S. Cotin, and H. Delingette. Towards an interactive electromechanical model of the heart. *Interface focus*, 3(2):20120091, 2013.

[Tra11] N. A. Trayanova. Whole-heart modeling applications to cardiac electrophysiology and electromechanics. *Circulation research*, 108(1):113–128, 2011.

[TSC+16] N. Tarabelloni, E. Schenone, A. Collin, F. Ieva, A. Paganoni, and J.-F. Gerbeau. Statistical assessment and calibration of numerical ECG models. *MOX-Report No. 32/2016*, 2016.

[TSD+] H. Talbot, F. Spadoni, C. Duriez, M. Sermesant, M. O'Neill, P. Jaïs, S. Cotin, and H. Delingette. Interactive training system for interventional electrocardiology procedures. *Medical Image Analysis*, 35:225–237, 2017/01/06.

[TSR+16] J. S. Tran, D. E. Schiavazzi, A. B. Ramachandra, A. M. Kahn, and A. L. Marsden. Automated tuning for parameter identification and uncertainty quantification in multi-scale coronary simulations. *Computers & Fluids*, ahead of print, 2016.

[VAP+10] F. Vadakkumpadan, H. Arevalo, A. J. Prassl, J. Chen, F. Kickinger, P. Kohl, G. Plank, and N. Trayanova. Image-based models of cardiac structure in health and disease. *Wiley Interdisciplinary Reviews: Systems Biology and Medicine*, 2(4):489–506, 2010.

[VAT02] E. J. Vigmond, F. Aguel, and N. A. Trayanova. Computational techniques for solving the bidomain equations in three dimensions. *IEEE Transactions on Biomedical Engineering*, 49(11):1260–1269, 2002.

[VDSP+08] E. Vigmond, R. W. Dos Santos, A. Prassl, M. Deo, and G. Plank. Solvers for the cardiac bidomain equations. *Progress in Biophysics and Molecular Biology*, 96(1):3–18, 2008.

[Ver03] K. Veroy. *Reduced-basis methods applied to problems in elasticity: Analysis and applications.* PhD thesis, Massachusetts Institute of Technology, 2003.

[VGG+15] K. Vincent, M. Gonzales, A. Gillette, C. Villongco, S. Pezzuto, J. Omens, M. Holst, and A. McCulloch. High-order finite element methods for cardiac monodomain simulations. *Frontiers in Physiology*, 6:217, 2015.

[VLC11] P. Valensi, L. Lorgis, and Y. Cottin. Prevalence, incidence, predictive factors and prognosis of silent myocardial infarction: a review of the literature. *Archives of Cardiovascular Diseases*, 104(3):178–188, 2011.

[VP05] K. Veroy and A. T. Patera. Certified real-time solution of the parametrized steady incompressible Navier–Stokes equations: rigorous reduced-basis a posteriori error bounds. *International Journal for Numerical Methods in Fluids*, 47(8-9):773–788, 2005.

[VPR+03] K. Veroy, C. Prud'Homme, D. V. Rovas, and A. T. Patera. A posteriori error bounds for reduced-basis approximation of parametrized noncoercive and nonlinear elliptic partial differential equations. In *Proceedings of the 16th AIAA Computational Fluid Dynamics conference*, volume 3847, pages 23–26, 2003.

[WJ63] J. H. Ward Jr. Hierarchical grouping to optimize an objective function. *Journal of the American statistical association*, 58(301):236–244, 1963.

[WKM+13] D. Wang, R. M. Kirby, R. S. MacLeod, and C. R. Johnson. Inverse electrocardiographic source localization of ischemia: an optimization framework and finite element solution. *Journal of computational physics*, 250:403–424, 2013.

[WP02] K. Willcox and J. Peraire. Balanced model reduction via the proper orthogonal decomposition. *AIAA journal*, 40(11):2323–2330, 2002.

[WTG+12] R. L. Winslow, N. Trayanova, D. Geman, and M. I. Miller. Computational medicine: translating models to clinical care. *Science translational medicine*, 4(158), 2012.

[XK02] D. Xiu and G. E. Karniadakis. The Wiener–Askey polynomial chaos for stochastic differential equations. *SIAM Journal on Scientific Computing*, 24(2):619–644, 2002.

[XW05] R. Xu and D. Wunsch. Survey of clustering algorithms. *IEEE Transactions on Neural Networks*, 16(3):645–678, 2005.

[Yan16] F. G. Yanowitz. *Introduction to ECG interpretation.* http://ecg.utah.edu/pdf/, 2016.

[YFR+05] A. M. Yue, M. R. Franz, P. R. Roberts, and J. M. Morgan. Global endocardial electrical restitution in human right and left ventricles determined by noncontact mapping. *Journal of the American College of Cardiology*, 46(6):1067–1075, 2005.

[YV16] H. Yang and A. Veneziani. Efficient estimation of cardiac conductivities via POD-DEIM model order reduction. *arXiv:1603.05722v2*, 2016.